

THE BELL SYSTEM TECHNICAL JOURNAL

VOLUME XLIII

MARCH 1964

NUMBER 2

Copyright 1964, American Telephone and Telegraph Company

Importance of Intrasublattice Magnetic Interactions and of Substitutional Ion Type in the Behavior of Substituted Yttrium Iron Garnets

By S. GELLER, H. J. WILLIAMS, G. P. ESPINOSA
and R. C. SHERWOOD

(Manuscript received November 6, 1963)

The results of measurements at moderate to high magnetic fields on a large number of nonmagnetic ion substituted yttrium iron garnets suggest that intrasublattice interactions play an important role in determining their spontaneous magnetizations and Curie temperatures. It is shown that the system $\{Y_{3-x}Ca_x\}[Fe_2](Fe_{3-x}Si_x)O_{12}$ is continuously related to the system $\{Y_{3-x}Ca_x\}[Zr_xFe_{2-x}](Fe_3)O_{12}$ or $\{Y_3\}[Sc_xFe_{2-x}](Fe_3)O_{12}$. It is concluded that in these systems the tetrahedral-tetrahedral (d-d) antiferromagnetic interactions are stronger than octahedral-octahedral (a-a) antiferromagnetic interactions. The changes in magnetic structure from an ideal ferrimagnet, yttrium iron garnet, to an end-member in which there are at least short-range antiferromagnetic interactions (i.e., in $\{Ca_3\}[Fe_2](Si_3)O_{12}$ or a hypothetical $\{YCa_2\}[Zr_2](Fe_3)O_{12}$) should bear an analogy to the crystal chemical changes. It is therefore proposed that when substitution is made exclusively in one sublattice, the moments of the Fe^{3+} ions in that sublattice remain parallel (as in the Yafet-Kittel theory), while the weakened average a-d interactions and the intrasublattice interactions lead to random canting of the Fe^{3+} ion moments of the other. This tendency occurs as soon as substitution begins. On continued substitution, a point is reached beyond which canting increases much more rapidly with increasing substitution. In this region, the intrasublattice interactions dominate the a-d interactions, but it is probable that the canting continues to be random.

In the $\{Y_3\}[Mg_xFe_{2-x}](Fe_{3-x}Si_x)O_{12}$ system, the point at which the tetrahedral intrasublattice interactions dominate is reached at about $x = 0.95$ as contrasted with $x \approx 0.70$ for the $\{Y_{3-x}Ca_x\}[Zr_xFe_{2-x}](Fe_3)O_{12}$ and $\{Y_3\}[Sc_xFe_{2-x}](Fe_3)O_{12}$ systems. The canting of the d-site ion moments increases at the same rate in the three systems to $x \approx 0.70$, but beyond this point, the canting in the Mg-Si substituted YIG is always substantially less than for the other two systems. This together with data on other substituted garnets indicates that the substitution of the Si^{4+} ions in the d-sites tends to decrease the average d-d interaction strength. Similarly, substitution in the a sites tends to decrease the average a-a interaction strength.

Measurements on some garnets in the systems $\{Y_{3-y}Ca_y\}[Sc_xFe_{2-x}]$ - $(Si_yFe_{3-y})O_{12}$, $\{Y_{3-y+x}Ca_{y-x}\}[Mg_xFe_{2-x}](Fe_{3-y}Si_y)O_{12}$ and $\{Y_{3-x-y}Ca_{x+y}\}$ - $[Zr_xFe_{2-x}](Si_yFe_{3-y})O_{12}$ indicate that different nonmagnetic ions may produce different magnetic behavior. This is especially noticeable in the region in which the intrasublattice interactions are dominant. Comparative behavior of the systems $\{Y_3\}[Sc_xFe_{2-x}](Fe_3)O_{12}$ and $\{Y_{3-x}Ca_x\}[Zr_xFe_{2-x}]$ - $(Fe_3)O_{12}$ and of the systems $\{Y_{3-x}Ca_x\}[Fe_2](Fe_{3-x}M_x)O_{12}$, $M \equiv Si$ and Ge , also indicates that the ion type is important in determining magnetic behavior. It is speculated that this results from effects on the interaction geometry, especially when the interactions are weak.

Results on garnets in systems $\{Y_{3-y}Ca_y\}[Sc_xFe_{2-x}](Fe_{3-y}Si_y)O_{12}$, $\{Y_{3-y+x}Ca_{y-x}\}[Mg_xFe_{2-x}](Fe_{3-y}Si_y)O_{12}$, and $\{Y_{3-x-y}Ca_{x+y}\}[Zr_xFe_{2-x}]$ - $(Si_yFe_{3-y})O_{12}$ also aided in substantiating the other ideas put forward as well as in determining the distribution of ions in the system $\{Y_3\}Fe_{5-x}Al_xO_{12}$, on which more extensive studies than heretofore were made. Some anomalies occur in this system for values of $x > 2.0$.

Application of the ideas derived from these studies are made to the ferrospinsels, and it is shown that one may thereby account for the high Curie temperature of lithium ferrite, the lower Curie temperature of nickel ferrite, and the substantially lower Curie temperature and low $0^\circ K$ moment of manganese ferrite.

It is noted that although the ideas presented may account in a general way for the behavior of the Sb^{5+} and V^{5+} ion substituted garnets, their behavior could not have been quantitatively predicted from the results of the present work. It is probable that the chemical bonding of the Sb^{5+} and V^{5+} ions has much greater effects on the magnetic behavior than does that of the various ions treated in this paper.

I. INTRODUCTION

Studies of substitutions for iron ions in yttrium iron garnet of non-magnetic ions which prefer exclusively (or almost exclusively) octa-

hedral sites have been reported earlier.^{1,2} The results of the study of the tin-substituted yttrium iron garnets led to Gilleo's statistical treatment,³ which appeared to account well for the 0°K moments and Curie temperatures in this system as well as in those involving zirconium,² scandium,^{2,4} and indium^{2,4} substitutions. However, the data available at the time of these developments were still not sufficient for a complete test of the method.

The study of substituted yttrium iron garnets has now been extended to systems in which substitution for Fe³⁺ ions is made exclusively in the tetrahedral sites (i.e., {Y_{3-x}Ca_x}[Fe₂](Fe_{3-x}Si_x)O₁₂), equally in both octahedral and tetrahedral sites

(i.e., {Y₃}[Mg_xFe_{2-x}](Fe_{3-x}Si_x)O₁₂, {Y_{3-x}Ca_x}[Sc_xFe_{2-x}](Fe_{3-x}Si_x)O₁₂, and



and unequally in the two sites



and {Y_{3-x-y}Ca_{x+y}}[Zr_xFe_{2-x}](Fe_{3-y}Si_y)O₁₂). Analogous germanium-substituted systems have also been studied. The system {Y_{3-x}Ca_x}[Zr_xFe_{2-x}](Fe₃)O₁₂ has been reinvestigated and the study of the {Y₃}[Sc_xFe_{2-x}](Fe₃)O₁₂ system extended to larger values of *x*. High-field measurements have been made on specimens when required. The study of the system Y₃Al_xFe_{5-x}O₁₂⁴ has been extended to large values of *x*, and the distribution of the ions vs *x* deduced.

The results of these investigations indicate that the Gilleo treatment does not in general give good agreement with the observed 0°K moments of the substituted yttrium iron garnets. Application of the Yafet and Kittel theory⁵ to the tin-substituted garnets was made by de Gennes.⁶ Agreement of 0°K moments appeared to be good, although not nearly as good as that shown^{2,3} by the Gilleo theory. However, an arithmetic error was made in de Gennes' calculation; when corrected, the agreement deteriorates. Furthermore, using the same approach as that of de Gennes for the silicon-substituted garnets, that is, assuming the Pauthenet⁷ molecular field coefficients of yttrium iron garnet to remain constant for the whole system, no semblance of agreement is found.

Contrary to earlier assumptions, there is substantial evidence that *intralattice* interactions are not negligible; they appear to play an important role in determining the spontaneous magnetizations and Curie

temperatures of the substituted garnets. It also must be concluded that different nonmagnetic ions may produce different effects on the magnetic behavior when the amounts of substituent for the Fe^{3+} ions in particular sites are the same.

In the course of our study of the yttrium iron garnet-calcium iron silicate system, on which a preliminary report was made some time ago,⁸ we learned that Smolenskii, Polyakov, and Iodin⁹ had reported on this system. However, their magnetic measurements were made at 77°K and presumably they did not make any high-field measurements.

The above description should make it clear that the problem of the behavior of the substituted garnets has increased in complexity with the number of experiments performed. Following the completion of the draft form of this manuscript, new garnets containing Sb^{5+} (Ref. 10), V^{5+} (Refs. 10-12), and Bi^{3+} (Refs. 10, 12, 13) ions were discovered. (Many of these no longer contain yttrium or rare earth ions.) The magnetic behavior of these garnets was in part unpredictable from the results given in the present paper. However, there are unifying consistent features of the garnet systems described herein and we feel it worthwhile to describe them.

Complete understanding, it is felt, will eventually come from various studies of single crystals in the various systems. Neutron diffraction studies should play an important role, but also of utmost importance, it would appear, are spectroscopic studies which would give an insight into the effects of changes in chemical bonding on changes in magnetic interactions.

II. EXPERIMENTAL

2.1 Preparation of Specimens

As we have recently described in some detail our present techniques for specimen preparation,¹⁴ we shall not do so here. Utmost care is required in these preparations, including the use of pure starting materials, correction for adsorbed moisture or CO_2 in the starting materials, proper mixing and avoidance of inhomogeneous loss of constituents, the insuring of the theoretical weight losses on firing, the careful examination of powder photographs or diffractometer patterns to be sure that single phases, preferably sharply defined ones, are obtained, and careful measurement of lattice constants to be sure that these fit properly on the curves characterizing the systems. The preparation of the specimens in most cases required several regrindings and refirings.

2.2 Magnetic Measurements

Measurements of magnetic moment were made in the temperature range 1.4–298°K at applied fields, H_a , to 15.3 koe, by means of a pendulum magnetometer described elsewhere.¹⁵ Calibration was carried out with spectroscopically pure Ni; measurements on Mohr's salt¹⁶ corroborated the calibration with Ni.

Measurements at fields to 80 koe were made with the Bitter-type magnet and an extraction method used for determination of the moment. Calibration was carried out with spectroscopically pure Ni.

2.3 Crystallographic Measurements

Lattice constants were obtained from measurements of powder photographs taken with Norelco Straumanis-type cameras of 114.6-mm diameter and CrK radiation.

III. MAGNETIC AND CRYSTALLOGRAPHIC DATA

3.1 The Systems $\{Y_{3-x}Ca_x\}Fe_{5-x}M_x^{4+}O_{12}$, $M \equiv Si, Ge$

3.1.1 Magnetic Data

In the system $\{Y_{3-x}Ca_x\}Fe_{5-x}Si_xO_{12}$, specimens with $x \leq 1.77$ were saturated at fields ≤ 12.6 koe at 1.4°K. For $x \geq 1.88$, saturation was not attained at low fields, and therefore measurements were made at the high fields at 4.2°K. The specimen with $x = 1.88$ was saturated at 60 koe. None of the other specimens was saturated at fields below 80 koe and at 4.2°K. For these specimens the behavior of the magnetization at fields ≥ 50 koe was such that $n_B(H_a, T) = n_B(0, T) + \chi_n(H_a, T)H_a$; the values of $n_B(0, T)$ in these cases were determined by extrapolation to $H_a = 0$.

Typical curves of $n_B(H_a, T)$ vs T obtained with the pendulum magnetometer are shown in Figs. 1 and 2. When $x = 2.25$ (Fig. 2), the magnetization curves at the two higher fields appear to reach a maximum at about 40°K, then decrease, cutting the ordinate with positive slope. At 5 koe, the curve cuts the ordinate with zero slope. The curves for $x = 2.50$ behave similarly.

In Fig. 3, curves of n_B vs H_a at 4.2°K for $x = 2.00, 2.25$, and 2.50 are shown. For all these, measurements were made on sintered specimens. For $x = 2.25$, measurements were also made on the finely powdered specimen. Note that although the slope is greater for the sintered speci-

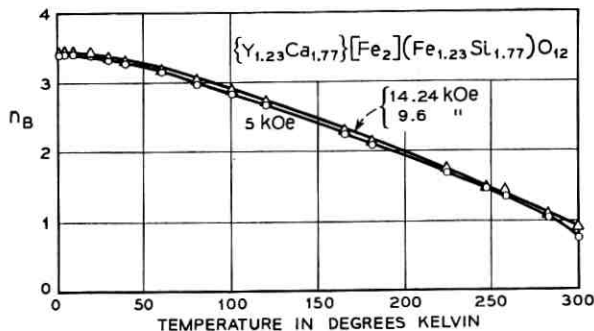


Fig. 1 — n_B vs T at different magnetic fields for $\{Y_{1.23}Ca_{1.77}\}[Fe_2](Fe_{1.23}Si_{1.77})O_{12}$.

men, extrapolation to $H_a = 0$ leads to insignificant difference in n_B . However, when a plot of n_B vs $1/H_a$ is extrapolated to $1/H_a = 0$, these values of n_B are 3.5 and 4.0 for the powdered and sintered specimens respectively.

In Table I, the spontaneous moments listed for specimens with $x \leq 1.77$ are extrapolated to 0°K; for specimens with $x \geq 1.88$, the values are those extrapolated to $H_a = 0$ at 4.2°K.¹⁷ These are plotted vs x in Fig. 4. Negative values of n_B mean that the moment of the octahedral sublattice is dominant.

Where possible, Curie temperatures (Table I and Fig. 5) were obtained from extrapolation of a plot of $n_B^2(0,T)$ vs T to $n_B^2(0,T) = 0$

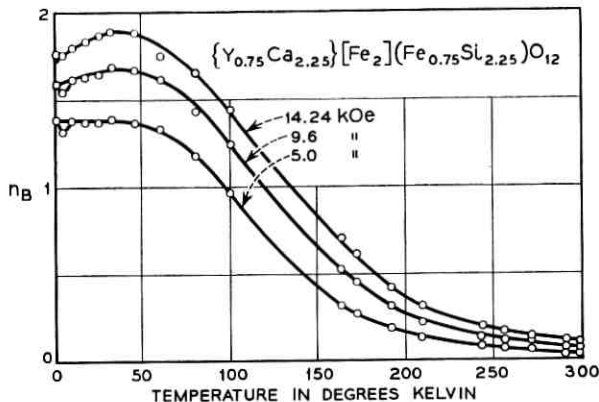


Fig. 2 — n_B vs T at different magnetic fields for $\{Y_{0.75}Ca_{2.25}\}[Fe_2](Fe_{0.75}Si_{2.25})O_{12}$.

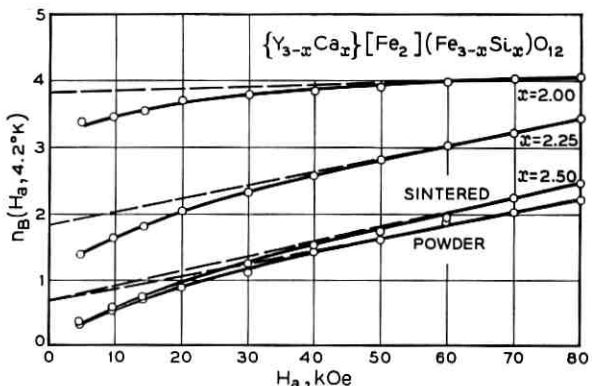


Fig. 3 — n_B vs applied field, H_a , at 4.2°K , for some specimens in the system $\{\text{Y}_{3-x}\text{Ca}_x\}[\text{Fe}_2](\text{Fe}_{3-x}\text{Si}_x)\text{O}_{12}$.

and from extrapolation of $1/\chi_n$ vs T to $1/\chi_n = 0$ when T_c was sufficiently below room temperature. (See Ref. 14.)

The garnet $\{\text{Ca}_3\}[\text{Fe}_2](\text{Si}_3)\text{O}_{12}$ cannot be made by solid-state reaction at atmospheric pressure. Small crystals were grown by Van Uitert and Bonner, and magnetic measurements were made on 2.99 g of these over

TABLE I — MAGNETIC AND CRYSTALLOGRAPHIC DATA FOR THE GARNETS $\{\text{Y}_{3-x}\text{Ca}_x\}\text{Fe}_{5-x}\text{M}_x^{4+}\text{O}_{12}$, $\text{M} \equiv \text{Si}, \text{Ge}$

x	$\text{M} \equiv \text{Si}$			$\text{M} \equiv \text{Ge}$		
	n_B^a	T_c ($^\circ\text{K}$)	$a(\text{\AA})$	n_B^a	T_c ($^\circ\text{K}$)	$a(\text{\AA})$
0.00	5.01	553 ^b	12.376 \pm 0.003	5.01	553 ^b	12.376 \pm 0.003
0.40	2.98	543 ^c	12.344			12.375
0.70						
0.75		508 ^c	12.314			
1.00	0.06		12.291	0.18		12.372
1.01	-0.07		12.291			
1.02	-0.14		12.291			
1.50	-2.36	367	12.243	-2.31	365	12.365
1.75	-3.40	312	12.212	-3.15	316	12.360
1.88	-3.8	280	12.202			
2.00	-3.8	266	12.186 \pm 0.005	-3.15	258	12.355
2.25	-1.9	180	12.157	-1.55	180	12.348 \pm 0.004
2.50	-0.65	86	12.126	-0.35	80 (?)	12.339
2.75			12.093 ^d	0		12.329
3.00	0		12.048 ^e \pm 0.003	0 ^f		12.320 ^g

^a For $\text{M} \equiv \text{Si}, \text{Ge}$ and $x < 1.88, 1.75$ respectively, values are those from extrapolation to 0°K ; for $x \geq 1.88, 1.75$ respectively, values are at 4.2°K , extrapolated to $H_a = 0$. ^b From J. Loriers and G. Villers, Compt. Rend., **252**, 1590 (1961).

^c Measured by E. A. Nesbitt. ^d Not single-phase: see text. ^e From Ref. 20. ^f From Ref. 21. ^g From Ref. 38.

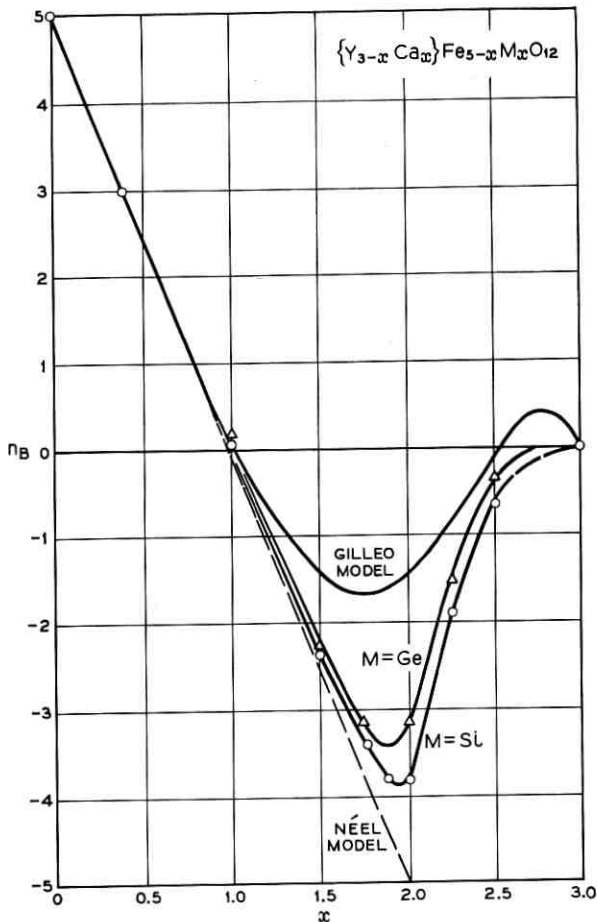


Fig. 4 — Spontaneous magnetizations vs composition for the silicon- and germanium-substituted yttrium iron garnets. For $x < 1.88$, saturation was attained at low fields and n_B values obtained by extrapolating $n_B(T)$ to $T = 0^\circ\text{K}$. For $x \geq 1.88$, saturation was not attained at low fields, and the n_B values were obtained by extrapolating $n_B(H_a)$ to $H_a = 0$ at 4.2°K (see Fig. 3). Shown also are the curves given by the Gilleo and Néel models for substitution by nonmagnetic ions exclusively on tetrahedral sites.

the temperature range 1.4 to 296°K . At a field of 5.0 koe, there was a peak in the susceptibility at about 9°K . However, the nature of the peak is not conclusive evidence of an antiferromagnetic transition. On the other hand, θ_p for the specimen is 29°K , which is indicative of antiferromagnetic interaction. The Curie constant $C = \Delta T / \Delta (1/\chi_n) = 1.47 \times 10^{-3}$, to be compared with the theoretical value of 1.56×10^{-3} .

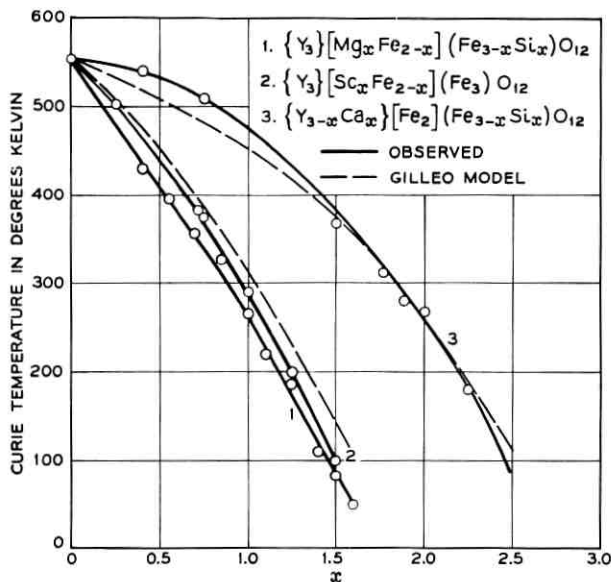


Fig. 5—Curie temperatures vs x for the systems (1) $\{Y_3\}[Mg_xFe_{2-x}](Fe_{3-x}Si_x)O_{12}$, (2) $\{Y_3\}[Sc_xFe_{2-x}](Fe_3)O_{12}$, (3) $\{Y_{3-x}Ca_x\}[Fe_2](Fe_{3-x}Si_x)O_{12}$.

In the system $\{Y_{3-x}Ca_x\}Fe_{5-x}Ge_xO_{12}$, specimens with $x \leq 1.50$ were saturated at fields ≤ 12.6 koe at $1.4^\circ K$. In measurements with the pendulum magnetometer, the specimen with $x = 1.75$ appeared to be saturated at 9.6 koe at both 1.4 and $4.2^\circ K$. Measurements on the sintered specimen at high fields at $4.2^\circ K$ indicated that saturation was not attained until about 50 koe. However, the difference in n_B is only $0.1 \mu_B$. For the specimens with $x \geq 2.00$, saturation was not attained at 1.4° or at $4.2^\circ K$ at fields below 80 koe. As in the case of the first system discussed, n_B ($0, 4.2^\circ K$) was determined by extrapolation of the straight line portion of the $n_B(H_a, 4.2^\circ K)$ vs H_a curve to $H_a = 0$. The magnetization curves in this system were similar in character to those of the specimens in the analogous Si system. Curie temperatures (Table I) were determined as described above. The spontaneous magnetizations extrapolated to $T = 0, H_a = 0$ or at $T = 4.2^\circ K, H_a = 0$ are listed in Table I and plotted vs x in Fig. 4.

3.1.2 Crystallographic Data

The lattice constants of specimens in these systems are listed in Table I and plotted vs x in Fig. 6. All garnets involving Ge substitution gave

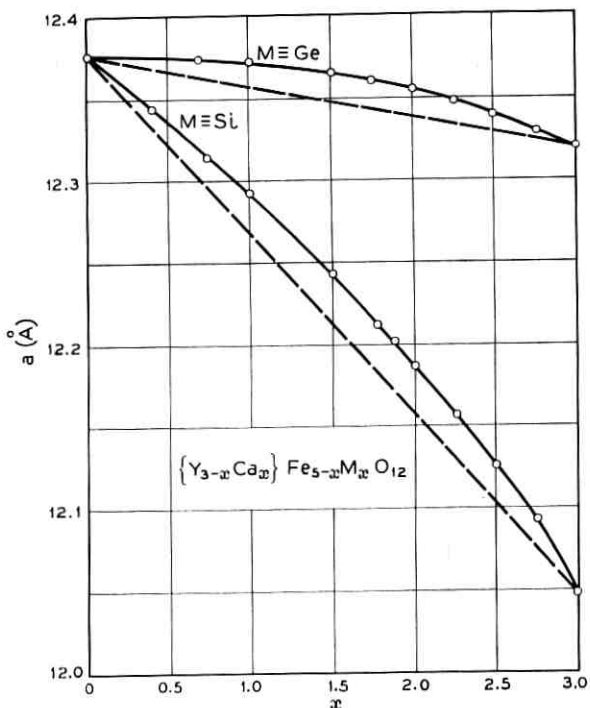


Fig. 6.—Lattice constants vs composition of silicon- and germanium-substituted garnets.

final powder photographs having sharp back-reflection lines. However, in a few cases of the silicon-rich specimens (that is, with $x = 2.25$ and 2.50) sharp back-reflection lines appeared to be unattainable. Because no extraneous phases appeared to be present, it seemed worthwhile to carry out the magnetic measurements on these anyway. In some cases, the indicated larger limits of error on the lattice constants are a result of only few back-reflection lines on which the measurements are based. However, because of the smoothness of the curves which may be passed through the central values, all the indicated estimates of limits of error (Table I) are felt to be conservative.

In both systems, the lattice constant vs composition behavior is nonlinear; such behavior has been observed in other garnet systems.^{1,14,18,19} We might expect the larger volumes than given by the straight line joining the lattice constants of the end-members to indicate greater entropies, the disorder apparently arising from the dis-

parity of the sizes and possibly of the electrostatic charges of tetrahedrally coordinated ions of Fe^{3+} vs Si^{4+} or vs Ge^{4+} . However, the lattice constant itself is not always indicative of the disorder which may exist in a solid solution. The latter cannot obey the third law of thermodynamics because the crystalline fields about space group equipoints cannot all be the same, even if the lattice constant-composition behavior is a linear one.

An attempt was made to prepare the specimen with $M \equiv \text{Si}$, $x = 2.75$; a slight amount of an extra unidentified phase was observed in this case. The lattice constant (Table I) indicated that the garnet phase present had almost the composition sought. However, it is possible that some excess silicon with divalent iron could be present in this garnet.¹⁴

The specimen of $\text{Ca}_3\text{Fe}_2\text{Si}_3\text{O}_{12}$ prepared by Van Uitert and Bonner had a lattice constant of $12.067 \pm 0.003 \text{ \AA}$. This is substantially larger than the 12.048 \AA reported²⁰ for a specimen prepared at high pressure. The difference in lattice constant implies that at least one of the specimens contains impurity ions. However, our main interest was to show the presence of antiferromagnetic interaction in $\text{Ca}_3\text{Fe}_2\text{Si}_3\text{O}_{12}$, and it does not seem that the impurity ion (or ions) could introduce it in this case. Magnetic measurements were also made on a mineral specimen from Graham County, Arizona, having a lattice constant of $12.068 \pm 0.003 \text{ \AA}$, with essentially the same results as obtained on the synthetic.

3.1.3 Discussion of the Garnets $\{\text{Y}_2\text{Ca}\}[\text{Fe}_2](\text{Fe}_2\text{Si})\text{O}_{12}$ and $\{\text{Y}_2\text{Ca}\}\text{Fe}_4\text{GeO}_{12}$

The present work indicates that earlier results²¹ on these garnets are erroneous. The 0°K moments reported earlier were 0.5 and $1.5 \mu_B$ respectively, as compared with 0.06 and $0.18 \mu_B$ obtained in the present work. That the latter two results are the more reliable is easily ascertained by examination of Fig. 4; these points lie well on the curves for the appropriate systems.

It is precisely in sensitive regions where the greatest care in preparation must be exercised. In the case of the Si-substituted garnet, we can only guess that perhaps there was present in the earlier preparation an extraneous phase which was not observed on the powder photograph or, that despite the good agreement between lattice constants (see Tables I of Ref. 21 and of this paper), the stoichiometry was not exact. For example, excess Si^{4+} ions would cause the reduction of some Fe^{3+} to Fe^{2+} ions. While the excess Si^{4+} ions would tend to reduce the lattice

constant, the presence of Fe^{2+} would tend to increase it.¹⁴ Also, any deviation in stoichiometry would tend to increase the absolute value of the spontaneous moment.

In fact, the observed deviation, 0.06 μ_B from exactly 0.00 μ_B for $\{\text{Y}_2\text{Ca}\}[\text{Fe}_2](\text{Fe}_2\text{Si})\text{O}_{12}$, amounts to only 0.5 mg of SiO_2 in the 0.001 mole of specimen prepared. The specimens with $x = 1.01$ and 1.02 were also prepared in an attempt to find the exact zero spontaneous magnetization at 0°K for this system. However (see Table I), neither of these gave exactly zero values. It would appear from the results that the experimental error could be as large as the equivalent of 0.01 of a Si^{4+} ion or 0.05 μ_B in this region of the system.

The high value previously obtained for the garnet $\{\text{Y}_2\text{Ca}\}\text{Fe}_4\text{GeO}_{12}$ is more easily explained, and a number of experiments (see Table II) were carried out to prove this contention. Examination of Fig. 6 shows that the change of lattice constant with x in the system $\{\text{Y}_{3-x}\text{Ca}_x\}\text{Fe}_{5-x}\text{Ge}_x\text{O}_{12}$ is not very large over rather large ranges of x . At $x = 1.00$, a change of $\pm 0.003 \text{ \AA}$ (our quoted limits of error) implies a change of -0.25 or +0.20 respectively in x , which in turn implies a change (Fig. 4) of $\pm 1.00 \mu_B$ in 0°K moment. The broadness of back-reflection lines in the x-ray powder photograph may indicate a variation in range greater than $0.75 \leq x \leq 1.20$. As shown in Table II, repro-

TABLE II — EXPERIMENTS TO OBTAIN THE CORRECT DATA FOR
 $\{\text{Y}_2\text{Ca}\}\text{Fe}_4\text{GeO}_{12}$

Specimen	$a(\text{\AA})$	$\frac{\mu_B}{(1.4^\circ\text{K})}$	$\frac{\mu_B}{(77^\circ\text{K})}$	Description
594	12.372	1.00		After firing 16 hrs. at 1300°C, then 16 hrs. at 1350°C. Specimen contained 6.5% excess GeO_2 (based on total GeO_2). Broad 116 ^a line.
	12.371	0.23		After third firing 39 hrs. at 1425°C. Specimen contained 4.1% excess GeO_2 . Sharp 116 line.
602	12.371	0.18	0.17	After firing 19 hrs. at 1405°C, then 63 hrs. at 1400°C. Sharp 116 line.
	12.372		0.17	After third firing 66 hrs. at 1300°C. Sharp 116 line.
606		1.12	1.08	After firing 16 hrs. at 1315°C, then 16 hrs. at 1300°C. Broad 116 line.
			0.96	After third firing 64 hrs. at 1275°C. 116 line still broad.
			0.28	After fourth firing 17 hrs. at 1410°C. 116 line much sharper.
	12.372		0.18	After fifth firing 16 hrs. at 1410°C. 116 line sharp.

^a That is, $h^2 + k^2 + l^2 = 116$.

ducible results are obtained for single sharply defined stoichiometric phases.

The preparation of $\{Y_2Ca\}Fe_4GeO_{12}$ requires a temperature of about 1400°C; even rather long firings at about 1300°C did not produce homogeneity. On the other hand (see Table II, specimen 602), firing at 1300°C for a long period produced no significant change in a homogeneous specimen formed at 1400°C.

Because of its volatility, an excess of GeO_2 is usually added to the reactants required for the preparation of Ge^{4+} ion substituted garnets. Firings are carried out until this excess is lost. It is possible, however, to add too great an excess and it is then best to discard the specimen. However, as seen in Table II, for specimen 594, an excess of 4.1 per cent GeO_2 was not as important as the correct firing temperature.

3.2 The Systems $\{Y_3\}[Sc_xFe_{2-x}](Fe_3)O_{12}$ and $\{Y_{3-x}Ca_x\}[Zr_xFe_{2-x}](Fe_3)O_{12}$

3.2.1 Magnetic Data

Part of the $\{Y_3\}[Sc_xFe_{2-x}](Fe_3)O_{12}$ system⁴ and the whole $\{Y_{3-x}Ca_x\}-[Zr_xFe_{2-x}](Fe_3)O_{12}$ system² have been investigated earlier in these laboratories. In the present investigation several new specimens have been prepared and high-field measurements made on specimens with $x \geq 0.72$. For values of $x \leq 0.60$, specimens were magnetically saturated at an applied field of 9.6 koe at 1.4°K. For $x = 0.72$, the specimens were saturated at 60–70 koe at 4.2°K, and for $x > 0.72$, saturation was not attained at fields to 80 koe at 4.2°K. In these cases the spontaneous magnetizations, $n_B(0,4.2^\circ)$, were obtained by extrapolating the straight line portions of the $n_B(H_a,4.2^\circ)$ to $H_a = 0$. The values thus obtained are listed in Table III; the actual spontaneous magnetizations of 0°K may, of course, be slightly higher.¹⁷ Spontaneous magnetizations obtained by extrapolating $n_B(H_a,4.2^\circ)$ vs $1/H_a$ to $1/H_a = 0$ are also shown in Table III. The spontaneous magnetizations are plotted vs x in Fig. 7. Curie temperatures (Table III, Fig. 5) of specimens in these systems were determined as described above. For $x \geq 1.50$, results were inconclusive. Examples of plots of n_B vs T for specimens in these systems have been given in other papers. The behavior of n_B vs T for high substitution is similar to that of the $\{Y_{3-x}Ca_x\}[Fe_2](Fe_{3-x}Si_x)O_{12}$ system for high x .

The values $n_B(H_a,4.2^\circ)$ vs H_a for high x of specimens in both sys-

TABLE III — MAGNETIC AND CRYSTALLOGRAPHIC DATA FOR GARNETS
 $\{Y_3\}[Sc_xFe_{2-x}](Fe_3)O_{12}$ AND $\{Y_{3-x}Ca_x\}[Zr_xFe_{2-x}](Fe_3)O_{12}$

x	Sc				Zr			
	n_B^a		$T_C(^{\circ}K)$	$a(\text{\AA})$	n_B^a		$T_C(^{\circ}K)$	$a(\text{\AA})$
	$H_a = 0$	$H_a = \infty$			$H_a = 0$	$H_a = \infty$		
0.20 ^b					5.9	5.9		12.404
0.25 ^c	5.99	5.99	504	12.392	6.7	6.7		12.434
0.40 ^b					7.39	7.39		12.470
0.60	7.44	7.44	408	12.424	7.6	7.6	386	12.490
0.72	7.65	7.65	386	12.433				
0.75 ^c			375	12.438				
0.80	7.1	8.1		12.442	6.9	8.2		12.501
1.00	5.7	7.6	294	12.457	5.2	6.6	288	12.534
1.25	3.1	6.2	200	12.478	2.8	5.7	200	12.573
1.50	1.4	4.6	100(?)	12.497	1.1	4.0	65(?)	12.614
1.75					0.4	2.0	48(?)	12.653
1.95					0.0			12.684

^a For $x < 0.72$, n_B was obtained by extrapolation to $T = 0$; for $x \geq 0.72$, n_B is at 4.2°K . ^b Data from Ref. 2. ^c Data from Ref. 4.

tems are plotted in Fig. 8. In all cases, for the same value of x , the values of n_B at the same H_a are higher for Sc substitution than for Zr substitution. This will be discussed further later.

A plot of $1/\chi_n$ vs T for $\{Y_{1.05}Ca_{1.95}\}[Zr_{1.95}Fe_{0.05}](Fe_3)O_{12}$ is given in Fig. 9. A conclusive antiferromagnetic transition was not observed at fields as low as 4.9 koe. Above 70°K , $1/\chi_n$ follows a Curie-Weiss law with C equal to the calculated theoretical value for 3.05 Fe^{3+} ions per formula unit. The linear portion of $1/\chi_n$ vs T intersects the abscissa at -66°K , indicating that there is antiferromagnetic interaction among the Fe^{3+} ions at low temperatures.

Shown also in Fig. 9 is a plot of $1/\chi_n$ vs T for $\{YCa_2\}[Zr_2](\text{Ga}_{0.25}\text{Fe}_{2.75})O_{12}$. In this case again, there was no conclusive evidence of a transition to long-range antiferromagnetic order, but the intersection of the extrapolated linear portion of $1/\chi_n$ vs T with the abscissa, -40°K , indicates that antiferromagnetic interaction is present at low temperatures. As one would expect, the interaction strength is weaker than for $\{Y_{1.05}Ca_{1.95}\}[Zr_{1.95}Fe_{0.05}](Fe_3)O_{12}$.

For both specimens, there does not appear to be any indication of weak ferromagnetism.²² Below the linear portions of $1/\chi_n$ vs T , the curves are concave upwards and neither specimen appears to have a residual moment at 1.4°K .

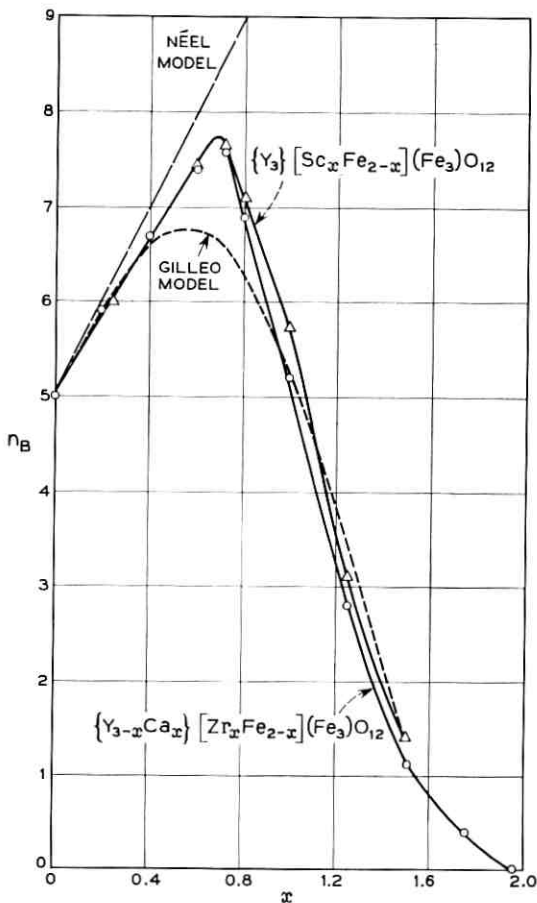


Fig. 7 — Spontaneous magnetizations vs composition for the zirconium- and scandium-substituted yttrium iron garnets. For $x < 0.72$, saturation was attained at low fields and the n_B values were obtained by extrapolating $n_B(T)$ to $T = 0^\circ\text{K}$. For $x \geq 0.72$, saturation was not attained at low fields and the n_B values were obtained by extrapolating $n_B(H_a)$ to $H_a = 0$ at 4.2°K (see Fig. 8). Shown also are the curves given by the Gilleo and Néel models for substitution by nonmagnetic ions exclusively on octahedral sites.

3.2.2 Crystallographic Data

Lattice constants for these systems are given in Table III and plotted vs x in Fig. 10. Shown also in Fig. 10 are values obtained in the former studies made in these laboratories. For the most part, agreement of the former with the present values is good. However, in the present study,

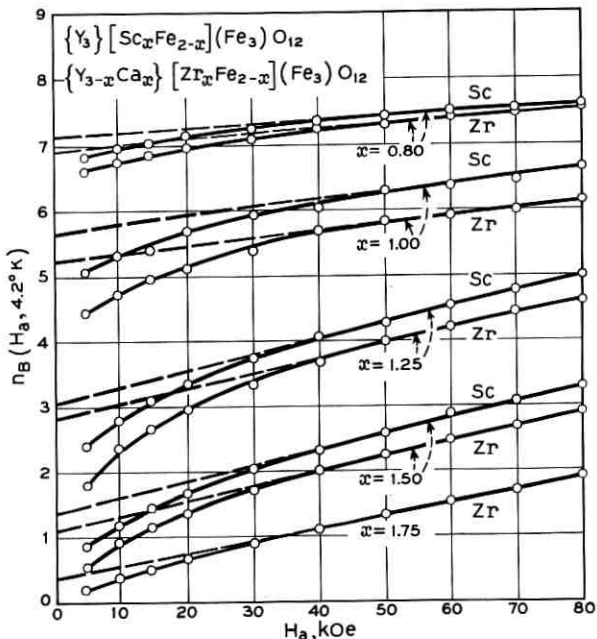


Fig. 8 — n_B vs applied field H_a , at 4.2°K , for some scandium- and zirconium-substituted yttrium iron garnets.

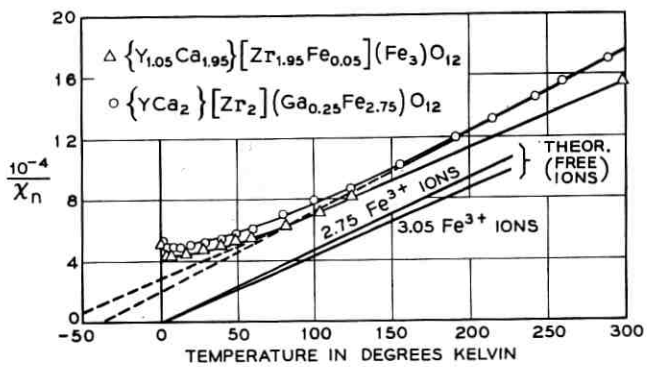


Fig. 9 — Reciprocal susceptibility (χ_n in Bohr magnetons per oersted per formula unit) vs temperature for the garnets $\{\text{Y}_{1.05}\text{Ca}_{1.95}\}[\text{Zr}_{1.95}\text{Fe}_{0.05}](\text{Fe}_3)\text{O}_{12}$ and $\{\text{YCa}_2\}[\text{Zr}_2](\text{Ga}_{0.25}\text{Fe}_{2.75})\text{O}_{12}$.

all points for both systems lie almost exactly on the two straight lines (Fig. 10) and, where differences occur, the present values are considered to be the more reliable ones.

An attempt to prepare $\{Y_3\}[Sc_x(Fe_{2-x})O_{12}]$ produced a specimen containing an extraneous perovskite-type phase and a garnet phase with lattice constant 12.508 Å. This value corresponds to the composition $x = 1.62$, which is the maximum value attainable, at least under the conditions of preparation.

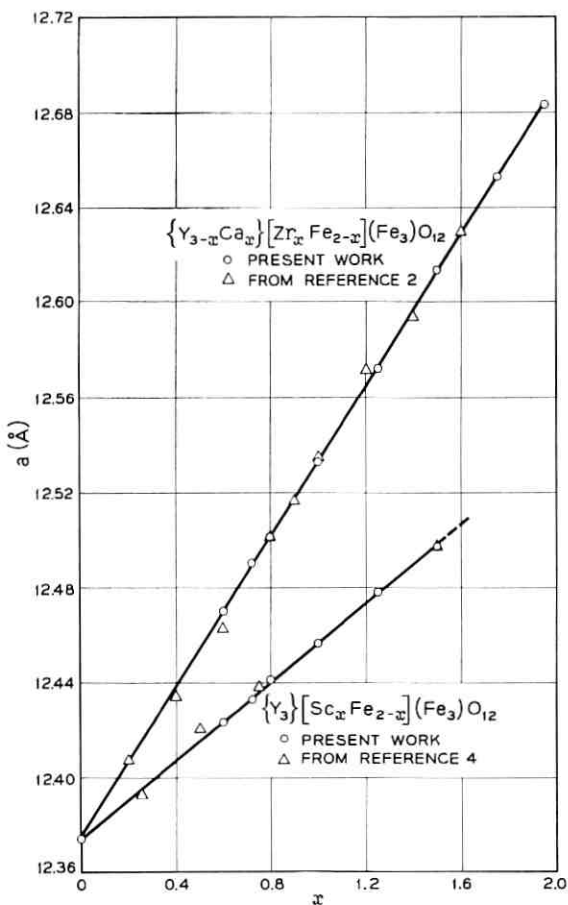


Fig. 10 — Lattice constants vs composition for the scandium- and zirconium-substituted yttrium iron garnets.

In the case of Zr substitution, previously we reported² obtaining a specimen with $x = 2.00$. However in attempting to reproduce this composition, very careful examination of x-ray data indicated a slight amount of extraneous phase. The garnet present had a lattice constant 12.686 Å, indicating a maximum $x = 1.96$. It was possible, however, to make the garnet $\{\text{YCa}_2\}[\text{Zr}_2](\text{Ga}_{0.25}\text{Fe}_{2.75})\text{O}_{12}$ ²³ with lattice constant 12.681 ± 0.003 Å.

3.3 The System $\text{Y}_3[\text{Mg}_x\text{Fe}_{2-x}](\text{Fe}_{3-x}\text{Si}_x)\text{O}_{12}$

3.3.1 Magnetic Data

For values of $x \leq 0.85$, all specimens in this system were essentially saturated over the whole temperature range at fields of 9.6–12.6 koe. For $x = 0.90$, measurements were made only at 1.4°K; the specimen was saturated at 11.3 koe. For $x = 1.00$, saturation was attained at 11.3 koe at 1.4°K, yielding a spontaneous magnetization of $3.5 \mu_B$ per formula unit. However, subsequent high-field measurements showed that this specimen was more likely saturated at 70 koe with a moment of $3.8 \mu_B$.

For $x \geq 1.10$, saturation was not attained at 1.4°K and at fields ≤ 14.24 koe; therefore high-field measurements were made on these specimens at 4.2°K. The specimen with $x = 1.10$ was saturated at 70 koe. All others were not saturated below 80 koe; in these cases the values of spontaneous magnetization were obtained by extrapolation of the linear portions of the n_B vs H_a curves to $H_a = 0$. Values of moments were also obtained by extrapolation of n_B vs $1/H_a$ to $1/H_a = 0$. Both sets of values are given in Table IV and plotted vs x in Fig. 11. Note that the points for $x = 1.00$ and 1.10, which must lie on a reasonable curve representing the system, fit distinctly better on the $n_B(0)$ than on the $n_B(\infty)$ curve.

Curves of n_B vs T at 14.24 koe for various specimens are given in Fig. 12. To show the effect of different fields on the magnetization when saturation is not attained, typical curves for the specimen with $x = 1.25$ are given in Fig. 13.

When $x = 1.7$, there appears to be an antiferromagnetic transition at about 10°K. This is seen at fields of 9.6 koe or lower. There appears also to be a residual moment of $\approx 0.2 \mu_B$ at 4.2°K.

Measurements were made on the specimen with $x = 0.55$ at fields from 4.8 to 80 koe at 4.2°K. Saturation was attained at 4.8 koe; the moment obtained was $4.62 \mu_B$, an excellent corroboration of the value obtained with the pendulum magnetometer (Fig. 12).

Curie temperatures, obtained from plots of $n_B^2(0,T)$ vs T (see above)

TABLE IV — CRYSTALLOGRAPHIC, MAGNETIC AND PREPARATION DATA FOR $\{Y_3\}[Mg_xFe_{2-x}](Fe_{3-x}Si_x)O_{12}$ SYSTEM

x	$a(\text{\AA})$	n_B^a	$T_C(\text{^{\circ}K})$	Firing Procedure, ^b Temp., °C (hr)
0.40	12.348	4.65	432	1250(2), 1425(2½), 1445(2½)
0.55	12.336	4.60	396	1400(½), 1450(2½), 1465(2½)
0.70	12.321	4.35	356	1450(½), 1480(3), 1500(3)
0.85	12.308	4.25	327	1400(½), 1490(2), 1500(2), 1550(2)
0.90	12.305	4.17		1400(½), 1460(2), 1540(2)
1.00	12.289	3.8(3.8) ^c	265	1420(¾), 1480(3), 1520(3), 1500(2)
1.10	12.282	3.2(3.2)	220	1420(1), 1480-1500(4½), 1520(4)
1.25	12.265	2.2(3.4)	187	1450(½), 1525(3), 1550(3)
1.40	12.252	1.25(2.7)	110	1400(½), 1500(2), 1560(2)
1.50	12.237	0.9(2.4)	84	1400(½), 1500(4), 1525(5), 1550(5)
1.60	12.229	0.55(2.0)	50(?)	1400(½), 1500(3), 1525(2), 1560(2)
1.70	12.220	0.35(2.25)		1375(1), 1500(2), 1550(4), 1590(4), 1575(4)
1.85	12.197			1300(1), 1500(4), 1525(4), 1535(7)

^a For $x \leq 0.90$, n_B was obtained by extrapolation to $T = 0$; for $x > 0.90$, n_B is at 4.2°K. ^b All specimens were first calcined at 500–900°C over a period of 1 hr. ^c Numbers in parentheses are from extrapolation to $H_a = \infty$, others to $H_a = 0$.

and $1/\chi_n$ vs T when possible, are listed in Table IV and plotted vs x in Fig. 5. The Curie temperatures obtained from the Gilleo treatment agree almost perfectly with those observed. The discrepancies are noticeable only at high x : for $x = 1.5$, it is 9°K, for $x = 1.6$ it is 14°K.

3.3.2 Crystallographic Data

Lattice constants for this system are given in Table IV and plotted vs x in Fig. 14. The limits of error assigned to each lattice constant are $\pm 0.003 \text{ \AA}$. All points but one deviate no more than 0.002 \AA from the curve a vs x , and in no case is more than a deviation of $x = 0.02$ implied by any deviation of lattice constant; in fact, a deviation of $x = 0.02$ is implied for only three out of thirteen specimens, namely for those with $x = 0.90$, 1.00 and 1.70.

Careful examination of the powder data, both photographic and diffractometric, indicated that specimens with $x = 1.90$, 1.95 and 2.00 were not single-phase. As it is known that the Mg^{2+} ion may also occupy c sites in garnets, at least one specimen was made in which substitution was made in both c and a sites simultaneously. The garnet $\{Y_{2.8}Mg_{0.2}\} \cdot [Mg_{1.7}Fe_{1.3}](Fe_{1.1}Si_{1.9})O_{12}$ has a lattice constant of $12.177 \pm 0.003 \text{ \AA}$.

Because such substitution is feasible, the *exact* maximum value of x in the $\{Y_3\}[Mg_xFe_{2-x}](Fe_{3-x}Si_x)O_{12}$ system cannot really be obtained and the preparation of specimens in this system requires more care perhaps than those in which a substituent ion prefers one site exclusively. (For this reason, we have included the firing data in Table IV.)

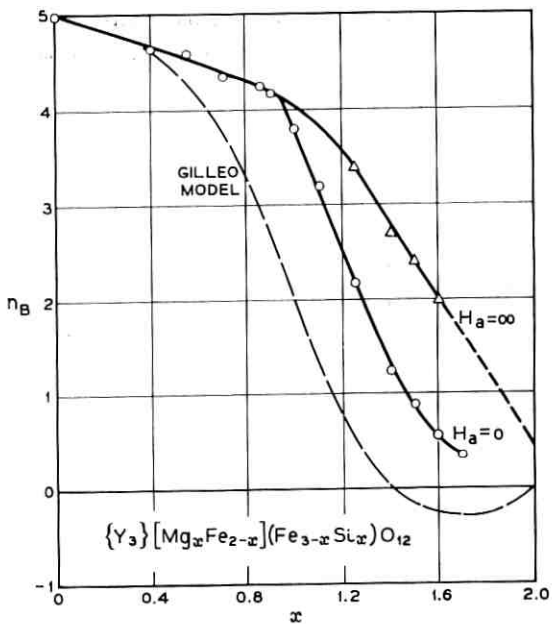


Fig. 11 — Spontaneous magnetizations vs composition for the system $\{Y_3\} \cdot [Mg_xFe_{2-x}](Fe_{3-x}Si_x)O_{12}$. For $x \leq 0.90$, saturation was attained at low fields and the n_B values were obtained by extrapolating $n_B(T)$ to $T = 0^{\circ}\text{K}$. For $x \geq 1.00$, saturation was not attained at low fields and the n_B values were obtained at 4.2°K by extrapolating $n_B(H_a)$ to $H_a = 0$ and $n_B(1/H_a)$ to $1/H_a = 0$. Shown also is the curve given by the Gilleo model.

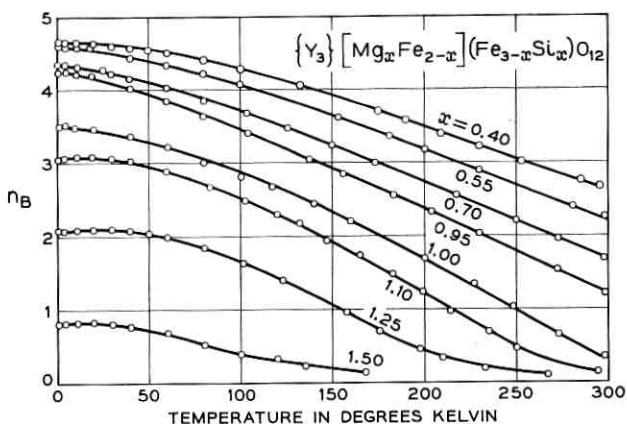


Fig. 12 — $n_B(14.24 \text{ koe}, T)$ vs T for specimens in the system $\{Y_3\} [Mg_xFe_{2-x}](Fe_{3-x}Si_x)O_{12}$.

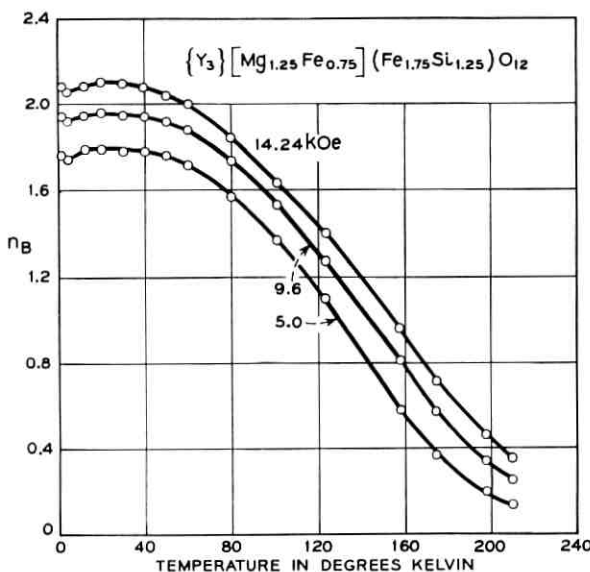


Fig. 13 — n_B vs T at different magnetic fields for $\{Y_3\}[Mg_{1.25}Fe_{0.75}](Fe_{1.75}Si_{1.25})O_{12}$.

The behavior of the lattice constant vs composition (Fig. 14) is again not linear for the $\{Y_3\}[Mg_xFe_{2-x}](Fe_{3-x}Si_x)O_{12}$ system. However, as will be shown later, of all the ions substituted for trivalent iron, the Mg^{2+} ion appears to make the "best fit," in the octahedral sites.

3.4 Miscellaneous Specimens in the Systems $\{Y_{3-y}Ca_y\}[Sc_xFe_{2-x}]$ - $(Si_yFe_{3-y})O_{12}$, $\{Y_{3-y+x}Ca_{y-x}\}[Mg_xFe_{2-x}](Si_yFe_{3-y})O_{12}$ and $\{Y_{3-x-y}Ca_{x+y}\}[Zr_xFe_{2-x}](Si_yFe_{3-y})O_{12}$

Measurements were made on various specimens in these systems for the purpose of making certain points to be given later. In some cases, magnetic saturation was attained at low fields, in some at high fields, and not in some at fields to 80 koe. Results are given in Table V. Several Ge-substituted garnets analogous to the Si-substituted ones were also made. Data for these are given in Table VI.

3.5 The System $Y_3Al_xFe_{6-x}O_{12}$

3.5.1 Magnetic Data

Results obtained in these laboratories on part of this system were reported several years ago.⁴ In the present investigation, the range of

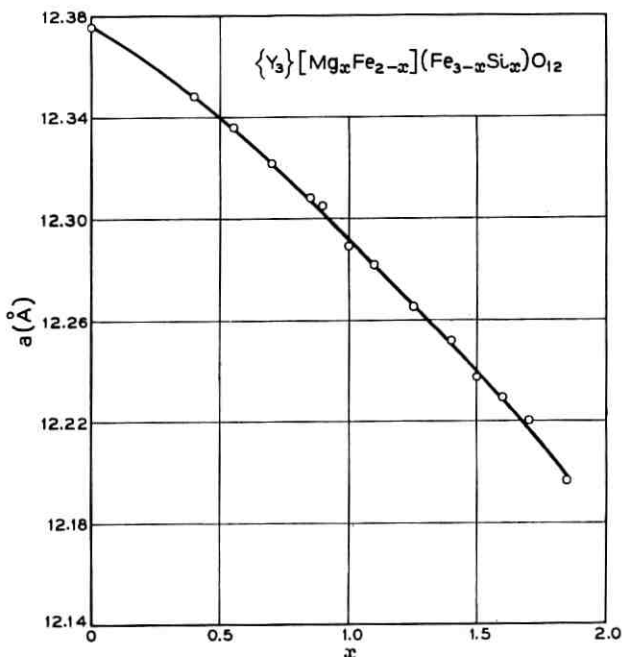


Fig. 14 — Lattice constant vs composition for the system $\{Y_3\}[Mg_xFe_{2-x}](Fe_{3-x}Si_x)O_{12}$.

substitution has been extended. In this system, for $x \leq 1.75$, magnetic saturation was attained at 1.4°K at applied fields ≤ 9.6 koe.

Although there is no doubt that the specimen with $x = 2.0$ has a spontaneous magnetization, the results on the two specimens with $x = 2.5$ and 3.0 are not conclusive. In both cases, there appears to be an antiferromagnetic transition at about 10°K (see Fig. 15) which appears at fields of 4.8 and 9.6 koe, but not at 14.24 koe. The plots of $1/\chi_n$ vs T follow a Curie-Weiss law. For $x = 2.5$, the straight line portion of $1/\chi_n$ vs T intersects the T axis at -40°K and for $x = 3.0$ at -20°K . (See Fig. 16.) The values of μ_{eff} are 3.29 and 3.34 μ_B respectively. These results indicate that at least short-range antiferromagnetic interaction is present over a wide temperature range.

High-field measurements at 4.2°K were made on specimens with $x = 2.0$, 2.5, and 3.0. Each showed a residual moment when $n_B(H_a)$ was extrapolated to $H_a = 0$. The values obtained lie on the smooth curve joining the points at values of $x < 2.0$. This, however, may be fortuitous.

TABLE V — MAGNETIC AND CRYSTALLOGRAPHIC DATA FOR GARNETS
 $\{Y_{3-y+x}Ca_{y-x}\}[Mg_xFe_{2-x}](Si_yFe_{3-y})O_{12}$, $\{Y_{3-y}Ca_y\}[Sc_xFe_{2-x}]$ -
 $(Si_yFe_{3-y})O_{12}$ AND $\{Y_{3-x-y}Ca_{x+y}\}[Zr_xFe_{2-x}](Si_yFe_{3-y})O_{12}$

Octahedral Ion	<i>x</i>	<i>y</i>	<i>n_B</i> ^a	<i>T_C</i> , (°K)	Approx. Saturation Field, koe	<i>a</i> (Å)
Mg^{2+}	0.175	0.825	1.64	450	4.8	12.309
	0.30	1.47	-0.92		4.8	12.246
	0.18	1.57	-1.83		7.3	12.237
	0.90	1.10	3.2		9.6	12.283
	0.50	1.50	-0.24		9.6	12.244
	0.44	1.76	-1.29		9.6	12.223
	0.22	1.98	-3.1		60	12.191
	0.75	1.75	-0.18		11.3	12.214
	0.85	0.85	4.0		12.6	12.381
	0.30	1.47	-0.92		4.8	12.270
Sc^{3+}	0.30	1.52	-1.12	<4.8	<4.8	12.265
	0.30	1.60	-1.39		<4.8	12.258
	1.10	0.90	2.8		>70	12.398
	1.00	1.00	2.9		>70	12.380
	0.90	1.10	2.8		>70	12.362
	0.76	0.24	5.9		>70	12.475
	0.60	0.60	4.39		9.6	12.421
	0.35	1.15	0.88		4.8	12.331
	0.30	1.20	0.41		9.6	12.319
	0.85	0.85	3.6		70	12.440
Zr^{4+}	0.30	1.60	-1.40	340	4.8	12.277
	1.10	0.90	1.8		>70	12.477
	1.00	1.00	2.1		>70	12.450
	0.90	1.10	1.9		>70	12.426
	0.60	1.60	-0.3		200	12.32
	1.25	1.25				12.466

^a When approximate saturation field is ≥ 60 koe, these values are at 4.2°K; when >70 , they are extrapolated to $H_a = 0$. All others at 0 or 1.4°K.

TABLE VI — MAGNETIC AND CRYSTALLOGRAPHIC DATA FOR GARNETS
 $\{Y_{3-y+x}Ca_{y-x}\}Mg_xFe_{5-x-y}Ge_yO_{12}$, $\{Y_{3-y}Ca_y\}Sc_xFe_{5-x-y}Ge_yO_{12}$
 AND $\{Y_{3-x-y}Ca_{x+y}\}Zr_xFe_{5-x-y}Ge_yO_{12}$

Octahedral Ion	<i>x</i>	<i>y</i>	<i>n_B</i> [*]	<i>T_C</i> (°K)	Saturation Field, koe	<i>a</i> (Å)
Mg^{2+}	1.00	1.00	3.9	360	60	12.364
	1.25	1.25	2.2		>70	12.362
Sc^{3+}	1.00	1.00	2.9	360	>70	12.457
	0.60	0.60	4.35		9.6	12.467
Zr^{4+}	0.85	0.85	2.9	>70	>70	12.506
	1.00	1.00	1.6		>70	12.530

* See footnote, Table V.

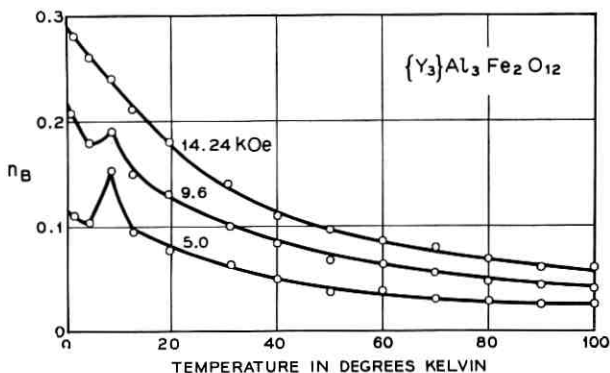


Fig. 15 — n_B vs T at different magnetic fields for $\text{Y}_3\text{Al}_3\text{Fe}_2\text{O}_{12}$.

The values of n_B at $H_a = 0$, $T = 0$ are listed in Table VII and plotted vs x in Fig. 17. The value for the specimen with $x = 1.00$ fits the curve somewhat better than that obtained in the previous work.⁴ Curie temperatures, obtained as described earlier, are given in Table VII and plotted vs x in Fig. 18. Shown also are the values of T_c obtained from the Gilleo theory (see discussion).

3.5.2 Crystallographic Data

The lattice constants for specimens in this system are listed in Table VII and plotted vs x in Fig. 19. Shown also are the values obtained in

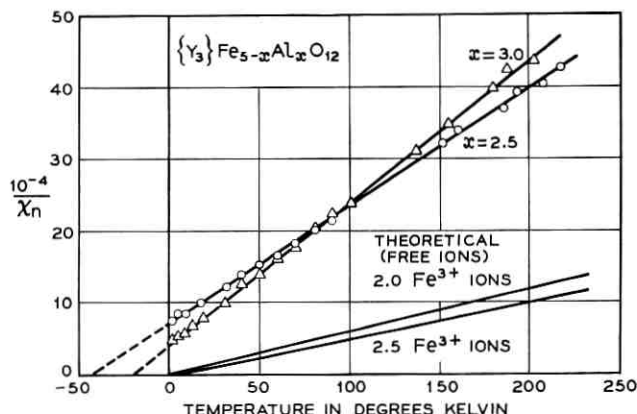


Fig. 16 — Reciprocal susceptibility vs temperature for $\text{Y}_3\text{Al}_{2.5}\text{Fe}_{2.5}\text{O}_{12}$ and for $\text{Y}_3\text{Al}_3\text{Fe}_2\text{O}_{12}$.

TABLE VII — MAGNETIC AND CRYSTALLOGRAPHIC DATA FOR GARNETS
 $\text{Y}_3\text{Al}_x\text{Fe}_{5-x}\text{O}_{12}$

x	n_B		$T_C(\text{°K})$		$a(\text{\AA})$	
	Present Work	Ref. 4	Present Work	Ref. 4	Present Work	Ref. 4
0.00	5.01	4.96		545	12.376	12.376
0.33		3.50		497		12.353
0.67						12.331
1.00	1.73	1.63	430	415	12.311	12.306
1.50	0.94		365		12.276	
1.67						12.265
1.75	0.55		295		12.256	
2.00	0.15		240		12.239	
2.33						12.215
2.50	-0.15(?)				12.206	
3.00	-0.25(?)				12.164	
3.00					12.161	12.159
5.00						12.003

the earlier investigation in these laboratories. Except for $x = 1.00$, the latter values lie within individual experimental error on the curve given by those more recently obtained and which are considered to be improved. To a value of $x = 2.5$, the a vs x behavior of the $\text{Y}_3\text{Fe}_{5-x}\text{Al}_x\text{O}_{12}$ system is linear (and extrapolates to a value of 12.030 Å for $\text{Y}_3\text{Al}_2\text{Al}_3\text{O}_{12}$). However, beyond this point, there appears to be an inflection toward the abscissa. Two specimens with $x = 3.00$ were carefully prepared,

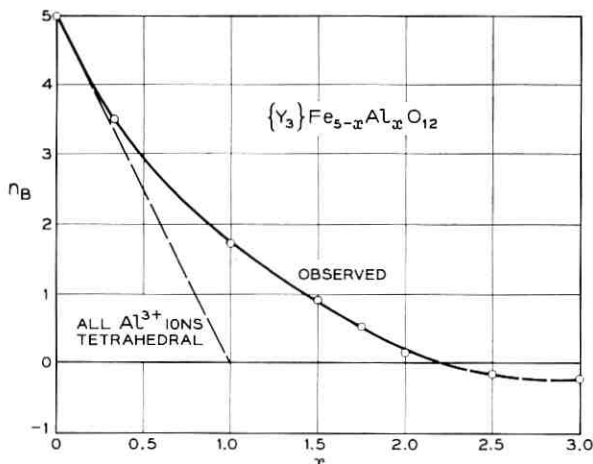


Fig. 17 — Spontaneous magnetization vs composition for aluminum-substituted yttrium iron garnets. (See text for explanation of values for $x > 2.0$.) Shown also is the line expected, when $0 \leq x \leq 1.0$, if all Al^{3+} ions replaced Fe^{3+} ions in tetrahedral sites.

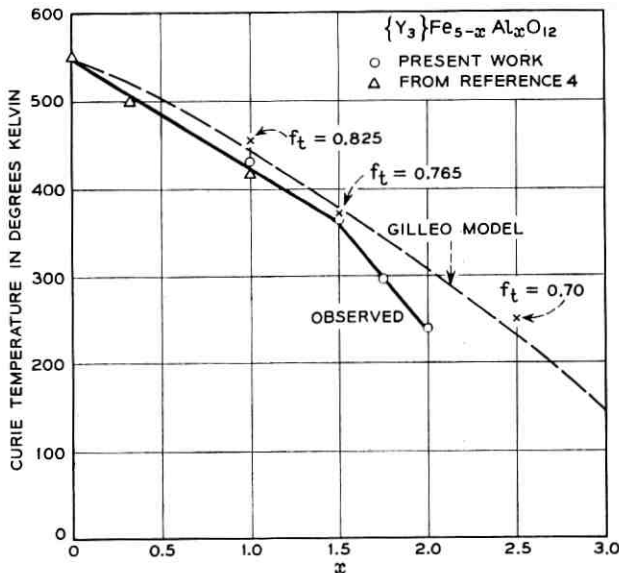


Fig. 18 — Curie temperatures vs composition for the aluminum-substituted yttrium iron garnets. Shown also is the curve obtained from the Gilleo model based on the distributions given in Fig. 29. The points denoted by crosses were obtained from specimens in which Mg^{2+} or Zr^{4+} were substituted for Fe^{3+} ions in octahedral sites and Si^{4+} for Fe^{3+} ions in tetrahedral sites, with required electrostatic balance by Ca^{2+} ions in dodecahedral sites (see text).

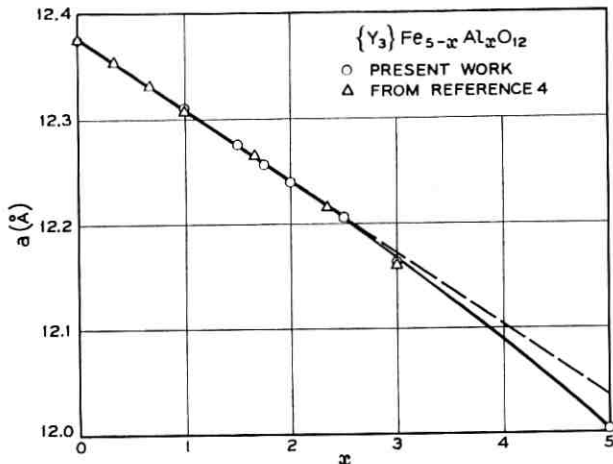


Fig. 19 — Lattice constant vs composition for aluminum-substituted yttrium iron garnets.

one with ultra-pure Al_2O_3 ; the lattice constants obtained for the two specimens are 12.164 and 12.161 Å (the latter for the ultra-pure specimen). The larger of the two values still is far from the straight line of the first half of the system (Fig. 19). As will be shown in a subsequent paper, a vs x for the $\text{Gd}_3\text{Fe}_{5-x}\text{Al}_x\text{O}_{12}$ system also does not behave exactly linearly, although the inflection occurs at a much lower value of x .

IV. GENERAL DISCUSSION

The original purpose of this investigation was to test further the Gilleo theory³ and the extension thereof to substituted rare earth iron garnets.²⁵ Following this paper, we shall publish one concerned with the latter systems which will show, unfortunately, that this extension²⁵ of the theory does not fit the results because, as the present paper will show, the Gilleo theory for substituted yttrium iron garnets does not fit the results. In fact, no existing theory accounts for the observations quantitatively, and though the over-all agreement is rather poor, the Gilleo theory comes the closest.

In this paper, we shall develop a descriptive theory for substituted yttrium iron garnets which draws on various theories of Néel,²⁶ Yafet and Kittel,⁵ Gilleo³ and Anderson.²⁷ The possibility of a quantitative theory which can predict the magnetic behavior of the substituted garnets is complicated by the various effects of substitution on the magnetic structure. These effects appear to be more complex for higher substitution, and in fact there is now evidence that, especially for high substitution, different nonmagnetic ions in the same site produce different behavior (see also Refs. 10–13 and Section 4.3). In a sense, this is a rather unfortunate result because, before we discovered it, we believed that even without a quantitative theory, we should be able from limited data to predict the magnetic behavior of any substituted yttrium iron garnet. Actually, as will be shown later, this can still be done within a certain range of substitution and for particular ions.

The present data strongly indicate that the Si^{4+} ion has a preference exclusively for tetrahedral sites in the garnets.²⁸ The preference of the Ge^{4+} ion for tetrahedral sites is not quite as great as that of the Si^{4+} ion; that is, with increasing Ge^{4+} ion substitution, there does appear to be some tendency for a small percentage of these ions to go into octahedral sites. However, this percentage is not nearly as large as previously²¹ indicated.

Assuming that our present conclusion regarding the site preference of the Si^{4+} ion is correct, we may compare Fig. 4 with the observed data,

$n_B(0^\circ\text{K})$ vs x calculated on the basis of a simple Néel model²⁶ and on that proposed by Gilleo.³ It is seen that neither model gives satisfactory agreement with the observations over the whole range of substitution. In the range to $x \approx 1.9$ there is apparently better agreement with the simple Néel model than with the Gilleo one. The observed minimum, $-3.85 \mu_B$, occurs at $x = 1.94$; the minimum predicted by the Gilleo model is $-1.8 \mu_B$ at $x = 1.77$; the Néel theory does not predict a minimum, but does not preclude one (see Section 11 of Ref. 26). Agreement of observed 0°K moments for octahedral substitution (see Fig. 7) with those calculated with the Gilleo theory is somewhat better than for tetrahedral ion substitution, but it cannot be said to be satisfactory. For the $\{\text{Y}_3\}[\text{Mg}_x\text{Fe}_{2-x}](\text{Fe}_{3-x}\text{Si}_x)\text{O}_{12}$ system (see Fig. 11), the moments calculated with the Gilleo theory are also not in good agreement with the observed values. Thus, although the Gilleo theory predicts a maximum for octahedral and a minimum for tetrahedral substitution, it does not appear to account quantitatively for the observed moments in any of the systems. It should be pointed out, however, that unlike others, this theory takes into account the statistical nature of the problem, while on the other hand it has neglected the importance of intrasublattice interactions.

Wojtowicz²⁹ has shown that intrasublattice interactions are negligible in the (unsubstituted) yttrium and lutecium iron garnets, while the results of Pauthenet⁷ and of Aleonard³⁰ based on the Weiss molecular field theory (as applied by Néel to ferrospins) show that they are important. The theory of Yafet and Kittel,⁵ also based on the Weiss molecular field theory, leads to the result that at a certain concentration of nonmagnetic ions in a particular site in a ferrospinel, a transition occurs to a ground state in which there is canting of moments in the unsubstituted sublattice. We shall show below that this theory also does not account for the behavior of the substituted garnets. Nevertheless, an important implication of our structural argument is the importance of intrasublattice interactions.

As indicated earlier, there is an arithmetic error in the de Gennes application⁶ of the Yafet-Kittel theory to the Sn^{4+} ion substituted garnets: the molecular field equations for YIG determined by Pauthenet⁷ should have been written

$$H_A = -7000 M_A - 14,800 M_B$$

$$H_B = -14,800 M_A - 4200 M_B$$

from which $n = +14,800$, $\alpha_2 = -0.95$, $\gamma_2 = -0.57$. Thus according to the theory it is at $y = 0.57$ or $x = 0.29$ that the canting first occurs.

Also, the maximum moment, $6.45 \mu_B$, in the system should then be attained at $x = 0.29$. Actually, if this system is assumed to behave similarly to those of Fig. 7, the maximum moment of $7.8 \mu_B$ is attained at about $x = 0.7$ and the canting appears experimentally to occur earlier (see later discussion).

But the discrepancies for the silicon-substituted yttrium iron garnet are even worse. Again using the Pauthenet equations, the triangular configuration (*c*) of the Yafet-Kittel theory would be expected, that is, for $1/|\alpha_2| < y$. The system is $\{Y_{3-x}Ca_x\}[Fe_2](Fe_{3-x}Si_x)O_{12}$; thus $y = 2/(3-x)$. Canting should therefore begin at $x = 1.1$. For $x < 1.1$, $n_B(0^\circ K) = 5(1-x)$ while for $x > 1.1$,

$$n_B(0^\circ K) = 5(3-x)(1 - 1/|\alpha_2|) = -0.25(3-x).$$

The algebraic minimum, $-0.5 \mu_B$, should occur at $x = 1.1$; the observed values are $-3.85 \mu_B$ at $x = 1.94$.

For the $\{Ca_3\}[Fe_2](Si_3)O_{12}$ specimen, the value of $1/\chi_o$ in units comparable to those used by Aleonard,³⁰ is -1.9 . Thus $n_{aa} = -1.9$, which is about $\frac{1}{12}$ the value of n_{aa} in YIG. This value of n_{aa} indicates very weak magnetic interaction in line with the θ_p of $29^\circ K$ and the possible Néel temperature of $9^\circ K$ and also implies that the interaction coefficients change with substitution. Thus it appears that the use of the interaction coefficients of YIG to predict the behavior of the entire system is not correct.

In a first approximation, it appears now that the following picture of the behavior of the substituted yttrium iron garnets (discussed in this paper) is a plausible one. Yttrium iron garnet itself may be considered an ideal Néel ferrimagnet; that is, at $0^\circ K$, the moments of all *a*-site Fe^{3+} ions are exactly parallel, the moments of all *d*-site Fe^{3+} ion moments are exactly parallel and the moments of *a*-site Fe^{3+} ions are exactly antiparallel to those in the *d*-sites. Under these circumstances the theoretical moment, $5.0 \mu_B$ per formula unit, should be and is observed. When the *d*-sites are filled with nonmagnetic ions, as in $Ca_3Fe_2Si_3O_{12}$, at the very least, short-range antiferromagnetic order occurs among the moments of the *a*-site Fe^{3+} ions. When the *a*-sites are filled with nonmagnetic ions, as for example in hypothetical $\{YCa_2\}[Zr_2](Fe_3)O_{12}$, at the very least, short range antiferromagnetic order occurs among the moments of the *d*-site Fe^{3+} ions (see also Ref. 27).

Thus, on a structural basis, replacement of Fe^{3+} ions in a particular site by nonmagnetic ions must ultimately change a ferrimagnetic to some type of antiferromagnetic structure. Figs. 4 and 7 show that this occurs continuously; Figs. 20 and 21 show the connection between the

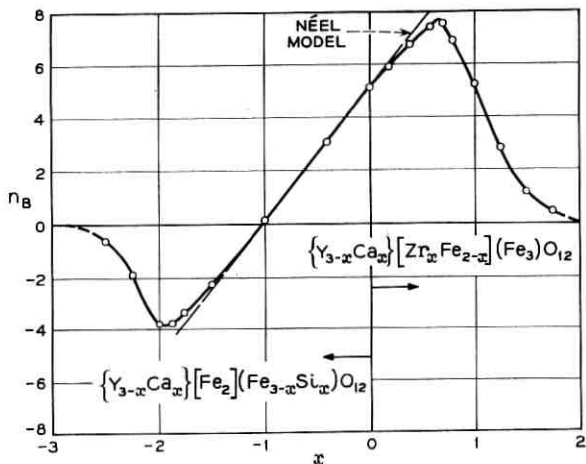


Fig. 20 — Continuous relation between the systems $\{Y_{3-x}Ca_x\}[Fe_2](Fe_{3-x}Si_x)O_{12}$ and $\{Y_{3-x}Ca_x\}[Zr_xFe_{2-x}](Fe_3)O_{12}$.

silicon- and zirconium-substituted yttrium iron garnet systems and give a pictorial summary of the behavior of these systems. Now, let us assume (see Fig. 21) that in the silicon-substituted garnets at 0°K, only the effective moment³¹ of the octahedral Fe^{3+} ion sublattice is reduced by canting of the moments of these ions because of linkages to tetrahedral nonmagnetic ions and the effect of *a-a* antiferromagnetic interaction. Analogously, we assume (see Fig. 21) that in the zirconium (or similar) ion substituted garnets, only the effective moment of the tetrahedral Fe^{3+} ion sublattice is reduced. We can then determine the average effective³¹ moment per octahedral and per tetrahedral Fe^{3+} ion, respectively, as a function of x . The results (Fig. 22, curves 1 and 4) indicate that far more silicon than zirconium substitution is always required to cause reduction of the average Fe^{3+} ion moment in the octahedral and tetrahedral sublattice, respectively.

A small part of the arrangement of cations in the *a* and *d* sites of a zirconium-substituted garnet crystal is shown in Fig. 23. For further clarity, we show in Fig. 24 the arrangement of cations in the three types of sites in four octants of the garnet unit cell. In yttrium iron garnet,³² each ion on an *a* site is linked through pairs of oxygen ions to eight *a*-site ions at distance 5.36 Å and through single oxygens to six *d*-site ions at 3.46 Å. Each *d*-site ion is linked through pairs of oxygens to four *d*-site ions at 3.79 Å and through single oxygens to four *a*-site ions at 3.46 Å. These distances and linkages through oxygen ions imply

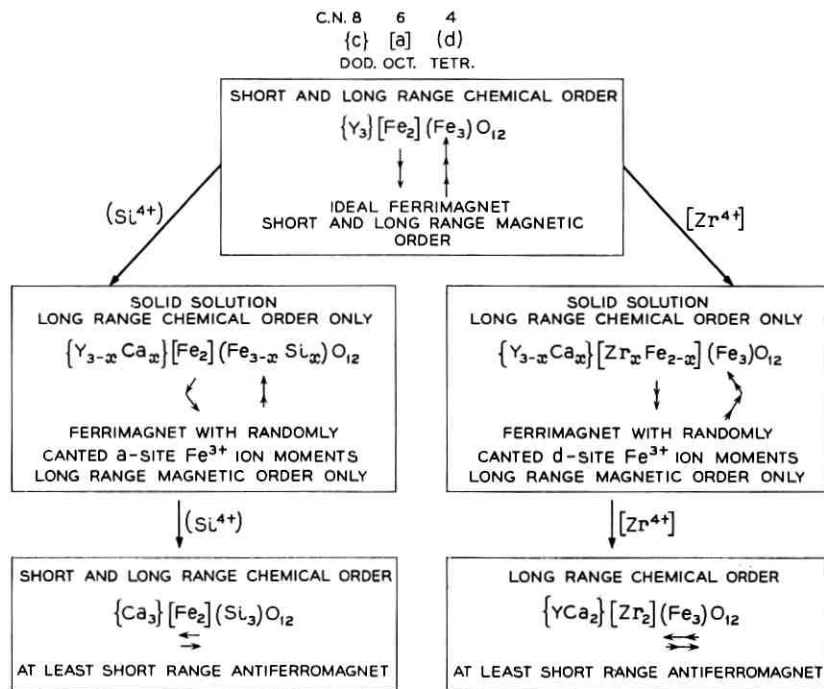


Fig. 21 — Summary of proposed explanation for the magnetic behavior of the systems $\{Y_{3-x}Ca_x\}[Fe_2](Fe_{3-x}Si_x)O_{12}$ and $\{Y_{3-x}Ca_x\}[Zr_xFe_{2-x}](Fe_3)O_{12}$.

that in YIG the *a-d* interaction should be strongest, next the *d-d* and finally the *a-a*.

The results shown in Fig. 22 indicate that the average *a-d* interaction weakens as substitution of nonmagnetic ions is made in either site. Nevertheless the *a-d* interactions remain dominant until the changes in direction of the curves are reached. At $x_o = 0.70$, a transition occurs to a state in which the *d-d* interactions are dominant.³³ Similarly at $x_t = 1.92$, a transition occurs to a state in which the *a-a* interactions are dominant.³³ Because the transition occurs for $x_t = 1.92$ as against $x_o = 0.70$, there is little question that the *d-d* interactions in the Zr^{4+} ion substituted garnets are stronger than the *a-a* interactions in the Si^{4+} ion substituted system. Moreover, as shown in Fig. 25, the ratio of x_t/x_o required to reduce the effective Fe^{3+} ion moment to a particular value is everywhere greater than 1.75.

The decreases in effective moments of the sublattices with increasing x are small but real until the transition points are reached. However, it

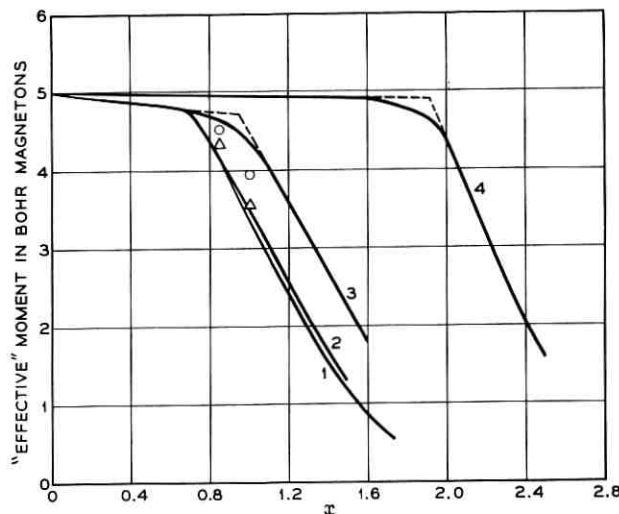


Fig. 22—“Effective” moment (see Ref. 28) per Fe^{3+} ion in (1) tetrahedral sites for $\{\text{Y}_{3-x}\text{Ca}_x\}[\text{Zr}_x\text{Fe}_{2-x}](\text{Fe}_3)\text{O}_{12}$ system; (2) tetrahedral sites for $\{\text{Y}_3\}[\text{Sc}_x\text{Fe}_{2-x}](\text{Fe}_3)\text{O}_{12}$ system; (3) tetrahedral sites for $\{\text{Y}_3\}[\text{Mg}_x\text{Fe}_{2-x}](\text{Fe}_{3-x}\text{Si}_x)\text{O}_{12}$ system; (4) octahedral sites for $\{\text{Y}_{3-x}\text{Ca}_x\}[\text{Fe}_2](\text{Fe}_{3-x}\text{Si}_x)\text{O}_{12}$ system. Circle points are for $\{\text{Y}_{3-x}\text{Ca}_x\}[\text{Sc}_x\text{Fe}_{2-x}](\text{Fe}_{3-x}\text{Si}_x)\text{O}_{12}$ specimens and triangles for $\{\text{Y}_{3-2x}\text{Ca}_{2x}\}[\text{Zr}_x\text{Fe}_{2-x}](\text{Fe}_{3-x}\text{Si}_x)\text{O}_{12}$ specimens (see text).

would appear from the Yafet-Kittel theory that if there were no short-range disorder, there should actually be no decrease in effective moments before the transitions are reached, since the ground state before the transition should be an ideal ferrimagnetic one, with no splitting of the sublattices. That is, because the *a-d* interactions are dominant, the molecular field of the *d* sublattice, in the case of tetrahedral substitution, would act to keep the *a* sublattice moments aligned antiparallel to the *d*; while in the case of octahedral substitution, the molecular field of the *a* sublattice would act to keep the *d* sublattice moments aligned antiparallel to the *a*. On the other hand, it would appear that chemical disorder which always exists in a solid solution would cause magnetic disorder. This chemical disorder implies further that distinct “sublattice splitting” does not really occur in these substituted garnets, but rather that the canting of the moments within a sublattice is random, and that since the crystals are ferrimagnetic, a statistical long-range order must exist.

We see also in Fig. 22 that although until the transition points are reached the rates of decrease in effective moments of the sublattices with increasing *x* are both small, that for tetrahedral substitution is

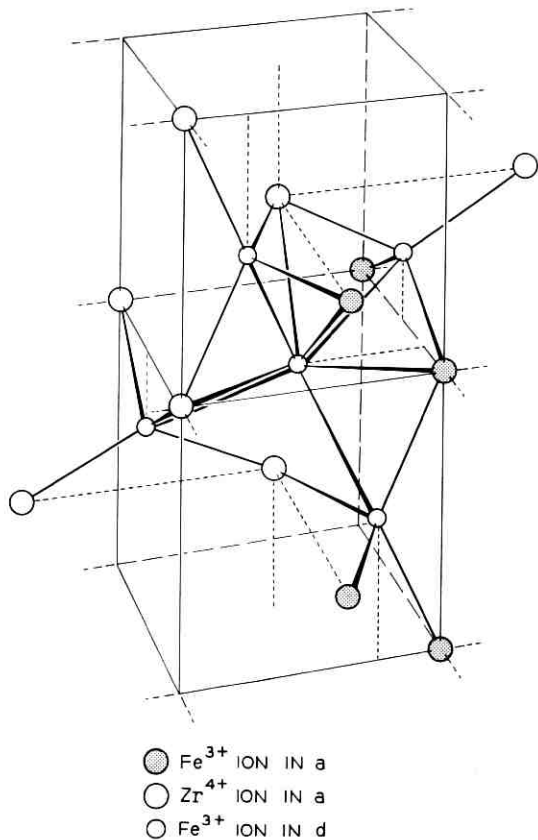


Fig. 23 — Part of the arrangement of cations in the *a* and *d* sites of a zirconium-substituted yttrium iron garnet crystal.

much smaller than for octahedral substitution. This shows again that the *d-d* interactions are stronger than the *a-a*. Now it is unlikely that short-range magnetic disorder occurs before the transition and not beyond it. Thus it appears that what is occurring differs from the idealization given by the Yafet-Kittel theory. The transition is almost surely one at which a change from dominance of the *a-d* to *a-a* or *d-d* interactions occurs, but not one in which there is an abrupt change from a strictly ferrimagnetic to a canted ground state. That is to say, there is always a competition among the various interactions, and as soon as the strictly antiparallel one is disrupted, one of the others may begin to manifest itself.

To emphasize at this point the importance of the competing inter-

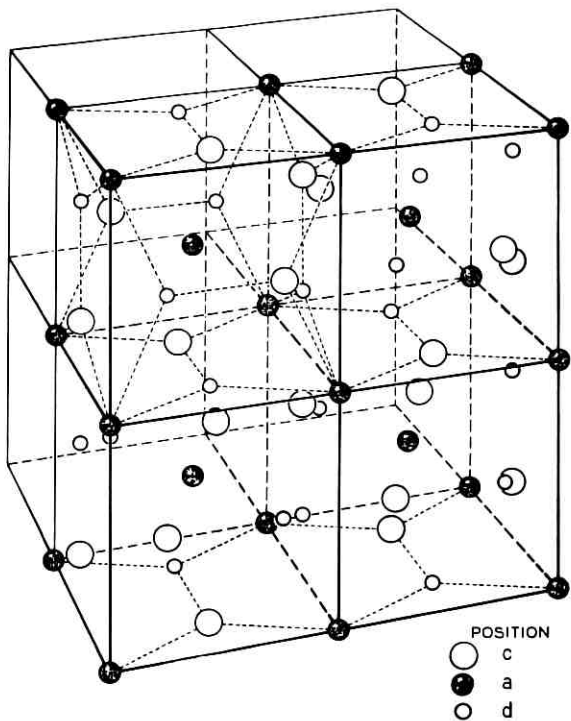


Fig. 24.—Arrangement of cations in *c*, *a*, and *d* sites in four octants of the garnet unit cell.

actions, we outline some further evidence to be discussed in more detail later. Suppose we look at a system in which substitution of nonmagnetic ions is made in both sites. We choose ions such as Sc^{3+} and Si^{4+} which we believe have exclusive preference for octahedral and tetrahedral sites respectively. A formula representing such a system is $\{\text{Y}_{3-y}\text{Ca}_y\}[\text{Sc}_x\text{Fe}_{2-x}](\text{Fe}_{3-y}\text{Si}_y)\text{O}_{12}$. Suppose we begin with $y = 0$ and $x = 0.30$. We see from Fig. 22 that some canting will occur among the Fe^{3+} ion moments on the tetrahedral sites. Now we keep x constant and increase y . As y increases, the canting of the *d*-site Fe^{3+} ion moments will decrease. A value of y will be reached for which the particular garnet will again appear to be an ideal Néel ferrimagnet. The value of y for which this occurs (see Table V) is 1.52, that is to say, for the garnet $\{\text{Y}_{1.48}\text{Ca}_{1.52}\}[\text{Sc}_{0.30}\text{Fe}_{1.70}](\text{Si}_{1.52}\text{Fe}_{1.48})\text{O}_{12}$. For this garnet, the difference in the number of Fe^{3+} ions in the two sites is 0.22, which according to the Néel model would give a 0°K spontaneous magnetization of $-1.10 \mu_B$; the

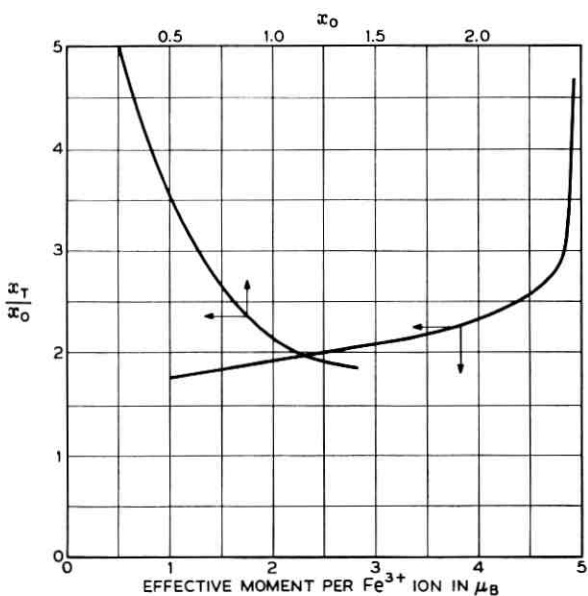


Fig. 25 — The ratio, x_t/x_o , of tetrahedral to octahedral nonmagnetic ions, required to produce the same effective moment per Fe^{3+} ion in the appropriate sublattice. Also shown is the curve x_t/x_o vs x_o .

observed value, $-1.12 \mu_B$, is in good agreement with this value. Note (Table V) that for the garnet $\{\text{Y}_{1.53}\text{Ca}_{1.47}\}[\text{Sc}_{0.3}\text{Fe}_{1.7}](\text{Si}_{1.47}\text{Fe}_{1.53})\text{O}_{12}$, the observed 0°K spontaneous magnetization is $-0.92 \mu_B$, to be compared with $-5 \times 0.17 = -0.85 \mu_B$ from the Néel model. Thus for this garnet canting of the Fe^{3+} ion moments occurs in the tetrahedral sites. On the other hand, in the case of the garnet $\{\text{Y}_{1.4}\text{Ca}_{1.6}\}[\text{Sc}_{0.3}\text{Fe}_{1.7}](\text{Si}_{1.6}\text{Fe}_{1.4})\text{O}_{12}$, the observed 0°K spontaneous magnetization is $-1.39 \mu_B$, to be compared with $-5 \times 0.30 = -1.50 \mu_B$ from the Néel model. Thus for this garnet canting of the Fe^{3+} ion moments occurs in the octahedral sites. (This example also demonstrates that the 0.3 Sc^{3+} ions are in octahedral sites exclusively.)

The above discussion has been concerned only with what occurs at or very near 0°K . It appears, however, that the behavior of these substituted garnets may be similar at higher temperatures. We note (see Fig. 5) that x_t/x_o required to give the same Curie temperature is everywhere greater than 1.68. Fig. 5 also shows the effect of transition from *a-d* to intrasublattice interaction dominance, even though, except for the $\text{Y}_3[\text{Mg}_x\text{Fe}_{2-x}](\text{Fe}_{3-x}\text{Si}_x)\text{O}_{12}$ systems, it does not show as clearly as Fig. 22 where the transition values of x are.

Also shown in Fig. 5 is the plot of T_c vs x obtained from the Gilleo theory. The agreement with observed Curie temperatures is rather good; for the $\{Y_3\}[Mg_xFe_{2-x}](Fe_{3-x}Si_x)O_{12}$ system, it is almost perfect. Thus it is possible that, although the Gilleo theory does not hold at low temperatures, it does at higher temperatures. However, it is also possible that this good agreement of Curie temperatures is fortuitous (see later discussion).

In the system $\{Y_3\}[Mg_xFe_{2-x}](Fe_{3-x}Si_x)O_{12}$ there is always 1.0 more Fe^{3+} ion per formula unit in the tetrahedral than in the octahedral sites. Thus the apparently continuous decrease in total 0°K moment (Fig. 11) in the early stages of substitution must, according to our model, mean that canting of the Fe^{3+} ion moments is occurring in the tetrahedral sites. If we assume that the moments of the a -site Fe^{3+} ions remain parallel we may determine for each composition the effective moment contributed to the ferrimagnetism by each tetrahedral Fe^{3+} ion, as shown in Fig. 22, curve 3.

We note that there are two main regions of behavior similar to those in the systems in which substitution of nonmagnetic ions is made exclusively either in octahedral or in tetrahedral sites. The decrease in effective moment (or increase in canting) is initially at the same rate as in the $\{Y_{3-x}Ca_x\}[Zr_xFe_{2-x}](Fe_3)O_{12}$ or $\{Y_3\}[Sc_xFe_{2-x}](Fe_3)O_{12}$ systems, but beyond $x \approx 0.7$ the rate of decrease of effective moment is lower than in the latter system. Thus we conclude tentatively (see later discussion) that:

- (1) canting of Fe^{3+} ion moments in the tetrahedral sublattice occurs from the beginning of substitution;
- (2) in the region $0 < x \leq 0.7$, the replacement of d -site Fe^{3+} ions by Si^{4+} ions does not have a significant effect on the average d - d interaction strength, but when $x > 0.7$, decreases the average d - d interaction strength; thus
- (3) in the $\{Y_3\}[Mg_xFe_{2-x}](Fe_{3-x}Si_x)O_{12}$ system, the transition to the dominance of the d - d interactions over the a - d interactions (see Ref. 33) occurs at $x \approx 0.95$ as against $x = 0.70$ in the $\{Y_{3-x}Ca_x\}[Zr_xFe_{2-x}](Fe_3)O_{12}$ system.

The Curie temperatures of the $\{Y_3\}[Mg_xFe_{2-x}](Fe_{3-x}Si_x)O_{12}$ system are shown in Fig. 5 (curve 1). The latter are almost everywhere smaller than those of the $\{Y_3\}[Sc_xFe_{2-x}](Fe_3)O_{12}$ system for the same x . However, the differences are nowhere greater than 35°K even though x in the $\{Y_3\}[Mg_xFe_{2-x}](Fe_{3-x}Si_x)O_{12}$ system represents as many nonmagnetic ions in d as in a sites, or twice as much *total* substitution of nonmagnetic ions. This comparison already indicates that the canting may also have

an effect on the Curie temperature; that is, that the intrasublattice interactions are important over a wide temperature range and not only at 0°K.

We may obtain a clearer idea of the effect of the intrasublattice interactions on the Curie temperatures by plotting T_c vs total per cent substitution of nonmagnetic for Fe^{3+} ions as in Fig. 26 for exclusively *a*-site, *d*-site and equal *a-d*-site substitution. Now we see that on this basis, the Curie temperatures for the $\{\text{Y}_3\}[\text{Mg}_x\text{Fe}_{2-x}](\text{Fe}_{3-x}\text{Si}_x)\text{O}_{12}$ system are everywhere substantially greater than those for the $\{\text{Y}_3\}[\text{Sc}_x\text{Fe}_{2-x}](\text{Fe}_3)\text{O}_{12}$ system for the same total per cent replacement of Fe^{3+} ions. Further, to about 37 per cent substitution, the values of T_c for the $\text{Y}_3[\text{Mg}_x\text{Fe}_{2-x}](\text{Fe}_{3-x}\text{Si}_x)\text{O}_{12}$ system are lower than for the $\{\text{Y}_{3-x}\text{Ca}_x\}[\text{Fe}_2](\text{Fe}_{3-x}\text{Si}_x)\text{O}_{12}$ system. (The actual values of x are about 0.9 and 1.85 for the systems, respectively.) In the region below 37 per cent substitution, canting of *d*-site moments in the former system is greater than canting of *a*-site moments in the latter (Fig. 22). In the region above 37 per cent the

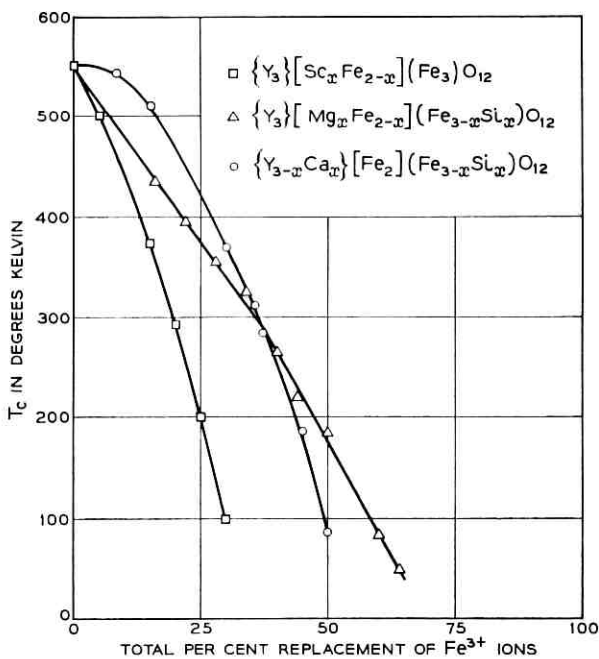
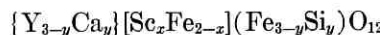


Fig. 26 — Curie temperatures vs total per cent replacement of Fe^{3+} ions.

reverse is true. For example, for 50 per cent substitution the formulas are respectively $\text{Y}_3[\text{Mg}_{1.25}\text{Fe}_{0.75}](\text{Fe}_{1.75}\text{Si}_{1.25})\text{O}_{12}$ and $\{\text{Y}_{0.5}\text{Ca}_{2.5}\}[\text{Fe}_{2-}](\text{Fe}_{0.5}\text{Si}_{2.5})\text{O}_{12}$; Fig. 22 shows that the effective moment of the *d*-site Fe^{3+} ion in the former is $3.35 \mu_B$ while that of the *a*-site Fe^{3+} ion in the latter is $1.6 \mu_B$. [Thus we see also why even when there are only 1.8 Fe^{3+} ions left per formula unit, i.e., $\{\text{Y}_3\}[\text{Mg}_{1.6}\text{Fe}_{0.4}](\text{Fe}_{1.4}\text{Si}_{1.6})\text{O}_{12}$, we still have a ferrimagnetic specimen with $T_c = 50^\circ\text{K}$. In fact, even when $x = 1.7$ (1.6 total Fe^{3+} ions per formula unit), the garnet may still be ferrimagnetic.]

We should expect that in the general system $\{\text{Y}_{3+x-y}\text{Ca}_{y-x}\}[\text{Mg}_x\text{Fe}_{2-x}](\text{Fe}_{3-y}\text{Si}_y)\text{O}_{12}$ there will be, for a given ($x + y$), a value of x (or $f_t = y/x + y$) such that there will be no canting of Fe^{3+} ion moments in either sublattice. We saw above for $x + y = 2.50$ (50 per cent substitution) that the effective moments when $x = y = 1.25$ ($f_t = 0.5$) and when $x = 0, y = 2.50$ ($f_t = 1.0$) are both lower than $5.0 \mu_B$. Because canting occurs in different sublattices for these two garnets, the garnet in which no canting will occur [for this value of ($x + y$)] should have $0.5 < f_t < 1.0$. Moreover, this garnet should have the maximum Curie temperature for $x + y = 2.50$. We have not attempted to obtain this particular garnet, but in the course of our investigations we have made one very close to it. The garnet with formula $\{\text{Y}_2\text{Ca}\}[\text{Mg}_{0.75}\text{Fe}_{1.25}](\text{Fe}_{1.25}\text{Si}_{1.75})\text{O}_{12}$ ($f_t = 0.70$) has a 0°K moment of $-0.18 \mu_B$ (Table V). Our accumulated data indicate that the canting occurs in the tetrahedral sites (the octahedral sublattice then dominates, therefore the choice of negative sign); the effective moment of a tetrahedral Fe^{3+} ion is $4.85 \mu_B$. The Curie temperature is 250°K ; for $f_t = 0.50$ and 1.00 , the Curie temperatures (see Tables I and IV, respectively) are 187 and 86°K respectively. It is also noteworthy that the garnet with $f_t = 0.70$ saturates at low temperatures at about 10 koe, whereas the other two do not.

In the foregoing discussion, it would appear that it was tacitly assumed that the 0°K moments and Curie temperatures do not depend significantly on the *type* of nonmagnetic ion substituted for the Fe^{3+} ion in yttrium iron garnet. That is to say, it would appear that we had implied that a garnet such as $\{\text{Y}_{3-x-y}\text{Ca}_{x+y}\}[\text{Zr}_x\text{Fe}_{2-x}](\text{Fe}_{3-y}\text{Si}_y)\text{O}_{12}$ will have the same 0°K moment and Curie temperature as



or as $\{\text{Y}_{3+x-y}\text{Ca}_{y-x}\}[\text{Mg}_x\text{Fe}_{2-x}](\text{Fe}_{3-y}\text{Si}_y)\text{O}_{12}$ provided all x 's are the same and all y 's are the same. This appears to be a generally accepted idea.

However, there now appears to be some evidence that this is not generally true (see also Refs. 10-13 and Section 4.3). In Fig. 7 and Table III, it will be noted that beyond about $x = 0.7$ the moments for the system $\{Y_{3-x}Ca_x\}[Zr_xFe_{2-x}](Fe_3)O_{12}$ are lower than those for the system $\{Y_3\}[Sc_xFe_{2-x}](Fe_3)O_{12}$. The differences are outside experimental error. We shall discuss substituted gadolinium iron garnets fully in a future paper, but as further evidence of the reality of the differences in the two systems we point out here the moments obtained from high-field measurements at 4.2°K of $\{Gd_2Ca\}[ZrFe](Fe_3)O_{12}$ and $\{Gd_2Y\}[ScFe](Fe_3)O_{12}$. Extrapolation of $n_B(H_a)$ vs H_a to $H_a = 0$ gives 5.3 and 4.6 μ_B for these, respectively. Extrapolations of $n_B(H_a)$ vs $1/H_a$ to $1/H_a = 0$ give 7.1 and 6.7 μ_B for these respectively. Regardless of which values are more nearly the correct ones for these garnets, the moment of the Zr-substituted gadolinium iron garnet is significantly higher than that for the Sc-substituted one. Because the net moments from the iron sublattices of these garnets are antiparallel to those of the gadolinium sublattices, the net moment per formula unit of the Zr-substituted gadolinium iron garnet *should* be larger than that of the Sc-substituted gadolinium iron garnet, if the moments of the analogous substituted yttrium iron garnets are in the reverse order.

One may well ask whether these differences are a result of some Zr^{4+} or Sc^{3+} ions being in tetrahedral sites. While this possibility cannot be completely eliminated, evidence will be presented which indicates that it does not account for the results. Now, the Zr^{4+} ion is a rather large one; in ZrO_2 it prefers eight-coordination,³⁴ while in zirconates it prefers six-coordination. Lower coordination for Zr^{4+} has, as far as we know, not been reported, although there is no *a priori* reason to deny its possibility. If we, however, assume that all Zr^{4+} ions go into octahedral sites in the garnets, we may ask if some Sc^{3+} ions go into tetrahedral sites. Consideration of this possibility leads to the conclusion that if some Sc^{3+} ions do go into tetrahedral sites, the percentage doing so decreases to a minimum and then increases again.

We arrive at this conclusion in the following way. We assume that a small amount of Sc^{3+} ions in the tetrahedral sites does not alter the effect of the presence of the large amount of Sc^{3+} ions in octahedral sites on the moments of the Fe^{3+} ions in the tetrahedral sites. Thus for one Sc^{3+} , if we assume a formula of $\{Y_3\}[Sc_{0.9}Fe_{1.1}](Fe_{2.9}Sc_{0.1})O_{12}$, the effective moment (Fig. 23) of a tetrahedral Fe^{3+} ion will be 3.85 μ_B . The 0°K spontaneous magnetization per formula unit would then be 5.7 μ_B , in agreement with the observed value. A distribution given by $\{Y_3\}[Sc_{0.95}Fe_{1.05}](Fe_{2.95}Sc_{0.05})O_{12}$ gives a moment per formula unit of

5.4 μ_B . For 1.25 Sc³⁺ ions with a distribution given by $\{Y_3\}[Sc_{1.2}Fe_{0.8}](Fe_{2.95}Sc_{0.05})O_{12}$, the effective tetrahedral Fe³⁺ ion moment is 2.43 μ_B and the 0°K moment per formula unit is 3.16 μ_B , which is in good agreement with the observed value. The distribution $\{Y_3\}[Sc_{1.15}Fe_{0.85}](Fe_{2.90}Sc_{0.10})O_{12}$, however, leads to a 0°K moment per formula unit of 3.4 μ_B . For 1.50 Sc³⁺ ion with a distribution given by $\{Y_3\}[Sc_{1.4}Fe_{0.6}](Fe_{2.9}Sc_{0.1})O_{12}$, the derived 0°K moment per formula unit is 1.4 μ_B , in agreement with the observed values.

One can see then from these examples that if the assumptions were correct, the percentages of Sc³⁺ ions entering tetrahedral sites would be 10, 4 and 6.7 respectively. Such a situation is felt to be rather unlikely; one would expect the fraction of Sc³⁺ ions going into tetrahedral sites to increase monotonically. Under such conditions, the curves of Fig. 7 for the Zr- and Sc-substituted yttrium iron garnets should actually cross at a value of $x > 0.70$. It is still possible that very small amounts of Zr⁴⁺ ions may go into tetrahedral sites, in which case, if Sc³⁺ ions also go into tetrahedral sites, the situation would be more complex; but there is further evidence that this alone would still not account for the observations.

Fig. 4 indicates a resemblance of the behavior of the Ge- and Si-substituted yttrium iron garnets to those of the Zr- and Sc-substituted garnets. At $x > 1.0$, the 0°K moments per formula unit (absolute values) of the Ge-substituted garnets are lower than those for the Si-substituted garnets. Now, in Figs. 7 and 23 and Table III it will be noted that to $x = 0.70$ the Zr and Sc-substituted garnet systems behave in very nearly the same way. Below $x = 0.70$, it is expected that all these garnets will saturate magnetically at moderate fields. It is mainly in the region in which the intrasublattice interactions become dominant that substantial differences occur (but see Refs. 10–13 and Section 4.3); this is the region in which saturation is not attained at fields to 80 koe.

As pointed out earlier, it is now felt that it is unlikely that Si⁴⁺ ions enter the octahedral sites in the garnets. Thus it may be concluded that because between $x \approx 1.0$ and 1.92 the Ge-substituted garnets have lower moments (absolute values) than the analogous Si⁴⁺ ion substituted garnets, some Ge⁴⁺ ions do enter octahedral sites. When $x = 1.00$, the distribution of ions is probably given by $\{Y_2Ca\}[Fe_{1.99}Ge_{0.01}](Fe_{2.01}Ge_{0.99})O_{12}$. When $x = 1.92$, the distribution is probably given by $\{Y_{1.08}Ca_{1.92}\}[Fe_{1.94}Ge_{0.06}](Fe_{1.14}Ge_{1.86})O_{12}$. However, if the percentage of Ge entering octahedral sites increases with increasing total substitution, and if there are no other effects on the spontaneous magnetization resulting from the particular ion, the curve for Ge substitution should cross that for Si substitution.

If, for the sake of discussion, a linear relation between percentage Ge in octahedral sites vs total Ge substitution is assumed for $x > 1.0$, the distribution for $x = 2.0$ would be given by $\{YCa_2\}[Fe_{1.93}Ge_{0.07}]$ - $(Fe_{1.07}Ge_{1.93})O_{12}$ and for

$$x = 2.25, \{Y_{0.75}Ca_{2.25}\}[Fe_{1.91}Ge_{0.09}](Fe_{0.84}Ge_{2.16})O_{12}.$$

Using Fig. 22, the effective moments of the octahedral Fe^{3+} ions would be 4.70 and $3.40 \mu_B$ respectively. The $0^\circ K$ moments then should be -4.0 and $-2.3 \mu_B$ respectively, as compared with the observed values -3.15 and $-1.55 \mu_B$ respectively. Note (see Fig. 4) that the observed value for 2.0 Si is $-3.8 \mu_B$. It is probable that for $x = 1.92$ there is somewhat less than 0.06 Ge in octahedral sites, but regardless of the actual amounts, the single assumption of some Ge^{4+} ions in octahedral sites *cannot* account for the observations if it is also assumed that Si^{4+} ions go only into tetrahedral sites in the garnets. But even if the latter assumption were unacceptable, it is certain that the Si^{4+} ions would have a greater preference for the tetrahedral sites than Ge^{4+} ions. And it would then still appear necessary for the Ge curve to cross the Si curve if there were no additional effect resulting from the substitution of a particular ion.

This conclusion also is perhaps contrary to the thinking on ferromagnetic materials. Generally, it is believed that for a given total substitution, when the net difference in the number of Fe^{3+} ions is greater, the moment per formula unit should be greater. However, there is concrete evidence that the conclusion is correct.

This may be illustrated by the following example. The garnet $\{Y_{1.24}Ca_{1.76}\}[Mg_{0.22}Fe_{1.78}](Fe_{1.02}Si_{1.98})O_{12}$ has a $0^\circ K$ moment of $-3.1 \mu_B^{35}$ and a Curie temperature of $245^\circ K$. The garnet $\{Y_{0.8}Ca_{2.2}\}[Fe_2]$ - $(Fe_{0.8}Si_{2.2})O_{12}$ has a $0^\circ K$ moment (see Fig. 4) of $-2.3 \mu_B$ and a Curie temperature (see Fig. 5) of $200^\circ K$. (Note that the difference in the number of Fe^{3+} ions in the former is 0.76 and in the latter 1.2.) If it is again assumed that the tetrahedral Fe^{3+} ion moments remain parallel, then in the former the effective moment of an octahedral Fe^{3+} ion is $4.5 \mu_B$. Examination of Fig. 22 shows that this is just slightly larger than the effective moment of the octahedral Fe^{3+} ion in $\{Y_{1.02}Ca_{1.98}\}$ - $[Fe_2](Fe_{1.02}Si_{1.98})O_{12}$. The $45^\circ K$ lower Curie temperature of $\{Y_{0.8}Ca_{2.2}\}$ - $[Fe_2](Fe_{0.8}Si_{2.2})O_{12}$ than that of $\{Y_{1.24}Ca_{1.76}\}[Mg_{0.22}Fe_{1.78}](Fe_{1.02}Si_{1.98})O_{12}$ is in accord with the stronger interactions in the latter. The Curie temperature of the latter is $25^\circ K$ lower than that of $\{Y_{1.02}Ca_{1.98}\}[Fe_2]$ - $(Fe_{1.02}Si_{1.98})O_{12}$ (Fig. 5), which has a larger number of interactions of about the same strength.

The effects of different ions on magnetic behavior are more marked

in several of the specimens shown in Tables IV and V. The systems involved are $\{Y_{3-y}Ca_y\}[Sc_xFe_{2-x}](Si_yFe_{3-x})O_{12}$, $\{Y_{3-y+x}Ca_{y-x}\}[Mg_xFe_{2-x}](Si_yFe_{3-y})O_{12}$, and $\{Y_{3-x-y}Ca_{x+y}\}[Zr_xFe_{2-x}](Si_yFe_{3-y})O_{12}$. The results for specimens with values of x and y : $x = y = 0.85$; $x = y = 1.00$; $x = 0.90$, $y = 1.10$; and $x = 1.10$, $y = 0.90$ are retabulated in Table VIII. In the last case, it is not now possible to prepare the specimen in which $M = Mg^{2+}$ because electrostatic balance with a tetravalent ion in the c -sites would be required. It is seen that the moments and Curie temperatures decrease in the order Mg, Sc, Zr and that saturation is more easily attained in those garnets containing magnesium than in the others. If we assume for the time being that all the Mg^{2+} ions go into octahedral sites, it appears that if it were possible to find a tetravalent ion to balance electrostatically the Mg^{2+} ions as in a hypothetical system $\{Y_{3-x}Me_x^{4+}\}[Mg_x^{2+}Fe_{2-x}](Fe_3)O_{12}$, the effective moment of a tetrahedral Fe^{3+} ion for given x would be higher than for an analogous Sc^{3+} -substituted yttrium iron garnet. This, of course, neglects any effect that the ions substituted in the c -sites would have on the magnetic structure. There are probably effects of the c -site substituted ions,¹³ but it is impossible to determine them for divalent ions such as Ca^{2+} separately. It should be pointed out that when $x = y$ no substitution for Y is necessary when $M = Mg^{2+}$; $x Ca^{2+}$ is necessary when $M = Sc^{3+}$, and $2x Ca^{2+}$ is necessary when $M = Zr^{4+}$.

The important question again arises: are some of the ions assumed to be in octahedral sites actually in tetrahedral sites? To try to answer this question directly, we have taken quantitative x-ray intensity data

TABLE VIII—RETABULATION OF DATA FROM SELECTED SPECIMENS FROM TABLES IV, V AND VI

Octahedral Ion	$H_a = 0$	$T_C, ^\circ K$	Saturation Field, koe
Mg	$x = y = 0.85$ 4.25	327	11.3
Sc	4.0		12.6
Zr	3.6		70
	$x = y = 1.00$		
Mg	3.8	265	70
Sc	2.9	235	>70
Zr	2.1	200	>70
	$x = 0.90, y = 1.10$		
Mg	3.2	294	9.6
Sc	2.8	260	>70
Zr	1.9	210	>70
	$x = 1.10, y = 0.90$		
Sc	2.8	220	>70
Zr	1.8	190	>70

from the specimens of $\{Y_{0.5}Ca_{2.5}\}[Zr_{1.25}Fe_{0.75}](Fe_{1.75}Si_{1.25})O_{12}$ and $\{Y_3\}[Mg_{1.85}Fe_{0.15}](Fe_{1.15}Si_{1.85})O_{12}$. The data were collected with the Noreco powder diffractometer using $CuK\alpha$ radiation. Integrated intensities were measured on the charts with a Keuffel and Esser polar planimeter. In the calculations of intensities, corrections were made for anomalous dispersion,³⁶ the imaginary parts being included.³⁷ Estimates of oxygen ion positions were as far as possible based on interatomic distances expected between the ions involved. Calculations were made for the above distributions and also for $\{Y_{0.5}Ca_{2.5}\}[Zr_{1.00}Fe_{1.00}](Fe_{1.50}Zr_{0.25}Si_{1.25})O_{12}$ and $\{Y_3\}[Mg_{1.70}Fe_{0.30}](Fe_{1.0}Mg_{0.15}Si_{1.85})O_{12}$.

The results indicated that the x-ray data cannot give unequivocal conclusions regarding the exact distribution of the ions in these garnets. However, the assumptions that the Mg^{2+} and Zr^{4+} ions substitute only in the octahedral sites in the two garnets are certainly compatible with the data. Furthermore, examination of powder photographs of related garnets indicates that it is more likely that the Zr^{4+} and Mg^{2+} ions prefer octahedral sites exclusively than that some enter tetrahedral positions.

If, however, we examine the Curie temperatures in each x,y (for $x+y=2.0$) group of Table VIII, we might be led to believe that if all Zr^{4+} ions are considered to be in octahedral sites, because substitution in the octahedral sites has a far greater effect on Curie temperature than tetrahedral substitution in this region of x and y , some Sc^{3+} ions go into tetrahedral sites and more Mg^{2+} ions do. On the other hand, we note that for Zr^{4+} ion substitution the highest moment is obtained for $x=y=1.00$, those for $x=0.90$, $y=1.10$ and $x=1.10$, $y=0.90$ being lower. In fact, the same seems to be true for Mg^{2+} and for Sc^{3+} substitution. It thus appears unlikely that the results can be explained on the basis that the distributions of ions are different from those assumed.

To examine this conclusion further, we note the results on several other specimens. Table VI lists some Ge^{4+} ion substituted specimens analogous to those in Tables IV and V. For $Y_3MgFe_3GeO_{12}$, $Y_3Mg_{1.25}Fe_{2.50}Ge_{1.25}O_{12}$ and for $\{Y_2Ca\}ScFe_3GeO_{12}$, Ge does not have a significant effect. But for $\{Y_{1.3}Ca_{1.7}\}Zr_{0.85}Fe_{3.5}Ge_{0.85}O_{12}$ and for $\{YC_{2}\}ZrFe_3GeO_{12}$ the differences are substantial. These differences may be partly a result of a substantially different effect on the interaction geometry by the Ge^{4+} ion as compared with the Si^{4+} ion and partly because some of the Ge^{4+} ions enter octahedral sites in these garnets.

We have also prepared and made measurements on $\{Y_{1.8}Ca_{1.2}\}[Zr_{0.6}Fe_{1.4}](Si_{0.6}Fe_{2.4})O_{12}$ and $\{Y_{1.8}Ca_{1.2}\}Zr_{0.6}Fe_{3.8}Ge_{0.6}O_{12}$ (Tables V and VI) for comparison with $\{Y_3\}[Mg_{0.6}Fe_{1.4}](Si_{0.6}Fe_{2.4})O_{12}$ (Fig. 11).

Although the differences are small, they could be real. The Mg-substituted garnet has the highest moment and the Zr-Ge substituted one the lowest. Again in the latter case, it is possible that some Ge⁴⁺ ions substitute in octahedral sites.

For the most part, however, in the region in which magnetic saturation is attained, differences in behavior for different nonmagnetic ions are either insignificant or small, as can be seen from an examination of Tables IV, V and VI and from later discussion. There is one garnet listed in Table V which behaves anomalously, as will be seen more clearly later; it is $\{Y_{0.8}Ca_{2.2}\}[Zr_{0.6}Fe_{1.4}](Fe_{1.4}Si_{1.6})O_{12}$. Although its moment appears to be right, its Curie temperature appears to be too low. This garnet, however, was very difficult to make. Although its lattice constant indicates that the composition is as given, the back-reflection lines in the powder photograph were not sharp.

It appears then that we must conclude that, especially in the regions of substitution in which intrasublattice interactions are dominant, there is a substantial effect on the magnetic structure of the types of ions substituted. Once it is realized that this occurs, it is not too difficult to find reasons that it should.

It has been shown that the *geometry* of different garnets may differ substantially. For example in a grossularite ($\{Ca_3\}[Al_2](Si_3)O_{12}$),³⁸ the oxygen octahedron is much more nearly regular than in yttrium iron garnet.³² Also, the oxygen tetrahedron about the Si⁴⁺ ion is more regular than that about the Fe³⁺ ion in yttrium iron garnet. However the oxygen dodecahedron about the Ca²⁺ ion is more irregular than that about the Y³⁺ ion in yttrium iron garnet. The Si-O-Al angle in the grossularite is 136°, while the Fe(*a*)-O-Fe(*d*) angle in yttrium iron garnet is 127°.

Because ions of different valence and size produce different effects on the geometry (a manifestation of differences in chemical bonding) or crystal structure, it may be speculated that they will also produce different effects on the magnetic structure, especially when weak interactions are important (see also Refs. 21, 24 and 10-13).

In the earlier discussion of the $\{Y_3\}[Mg_xFe_{2-x}](Fe_{3-x}Si_x)O_{12}$ system, it was pointed out that the substitution of Si⁴⁺ ions in the tetrahedral sites, had, beyond $x = 0.70$, the tendency to weaken the *d-d* interactions. However, it is now seen that the Mg²⁺ ion appears also to disrupt the magnetic structure less than does Sc³⁺ or Zr⁴⁺ substitution. Unfortunately, it is again not possible to determine experimentally the separate effect of the Mg²⁺ ion. Nevertheless, if our assumption requiring the moments in one sublattice to remain parallel is valid, then our conclu-

sions appear thus far to be plausible. In Fig. 22 we have plotted points for the effective moments of the tetrahedral Fe^{3+} ions for $x = 0.85$ and 1.00 in the garnets $\{\text{Y}_{3-2x}\text{Ca}_{2x}\}[\text{Zr}_x\text{Fe}_{2-x}](\text{Fe}_{3-x}\text{Si}_x)\text{O}_{12}$ and $\{\text{Y}_{3-x}\text{Ca}_x\}[\text{Sc}_x\text{Fe}_{2-x}](\text{Fe}_{3-x}\text{Si}_x)\text{O}_{12}$. It is seen that these are higher than for the analogous garnets $\{\text{Y}_{3-x}\text{Ca}_x\}[\text{Zr}_x\text{Fe}_{2-x}](\text{Fe}_3)\text{O}_{12}$ and $\{\text{Y}_3\}[\text{Sc}_x\text{Fe}_{2-x}](\text{Fe}_3)\text{O}_{12}$ respectively.

If there were no effect of particular nonmagnetic ions substituted for the Fe^{3+} ions, it would be possible to plot a series of curves of 0°K moment vs $f_t = y/(x+y)$, where x,y equals the number of nonmagnetic ions in the octahedral, tetrahedral sites respectively. Thus it would have been possible with limited data to predict the moments for all nonmagnetic ion substituted yttrium iron garnets. Within the range that the $a-d$ interactions are everywhere dominant, this is still possible for the garnets discussed here. We have seen that even when $x+y$ is large, if y is substantially larger than x , the $a-d$ interactions may still be dominant and therefore such curves would still be valuable.

Some curves of this type are plotted in Fig. 27. Included are curves

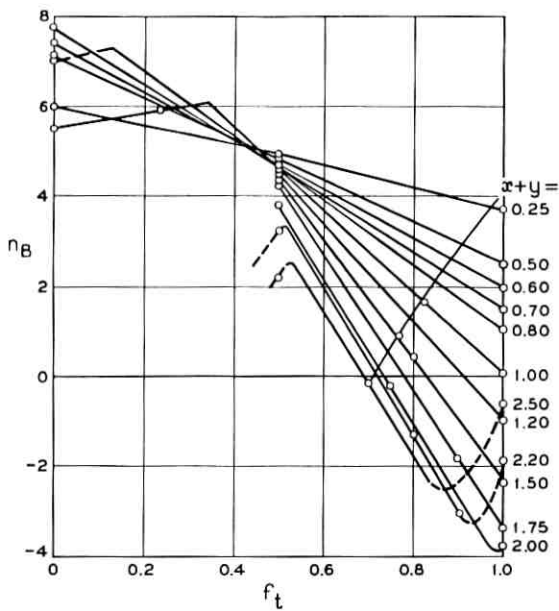


Fig. 27 — Spontaneous magnetizations, $n_B(0,0)$ of substituted yttrium iron garnets vs f_t , the fraction of nonmagnetic ions in the tetrahedral sites. [x = number of nonmagnetic ions in octahedral sites; y = number of nonmagnetic ions in tetrahedral sites; $f_t = y/(x+y)$.] Shown also is the curve for the $\text{Y}_3\text{Fe}_{5-x}\text{Al}_x\text{O}_{12}$ system.

which have regions in which the intrasublattice interactions are dominant. Points in the region $f_t \geq 0.5$ are mostly from the system $\{Y_{3+x-y} Ca_{y-x}\}[Mg_x Fe_{2-x}](Fe_{3-y} Si_y)O_{12}$. In Fig. 28, Curie temperatures vs f_t are shown for some values of $x + y$. The curves should be considered rather rough, because not many points have been obtained.

Fig. 27 shows that for $x + y = 2.0$, there is an algebraic minimum in the curve at $f_t \approx 0.98$. For $x + y = 2.20$ the algebraic minimum is more pronounced and occurs at $f_t \approx 0.93$. This makes clearer the discussion given above regarding the occurrence of garnets in which, for a given $x + y$, there is a higher (absolute value) moment when $|(3 - y_1) - (2 - x_1)| < |(3 - y_2) - (2 - x_2)|$. Note also that there are algebraic maxima in the curves for values of $x + y > 0.70$. The value of $x + y$ at which the maximum or the minimum first occurs appears to be at the point at which the intrasublattice interactions become dominant in the exclusively octahedral and tetrahedral ion substituted garnets respectively (see above). The crossover point for the Ge-substituted system should then be at the point of the algebraic minimum for the Si-substituted system. Examination of Fig. 4 shows that extension of the curve for the former system does intersect that of the latter system at about the predicted point.

The arguments regarding the effects of particular ions may be made still clearer. Referring again to Table VIII, we see that if one wished to

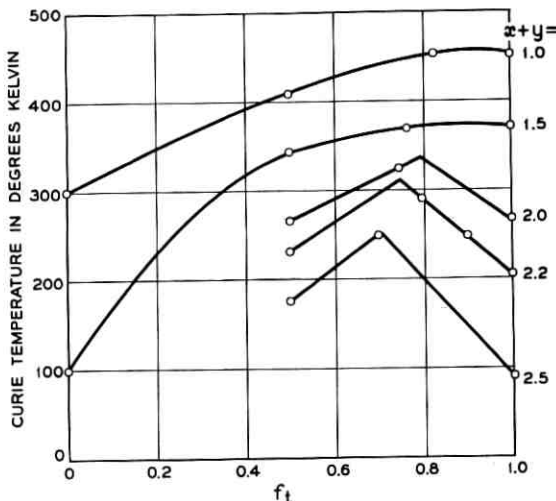


Fig. 28 — Curie temperatures vs f_t for various substituted yttrium iron garnets. (The lines connecting the points are, in this case, somewhat speculative.)

assume that the lower moments for Sc^{3+} and Zr^{4+} substitution when $x = y = 1.0$ (that is, with one Si^{4+} in tetrahedral sites) resulted from some Sc^{3+} or Zr^{4+} ions entering tetrahedral sites, f_t for the former would be 0.56 and for the latter 0.60 (Fig. 27). But then in Fig. 28 we see that the Curie temperatures should be in reverse order from those observed. Furthermore, magnetic saturation should also be more, rather than less, easily attainable than for the analogous Mg^{2+} ion substituted garnet. The garnet $\{\text{Y}_2\text{Ca}\}[\text{Mg}_{0.5}\text{Fe}_{1.5}](\text{Fe}_{1.5}\text{Si}_{1.5})\text{O}_{12}$ ($f_t = 0.75$) saturates at ≈ 9.6 koe at 1.4°K (see Table V).

Fig. 28 also appears to corroborate the idea that the intrasublattice interactions are effective over the whole temperature range, since for a given value of $x + y$, the maximum value of T_c is almost surely attained when the effective moments are at a maximum. It should be kept in mind, however, that Figs. 27 and 28 are based mainly on data from garnets which are magnetically saturated at 1.4°K and the data from the system $\{\text{Y}_{3+x-y}\text{Ca}_{y-x}\}[\text{Mg}_x\text{Fe}_{2-x}](\text{Fe}_{3-y}\text{Si}_y)\text{O}_{12}$. The data from the system $\{\text{Y}_{3-y}\text{Ca}_y\}[\text{Sc}_x\text{Fe}_{2-x}](\text{Fe}_{3-y}\text{Si}_y)\text{O}_{12}$ in the region where saturation is not attained must be treated separately, as must the data from such a system as $\{\text{Y}_{3-x-y}\text{Ca}_{x+y}\}[\text{Zr}_x\text{Fe}_{2-x}](\text{Fe}_{3-y}\text{Si}_y)\text{O}_{12}$. This results, as shown above, from the effect of the individual nonmagnetic ions on the magnetic structure.

Knowing that the Gilleo theory does not account for the 0°K moments of the substituted garnets and also that the x-ray method is not apt to give very narrow limits for the ionic distribution in the system $\text{Y}_3\text{Fe}_{5-x}\text{Al}_x\text{O}_{12}$, it was felt that it might be determined from such data as plotted in Fig. 27. If the particular ion effect is neglected, one may draw a curve (see Fig. 27) intersecting those for particular³⁹ $x + y$ at values of n_B found in the $\text{Y}_3\text{Fe}_{5-x}\text{Al}_x\text{O}_{12}$ system and thereby find f_t for each $x + y$ in this system, as plotted in Fig. 29.

The results obtained appear to be reasonable. It will be noted first

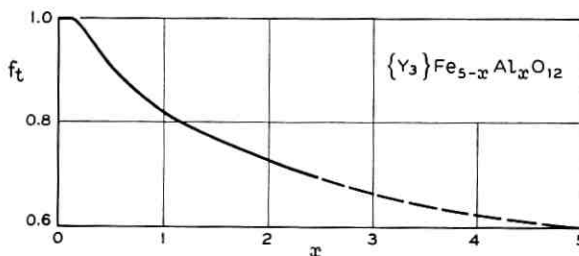


Fig. 29 — f_t vs x for the system $\text{Y}_3\text{Fe}_{5-x}\text{Al}_x\text{O}_{12}$ as derived from Fig. 27.

that the curve extends naturally from³⁹ $x + y = 2.5$ to $x + y = 5.0$, in which f_t must be 0.60. Secondly, for $x < 2.00$, (x as in $\text{Y}_3\text{Fe}_{5-x}\text{Al}_x\text{O}_{12}$) magnetic saturation is obtained at low fields at 1.4°K . Furthermore, two specimens in the system $\{\text{Y}_{3+x-y}\text{Ca}_{y-x}\}[\text{Mg}_x\text{Fe}_{2-x}](\text{Fe}_{3-y}\text{Si}_y)\text{O}_{12}$, namely those for $x = 0.175$, $y = 0.825$ and $x = 0.75$, $y = 1.75$ and a third $\{\text{Y}_{1.50}\text{Ca}_{1.50}\}[\text{Zr}_{0.35}\text{Fe}_{1.65}](\text{Fe}_{1.85}\text{Si}_{1.15})\text{O}_{12}$ give very good checks on the moments found in the $\text{Y}_3\text{Fe}_{5-x}\text{Al}_x\text{O}_{12}$ system (see Tables V and VII). The Curie temperatures for the three specimens are plotted vs $x + y$ in Fig. 18 together with those found for the specimens in the $\text{Y}_3\text{Fe}_{5-(x+y)}\text{Al}_{(x+y)}\text{O}_{12}$ system. The agreement in the region $x + y \leq 1.50$ is good but deteriorates in the region $x + y > 1.50$. This may again be an indication of the "particular ion effect."

Now consider a set of substituted garnets which have the same Curie temperature and which saturate magnetically at low fields. It is uncertain whether at a given temperature below T_c the values of the intrinsic spontaneous moments per octahedral Fe^{3+} ion, M_o , will all be the same, and similarly whether those of the tetrahedral Fe^{3+} ions, M_t , will be the same. It is unlikely, however, that they will differ greatly, and we shall assume that they are the same.

We take the three garnet specimens with measured extrapolated or interpolated Curie temperatures 367 – 375°K :

- (1) $\{\text{Y}_{1.50}\text{Ca}_{1.50}\}[\text{Zr}_{0.35}\text{Fe}_{1.65}](\text{Fe}_{1.85}\text{Si}_{1.15})\text{O}_{12}$ ($T_c = 370^\circ\text{K}$)
- (2) $\{\text{Y}_{1.50}\text{Ca}_{1.50}\}[\text{Fe}_2](\text{Fe}_{1.50}\text{Si}_{1.50})\text{O}_{12}$ ($T_c = 367^\circ\text{K}$)
- (3) $\{\text{Y}_3\}[\text{Mg}_{0.62}\text{Fe}_{1.38}](\text{Fe}_{2.38}\text{Si}_{0.62})\text{O}_{12}$ ($T_c = 375^\circ\text{K}$).

(For all these, the values calculated on the basis of the Gilleo model differ by $\leq 11^\circ\text{K}$.) The observed spontaneous moments at 0, 100, 200, and 300°K are respectively as follows:

- (1) 0.88, 0.79, 0.59, 0.38 μ_B
- (2) -2.36, -2.15, -1.65, -1.08 μ_B
- (3) 4.46, 4.00, 3.04, 2.00 μ_B (by interpolation; see Fig. 30).

In specimen (1) the canting must take place in the d sites, the sine of the angle being 0.99 [i.e., $\{5(1.65) + 0.88\}/(1.85)5$]. In (2) the canting occurs in the octahedral sites, the sine of the angle being 0.99. Designating the octahedral and tetrahedral moments M_o and M_t respectively, we have from (1) and (2) at 100°K :

$$1.85(0.99)M_t - 1.65M_o = 0.79 \mu_B$$

$$1.50M_t - 2(0.99)M_o = -2.15 \mu_B$$

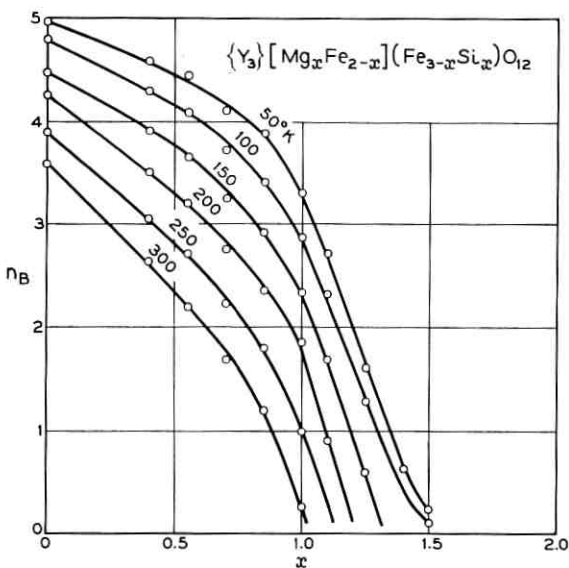


Fig. 30.—Spontaneous magnetizations, $n_B(H_a = 0)$, vs x for given temperatures in the $\{Y_3\}[Mg_xFe_{2-x}](Fe_{3-x}Si_x)O_{12}$ system.

for which

$$M_t = 4.44 \mu_B$$

and

$$M_o = 4.45 \mu_B .$$

For (3), we should have

$$2.38(0.96)M_t - 1.38M_o = 4.00 \mu_B ,$$

the canting angles being obtained from the effective moments given in Fig. 22. Putting the moments obtained from (1) and (2) into the expression for (3), we obtain $4.00 \mu_B$.

To obtain the other values for (3) we substitute the 200 and 300°K moments in turn for the 100°K ones. At 200°K, we obtain from (1) and (2) $M_t = 3.36$, $M_o = 3.38 \mu_B$, and the net moment for (3) calculated from these Fe^{3+} ion moments is $3.01 \mu_B$, to be compared with $3.04 \mu_B$ observed. At 300°K, (1) and (2) yield $M_t = 2.14 \mu_B$, $M_o = 2.17 \mu_B$; the net moment calculated for (3) from these is $1.89 \mu_B$, to be compared with $2.00 \mu_B$ observed. The agreement of calculated with observed values is generally good.

Now we try the same procedure with the Gilleo model. The three equations would be

$$(1) \quad 1.85(0.97)M_t - 1.65(0.96)M_o = n_B^{(1)}(T)$$

$$(2) \quad 1.50M_t - 2.00(0.89)M_o = n_B^{(2)}(T)$$

$$(3) \quad 2.38(0.91)M_t - 1.38(0.99)M_o = n_B^{(3)}(T).$$

If we solve (2) and (3) of the Gilleo model for $T = 100^{\circ}\text{K}$, we obtain $M_t = 5.57 \mu_B$ and $M_o = 5.90 \mu_B$, clearly impossible values, and there is therefore no point in checking these equations further.

It therefore appears that the intrasublattice interactions in these garnets may be important over the whole temperature range to or near T_c and that the Gilleo model is inapplicable in this range. However, the agreement of observed Curie temperatures with those predicted by the Gilleo theory is so good as to indicate either that the Gilleo theory is applicable very near the Curie temperature or that agreement is somehow fortuitous. In any case the Gilleo formula for Curie temperature is useful for the garnets of the systems discussed here.

When the canting model favored in this paper is used to calculate the intrinsic moments of the Fe^{3+} ions in the two different sites, the values obtained are only slightly different; in fact, the difference is so slight as to appear insignificant. The work of Bertaut et al.,⁴⁰ Prince⁴¹ and Kuzminov et al.,⁴² indicates that in yttrium iron garnet itself, the moments at temperatures above 110°K of the crystallographically different Fe^{3+} ions are substantially different. This is not corroborated, at least by the results on the substituted garnets.

There is some question as to how the determinations of the spontaneous magnetizations should be made when saturation is not attained at fields up to 14.24 koe. This "unsaturation" occurs noticeably after the intrasublattice interactions become dominant, an indication that the tendency not to saturate is associated with the canting. It is probable that when a specimen appears not to be saturated it is, in a sense, "oversaturated"; that is, the applied field disrupts the true zero-field structure by causing some alignment of the canted moments. If such were the case, it would appear that extrapolation to zero field would yield the more nearly correct results. This was especially well demonstrated by the results on the $\{\text{Y}_3\}[\text{Mg}_x\text{Fe}_{2-x}](\text{Fe}_{3-x}\text{Si}_x)\text{O}_{12}$ system. It is possible, however, that increased anisotropy also plays a role in preventing saturation. Measurements on single crystals, not now available, should aid in clarifying this situation.

In Gilleo's theory, an Fe^{3+} ion in one coordination not linked to at

least two Fe^{3+} ions in the other coordination does not participate in the ferrimagnetism, at least at temperatures above 20°K. Gillo points out³ that the ions thus excluded should behave nearly as free ions at these temperatures, i.e., between 20°K and T_c . We do not find this to be the case. For example, in the $\{\text{Y}_{3-x}\text{Ca}_x\}[\text{Fe}_2](\text{Fe}_{3-x}\text{Si}_x)\text{O}_{12}$ system, for substitutions which have the *a-d* interactions dominant, that is, for $x_t < 1.92$ and $x_o < 0.70$, the specimens are saturated or very nearly so at nominal fields. Beyond $x_t = 1.92$ or $x_o = 0.70$ saturation is not attained even at 1.4°K. But generally we observe that $n_B(H_a, T) - n_B(0, T)$ for fixed $H_a < 14.24$ koe is essentially constant to temperatures somewhat below the Curie temperature. For example, in the case of $\{\text{YCa}_2\}[\text{Fe}_2](\text{FeSi}_2)\text{O}_{12}$ with $T_c = 266^\circ\text{K}$, $n_B(H_a, T) - n_B(0, T)$ is approximately equal to $0.2 \mu_B$ at $H_a = 14$ koe to $T \approx 220^\circ\text{K}$. In the case of $\{\text{Y}_{0.5}\text{Ca}_{2.5}\}[\text{Fe}_2](\text{Fe}_{0.5}\text{Si}_{2.5})\text{O}_{12}$ with $T_c = 86^\circ\text{K}$, $n_B(H_a, T) - n_B(0, T)$ is approximately equal to $0.5 \mu_B$ at $H_a = 14$ koe to $T \approx 80^\circ\text{K}$.

4.1 Application to Ferrospinsels

In the present article, it has been shown that the substitution of any nonmagnetic ion for an Fe^{3+} ion in the garnets tends to weaken the average *a-d* interaction. In a previous paper,¹⁴ it was shown that divalent paramagnetic ions and Cr^{3+} ions also tend to weaken the average *a-d* interaction when substituted for the Fe^{3+} ions. The weakening of these interactions also results in an apparent reduction of the effective moment of the magnetic ions in at least one of the sublattices. We have put forward the idea that this reduction may be the result of random canting of these moments resulting from the intrasublattice antiferromagnetic interactions.

The ideas discussed in this paper should be applicable to the ferrimagnetic spinels. In a spinel, there is one cation in a tetrahedral site and there are two cations in octahedral sites per formula unit AB_2O_4 . The antiferromagnetic interactions between magnetic ions on the two different sites would be expected to be the strongest present in the crystal; the antiferromagnetic interactions within the octahedral sublattice would be expected to be stronger than the antiferromagnetic interactions within the tetrahedral sublattice.

In the system $\{\text{Y}_{3-x}\text{Ca}_x\}[\text{Fe}_2](\text{Fe}_{3-x}\text{Si}_x)\text{O}_{12}$, there is very little effect on the effective moment of the Fe^{3+} ions in octahedral sublattice of substitution to $x = 1.0$, and only small effect even to $x = 1.50$. Thus one would predict that substitution in the octahedral sublattice of a ferrospinel would give similar behavior. On the other hand, substitution for

a-site Fe^{3+} ions in the garnets has almost an immediately obvious effect on the effective moments of the Fe^{3+} ions in the *d* sites. Similarly, substitution in the tetrahedral sites of the ferrospinel might be expected to have a substantially larger effect than an analogous (twofold) substitution in the octahedral sites.

Lithium ferrite, $(\text{Fe})[\text{Li}_{0.5}\text{Fe}_{1.5}]\text{O}_4$, accordingly has the highest Curie temperature, 953°K ,⁴³ among the ferrospinels. Any substitution — i.e., by paramagnetic or nonmagnetic ions — for trivalent Fe^{3+} ions in this spinel reduces the Curie temperature.⁴³ Now the spinel nickel ferrite is inverse,⁴⁴ i.e., the formula may be written $(\text{Fe})[\text{NiFe}]\text{O}_4$. In the garnet $\{\text{Y}_3\}[\text{Ni}_2](\text{FeGe}_2)\text{O}_{12}$, the $\text{Ni}^{2+}\text{-O}^{2-}\text{-Fe}^{3+}$ interaction is about $\frac{1}{3}$ as strong as the $\text{Fe}^{3+}\text{-O}^{2-}\text{-Fe}^{3+}$ interaction.¹⁴ In $(\text{Fe})[\text{Li}_{0.5}\text{Fe}_{1.5}]\text{O}_4$, each tetrahedral Fe^{3+} ion is linked through oxygen ions, on the average, to three Li^{3+} and nine Fe^{3+} ions in the octahedral sublattice; in $(\text{Fe})[\text{NiFe}]\text{O}_4$ each tetrahedral Fe^{3+} ion is linked, through oxygen ions, on the average to six Ni^{2+} and six Fe^{3+} octahedral ions. In both cases, octahedral ions are linked only to Fe^{3+} ions in the tetrahedral sublattice. The average interaction strength in $(\text{Fe})[\text{Li}_{0.5}\text{Fe}_{1.5}]\text{O}_4$ is then $\approx 9/8$ of that in $(\text{Fe})[\text{NiFe}]\text{O}_4$. If there were at least an approximately linear relationship between Curie temperature and interaction strength,⁴⁵ the Curie temperature of $(\text{Fe})[\text{NiFe}]\text{O}_4$ should be $\approx 850^\circ\text{K}$. This value compares favorably with that observed, 853°K .

Several investigators have sought an explanation for the low 0°K moment observed for manganese ferrite. As far as we know, there has been no *direct* evidence of other than divalent manganese and trivalent iron in a carefully prepared ferrite of composition MnFe_2O_4 . Now manganese ferrite has a low Curie temperature, 603°K , as compared with nickel ferrite. Our work on the garnets would indicate that the strength of the $\text{Mn}^{2+}\text{-O}^{2-}\text{-Fe}^{3+}$ interaction should not differ substantially from that of the $\text{Ni}^{2+}\text{-O}^{2-}\text{-Fe}^{3+}$ interaction. Thus, the low Curie temperature must be associated with the evidence that MnFe_2O_4 is actually an almost normal spinel, that is, the distribution of ions is given by



But this is analogous to the substitution in the *a* sites in yttrium iron garnet. Now an Fe^{3+} ion in an octahedral site in the ferrite is linked to mostly Mn^{2+} ions in tetrahedral sites; thus the average *a-d* interaction is substantially weaker in this ferrite than in lithium ferrite, and accordingly the Curie temperature is substantially lower.

We have shown¹⁴ also that even substitution of 0.4 Mn^{2+} in the *a* sites of yttrium iron garnet causes canting of the *d*-site ion moments.

We propose that the behavior of manganese ferrite is similar to that of the divalent magnetic ion substituted garnets; that is, that the substitution of *any* ions for Fe^{3+} ions causes a weakening of the *a-d* interactions, whereupon the competing intrasublattice interaction manifests itself. For MnFe_2O_4 the usually observed value of the spontaneous magnetization at 4.2°K is $4.6 \mu_B$. Hastings and Corliss⁴⁶ have measured three specimens which give this value and very nearly the same ionic distribution. However, they could not resolve the problem of the low moment.

It is possible that if the specimens were not stoichiometric a low value could be obtained. However, if it is accepted that $4.6 \mu_B$ is the correct value of spontaneous magnetization at 4.2°K , then we have, analogously to the garnets, that the canting may occur among the Fe^{3+} and Mn^{2+} ion moments on the *d*-sites. The effective moment (i.e., the component antiparallel to the *a* sublattice Fe^{3+} ion moments) of a *d*-site ion would then be $4.8 \mu_B$. In the garnet $\{\text{Y}_3\}[\text{Mn}_{0.4}\text{Fe}_{1.6}](\text{Fe}_{2.6}\text{Si}_{0.4})\text{O}_{12}$, the effective *d*-site Fe^{3+} ion moment is 4.96. Comparisons (see Fig. 22) with the effects of substitution of nonmagnetic ions in the garnets lead intuitively to the conclusion that the proposed amount of canting of the octahedral cation moments in manganese ferrite is plausible.

In discussing this conclusion with Hastings and Corliss, they have informed us that in the course of their investigation of MnFe_2O_4 they considered the moments proposed by us but concluded that the value of $4.6 \mu_B$ for the average moment per ion in each sublattice gave a better fit with the observed data. This conclusion has not been changed after recent further consideration; however, the authors inform us that the model proposed by us cannot be ruled out by the existing data.

4.2 Neutron Diffraction Studies

We should mention what our ideas mean as far as neutron diffraction studies are concerned. First, consider a crystalline substance which is a solid solution. Coherent x-ray diffraction effects average over the crystal; that is, they do not tell us about local or short-range structure. For example, if two chemically different kinds of atoms may be thought to occupy highly specialized space group positions (i.e., with no allowable degrees of freedom), these are seen by the coherent x-ray "reflections" as having a weighted average atomic form factor of the two different atoms. Further, it could happen that these atoms, in the short range, may not lie exactly on the space group sites, but over the crystal space; that is, in the long range, appear to lie on these sites. In such a case the

average thermal parameter may look too high, because the displacements of the atoms from the exact sites will appear from the coherent x-ray diffraction effects to be vibrations. Only the incoherent scattering will contain the information sought, but this may be too complicated to interpret.

Similarly, coherent neutron diffraction reflections may not give us a direct insight into the short-range magnetic disorder of the substituted garnets. They will give us only the average effective moment per ion of the particular sublattice. Incoherent neutron scattering might, however, be more elucidating.

4.3 Garnets Containing Pentavalent Vanadium and Antimony

Recently we have discovered new garnets containing pentavalent vanadium and antimony ions. In the case of V^{5+} ion substitution Smolenskii et al.⁹ had reported on the system $x \{YCa_2\}Fe_4VO_{12} - (1-x) Y_3Fe_2Fe_3O_{12}$ but could not obtain a single-phase specimen with $x = 1.0$. We found that we could obtain a single-phase garnet with formula $\{Ca_3\}[Fe_2](Fe_{1.5}V_{1.5})O_{12}$ and that the complete solid solution range in the system $\{Y_{3-2x}Ca_{2x}\}[Fe_2](Fe_{3-x}V_x)O_{12}$ exists.^{11,12} The end member, i.e., with $x = 1.5$, has a 0°K moment not significantly different from that of the Si^{4+} ion substituted garnet $\{Y_{1.5}Ca_{1.5}\}[Fe_2](Fe_{1.5}Si_{1.5})O_{12}$, but its Curie temperature, 493°K, is 126°K higher than that of the Si^{4+} ion substituted garnet. In the range of x studied, the Curie temperatures of the system $\{Y_{3-2x}Ca_{2x}\}[Fe_2](Fe_{3-x}V_x)O_{12}$ are all higher than those for $\{Y_{3-x}Ca_x\}[Fe_2](Fe_{3-x}Si_x)O_{12}$ for the same x . In fact, the Curie temperature, 563°K, of $\{Y_{2.2}Ca_{0.8}\}[Fe_2](Fe_{2.6}V_{0.4})O_{12}$ is even higher than that of YIG itself. This behavior could not have been predicted from the results on the systems discussed in detail in this paper.

It was also found¹² that garnets in the yttrium-free $\{Bi_{3-2x}Ca_{2x}\}[Fe_2](Fe_{3-x}V_x)O_{12}$ system could be prepared, the probable range of x being $1.5 > x > 0.8$. In particular the magnetic behavior of $\{Bi_{0.5}Ca_{2.5}\}[Fe_2](Fe_{1.75}V_{1.25})O_{12}$ is essentially the same as that of the yttrium analog, despite the fact that Bi^{3+} for Y^{3+} ion substitution in YIG, i.e., in the system $\{Y_{3-x}Bi_x\}Fe_2Fe_3O_{12}$, resulted in increased Curie temperature.¹³

Pentavalent antimony may be put into garnets,¹⁰ as in the system $\{Y_{3-2x}Ca_{2x}\}[Fe_{2-x}Sb_x](Fe_3)O_{12}$; garnets exist over the whole range $0 \leq x \leq 1.5$. To $x \approx 0.6$ this system behaves similarly to the Sc^{3+} and Zr^{4+} ion substituted systems at 0°K, but with some differences at higher temperatures. In the high substitution region, 0°K moments of the system are substantially lower than those of the Sc^{3+} and Zr^{4+} ion

substituted systems. The turn down (see Fig. 4) of 0°K moment occurs sooner for the Sb⁵⁺ ion substituted system¹⁰ than for the other two.

The end-member $\{\text{Ca}_3\}[\text{Sb}_{1.5}\text{Fe}_{0.5}](\text{Fe}_3)\text{O}_{12}$ forms a complete solid solution range with $\{\text{Ca}_3\}[\text{Fe}_2](\text{Fe}_{1.5}\text{V}_{1.5})\text{O}_{12}$; the system may be written $\{\text{Ca}_3\}[\text{Sb}_x\text{Fe}_{2-x}](\text{Fe}_{1.5+x}\text{V}_{1.5-x})\text{O}_{12}$. The behavior of this system¹⁰ could, in part, have been predicted from the results given in this paper. However, for $x = 0.75$, for example, the specimen does not saturate at moderate fields and its moment at 4.2°K is $2.5 \mu_B$. This may be compared with the 0°K moment, $4.35 \mu_B$, of $\{\text{Y}_3\}[\text{Mg}_{0.75}\text{Fe}_{1.25}](\text{Fe}_{2.25}\text{Si}_{0.75})\text{O}_{12}$, which is magnetically saturated at moderate fields.

Further details regarding these garnets and others involving Sb⁵⁺ and V⁵⁺ ion substitution will be found in Refs. 10-12. In the cases of Sb⁵⁺ and V⁵⁺ ions, their effects on the magnetic interactions occur even when substitution is not large. Therefore, even in these regions, all the results could not have been predicted from those of the present paper. Nevertheless, the ideas given in the present paper may still account for the behavior; we have pointed out earlier that systems which show large differences must be treated separately.

IV. ACKNOWLEDGMENTS

We wish to thank Y. Yafet for discussions of the theory of which he is coauthor, E. A. Nesbitt for the Curie temperature measurements as indicated in Table I, and A. J. Williams for technical assistance. Fig. 23 was drawn by H. J. Seubert and Fig. 24 is reproduced from Ref. 48.

Note Added in Proof

To ensure that the reader who so wishes may be able to duplicate our results, we have decided to list the preparation conditions of all specimens, rather than only those of Table IV. In Table IX the firing temperature is given, followed by the number of hours at that temperature. Each comma represents a regrinding and recompacting of the specimen. All firings were carried out in air except as indicated. In garnets containing Ca²⁺ and Mg²⁺ ions, starting materials were carbonates of these; in such cases a calcining was carried out. Usually, this consisted of varying the temperature in the initial firing from 500 to 900°C over a period of 1-2 hours.

It should be emphasized that the magnetic and crystallographic measurements were always made on the specimens quenched rapidly in air from the last firing temperature.

TABLE IX — PREPARATION DATA

<i>x</i>	<i>y</i>	Firing conditions, °C (hr.)
$\{Y_{3-x}Ca_x\}[Fe_2](Fe_{3-x}Si_x)O_{12}$		
0.00		1405(16)
0.40		1435(15)
0.75		1150(3), 1375(23)
1.00		1410(16), 1435(16), 1400(18), 1450(66)
1.01		1250(2), 1380(16), 1330(18), (75)
1.02		1250(3), 1285(17), 1275(20), 1415(7)
1.50		1280(16), 1300(19), (68), 1350(40)
1.77		1235(1), 1275(4), 1295(2), 1300(40), (?) ^a
1.88		1225(1), 1265(5), 1280(18), 1300(16)
2.00		1200(2), 1270(2), 1300(2½), (18), (19)
2.25		1225(3), 1265(2), (2), 1285(6)
2.50		1225(1), 1260(2), 1265(48), 1260(1), 1270(2½)
2.75		1225(3), 1200(64), 1220(22), 1240(19), 1245(64)
$\{Y_{3-x}Ca_x\}Fe_{5-x}Ge_xO_{12}$		
0.70		1225(3), 1350(8), 1390(19)
1.00		1340(16), 1320(16), 1300(66), 1435(17), (6)
1.50		1280(16), 1300(19), (68), 1350(40)
1.75		1225(3), 1260(1½), 1300(2), 1350(2½), 1385(1½)
2.00		1225(1), 1250(2), 1280(2), 1330(2½), 1385(1½)
2.25		1225(3), 1250(2), 1300(2), 1350(2)
2.50		1225(1), 1260(1) ^b , 1280(2) ^b , 1330(3) ^b , 1360(2) ^b , 1400(4½) 1420–1370(17)
2.75		1225(1½), 1300(2), 1350(3), 1365(2), 1225(7)
$\{Y_3\}[Sc_xFe_{2-x}](Fe_3)O_{12}$		
0.60		1300(1), 1350(2½), 1395(21)
0.72		1250(3), 1300(2), 1350(2½), 1400(2), 1425–1450(4)
0.80		1300(3), 1400(3), 1420(17)
1.00		1250(3), 1325(4), 1400(16), 1440(21)
1.25		1300(1), 1350(2½), 1400(4½), 1420(21)
1.50		1300(1), 1350(2½), 1400(4½), 1420(21)
$\{Y_{3-x}Ca_x\}[Zr_xFe_{2-x}](Fe_3)O_{12}$		
0.60		1280(1), 1320(19), 1300(65), 1325(40)
0.72		1300(3), 1350(2½), 1350(3), 1380(2), 1425(14), 1400(19)
0.80		1350(3), (5), (5), 1355(22), 1400(16), 1450–1430(18)
1.00		1250(3), 1325(4), 1350(4), 1400(16)
1.25		1300(3), 1350(5), (16)
1.50		1300(3), 1350(3), 1320(16½)
1.75		1300(3), 1350(5), (16)
1.95		1300(3), 1350(3), 1320(16½)
$\{Y_{3-y+x}Ca_{y-x}\}[Mg_xFe_{2-x}](Si_yFe_{3-y})O_{12}$		
0.175	0.825	1275(3), 1350(2), 1390(2), 1400(2½), 1315(18)
0.30	1.47	1300(1), 1350(4), 1375–1400(5), 1180(63), 1275(16), 1360(16)
0.18	1.57	1205(3), 1300(3), 1330(4), 1390–1360(22)
0.90	1.10	1300(3), 1450–1420(17), 1400(6)
0.50	1.50	1300(3), 1375(2), 1380(3), 1385(2)
0.44	1.76	1300(3), 1375(2), 1385(2), 1380(3½)
0.22	1.98	1250(3), 1300(2), 1315(2), 1300(2½), (16), 1200(19), 1340–1345(68)
0.75	1.75	1290(3), 1325(5), 1395(4), 1340(70), 1400(20), 1190(17)

TABLE IX—PREPARATION DATA—continued

<i>x</i>	<i>y</i>	Firing conditions °C (hr.)
$\{Y_{3-y}Ca_y\}[Sc_xFe_{2-x}](Si_yFe_{3-y})O_{12}$		
0.85	0.85	1225(½), 1350(3), 1400(16), 1395(20), 1425(5)
0.30	1.47	1285(1), 1325(4), 1350–1310(21), 1345(29)
0.30	1.52	1275(1), 1300(5), 1340(23), 1320(19), 1350(17)
0.30	1.60	1250(1), 1300–1330(3), 1340(21), 1360(22)
1.10	0.90	1300(½), 1400(3), (16), 1450(16)
1.00	1.00	1300(½), 1325(2½), 1400(5), 1450(3), 1500(4)
0.90	1.10	1300(1), 1355(3), 1400(20), (16)
$\{Y_{3-x-y}Ca_{x+y}\}[Zr_xFe_{2-x}](Si_yFe_{3-y})O_{12}$		
0.76	0.24	1285(½), 1360(2), (2), 1395(3), 1330(16), (42)
0.60	0.60	1275(1), 1300(4), 1310(22), 1340(23), 1365(70)
0.35	1.15	1225(½), 1325(3½), 1360(2), 1250(16), 1300(21) ^b
0.30	1.20	1250(½), 1350(4), 1375–1400(20), 1400(65), 1315(21), 1300–1275(41)
0.85	0.85	1200(½), 1325(4), 1375(5), 1360(16), 1210(68) ^b
0.30	1.60	1200(½), 1325(4), 1330(20), 1210(68), ^b 1330(16), 1350(21)
1.10	0.90	1300(1), 1355(3), 1375(23)
1.00	1.00	1275(½), 1350(2), 1360(2½), (2½), 1305(21), 1300(16), 1360(20), 1400–1385(66)
0.90	1.10	1200(½), 1325(4), 1375(5), 1360(16), 1210(68) ^b , 1280(23)
0.60	1.60	1200(1), 1260(4), 1300(4), 1350(4), 1375(4), 1360(16), 1355(16), 1300(70), (118), 1180(63)
1.25	1.25	1250(½), 1325(4), 1350(4), 1355(16), 1375(20), 1270(64), 1350(19)
$\{Y_{3-y+x}Ca_{y-x}\}Mg_xFe_{5-x-y}Ge_yO_{12}$		
1.00	1.00	1250(½), 1300(4), 1395(5), 1450–1460(3), 1500–1525(28), 1340(16)
1.25	1.25	1330(½), 1400(4), 1410(16), 1400(22)
$\{Y_{3-y}Ca_y\}Sc_xFe_{5-x-y}Ge_yO_{12}$		
1.00	1.00	1200(½), 1300(4½), 1390(21), 1400(22)
$\{Y_{3-x-y}Ca_{x+y}\}Zr_xFe_{5-x-y}Ge_yO_{12}$		
0.60	0.60	1275(1), 1300(4), 1310(22), 1340(22), 1365(70), 1385(16)
0.85	0.85	1200(½), 1300(3½), 1330(16), 1340(21), 1315(16), 1340(23), 1375(18)
1.00	1.00	1250(½), 1325(2½), 1375(4), 1425(20), 1450(3)
$Y_3Al_xFe_{5-x}O_{12}$		
1.00		1400(1), 1440(16), 1475(48)
1.50		1450(2), 1500(16), 1475(40)
1.75		1300(1), 1450(2), 1490(2), (2), 1510(4)
2.00		1400(1), 1500(19)
2.50		1450(1), 1525(2½), 1540(17), 1530(64), 1600–1660(5)
3.00		1300–1340(2), 1350–1430(3), 1420(40), 1520(42)
3.00		1425(1), 1445–1520(5), 1480(40), 1500(16), 1535(24)

^a Unknown because of furnace burn-out.^b Fired in O₂.

REFERENCES

1. Geller, S., Bozorth, R. M., Gilleo, M. A., and Miller, C. E., *J. Phys. Chem. Solids*, **12**, Jan., 1960, p. 111.
2. Geller, S., Bozorth, R. M., Miller, C. E., and Davis, D. D., *J. Phys. Chem. Solids*, **13**, May, 1960, p. 28.
3. Gilleo, M. A., *J. Phys. Chem. Solids*, **13**, May, 1960, p. 33.
4. Gilleo, M. A., and Geller, S., *Phys. Rev.*, **110**, Apr., 1958, p. 73.
5. Yafet, Y., and Kittel, C., *Phys. Rev.*, **87**, July, 1952, p. 290.
6. de Gennes, P. G., *Phys. Rev. Letters*, **3**, Sept. 1, 1959, p. 209.
7. Pauthenet, R., *Ann. Phys.*, **3**, Apr., 1958, p. 424.
8. Geller, S., Williams, H. J., Espinosa, G. P., and Sherwood, R. C., *Bull. Amer. Phys. Soc.*, Ser. II, **7**, 1962, p. 279.
9. Smolenskii, G. A., Polyakov, V. P., and Iodin, V. M., Akad. Nauk. SSSR, *Izvestia, Ser. fiz.*, **25**, 1961, p. 1396.
10. Geller, S., Williams, H. J., Espinosa, G. P., and Sherwood, R. C., *J. Appl. Phys.*, Mar., 1964.
11. Geller, S., Espinosa, G. P., Williams, H. J., Sherwood, R. C., and Nesbitt, E. A., *Appl. Phys. Letters*, **3**, Aug. 15, 1963, p. 60.
12. Geller, S., Espinosa, G. P., Williams, H. J., Sherwood, R. C., and Nesbitt, E. A., *J. Appl. Phys.*, Mar., 1964.
13. Geller, S., Williams, H. J., Espinosa, G. P., Sherwood, R. C., and Gilleo, M. A., *Appl. Phys. Letters*, **3**, July 15, 1963, p. 21.
14. Geller, S., Williams, H. J., Sherwood, R. C., and Espinosa, G. P., *J. Phys. Chem. Solids*, **23**, 1962, p. 1525; see also *J. Appl. Phys.*, **33**, Mar., 1962, p. 1195.
15. Bozorth, R. M., Williams, H. J., and Walsh, D. E., *Phys. Rev.*, **103**, Aug. 1, 1956, p. 572.
16. Candela, G. A., and Mundy, R. E., *Rev. Sci. Instr.*, **32**, 1961, p. 1056.
17. In subsequent discussion, these will be considered to be indistinguishable from the 0°K moments, although they may differ slightly from them.
18. Geller, S., and Miller, C. E., *Amer. Min.*, **44**, Nov.-Dec., 1959, p. 1115.
19. Yoder, H. S., and Keith, M. L., *Amer. Min.*, **36**, July-Aug., 1951, p. 519.
20. Skinner, B. J., *Amer. Min.*, **41**, May-June, 1956, p. 428.
21. Bozorth, R. M., and Geller, S., *J. Phys. Chem. Solids*, **11**, Oct., 1959, p. 263.
22. In a previous paper,² it was reported that $\{YCa_2\}[Zr_2](Fe_3)O_{12}$, $\{YCa_2\}[Zr_2](Al_{0.5}Fe_{2.5})O_{12}$ and $\{YCa_2\}[Zr_2](Ga_{0.5}Fe_{2.5})O_{12}$ had residual moments at 1.4° K. It now appears (see text which follows) that both $\{YCa_2\}[Zr_2](Fe_3)O_{12}$ and $\{YCa_2\}[Hf_2](Fe_3)O_{12}$, also reported in that paper, could not have been precisely single-phase garnet specimens and that this was not discernible at the time of that investigation. With regard to the 0.5 Al and 0.5 Ga specimens, although these should exist as single-phase garnets, it is possible that these also were not phase pure; the present result on the 0.25 Ga specimen is considered to be more reliable.
23. The successful preparation of this garnet is a consequence of the fact that the tetrahedral $Ga^{3+}-O^{2-}$ distance is expected to be substantially shorter than the tetrahedral $Fe^{3+}-O^{2-}$ distance. See Geller, S., *J. Chem. Phys.*, **33**, 1960, p. 676, and Refs. 14 and 24.
24. Geller, S., *J. Appl. Phys.*, **31**, May, 1960, p. 30S.
25. Geller, S., *J. Phys. Chem. Solids*, **16**, 1960, p. 21.
26. Neel, L., *Ann. Phys.*, **3**, 1948, p. 137.
27. Anderson, P. W., *Phys. Rev.*, **102**, May 15, 1956, p. 1008.
28. Until recently, silicon has been known to have only tetrahedral coordination to oxygens in oxide systems. A rutile type SiO_2 (i.e., with Si having octahedral coordination to oxygens) was shown to occur at very high pressure, 160,000 kg/m², and a temperature of 1200-1400°C. (Stishov, S. M. and Popova, S. V., *Geokhimiya*, 1961, p. 837.)
29. Wojtowicz, P. J., *J. Appl. Phys.*, **33**, June, 1962, p. 1957.
30. Aleonard, R., *J. Phys. Chem. Solids*, **15**, Aug., 1960, p. 167.
31. The term "effective moment" is used rather loosely here to prevent awkwardness in the presentation. Throughout the discussion, we shall mean

by this term the average *component* of the moment which is antiparallel to the Fe³⁺ ion moments of the sublattice in which there is no canting.

32. Geller, S., and Gillo, M. A., J. Phys. Chem. Solids, **3**, 1957, p. 30; **9**, 1959, p. 235.
33. That is, the average *d-d* (*a-d*) interaction strength multiplied by the number of nearest neighbor *d(a)* cations, 4(8), is greater than six times the average *a-d* interaction strength.
34. v. Náray-Szabó, St., Z. Kristallogr., (A), **94**, 1936, p. 414.
35. The minus sign, as usual, indicates that the octahedral sublattice contribution to the spontaneous magnetization is dominant. The Gillo theory predicts a moment of $-0.65 \mu_B$, but a Curie temperature of 242°K for this garnet.
36. Dauben, C. H., and Templeton, D. H., Acta Cryst., **8**, 1955, p. 841.
37. Geller, S., Miller, C. E., and Treuting, R. G., Acta Cryst., **13**, 1960, p. 179.
38. Abrahams, S. C., and Geller, S., Acta Cryst., **11**, 1958, p. 437.
39. In $\text{Y}_3\text{Fe}_{5-x}\text{Al}_x\text{O}_{12}$, x is the *total* substitution of Al distributed over *a* and *d* sites, and therefore is equivalent to $x + y$ of Fig. 27.
40. Bertaut, F., Forrat, F., Herpin, A., and Meriel, P., Compt. Rend. **243**, 1956, p. 898.
41. Prince, E., Acta Cryst., **10**, 1957, p. 787.
42. Kuzminov, U. S., Yamzin, I. I., and Belov, N. V., Kristallografiya, **7**, 1962, p. 1946.
43. Gorter, E. W., Philips Res. Rept., **9**, August, 1954, p. 403.
44. Hastings, J., and Corliss, L., Rev. Mod. Phys., **25**, Jan., 1953, p. 114.
45. Gillo, M. A., Phys. Rev., **109**, Feb. 1, 1958, p. 777 and pertinent references therein.
46. Hastings, J., and Corliss, L., Phys. Rev., **104**, 1956, p. 328.
47. Nozik, Yu. Z., and Yamzin, I. I., Kristallografiya, **6**, 1961, p. 923.
48. Geller, S., Acta Cryst., **12**, 1959, p. 944.

Pulse Sharpening and Gain Saturation in Traveling-Wave Masers*

By E. O. SCHULZ-DUBOIS

(Manuscript received September 12, 1963)

A pair of coupled nonlinear differential equations is given which describes the reduction of gain in a traveling-wave maser due to high-power signals. Integrals in closed form are obtained for two cases of interest. The first applies to pulsed optical amplifiers where no replacement of stored energy occurs during a signal pulse. The result is a pulse sharpening phenomenon; i.e., the leading edge of an input pulse is amplified by the original full gain while later parts of the signal experience reduced gain. The second case is that of steady-state gain saturation in the presence of a continuous pumping process. The results describe the observed gain compression of microwave ruby traveling-wave masers.

I. INTRODUCTION

This paper presents earlier considerations concerning the gain process in traveling-wave masers in cases where the signal energy, over an appropriate period of time, is comparable to the energy stored in the maser material. The results were communicated several years ago in reports with limited circulation.^{1,2,3} The studies were prompted originally by the development of microwave masers, in particular the ruby comb-structure traveling-wave maser.⁴ Here gain saturation is of interest primarily in a negative sense: it is a condition that should be avoided in system applications. The maser may handle input signals up to some typical saturation limit which depends on the tolerable gain compression, the signal duty ratio, and the low-power gain. Thus the situation of drastic gain reduction due to saturation is largely of academic interest. It may be used, however, as a check on the theoretical understanding of the maser gain process.³ It should be added that even with drastically compressed gain the maser is still a linear amplifier in the sense that it does

* This work was supported in part by the U.S. Army Signal Corps under contracts No. DA 36-039 SC-73224 and SC-85357.

not create intermodulation frequencies due to a nonlinear mixing interaction. Rather, the output is still a faithfully scaled replica of the input signal.^{5,6}

The advent of optical masers in more recent years^{7,8,9} has led to a more genuine interest in maser high-power saturation phenomena. The generation of high-power ("giant") pulses by the Q-switching technique,¹⁰ for example, makes use of the fast exhaustion of the energy stored in the maser material. Similarly, pulse sharpening is an inevitable and in some applications a desirable effect in a pulsed high-power postamplifier.^{11,12} The more prominent role of high-power phenomena in the optical maser field has suggested the present, more complete publication of the earlier reports.

The theory of masers is largely identical for those in the microwave and in the optical range. This applies, for example, to the derivations of the gain and noise behavior. The same is true for the high-power phenomena treated in the present paper. Thus the term traveling-wave maser (TWM) can be used without further distinction except in numerical examples.

The coupled differential equations governing the TWM high-power behavior are given in the following section. The integral applicable to pulsed TWM's is derived in Section III. Some numerical consequences for pulse sharpening are discussed in Section IV, and an experimental example of pulsed optical TWM performance is analyzed in Section V. The integrals describing steady-state gain saturation are derived, and computed gain saturation curves are presented, in Section VI. Experimental gain saturation data obtained with a microwave TWM are shown for comparison in Section VII.

II. THE DIFFERENTIAL EQUATIONS

The gain process in the TWM is stimulated emission. It is the interaction of two forms of energy. One is the radiation energy of the mode under consideration. Its strength may be measured in terms of the number of photons per unit of time, $n'_t(z', t')$, which pass the maser or the mode cross-section at a point z' along the maser length and at a time t' . Here z' ranges from $z' = 0$ at the input to $z' = L$ at the output. In the absence of gain or loss interaction, the radiation energy propagates through the maser with a group velocity v_g , so that then $n'_t \equiv n'_t(z' - v_g t')$.

The other form of energy is that stored in the maser material. It can be given in terms of the number of available quanta per unit of maser

length, $n_z'(z', t')$, within the cross section occupied by the signal transmission mode. The number of available quanta is half the excess number of particles in the upper state of the signal transition over those in the lower state, $n_z' = \frac{1}{2}(n_2' - n_1')$. n_z' may depend on the length coordinate z' along the TWM and on time t' . A quantity N_z may be introduced as the "pumped-up value" of n_z' . It is the maximum value which n_z' may assume either with low signal power operation under steady-state conditions or before any signal energy withdrawal with pulsed pump operation.

Using these energy variables, a system of two coupled partial differential equations may be given which describes the high-power effects in TWMs. It is of first order and nonlinear

$$\frac{\partial n_t'}{\partial z'} + \frac{1}{v_g} \frac{\partial n_t'}{\partial t'} = an_t' n_z' - bn_t' \quad (1)$$

$$\frac{\partial n_z'}{\partial t'} = -an_t' n_z' + c(N_z - n_z'). \quad (2)$$

The first terms on the right-hand side are equal and opposite. This is an expression of energy conservation; i.e., each quantum of energy stored in the maser material is converted into a photon propagating in the signal mode. In a maser, energy conservation of this type may be a justified assumption, at least under high-power conditions where other processes such as spontaneous transitions are insignificant by comparison.

The dimensionless constant a describes the gain interaction between both forms of energy. In units of decibels, the low-power electronic gain of the TWM is $4.35 a N_z L$. This allows a numerical evaluation of the constant a from experimental data. The line shape of the maser transition is reflected in the frequency dependence of a . Implicit in such a treatment of line shape is the assumption that the maser transition considered is homogeneously broadened. However, the present theory may also be applied to lines with inhomogeneous broadening provided the energy diffusion across the overall line is rapid enough to prevent a line shape distortion or "hole burning" under high-power conditions. Formally, for a magnetic dipole transition at the maser signal line, a can be given in the form

$$a = \frac{2\pi\omega g(\nu - \nu_{nn'}) \int_{A_M} | < n' | g\beta \vec{H} \cdot \vec{S} | n > |^2 dA}{v_g h \mu_0 A_M \int_{A_S} | H |^2 dA}. \quad (3a)$$

Here $\omega/2\pi = \nu$ = signal frequency, $g(\nu - \nu_{nn'})$ = line shape function, $\langle n' | g\beta \vec{H} \cdot \vec{S} | n \rangle$ = matrix element of the transition, v_g = group velocity, h = Planck's constant, μ_0 = vacuum permeability, A_M = cross section of maser material, A_s = cross section of structure; finally, the ratio of the magnetic field energy integrals alone in (3a) defines the filling factor. The symbols used are those introduced in Ref. 4, to which the reader is referred for a derivation of traveling-wave maser theory. In the optical range it is more convenient to characterize a maser line by its spontaneous transition rate, $W(\theta, \varphi, \bar{P})$, which is a function of the direction of emission expressed by spherical angular coordinates θ and φ , and of the polarization \bar{P} of the emitted light. Using this term, a becomes

$$a = \frac{2\lambda_0^2 g(\nu - \nu_0) W(\theta, \varphi, \bar{P})}{\epsilon A_m} \quad (3b)$$

where λ_0 = vacuum wavelength of light, $g(\nu - \nu_0)$ = line shape function, ϵ = dielectric constant of maser material, A_m = cross section of amplified mode. These symbols are defined as in Ref. 11, where the theory of optical traveling-wave maser amplifiers is derived.

The constant b accounts for signal loss along the TWM. In a microwave TWM it may consist of ohmic structure losses (copper loss) and the forward attenuation of the isolator (ferrite loss). In an optical TWM, the losses may be contributed by scattering, diffraction and the isolator, although the latter two do not really occur in a distributed fashion. In units of decibels, the total propagation loss in the maser is $4.35 bL$.

For the case of CW pumping, a maser recovery rate c is included in (2). It is the reciprocal of the exponential time constant which describes the low-power gain recovery after a saturating pulse. In microwave masers the pump power usually available is relatively high, so that c is essentially given by the spin-lattice relaxation rate of the idler transition. In CW optical masers the pump levels usually available tend to be lower in terms of pump photons, so that c may be largely determined by the pump power.

The left-hand side of (1) is a combination of partial derivatives with respect to time t' and space z' , which indicates that signal propagation with a group velocity v_g is considered in the positive z' direction. Propagation in the negative z' direction would require a minus sign. The complication of propagation effects can be eliminated from (1) by a transformation

$$\begin{aligned} z &= z' & n_t' &= n_t \\ v_g t &= v_g t' - z' & n_z' &= n_z \end{aligned} \quad (4)$$

which results in the differential equations

$$\frac{\partial n_t}{\partial z} = an_t n_z - bn_t \quad (5)$$

$$\frac{\partial n}{\partial t} = -an_t n_z + c(N_z - n_z). \quad (6)$$

The physical situation and this transformation in particular are illustrated in the space-time diagram of Fig. 1. It is seen that the new time coordinate t remains constant for any part of the signal as it passes from the input to the output. For example, the leading edge of a pulse is char-

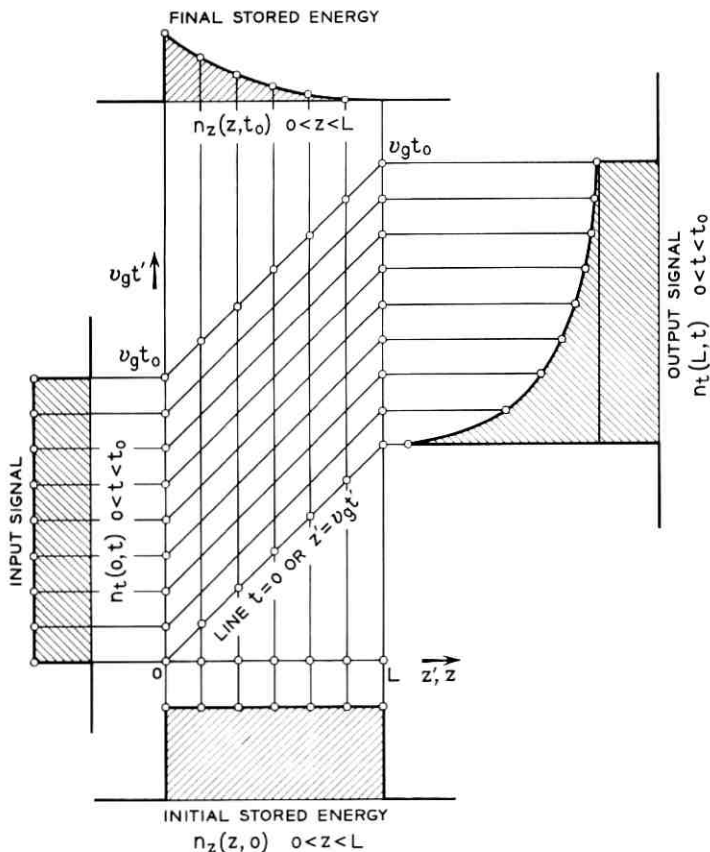


Fig. 1 — Schematic presentation of the maser gain process by removal of stored energy; also shown are space and time coordinate systems.

acterized by $t = 0$, whereas in real time it would pass the input at $t' = 0$ and the output at $t' = L/v_g$.

The figure also suggests that the problem contained in (5) and (6) is hyperbolic in nature; that is, it is characteristic of propagation. In the present case this implies that the physical situation at a point z,t is determined by all interactions which happened earlier, i.e., from time 0 to t , and closer, i.e., from 0 to z . Such a problem is not specified unless two boundary conditions are set up. The first is an initial condition which specifies the situation for values of z , $0 < z < L$, at the time $t = 0$. The second is an input condition which specifies the situation for times t , $t > 0$, at the input $z = 0$. Then the equations permit a unique evaluation of the variables at any point z and time t .

The boundary conditions for the present problem include the initial stored energy

$$n_z(z, t=0) = \begin{cases} n_z(z) & \text{for } 0 < z < L \\ 0 & \text{for } z < 0 \text{ and } L < z \end{cases} \quad (7a)$$

and in the simplest case may involve a uniform distribution of stored energy

$$n_z(z, t=0) = \begin{cases} N_z & \text{for } 0 < z < L \\ 0 & \text{for } z < 0 \text{ and } L < z. \end{cases} \quad (7b)$$

The other condition specifies the input signal

$$n_t(z=0, t) = \begin{cases} n_t(t) & \text{for } t > 0 \\ 0 & \text{for } 0 > t \end{cases} \quad (8a)$$

which in the simplest case may consist of a step function signal

$$n_t(z=0, t) = \begin{cases} N_t & \text{for } t > 0 \\ 0 & \text{for } 0 > t. \end{cases} \quad (8b)$$

It turns out that the equation system (5) and (6) with the boundary conditions (7) and (8) cannot be integrated in general. An exact integral can be obtained, however, for $b = c = 0$. It will be derived in the next section. This integral describes the response of a maser amplifier with negligibly small internal losses and no replacement mechanism for the drain of stored energy. It is of interest, since these mathematical conditions approximate very closely the physical situation of pulsed solid-state optical maser amplifiers.

Another integral can be readily obtained from (5) and (6) by letting

$\partial n_z / \partial t = 0$ in (6) and with $b \neq 0$ and $c \neq 0$. This leads to the steady-state gain saturation formulas which are discussed in the later parts of this paper and which are of interest in applications of microwave TWMs.

For numerical calculations it may not be too convenient to interpret n_t as the number of photons per unit time and n_z as the number of stored quanta per unit length. Instead n_z may be made to mean the stored energy in joules per unit of maser length and n_t the signal power in joules per second, i.e. watts. This new convention changes the definition of the constant a in (3). Now $4.35 a$ becomes equal to the decibel electronic gain of a TWM under consideration divided by the energy stored (in units of joules) in the same TWM.

III. SOLUTION FOR THE TRANSIENT CASE

For $b = c = 0$, (5) and (6) can be conveniently rewritten

$$\frac{\partial n_t}{\partial z} + \frac{\partial n_z}{\partial t} = 0 \quad (9)$$

$$-a \frac{\partial n_z}{\partial t} = a^2 n_t n_z. \quad (10)$$

In this form, (9) is recognized as a conservation law. Using the language of gas kinetic chemical reactions, (10) describes a bimolecular reaction whose yield is proportional to the density of either molecular species, the photons and stored quanta in this case.

The integration of the system (9), (10) subject to the boundary conditions (7a) and (8a) is outlined in the following paragraphs of this section. The method of integration was suggested to the author by J. A. Morrison. It is presented here because it does not follow an established standard approach.

A new function Φ is introduced subject to the requirements

$$\frac{\partial \Phi}{\partial z} = -an_z, \quad \frac{\partial \Phi}{\partial t} = an_t. \quad (11)$$

This "ansatz" satisfies (9) by definition, and the remaining differential equation (10) becomes

$$\frac{\frac{\partial}{\partial t} \frac{\partial \Phi}{\partial z}}{\frac{\partial \Phi}{\partial z}} = -\frac{\partial \Phi}{\partial t}. \quad (12)$$

Logarithmic integration with respect to t yields

$$\ln \frac{d\Phi}{dz} = -\Phi + \ln \frac{dF(z)}{dz} \quad (13)$$

where the last term is an integration constant which may be a function of z alone. After rearrangement this is

$$e^\Phi \frac{\partial \Phi}{\partial z} = \frac{dF(z)}{dz}. \quad (14)$$

A second integration is possible, with the result

$$e^\Phi = F(z) + K(t) \quad (15)$$

or

$$\Phi = \ln [F(z) + K(t)] \quad (16)$$

where K is an arbitrary function of t alone.

The as yet arbitrary functions F and K are specified by the boundary conditions (7a) and (8a). Using these and the definition of Φ in (11), one has

$$n_t(t) = \frac{1}{a} \frac{d\Phi(z=0)}{dt} = \frac{1}{a} \frac{\frac{dK(t)}{dt}}{F(0) + K(t)} \quad \text{for } t < 0 \quad (17)$$

$$n_z(z) = -\frac{1}{a} \frac{d\Phi(t=0)}{dz} = -\frac{1}{a} \frac{\frac{dF(z)}{dz}}{F(z) + K(0)} \quad \text{for } 0 < z < L. \quad (18)$$

These equations can be easily integrated and the results may be combined in the form

$$\begin{aligned} \exp \left[a \int_0^t n_t(s) ds \right] + \exp \left[-a \int_0^z n_z(u) du \right] - 1 \\ = \frac{F(z) + K(t)}{F(0) + K(0)}. \end{aligned} \quad (19)$$

When this result is inserted into (16) and the original definition of Φ , (11), the final solution is

$$n_t(z,t) = \frac{n_t(t)}{S(t)^{-1} + G(z)^{-1} - 1} \quad (20)$$

$$n_z(z,t) = \frac{n_z(z)}{S(t)^{-1} + G(z)^{-1} - 1} \quad (21)$$

where $G(z)$ is the initial power gain

$$G(z) = \exp \left[a \int_0^z n_z(u) du \right] \quad (22)$$

and $S(t)$ is the saturation parameter at the input, i.e., the fraction to which the original stored energy near the input is reduced after a time t

$$S(t) = \exp \left[-a \int_0^t n_t(s) ds \right]. \quad (23)$$

For the simpler boundary conditions (7b) of an initially uniform gain distribution and (8b) of a step function input signal, the solutions (20) and (21) take the form

$$n_t(z,t) = \frac{N_t \exp (aN_t t)}{\exp (aN_t t) + \exp (-aN_z z) - 1} \quad (24)$$

$$n_z(z,t) = \frac{N_z \exp (-aN_z z)}{\exp (aN_t t) + \exp (-aN_z z) - 1}. \quad (25)$$

The solutions (20) and (21) show a number of mathematical properties which should be expected in view of the physical situation. With general definitions for the gain and saturation parameters

$$\begin{aligned} G(z,t) &= n_t(z,t)/n_t(t) \\ S(z,t) &= n_z(z,t)/n_z(z) \end{aligned} \quad (26)$$

the following features may be mentioned:

- (i) The gain $G(z,t)$ decreases monotonically with time from the initial value (22) down to unity. $G(z,t)$ is greater for larger values of z .
- (ii) Similarly, the saturation parameter $S(z,t)$ decreases monotonically with time from the initial value of unity to zero. The drop is faster for greater values of z .
- (iii) $G(z,t)$ may be expressed in the form (20) using the initial gain, but it may be also obtained by computing the gain due to the instantaneous excess energy storage $n_z(z,t)$. Thus

$$G(z,t) = \frac{S(t)^{-1}}{S(t)^{-1} + G(z)^{-1} - 1} = \exp \left[a \int_0^z n_z(u,t) du \right]. \quad (27)$$

- (iv) A corresponding relation holds for $S(z,t)$

$$S(z,t) = \frac{G(z)^{-1}}{S(t)^{-1} + G(z)^{-1} - 1} = \exp \left[-a \int_0^t n_t(z,s) ds \right]. \quad (28)$$

- (v) Fig. 1 suggests that the situation at some time t_1 might be used as

a boundary condition instead of the initial condition at time $t = 0$. Thus there is an addition theorem for the gain formula

$$\begin{aligned} G(z, t_1 + t_2) &= \frac{S(t_1 + t_2)^{-1}}{S(t_1 + t_2)^{-1} + G(z)^{-1} - 1} \\ &= \frac{S(t_2)^{-1}}{S(t_2)^{-1} + G(z, t_1)^{-1} - 1}. \end{aligned} \quad (29)$$

(vi) A similar iteration formula applies to the saturation parameter, which may be defined either directly by the initial total gain and input saturation or by the initial gain of a part of the maser and the saturation at the beginning of this part

$$\begin{aligned} S(z_1 + z_2, t) &= \frac{G(z_1 + z_2)^{-1}}{S(t)^{-1} + G(z_1 + z_2)^{-1} - 1} \\ &= \frac{G(z_2)^{-1}}{S(z_1, t)^{-1} + G(z_2)^{-1} - 1}. \end{aligned} \quad (30)$$

(vii) Energy conservation requires that the excess of the output energy over the input energy equal the loss in stored energy

$$\int_0^t [n_t(z, s) - n_t(s)] ds = \int_0^z [n_z(u) - n_z(u, t)] du. \quad (31)$$

Equations (27) to (31) may be verified directly.

Equations (20) to (21) can be simplified if the original gain is large, $G(z) \gg 1$, and if the degree of saturation at the input is small,

$$a \int_0^t n_t(s) ds \ll 1.$$

The greater part of the decrease in gain occurs before this last condition is violated. With these approximations

$$\frac{n_t(z, t)}{n_t(t)G(z)} = \frac{1}{1 + G(z)a \int_0^t n_t(s) ds} \quad (32)$$

$$\frac{n_z(z, t)}{n_z(z)} = \frac{1}{1 + G(z)a \int_0^t n_t(s) ds}. \quad (33)$$

Equations (32) and (33) describe a hyperbola, as shown in Fig. 2. In the case of a step function input signal (8b), for example, the curve describes directly the shape of the output signal. The initial output power

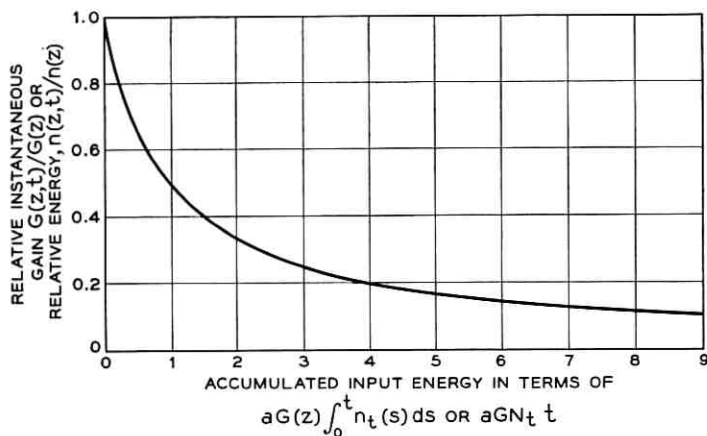


Fig. 2 — Decrease of gain as a function of input energy and decrease of stored energy vs input energy. The graph can be also interpreted as showing the shape of the output signal vs time if a step function input signal is applied.

in that case, of course, is given by the input signal multiplied by the original gain and the ordinate of the curve would have to be scaled accordingly. As one expects from energy conservation, the reciprocal scaling applies to the time scale on the abscissa. In other words, the drop of the output signal occurs faster if the input signal and the initial gain are higher. Also, as expected, the drop of the output sets in more slowly if the stored energy per db of initial gain, $(4.35 a)^{-1}$, is greater.

The curve in Fig. 2 also describes the reduction of stored energy as a function of input energy. Directly at the input, the stored energy decays by an exponential law (23). Further along the TWM at points z , where there is an appreciable initial gain $G(z)$, the reduction of stored energy follows the hyperbolic law. The initial drop is faster for higher $G(z)$, but then the loss of stored energy levels off, although it is always faster than directly at the input.

The reduction of gain with input energy is plotted in another way in Fig. 3. Roughly speaking, the plot is a double logarithmic presentation of the data in Fig. 2. The ordinate shows the gain in db. The abscissa shows the decibel degree of saturation at the input

$$10 \log_{10} S(t) = 4.35 a \int_0^t n(s) ds$$

plotted on a logarithmic scale. In this presentation, the hyperbola of Fig. 2 becomes a horizontal line curving into another line with a slope

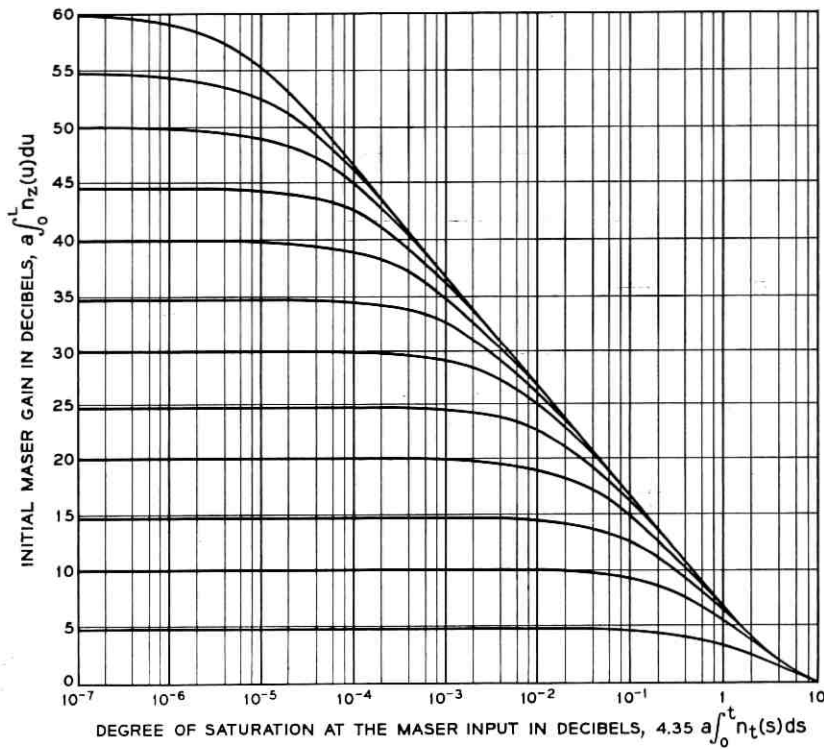


Fig. 3 — Drop of the initial gain in db vs integrated input energy, in db of saturation at the maser input. The plot shows that with the same constant input signal, the gain of a maser with initial 10 db higher gain drops 10 times faster.

of minus unity. A family of curves results because abscissa and ordinate now contain the initial gain explicitly. In this way the plot demonstrates that, of two otherwise identical TWMs excited by the same input signal, the one with a 10-db higher gain, for example, suffers gain reduction 10 times faster. In the lower right-hand of the figure it is seen that the asymptote to all curves is no longer a straight line but levels off. This is the region where the gain is very large compared to unity and the degree of saturation at the input is small. Thus there the expression (32) no longer approximates the gain behavior, and hence the exact formula (20) had to be used for plotting the curve.

IV. DISCUSSION OF PULSE SHARPENING

The results of the last section show that the instantaneous gain of a TWM is a decreasing function of time. The decrease can be particularly

rapid if the energy stored in the TWM is not too high. The question arises whether this phenomenon can be used as an optical pulse shaping mechanism. From a practical viewpoint, such a method of pulse generation would be of interest only if it could be used to produce pulses of higher peak power within a diffraction-limited beamwidth and/or of shorter duration than those produced by other methods. High peak power allows the study of nonlinear interactions in matter, and short pulses can be used in optical ranging devices with extremely high resolution. The generation of very short, very high-powered pulses will be discussed in this section with the aid of some numerical examples. These examples are deliberately chosen to be between the present state of the art and optimistic forecasts.

As a first example consider a step function input at a power of $N_t = 10^6$ watts incident on a unidirectional optical TWM of the type developed by Geusic and Scovil,¹¹ but with an initial gain of 40 db. The leading edge of the pulse experiences the initial gain and hence results in 10^{10} watts = 10 gigawatts at the output. The duration of the pulse may be defined as the time at which the output has dropped 3 db. It can be obtained from Fig. 2 or 3.

In the ruby optical TWM,¹¹ the stored energy is about 1 joule for every 6 db of gain, provided the signal transmission mode matches the cross section of the ruby rods. Thus $4.35 a = 6 \text{ db/joule}$. The gain is reduced 3 db after a time

$$t_{\frac{1}{2}} = (GaN_t)^{-1}. \quad (34)$$

For the numbers chosen, $t_{\frac{1}{2}} = 0.7 \times 10^{-10}$ seconds. The energy $\Delta E_{\frac{1}{2}}$ released by the TWM up to that time can be found, for example, by integrating (24) with respect to time. It can also be given without calculation, however, if one considers that at any time there is proportionality between the stored energy and the decibel gain. Thus $\Delta E_{\frac{1}{2}}$ is equal to the energy stored originally in a fraction of the amplifier length which initially gives rise to 3 db of gain:

$$\Delta E_{\frac{1}{2}} = \frac{3}{G_0(\text{db})} N_z L, \quad (35)$$

which is $\frac{1}{2}$ joule in the case considered.

With less stored energy in the amplifier, for example by signal transmission which utilizes only a fraction of the ruby cross section, the pulse duration $t_{\frac{1}{2}}$ would tend to be shorter. This is hardly possible, however, because the time given already comes close to the linewidth-limited rise time of the amplifier.

The computed pulse duration and peak power would seem rather attractive, and certainly they are beyond the capabilities of existing technology. It should be questioned whether the calculation is based on realistic assumptions. Geusic has operated a TWM with initial gain values of 20 to 30 db. Thus the assumed initial gain of 40 db is feasible. An optical power level in the megawatt range can be produced over short periods of time by the Q-switching technique.¹⁰ Usually, however, that power is spread over a larger beam divergence than the diffraction minimum. Only a diffraction-limited beam can be fed conveniently into an aperture-limited TWM. The greatest discrepancy exists, however, with respect to the rise time of the input pulse, or step function, as used in the calculation. The calculation presented and the results are meaningful only if the input power rises in a time short compared to t_4 or at least comparable to it. If this were the case, the pulse would have its original fast rise and the exhaustion of the gain mechanism discussed here would produce a reasonably sharp cutoff at the trailing edge. Realistic rise times for Q-switched giant pulses are about two orders of magnitude longer than the t_4 quoted. With such a pulse fed into a TWM, most of the stored energy and amplification would be depleted long before the input ever reached the assumed 1 megawatt level.

The question therefore arises as to what degree of pulse forming may be observed under conditions when the input signal is a rising function of time. The situation is schematically indicated in Fig. 4. The input signal may be the initial rise of a giant pulse. A TWM with initial gain G_1 will amplify the first portion of the input signal proportionally until a noticeable fraction of the stored energy is exhausted. The resulting drop of gain may be so rapid that a distinguishable pulse is obtained at the output. With higher initial gain $G_2 > G_1$ in the amplifier, the peak power of the pulse is greater, the peak is reached sooner and the subsequent drop to $\frac{1}{2}$ of the peak power occurs faster.

The rise of the input signal may be described by a power law

$$n_t(t) = (t/t_0)^n P, \quad n = 1, 2, 3 \dots \quad (36)$$

The numbers used in the example are a peak input power of $P = 10^6$ watt which is reached after a rise time of $t_0 = 10^{-8}$ second. The initial TWM gain considered is 60 db, $G(L) = 10^6$. Application of (32) shows that the peak of the output pulse occurs at a time t_{\max} where

$$(t_{\max})^{n+1} = \frac{n(n+1)t_0^n}{aPG(L)}. \quad (37)$$

The output power is down 3 db from the peak value at the time t_4 where

$$t_{\frac{1}{2}} \approx 2 \frac{n+1}{n} t_{\max}. \quad (38)$$

At the peak of the pulse the remaining gain is

$$G(L, t_{\max}) = \frac{1}{n+1} G(L) \quad (39)$$

and the peak output power $n_t(L, t_{\max})$ becomes

$$[n_t(L, t_{\max})]^{n+1} = \frac{PG(L)}{n+1} \left(\frac{n}{at_0} \right)^n. \quad (40)$$

Table I summarizes the numerical results. The true rise of the giant pulse may come sufficiently close to a cubic or quartic parabola. From the last two entries in the table one then can estimate that the peak of the output pulse will exceed the peak of the input by about 30 db. This is a sizable

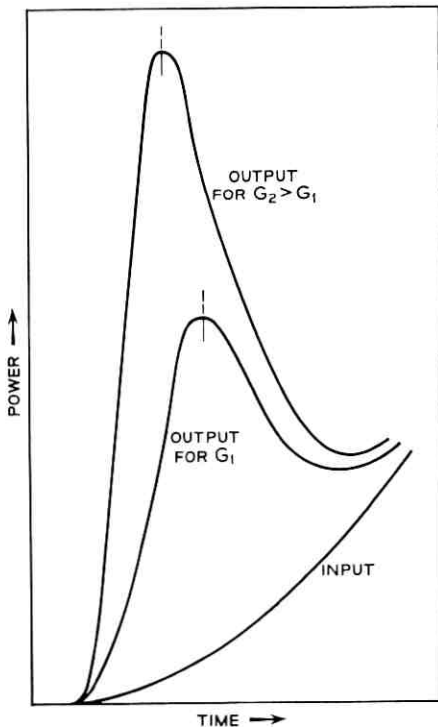


Fig. 4 — Pulse sharpening during rise time of input signal. The pulse is higher and the rise time shorter for higher initial gain.

TABLE I

Exponent of Input Rise [n in (36)]	Pulse Duration [$t_{\frac{1}{2}}$ in (38)]	Peak Pulse Power (watts) [$n_t(L, t_{\max})$ in (40)]
$n = 1$ Straight-line rise	4.8×10^{-10} sec	6×10^9
$n = 2$ Quadratic parabola	2.3×10^{-9} sec	1.9×10^9
$n = 3$ Cubic parabola	4.6×10^{-9} sec	1.3×10^9
$n = 4$ Quartic parabola	6.7×10^{-9} sec	1.1×10^9

Values used: input: rise time $t_0 = 10^{-8}$ sec
maximum power $P = 10^6$ watt
maser: initial gain $G(L) = 10^6$
energy storage $(4.35 a)^{-1} = 6$ db/joule

increase, although it is much less than the initial gain of 60 db. The pulse power obtained in this fashion from the TWM has essentially the same frequency spectrum and mode distribution as the input pulse. This can be understood by observing that the TWM is, for any short time element, a truly linear amplifier although the gain decreases continually with time. It is therefore clear that the output frequency spectrum is only slightly wider than that of the input, namely to the extent that the pulse duration was indeed shortened. Similarly, appreciable mode conversion by a TWM amplifier is possible only if the gain over the cross section is grossly nonuniform. In this sense, the TWM is a "faithful" amplifier even under high power saturating conditions. The duration of the pulse, measured here from $t = 0$ to the time $t_{\frac{1}{2}}$ when the output power has passed the peak value and dropped to $\frac{1}{2}$ of it, is at best not quite one order of magnitude shorter than the assumed initial build-up time t_0 of the input signal.

It is beyond the scope of this paper to suggest whether or not the pulse sharpening discussed is a practical way of producing the extreme in fast, high-power pulses. It is a way, however, where, although with diminishing returns, the peak power is only limited by whatever high-power limits exist in the stimulated emission process itself and in transmission through materials like glass and sapphire, and where the ultimate pulse rise time is limited only by the bandwidth of the maser signal line itself, not by the time for a round trip of light through the device, as in the Q-switched oscillator.

There remains one point which is more curious than serious. The reader might ask why the power law (36) was used for the input power in the pulse sharpening analysis. If instantaneous switching of the shutter can

be assumed, the initial rise of the giant pulse follows an exponential¹³

$$n_t(t) = P \exp(t/t_0) \quad -t_1 < t < 0. \quad (41)$$

Is it possible to use this input signal for pulse sharpening analysis?

It turns out that the ideal exponential rise, $-t_1 = -\infty$, does not produce an output pulse at all. Rather, the output becomes a monotonically increasing function of time. Loosely speaking, the exponential input clears the stored energy out of the TWM in such a smooth fashion, slowly at first while the gain is still high and more rapidly when the gain has started to decrease, that it never can develop the kind of "overswing" or "shock wave" indicated in Fig. 4. One consequence is therefore that deviations from the exponential rise in the actual input signal are significant and helpful for achieving pulse sharpening.

V. AN EXPERIMENTAL EXAMPLE OF PULSE SHARPENING

One of the aims of optical traveling-wave maser development is the generation of very high pulse power by amplification of an already high input signal. Pulse sharpening due to partial exhaustion of the maser energy storage is unavoidable in this situation, as pointed out in the paper on the optical traveling-wave maser.¹¹ Even with more moderate power levels, some pulse sharpening can be observed if pulse duration and initial gain are sufficiently large. Geusic and Scovil¹² demonstrated the effect in experiments with the optical TWM, and an example of their observations is given in Fig. 5. It shows the tracing of a dual-beam oscilloscope presentation of pulse amplification. Part of the amplifier input and output was detected by photomultipliers. A time constant of about a microsecond was used to smooth both responses. In reality the input signal contains spikes which appear faithfully amplified at the output. In the oscillogram of Fig. 5, the sensitivity of the output detection was reduced 15 db by inserting a grey glass attenuator, and the polarities of both signals are reversed for easier presentation of the data. The figure clearly indicates reduced gain for the later portions of the signal and the resulting pulse sharpening.

The data of Fig. 5 were used to evaluate the intrinsic gain decay curve shown in Fig. 6. Here the ordinate shows the numerical power gain, that is, essentially the amplitude ratio of Fig. 5. The abscissa represents the input energy which was obtained by numerical integration of the lower curve in Fig. 5. The circles show the numerical data points. According to the theory [see (32)], the reduction of gain in this presentation should follow a hyperbola such as shown in Fig. 2. The solid curve in Fig. 6 is a

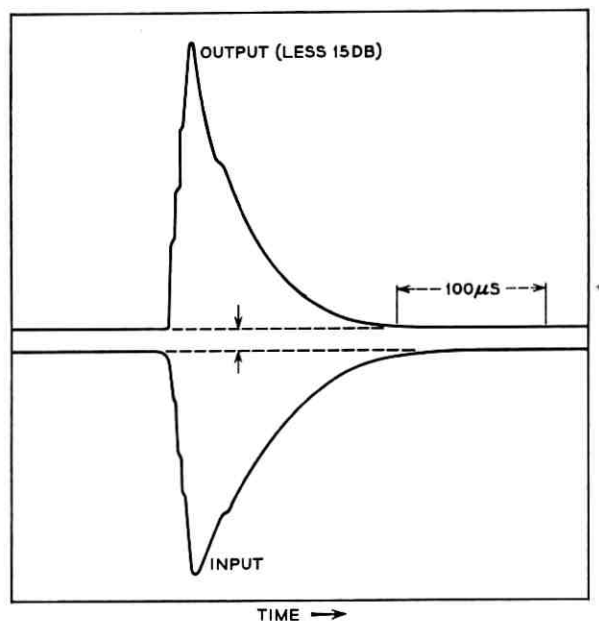


Fig. 5 — Dual-beam oscilloscope record of a pulse sharpening experiment taken with a ruby optical traveling-wave maser by J. E. Geusic.¹² The arrows indicate the time at which half of the energy stored in the amplifier was exhausted, thus reducing the numerical gain by a factor of 2 (or the db gain by 3 db).

hyperbola which was fitted to the data by adjusting two parameters. It should be mentioned that the first and last points of the data are appreciably uncertain because there the absolute magnitude of the signals is rather small. Considering this, the agreement between the data points and the curve is remarkably good. This may be taken as support for the theory. It would be impossible, for example, to fit the data with an exponential law.

Some further details may be read off the curve. The initial gain was 52 (17.2 db). At the time of the signal peak, the gain had already dropped by 1 db to 40.5 (16.1 db). At the point indicated by arrows, the gain is reduced by 3 db to 26 (14.2 db). The energy contained in the output pulse up to that time is equal to the energy originally stored in a 3-db section of the amplifier [(35) applies here, too]. This would be about $\frac{1}{2}$ joule if the output beam filled the entire aperture of the amplifier. Actually, the beam area in this experiment covered one-half of the ruby cross section, so that the output energy, taken from the rise of the pulse to the time marked by the arrows, was about $\frac{1}{4}$ joule. The corresponding average

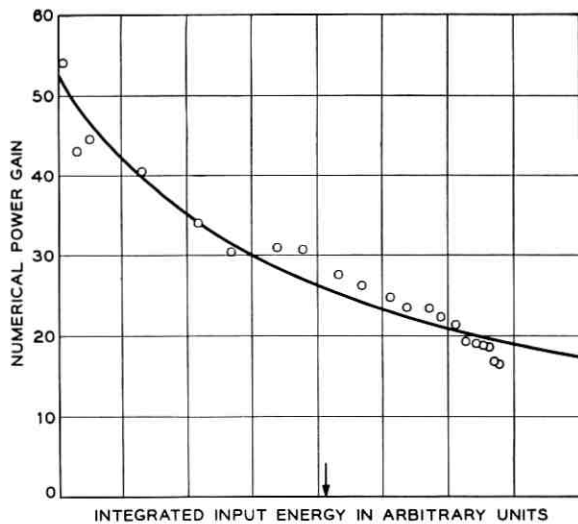


Fig. 6 — Replotting of the data of Fig. 5: numerical power gain is shown vs integrated input energy. Points are data read off Fig. 5 and solid line is hyperbola, predicted by theory, fitted to the data.

pulse power is 5 kilowatts. This power level, incidentally, implies a rather high power per solid angle. The acceptance angle of the amplifier, which was measured to be in agreement with the actual angular spread of the output pulse, is 10^{-3} radians. This comes close to the diffraction-limited beam spread of 10^{-4} radians for a $\frac{1}{4}$ -inch diameter ruby amplifier. Application of (33) allows one to evaluate the energy still stored, for example, at the 3-db time. At the output, the stored energy is then reduced to $\frac{1}{2}$ the original value. By comparison, at the input only $\frac{1}{52}$ of the total has been spent. For the latest portions of the signal, the gain has dropped to 20 (13 db), down 4 db from the initial value.

The presentation of the gain data in Fig. 6 shows two other points. Loss of stored energy due to spontaneous transitions is negligible; otherwise the gain would drop faster. This should not occur here, since the pulse is fast compared to the fluorescence decay. The other point concerns the pumping. Fig. 6 shows that the pumping process was completed at the time of the signal pulse, because otherwise an increase in gain with time should be observed.

VI. STEADY-STATE GAIN SATURATION

Under steady-state conditions, the differential equation (5) remains unaltered

$$\frac{dn_t}{dz} = an_t n_z - bn_t \quad (5)$$

and the differential equation (6) becomes the well-known saturation formula

$$n_z = \frac{N_z}{1 + n_t/P_c} \quad (42)$$

where a characteristic saturation power level P_c is defined by

$$P_c = c/a. \quad (43)$$

It is the level which reduces the stored energy to one-half. Another convenient definition is

$$R = aN_z/b \quad (44)$$

the ratio of low-power electronic gain to structure loss. Using (42), (43) and (44), (5) results in the ordinary differential equation

$$(aN_z - b) \frac{dz}{dn_t} = \frac{1}{n_t} + \frac{R}{P_c(R - 1) - n_t}. \quad (45)$$

Integration yields

$$\ln \frac{n_t(L)}{n_t(0)} - R \ln \frac{n_t(L) - P_c(R - 1)}{n_t(0) - P_c(R - 1)} = (aN_z - b)L. \quad (46)$$

This function is an implicit relation between input, $n_t(0)$, and output signal power, $n_t(L)$. If one considers $n_t(L)$ as a function of L , it is a function which has two branches. If

$$n_t(0) < P_c(R - 1)$$

a branch results which describes gain. For very small input powers, in particular

$$n_t(0) \ll P_c(R - 1) \quad (47)$$

the TWM has simply its low-power gain

$$n_t(L) = n_t(0) \exp (aN_z - b)L. \quad (48)$$

For

$$n_t(0) > P_c(R - 1)$$

(46) describes net loss. In particular, for very high input power

$$n_t(0) \gg P_c(R - 1) \quad (49)$$

the gain mechanism in the TWM is inactive and the device behaves as an attenuator

$$n_t(L) = n_t(0) \exp(-bL). \quad (50)$$

If the input signal assumes the value

$$n_t(0) = P_c(R - 1) \quad (51)$$

it can be shown that the maser exhibits neither gain nor loss; it is transparent

$$n_t(0) = n_t(L). \quad (52)$$

At this level, the energy stored in the TWM is uniformly distributed

$$n_z(z) = N_z/R. \quad (53)$$

Equation (46) loses its meaning for a TWM without intrinsic loss, $b = 0$. The relation valid in this case may be derived directly from the differential equation or by a limiting process for $R \rightarrow \infty$ applied to (46). The result is

$$\ln \frac{n_t(L)}{n_t(0)} + \frac{n_t(L) - n_t(0)}{P_c} = aN_z L. \quad (54)$$

This equation describes an exponential amplification under low signal conditions as before, but an additive amplification process for signal levels large compared to P_c . This means that every section of amplifier having a low-power gain of 4.35 db or a power gain factor of e increases the signal additively by P_c .

For the most interesting range, where input or output power levels are comparable to P_c , (46) has to be applied without approximations. The relation between input, $n_t(0)$, and output power $n_t(L)$ was machine-computed for a number of low-power gain values,

$$G_{\text{db}} = 4.35 (aN_z - b)L,$$

and gain-to-loss ratios, $R = aN_z/b$. These data are shown in a series of plots in Figs. 7 through 10. Each family of curves applies to masers with the same low-power net gain and with the intrinsic loss varied from 3 db to 18 db in 3-db steps. The six families of curves are characterized by low-power net gains from 15 db to 40 db in 5-db steps. Essentially all practical masers are designed for gain in this range. Fig. 7 presents the data as a relation between input and output power, both normalized to the characteristic saturation level, P_c . Fig. 8 shows the apparent gain as a function of input power and Fig. 9 as a function of output power.

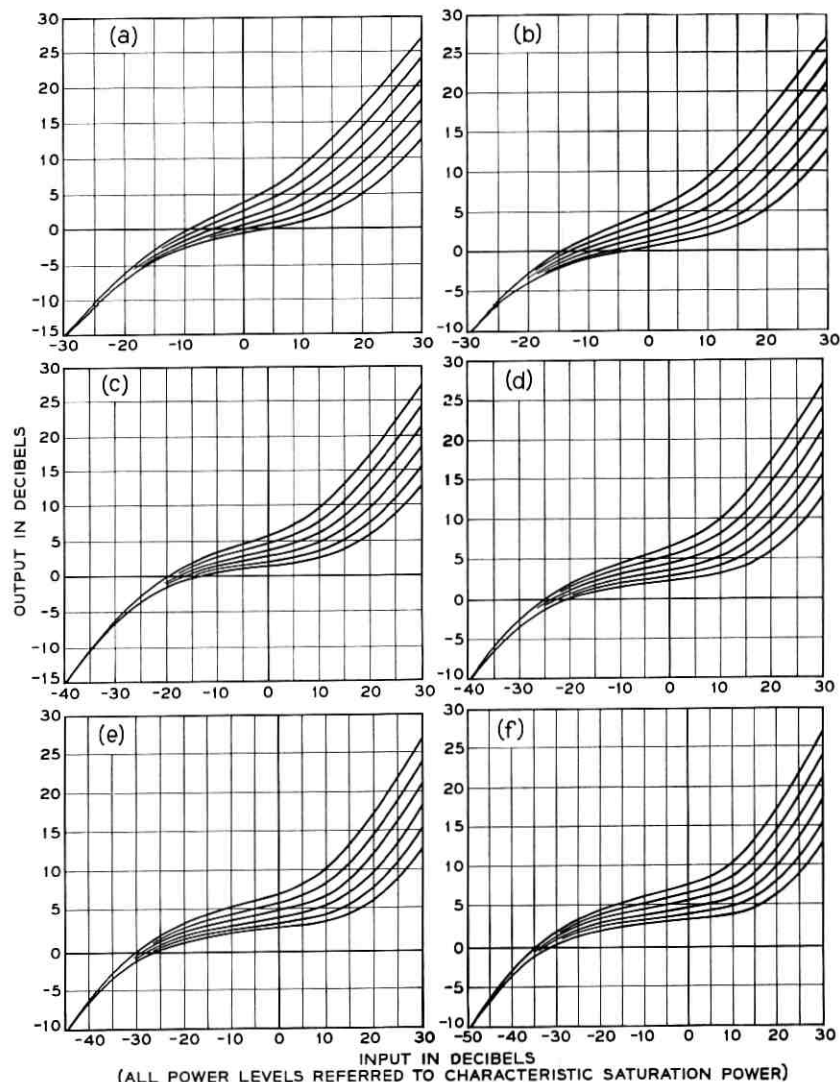


Fig. 7 — Output vs input power for traveling-wave masers having low-level net gain of (a) 15 db, (b) 20 db, (c) 25 db, (d) 30 db, (e) 35 db, and (f) 40 db. Intrinsic loss for each family of curves increases from 3 db to 18 db in steps of 3 db; all power levels are measured relative to characteristic saturation power.

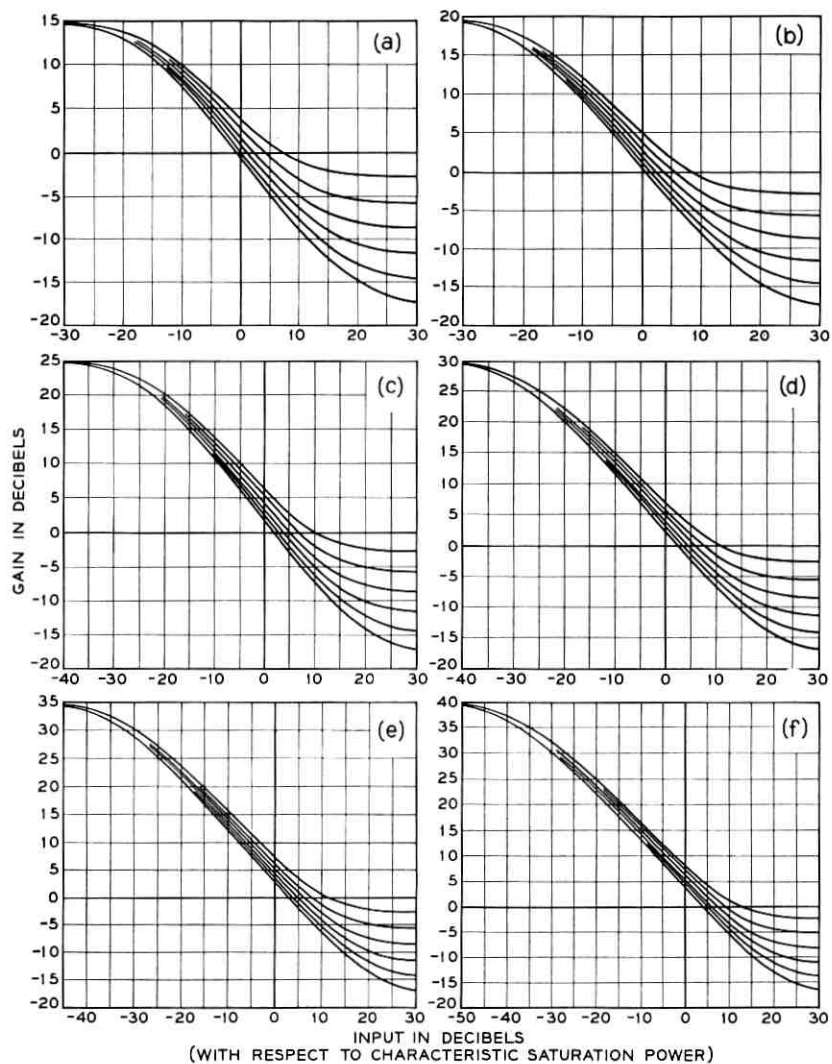


Fig. 8 — Plot of apparent gain vs input power for traveling-wave masers of Fig. 7.

For many applications, the onset of gain saturation in the maser is significant and, depending on the system function, gain compression of $\frac{1}{2}$, 1 or 3 db or even more may be tolerated. The region of beginning gain compression is shown in Fig. 10. It is a plot of apparent gain versus input power as in Fig. 8, although on an expanded scale.

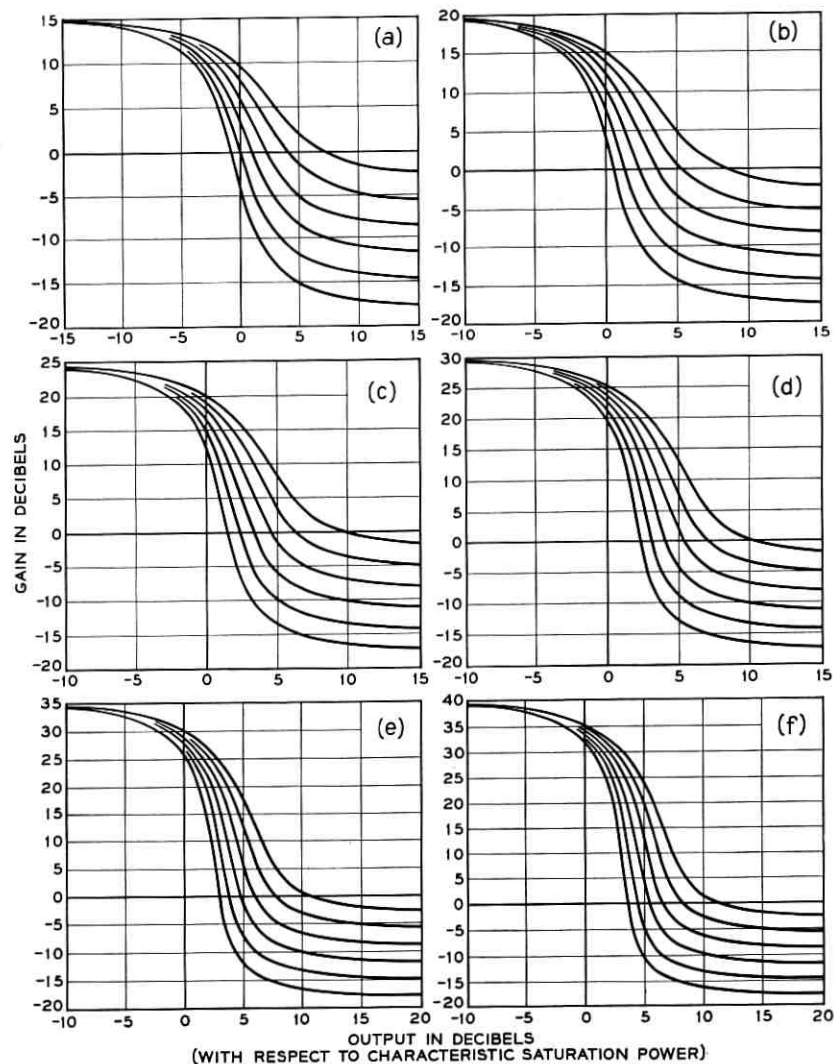


Fig. 9 — Plot of apparent gain vs output power for traveling-wave masers of Fig. 7.

Inspection of Fig. 7, for example, shows that in the range of drastic gain saturation, a TWM can be used for automatic gain control (AGC). Here the average output stays approximately constant for input variations almost as great as the electronic low-power gain. The AGC time constant is nearly, although usually somewhat shorter than, the recovery

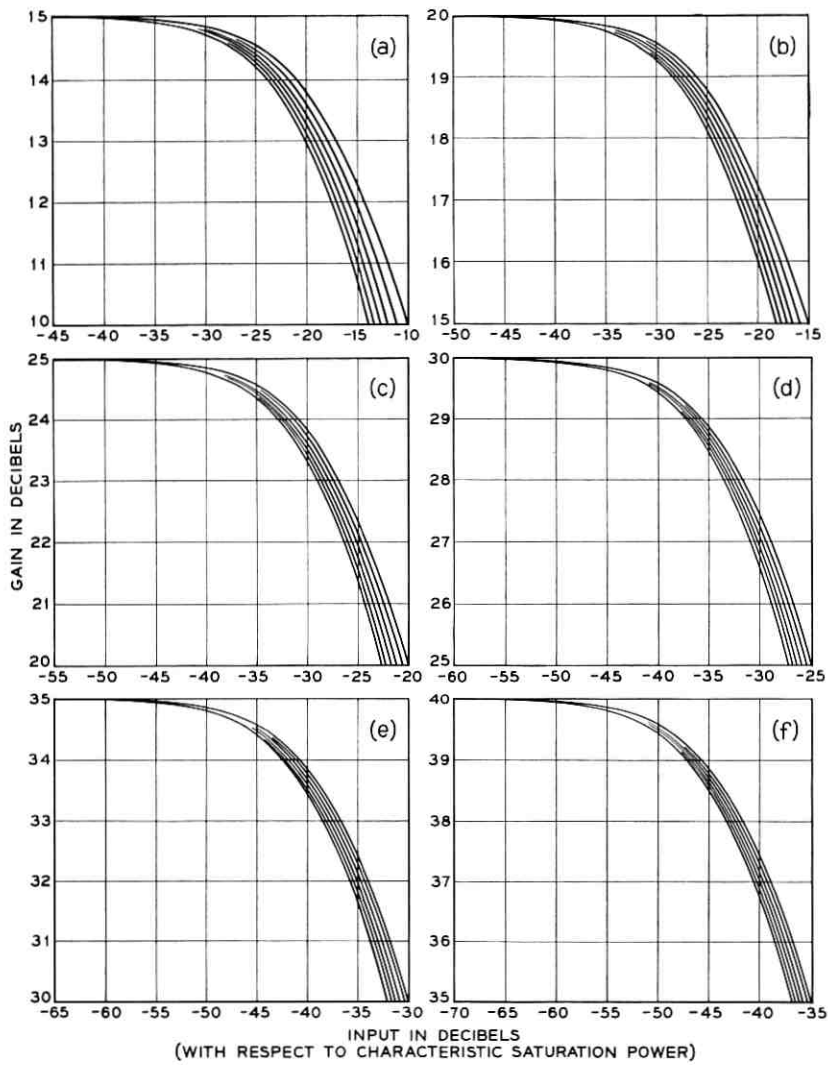


Fig. 10 — Beginning of gain saturation is shown on plot of apparent gain vs input power on an expanded scale for traveling-wave masers of Fig. 7.

time of the TWM, c^{-1} . Maser with high net gain and high intrinsic loss have close to ideal AGC characteristics. It should be pointed out that, over periods of time short compared to c^{-1} , the response of a TWM in an AGC application is still linear, i.e., rapid amplitude variations in the input are strictly reproduced at the output. This distinguishes AGC

action from that of a leveler which clips every power level above a certain minimum without delay. The instantaneous TWM response is more fully discussed in two other papers.^{5,6}

For small degrees of gain saturation such as those shown in Fig. 10, it is desirable to have a more manageable approximation of the rigorous, transcendental gain saturation formula (46). The result of a lengthy but straightforward expansion can be given in the form

$$n_t(0) \text{ (dbm)} + G(\text{db}) + A = P_c \text{ (dbm)} \quad (55)$$

where

$$A = 6.39 + 10 \log_{10} \frac{R}{R-1} - \Delta(\text{db}) - 10 \log_{10} [\Delta(\text{db})]. \quad (56)$$

This formula may be used to solve two typical experimental problems. First, it permits the evaluation of the characteristic saturation power P_c (in units of dbm) from gain saturation measurements. According to (55), P_c is found by the following prescription. Take the input level $n_t(0)$ in dbm at which the gain is reduced by $\Delta(\text{db})$, add to it the low-power gain $G(\text{db})$ and a constant A . Typical values of A are given in Table II. Second, the formula and the table (as well as Fig. 10) can be used to study the details of the gain saturation behavior, assuming that P_c is known. For this purpose it may be advantageous to rewrite (55) in terms of the output power

$$\begin{aligned} n_t(L) \text{ (dbm)} &= n_t(0) \text{ (dbm)} + G(\text{db}) - \Delta(\text{db}) \\ &= P_c \text{ (dbm)} - A - \Delta(\text{db}) \end{aligned} \quad (55')$$

According to (55') and the first row of A values, for example, it is apparent that the maser output at 0.5 db gain reduction is about 10 db lower than P_c . Similarly, at 3 db gain reduction the output is roughly 3 db below P_c . One also sees from the table, for example, that gain reduction by 1 db occurs at input levels 3.5 db higher than for a gain reduction of 0.5 db. Similarly, a gain tolerance of -3 db allows 10.3 db greater input signals than a permissible gain compression of 0.5 db. Formula (55) can, of course, also be used in reverse to calculate the

TABLE II — VALUE OF A

	$R = 2$	4	6	8	10
$\Delta(\text{db}) = 0.5$	11.9	10.1	9.6	9.4	9.3
1	8.4	6.6	6.1	5.9	5.8
3	1.5	-0.1	-0.7	-0.9	-0.9

maximum permissible input level $n_t(0)$ from a given gain tolerance $\Delta(\text{db})$ and the known saturation level P_c .

In the original paper on the microwave TWM,⁴ it was suggested that the degree of gain saturation in a maser depends only on average power. Thus the same amount of gain reduction was found with a certain CW power level and with pulses of a 30-db higher peak power applied with a 30-db duty ratio. This feature of maser gain saturation is examined here more closely.

Let t_1 be the duration of signal pulses and t_2 the time after which the pulse repeats. The leading edge of the pulse may be at $t = 0$. Then the energy storage is essentially determined by

$$\frac{\partial n_z}{\partial t} = -an_t n_z \quad 0 < t < t_1 \quad (57)$$

$$\frac{\partial n_z}{\partial t} = c(N_z - n_z) \quad t_1 < t < t_2. \quad (58)$$

In (57), spin recovery is neglected during pulse duration. This leads to a small error for short pulses. The error can be largely compensated for, however, if the recovery in (58) is formally extended over the whole period, $0 < t < t_2$. The solution n_z will be a steady-state solution if it repeats after a time t_2 , that is

$$n_z(z,0) = n_z(z,t_2). \quad (59)$$

From (57), (58), (59)

$$n_z(z,0) = \frac{N_z[1 - \exp(-ct_2)]}{1 - \exp\left[-a \int_0^{t_1} n_t ds - ct_2\right]}. \quad (60)$$

If the pulses repeat with a fast rate compared to the maser recovery time and if the energy per pulse is not very large, that is, if

$$ct_2 \ll 1 \quad (61)$$

and

$$a \int_0^{t_1} n_t(s) ds \ll 1 \quad (62)$$

then (60) can be approximated by

$$n_z(z,0) = \frac{N_z}{1 + \frac{1}{P_c} \frac{1}{t_2} \int_0^{t_1} n_t(s) ds}. \quad (63)$$

This equation is identical to (42), the usual saturation formula, except that here the average power takes the place of CW power in (42). Thus all statements made in the equations of this section and in Figs. 7 through 10 are applicable to pulse power, provided the terms used there are interpreted in terms of average power.

In the case of a ruby microwave TWM, the restrictions are not severe. If a safety factor of 10 is included on account of the inequality relations, (61) means that pulse repetition rates should be 100 pps or faster. Since the stored energy in typical microwave masers is between 10^{-6} and 10^{-7} joule, the condition (62) restricts the energy per pulse to about 10^{-8} joule. This may imply 0.1-microsecond pulses of 100 milliwatts or less, or 10-microsecond pulses of 1 milliwatt or less. It is of course possible to operate a TWM under conditions which violate (61) and (62). In that case, the graphs of Figs. 7 through 10 will no longer apply and there will be an appreciable extent of pulse sharpening, as discussed in the earlier sections of this paper.

VII. EXPERIMENTS ON GAIN SATURATION

In this section, some measurements of gain saturation in a microwave traveling-wave maser are reported. The measurements were carried out by F. S. Chen.³ The maser was developed by P. J. Pantano and W. J. Tabor,¹⁴ and it features the earlier design of a round-finger comb with a single slab of ruby on one side of the comb. The passband extends from 6.2 to 6.8 gc and the highest net gain occurs at 6.25 gc. Signal frequencies of 6.25, 6.35, and 6.45 gc which were used in the measurements are associated with phase shifts between comb fingers of about 20° , 45° , and 75° , respectively.

TWMs of a more advanced design with hobbed square fingers and double-sided ruby loading^{15,16} were under development at the time of this study, but they were not available for extended gain saturation measurements. Nevertheless, the general conclusions about gain saturation derived in this section should be equally applicable to those newer masers. The only difference might be the absolute value of the characteristic saturation power.

Four aspects of the TWM gain saturation theory presented in the previous section were studied by the experiments:

(i) The theory makes use of a single interaction constant a as defined in (3a). On closer examination this equation suggests, however, that the interaction depends on the local strength of the RF magnetic field, which is a function of the coordinates x, y within the maser material cross sec-

tion A_M . Thus the interaction should be described by a function $a(x,y)$ whose average is equal to the previously used constant a

$$\frac{1}{A_M} \int_{A_M} a(x,y) dx dy = a. \quad (64)$$

The use of a function $a(x,y)$ implies that there is a varying degree of saturation throughout the cross section of the maser material, i.e. the saturation formula (42) is replaced by

$$n_z(x,y) = \frac{N_z/A_M}{1 + a(x,y)n_t c^{-1}} \quad (65)$$

where

$$\int_{A_M} n_z(x,y) dx dy = n_z. \quad (66)$$

When introducing (65) into the earlier differential equation (5), it has to be observed that once again the gain interaction $a(x,y)$ varies over the cross section. Thus (5) takes the rigorous form

$$\frac{dn_t}{dz} = \frac{n_t N_z}{A_M} \int_{A_M} \frac{a(x,y) dx dy}{1 + n_t a(x,y) c^{-1}} - b n_t. \quad (67)$$

This equation takes into account the nonuniform exhaustion of stored energy within the maser material cross section, A_M . Parts of the maser material exposed to higher RF fields nearer the comb saturate at a lower signal power level and vice versa. The differential equation (67) predicts a more gradual drop of gain and a slower transition to net attenuation as the input power is increased than the corresponding equation (5) with an averaged value a .

The function $a(x,y)$ was evaluated by F. S. Chen's space harmonic analysis of the comb structure.¹⁷ It consists of a Fourier or space harmonic sum involving combinations of trigonometric and hyperbolic functions. Unfortunately, it is not possible to approximate the result by a simple analytical expression for $a(x,y)$. This is so mathematically because many terms in the sum are of appreciable magnitude, which in turn is due to the physical fact that several of the relevant dimensions are comparable. Thus, while the computed function $a(x,y)$ may be used in machine computations of the gain saturation from (67), this would require a separate set of computations for each comb design and for each phase shift value within the passband (in addition to the number of parameters already entering the computation). Clearly, such a procedure does not appear attractive. Instead, it would be more convenient if it were possible to

interpret the experimental data in terms of the theoretical curves in Figs. 7 to 10, which were computed on the basis of an averaged interaction constant a . In this case one should in principle expect some discrepancy between the theoretical curves and the observed results. The question arises whether this discrepancy, if observable at all, is of practical significance.

(ii) The characteristic saturation power, P_c , in (43) is independent of the amount of stored energy in the maser transition. Hence it should be independent of the degree of inversion or the amount of pump power supplied. This feature is obvious from maser theory and would perhaps not deserve experimental verification. For amplifiers other than the maser, however, it would be an unusual property. In conventional voltage amplifiers, for example, the maximum output voltage tends to be proportional to the supply voltage.

(iii) The phase shift between comb fingers and the RF magnetic field pattern changes with the signal frequency. This implies a change of $a(x,y)$ and possibly of the average value a with frequency. It is conceivable then that the saturation power P_c varies also with frequency.

(iv) The theoretically predicted equivalence of gain saturation by pulse and CW power of the same average value had not been checked before over a large range of power levels.

The experimental results are presented in Figs. 11 to 13. Theoretical

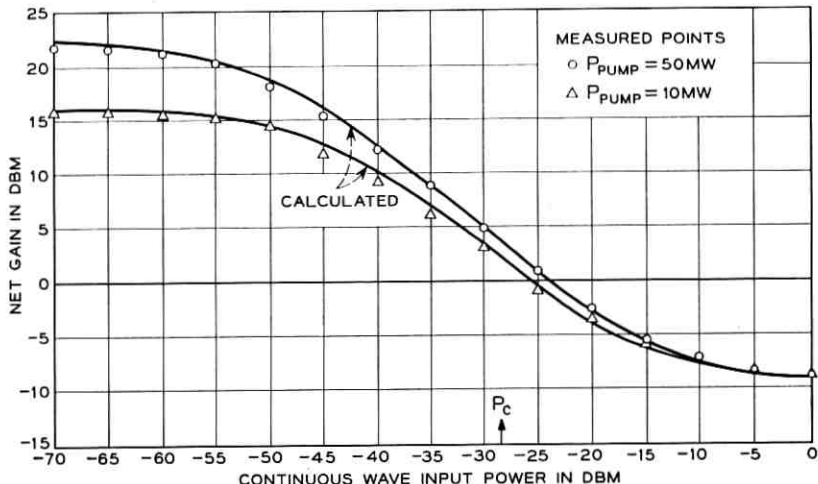


Fig. 11 — Measured and calculated gain saturation under CW conditions. Signal frequency is 6.25 gc and intrinsic circuit loss is 9 db. Fitting of theoretical curves to the data yields a characteristic saturation power level of -28.7 dbm for both curves.

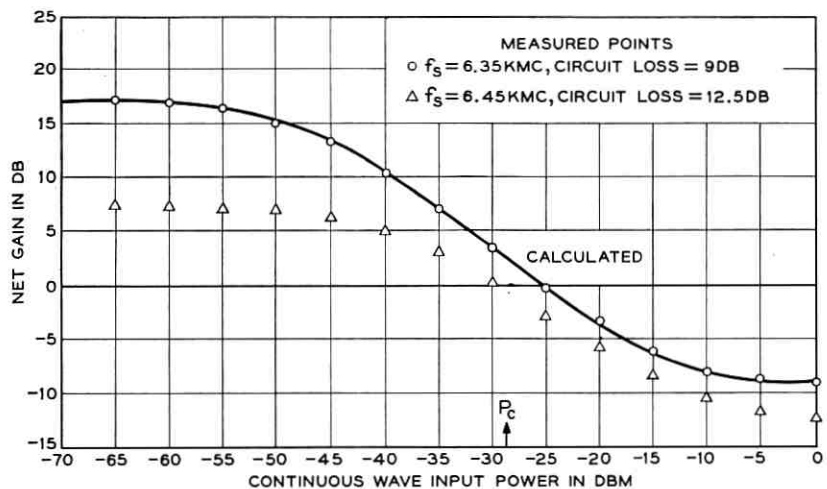


Fig. 12 — Gain saturation under CW conditions at signal frequencies of 6.35 ge (9 db circuit loss) and 6.45 ge (12.5 db circuit loss). The characteristic power level is -28.7 dbm for both curves.

curves taken from Fig. 8 are shown as solid lines, and the experimental data are shown by points and crosses. The theoretical curves were fitted to the data by adjusting the characteristic saturation power, P_c . The figures suggest the following conclusions:

(i) The theoretical curves fit the experimental data remarkably well.

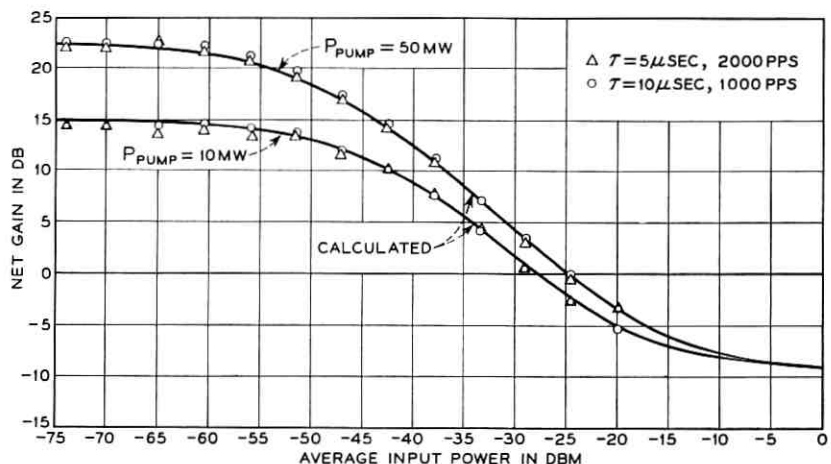


Fig. 13 — Measured net gain under pulse saturation conditions with -20-db duty ratio at signal frequency of 6.25 ge. Data taken with two different pump levels and with two different types of pulses are compared with theoretical curves.

The greatest deviations are ± 0.5 db and could in part be caused by experimental errors. There is a consistent tendency of the experimental points, however, to follow a slightly flatter curve than the theoretical one. Nevertheless, gain saturation follows the simplified theory sufficiently well for practical purposes. The discrepancies are ± 0.5 db here and could be ± 1 db for a maser with 40 db low-power gain. This result eliminates the need for more rigorous computations based on equation (65).

(ii) The two curves in Fig. 11, taken with pump power levels of 50 and 10 milliwatts, respectively, are characterized by the same saturation level, P_c , to within better than ± 0.25 db. This shows, in agreement with theory, that P_c is independent of the amount of pump power.

(iii) The curves in Figs. 11 and 12 result in the same value of P_c , again to better than ± 0.25 db for signal frequencies of 6.25, 6.35, and 6.45 ge. In the case of the 6.45-ge data, no compatible theoretical curve was available from Fig. 8, but P_c there was determined from the zero-db conditions (51) and (52). Since all these data were taken only in the lower half of the passband, it is not necessarily justified to assume the same constant P_c in the higher-frequency parts of the passband where the field is even more tightly bound to the comb.

It should be emphasized that a constant P_c across the signal band does not imply that at all frequencies the gain is reduced by 1 db, for example, at the same signal input level. As shown in formula (55), this level depends also on the ratio R and the low-power gain.

(iv) The curves of Fig. 13 show the same data with pulse measurements that Fig. 11 shows for CW measurements. Small discrepancies between both figures can be accounted for by the experimental errors inherent in pulse measurements, in particular in an accurate setting of the duty ratio. Taking this into account, the measurements prove over a 50-db range of input power that the degree of gain saturation depends only on average power.

CONCLUSIONS AND ACKNOWLEDGMENTS

The pulse sharpening phenomenon in an optical TWM is, in principle, a means of producing coherent optical pulses of higher peak power and shorter rise time than any other method. The peak power is limited only by the onset of nonlinearities in light transmission, and the rise time is limited only by the linewidth of the optical transition.

Considering the present optical maser technology, however, it would appear difficult to produce pulses of appreciably higher peak power and shorter duration by application of pulse sharpening, compared to those

which are available now by the giant pulse technique. This will have to wait for the development of TWMs which for very short periods of time exhibit very high gain despite the rapid exhaustion of stored energy due to saturation on the intrinsic spontaneous emission. It will also have to wait for the development of more rapid shutter techniques which, for example, may allow a further steepening of the initial rise of a giant pulse so that it may be used subsequently as the driver signal for the TWM pulse sharpening chain. It also should be mentioned that the pulses so produced will show the desirable extremely rapid rise, but a rather slow "hyperbolic" trailing edge. This, however, may be adequate for many purposes, such as high-resolution optical radar.

The analysis of recorded data from a pulse sharpening experiment using a maser of more moderate gain indicates agreement with the theoretical model derived in this paper, in particular with the predicted gain decay.

The gain saturation observed in a microwave TWM distinguishes this device from other amplifiers. In the range of reduced gain, the TWM acts as a slow time constant AGC circuit responding to the signal average power. More rapid signal variations such as modulation of any kind are transmitted and amplified without distortion. At very high signal power, the device is effectively an attenuator of moderate insertion loss. Gain saturation experiments covering power level variations of many orders of magnitude showed that the gain saturation theory derived in this paper is applicable with gratifying accuracy to practical comb structure ruby microwave TWMs. Experiments with pulsed signal power substantiated the suggestion that the degree of gain saturation depends only on the average power.

This work was aided by contributions from many individuals. H. E. D. Scovil predicted the pulse sharpening phenomenon and suggested a study more than four years ago. J. E. Geusic provided the experimental data shown in Fig. 5 on pulse sharpening in his optical TWM. J. A. Morrison conceived the method of solving the pulse sharpening differential equations as reproduced in (11) to (23). W. J. C. Grant programmed the machine plotting of Fig. 3. J. S. Wright programmed the numerical evaluation of (46) and the machine plotting of the data shown in Figs. 7 to 10. F. S. Chen provided the experimental data on gain saturation in a microwave TWM shown in Figs. 11 to 13. He also suggested the derivation of the small gain compression formula (55) and of the average pulse power formula (63). The author gratefully acknowledges these contributions.

Note added in proof. After completion of the manuscript, a paper on

"Pulse Propagation in a Laser Amplifier" by Frantz and Nodvik¹⁸ appeared in print. These authors independently derived some of the results contained in our 1959 report¹ and in certain parts of Sections II, III, and IV of the present paper.

REFERENCES

1. Schulz-DuBois, E. O., Microwave Solid State Devices, U. S. Army Signal Corps Contract DA 36-039 SC-73224, Eleventh Interim Report, November, 1959, p. 14. Available through ASTIA. Unpublished.
2. Wright, J. S., and Schulz-DuBois, E. O., Solid State Maser Research, U. S. Army Signal Corps Contract DA 36-039 SC-85357, Fifth Quarterly Report, September, 1961, p. 33. Available through ASTIA. Unpublished.
3. Chen, F. S., Solid State Maser Research, U. S. Army Signal Corps Contract DA 36-039 SC-85357, Seventh Quarterly Report, March, 1962, p. 11. Available through ASTIA. Unpublished.
4. DeGrasse, R. W., Schulz-DuBois, E. O., and Scovil, H. E. D., The Three-Level Solid State Traveling-Wave Maser, B.S.T.J., **38**, March, 1959, p. 305.
5. Tabor, W. J., Chen, F. S., and Schulz-DuBois, E. O., to be published.
6. Schulz-DuBois, E. O., to be published.
7. Schawlow, A., and Townes, C. H., Infrared and Optical Masers, Phys. Rev., **112**, December, 1958, p. 1940.
8. Maiman, T. H., Stimulated Optical Radiation in Ruby, Nature, **187**, August, 1960, p. 493; Optical Maser Action in Ruby, British Comm. Electron., **7**, September, 1960, p. 674.
9. Collins, R. J., Nelson, D. F., Schawlow, A. L., Bond, W., Garrett, C. G. B., and Kaiser, W., Coherence, Narrowing, Directionality and Relaxation Oscillations in the Light Emission from Ruby, Phys. Rev. Letters, **5**, October, 1960, p. 303.
10. Hellwarth, R. W., *Advances in Quantum Electronics*, ed. J. R. Singer, Columbia University Press, New York, 1961, p. 334; McClung, F. J., and Hellwarth, R. W., Giant Optical Pulsations from Ruby, J. Appl. Phys., **33**, March, 1962, p. 828; Characteristics of Giant Optical Pulsations from Ruby, Proc. IEEE, **51**, January, 1963, p. 46.
11. Geusic, J. E., and Scovil, H. E. D., A Unidirectional Traveling-Wave Optical Maser, B.S.T.J., **41**, July, 1962, p. 1371.
12. Geusic, J. E., and Scovil, H. E. D., Third Quantum Electronics Conference, Paris (1963), to be published.
13. Wagner, W. G., and Lengyel, B. A., Evolution of Giant Pulse in a Laser, J. Appl. Phys., **34**, July, 1963, p. 2040.
14. Pantano, P. J., and Tabor, W. J., Solid-State Maser Research, U. S. Army Signal Corps Contract No. DA 36-039 SC-85357, Fourth Quarterly Report, June 20, 1961, p. 35. Available through ASTIA. Unpublished.
15. Tabor, W. J., and Sibilia, J. T., Masers for the Telstar Satellite Communications Experiment, B.S.T.J., **42**, July, 1963, p. 1863.
16. Hensel, M. L., and Treacy, E. B., private communication.
17. Chen, F. S., Solid State Maser Research, U. S. Army Signal Corps Contract No. DA 36-039 SC-85357, Fourth Quarterly Report, June 20, 1961, p. 27; Fifth Quarterly Report, September 20, 1961, p. 17; Sixth Quarterly Report, September 20, 1961, p. 7; Seventh Quarterly Report, March 20, 1962, p. 1. Available through ASTIA. Unpublished.
18. Frantz, L. M., and Nodvik, J. S., J. Appl. Phys., **34**, Aug., 1963, p. 2346.

Microwave Heating of a Luneberg Lens

By SAMUEL P. MORGAN

(Manuscript received October 7, 1963)

A calculation is made of the maximum steady-state temperature rise due to a small amount of dielectric dissipation in a Luneberg lens which is continuously illuminated by a powerful microwave transmitter, when the surface of the lens is held at a constant temperature. The temperature distribution along the axis of the lens is computed both when the focus is at the surface, and also when it is outside the surface at a distance equal to one-tenth of the lens radius. The numerical results are given in such a form that the maximum temperature rise is easily deduced when the loss tangent is any linear function of the refractive index of the lens material. In general the maximum steady-state temperature occurs on the axis at some interior point between the center of the lens and the focus. The total power dissipated in the lens is also computed. Finally, a brief discussion is given of the time scale associated with transient heating of the lens.

1. INTRODUCTION AND SUMMARY

When a Luneberg lens is to be used as an antenna for a long-range radar,¹ it is important to know how much the lens will be heated by dielectric dissipation when it is illuminated by a powerful transmitter. This paper presents a calculation of the maximum steady-state temperature rise in the interior of the lens, when the surface is held at a constant temperature and only a small fraction of the incident power is dissipated. Since the maximum temperature rise depends critically on the loss tangent of the lens material, and since the loss tangent may vary with index of refraction, the results are given in such a form that the maximum temperature rise is easily deduced when the loss tangent is any linear function of the index of refraction. The index of refraction is assumed to vary with radius in a manner appropriate for a Luneberg lens of the desired focal length. Numerical computations have been made for the case in which the focus is at the surface of the lens, and also when it is outside the surface at a distance equal to one-tenth of the lens radius.

In the idealized problem to be studied, the temperature rise per watt of incident power will be the same for a distant transmitter, which illuminates the lens with an essentially uniform plane wave, as for a transmitter at the focus, with a feed pattern corresponding to a uniform plane emergent wave. In either case, if the lens is illuminated from a particular direction, and if the index of refraction and the loss tangent are functions of the radial coordinate only, the heat source distribution and the temperature distribution will be axially symmetric, and in all practical cases the maximum temperature will occur somewhere on the axis of the lens. Hence to find the maximum temperature we need only calculate the temperature distribution along the axis.

Suppose that the loss tangent of the lens material can be adequately represented by a linear function of the index of refraction; thus

$$\tan \delta = An + B, \quad (1)$$

where n is the refractive index and A and B are constants. Then we shall show that the axial temperature distribution can be written in the form

$$T(\xi) = (P_0/k\lambda)[AT_A(\xi) + BT_B(\xi)], \quad (2)$$

where ξ is axial distance in units of the lens radius, with $\xi = -1$ corresponding to the plane wave side and $\xi = +1$ to the side nearest the focus. P_0 is the total power incident on the lens, k is the thermal conductivity, and λ is the free-space wavelength. The dimensionless functions $T_A(\xi)$ and $T_B(\xi)$ are given in Table I of Section V and are plotted in Figs. 2 and 3 for lenses with normalized focal distances of 1.0 and 1.1, measured from the center. Note that the maximum temperature given by (2) is independent of the lens radius.

The foregoing remarks apply to the case in which the lens is illuminated from a single direction, so that the maximum temperature rise occurs on the axis. If the total power P_0 striking the lens comes from several different directions, we can deduce upper and lower bounds on the maximum temperature rise in the "multiaxial" case from a knowledge of the temperature distribution along the axis in the "uniaxial" case. Since the heat conduction equation is linear, the principle of superposition guarantees that the temperature at the center of the lens is the same in both cases. Also, the maximum temperature in the multiaxial case is less than the maximum temperature in the uniaxial case, since the maximum temperature point in the uniaxial case is on the axis defined by the incident beam, and this point is not on the other

axes in the multiaxial case. It follows that the maximum temperature rise in the multiaxial case is at least as great as the rise at the center of the lens in the uniaxial case, but not as great as the maximum rise in the uniaxial case. The numerical example in Section V indicates that in practical situations these two bounds may be so close together that a more detailed treatment of the multiaxial case would be superfluous.

The body of the paper is concerned with the determination of the functions $T_A(\xi)$ and $T_B(\xi)$ which occur in (2). In Section II we introduce a convenient approximation to the index of refraction of the Luneberg lens, which is exact if the focus is at the surface, and show that under this approximation the ray paths are ellipses. In Section III we compute the power flow through every element of a lossless lens, and the approximate rate of dissipation of heat, assuming small dissipation and a loss tangent of the form (1). An integral representation of the temperature along the axis is obtained in Section IV, as well as an expression for the total dissipated power. Results of numerical integrations carried out on an IBM 7090 are given in Section V. Appendix A contains a proof that in all practical cases the maximum "uniaxial" temperature occurs on the axis, while Appendix B is concerned with the nature of the mathematical singularity which occurs in the idealized model when the focal point is at the surface of the lens. The time scale for transient thermal effects is briefly discussed in Appendix C.

II. RAY PATHS IN A LUNEBERG LENS

The path of a typical ray in a Luneberg lens of normalized radius unity is shown schematically in Fig. 1. In general the path of a light

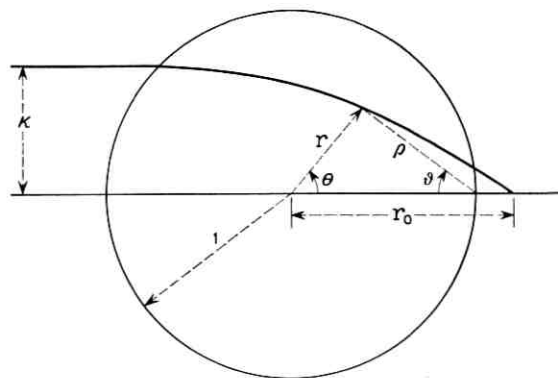


Fig. 1 — Typical ray path in a Luneberg lens.

ray in a radially symmetric medium with refractive index $n(r)$ is given by²

$$\theta - \theta_0 = \pm \int_{r_0}^r \frac{\kappa dr}{r[n^2 r^2 - \kappa^2]^{\frac{1}{2}}}, \quad (3)$$

where (r, θ) are polar coordinates in the plane of the ray, and κ is constant for a particular ray, being determined, together with the ambiguous sign, by the direction of the ray at the initial point (r_0, θ_0) . In the special case where the rays are all initially parallel, κ is equal to the initial distance of the given ray from the axis of the system.

In principle, (3) may be integrated to find the ray path whenever n is a known function of r . For a Luneberg lens with focal point offset from the surface, however, the relationship between n and r is given by two parametric equations² involving a function defined by a definite integral, and it does not seem possible to obtain the equation of the ray path explicitly in terms of known functions. An approximation to the refractive index which does permit analytic integration of (3) is

$$n = [n_0^2 - (n_0^2 - 1)r^2]^{\frac{1}{2}}, \quad (4)$$

where n_0 is the index at the center of the lens according to the accurate theory; n_0 is a decreasing function of the focal length r_0 . The relationship (4) is exact if the focus is at the surface ($n_0 = \sqrt{2}$), and is a good approximation if the distance from the focus to the surface is small.

To find the equation of a typical ray in a lens whose refractive index is given by (4), it is convenient first to locate the "turning point" (r^*, θ^*) at which the distance of the ray from the center of the lens is a minimum. The turning point is defined by²

$$r^* n(r^*) = \kappa, \quad (5)$$

which yields, using (4),

$$r^*(\kappa) = \left[\frac{n_0^2 - [n_0^4 - 4\kappa^2(n_0^2 - 1)]^{\frac{1}{2}}}{2(n_0^2 - 1)} \right]^{\frac{1}{2}}. \quad (6)$$

The corresponding angle is derived from (3), setting $\theta = \pi$ when $r = \infty$ and noting that θ and r decrease together. We obtain

$$\begin{aligned} \theta^*(\kappa) &= \pi + \int_{\infty}^1 \frac{\kappa dr}{r(r^2 - \kappa^2)^{\frac{1}{2}}} + \int_1^{r^*} \frac{\kappa dr}{r[r^2 n^2(r) - \kappa^2]^{\frac{1}{2}}} \\ &= \frac{3\pi}{4} - \sin^{-1} \kappa - \frac{1}{2} \tan^{-1} \frac{n_0^2 - 2\kappa^2}{2\kappa(1 - \kappa^2)^{\frac{1}{2}}}, \end{aligned} \quad (7)$$

on substituting (4) into the second integral and carrying out some straightforward integrations.

We can now determine the equation of the ray path inside the lens. Proceeding along the ray in either direction from the turning point, we have from (3) and (4),

$$\begin{aligned}\theta - \theta^*(\kappa) &= \pm \int_{r_*}^r \frac{\kappa dr}{r[n_0^2 r^2 - \kappa^2]^{\frac{1}{2}}} \\ &= \pm \frac{1}{2} \cos^{-1} \frac{2\kappa^2 - n_0^2 r^2}{r^2[n_0^4 - 4\kappa^2(n_0^2 - 1)]^{\frac{1}{2}}},\end{aligned}\quad (8)$$

or, by rearrangement,

$$F(r, \theta; \kappa) \equiv r^2 \{[n_0^4 - 4\kappa^2(n_0^2 - 1)]^{\frac{1}{2}} \cos 2(\theta - \theta^*) + n_0^2\} - 2\kappa^2 = 0. \quad (9)$$

Since $\theta^*(\kappa)$ is constant for a particular ray, it is easy to write (9) in rectangular coordinates and to verify that it is the equation of an ellipse.

III. RATE OF INTERNAL DISSIPATION OF HEAT

If the total dissipated power is a small fraction of the incident power, as it must be in a practical lens, then the heat losses may be regarded as a small perturbation on the power flux in the lossless case, which we shall now compute.

Henceforth we regard each ray as defining a surface of revolution, although the ray itself lies in a plane through the axis of the system. According to geometrical optics, the total power flow along the tube bounded by the ray surfaces corresponding to κ and $\kappa + d\kappa$ is constant. Let $d\nu$ be the elementary distance normal to the ray in the direction of increasing κ . If κ is regarded as a point function defined by (9), we have

$$\frac{\partial \kappa}{\partial \nu} = \left| \frac{\partial F / \partial \nu}{\partial F / \partial \kappa} \right| = \left| \frac{\nabla F}{\partial F / \partial \kappa} \right|, \quad (10)$$

where ∇F is evaluated by differentiating F with respect to the coordinate variables while holding κ fixed.

Now let $S(r, \theta)$ be the power flux along a ray at any point of the lens; appropriate units for S with the present normalization of lengths are watts/(radius)². The total power flow along an elementary tube is then

$$dP = 2\pi r \sin \theta S(r, \theta) d\nu = \text{constant}. \quad (11)$$

The constant can be evaluated by considering a ring-shaped element of area normal to the incident beam, where κ is just the distance of the

given ray from the axis. If P_0 is the total power incident on the lens, then

$$dP = 2P_0\kappa \, d\kappa. \quad (12)$$

Combining (10), (11), and (12) yields

$$S(r,\theta) = \frac{P_0\kappa}{\pi r \sin \theta} \frac{|\nabla F|}{|\partial F/\partial \kappa|}. \quad (13)$$

The attenuation constant α at any point of the lens is given by the well-known approximate relationship

$$\alpha = (\pi n/\lambda) \tan \delta, \quad (14)$$

where n is the refractive index, $\tan \delta$ is the loss tangent (assumed small), and λ is the free-space wavelength, measured here in units of the lens radius. Hence the rate of energy dissipation per unit volume, in watts/(radius)³, is

$$Q(r,\theta) = 2\alpha S(r,\theta) = \frac{2P_0\kappa n \tan \delta}{\lambda r \sin \theta} \frac{|\nabla F|}{|\partial F/\partial \kappa|}. \quad (15)$$

On the right side of (15), κ is defined implicitly by (7) and (9) as a function of r and θ . The refractive index $n(r)$ is given by (4), and $\tan \delta$ is supposed to be a known function of n . Differentiation of (7) and (9) yields

$$\frac{\partial F}{\partial r} = 2r\{[n_0^4 - 4\kappa^2(n_0^2 - 1)]^{\frac{1}{2}} \cos 2(\theta - \theta^*) + n_0^2\}, \quad (16)$$

$$\frac{1}{r} \frac{\partial F}{\partial \theta} = -2r\{[n_0^4 - 4\kappa^2(n_0^2 - 1)]^{\frac{1}{2}} \sin 2(\theta - \theta^*)\}, \quad (17)$$

$$\begin{aligned} \frac{\partial F}{\partial \kappa} &= r^2 \left\{ -\frac{4\kappa(n_0^2 - 1)}{[n_0^4 - 4\kappa^2(n_0^2 - 1)]^{\frac{1}{2}}} \cos 2(\theta - \theta^*) \right. \\ &\quad \left. + 2[n_0^4 - 4\kappa^2(n_0^2 - 1)]^{\frac{1}{2}} \sin 2(\theta - \theta^*) \frac{d\theta^*}{d\kappa} \right\} - 4\kappa, \end{aligned} \quad (18)$$

$$\frac{d\theta^*}{d\kappa} = -\frac{1}{(1 - \kappa^2)^{\frac{1}{2}}} \frac{(n_0^2 - 2\kappa^2)(n_0^2 - 1)}{n_0^4 - 4\kappa^2(n_0^2 - 1)}. \quad (19)$$

Hence in principle the rate of heat generation $Q(r,\theta)$ is a known function of position within the lens.

To determine the power flux from (13) and (16)–(19) when $\kappa = 0$ or $\kappa = 1$ requires the evaluation of some indeterminate forms. Derivations of the following results are straightforward and will be omitted.

The power flux along the axis is given by

$$S(\xi) = \frac{P_0}{\pi} \left[\frac{n_0^2}{[n_0^2 - (n_0^2 - 1)\xi^2]^{\frac{1}{2}} - (n_0^2 - 1)\xi} \right]^2, \quad (20)$$

where ξ is the normalized axial coordinate defined below (2) of Section I. The power flux at the equator of the lens is

$$\lim_{r \rightarrow 1^-} S(r, \pi/2) = P_0/\pi n_0^2. \quad (21)$$

If the focus is at the surface of the lens ($n_0 = \sqrt{2}$), then

$$\lim_{r \rightarrow 1^-} S(r, \theta) = 0, \quad 0 < \theta < \pi/2. \quad (22)$$

In this case, particular interest attaches to the power flux in the immediate neighborhood of the focal point. It is convenient to introduce new polar coordinates ρ, ϑ , with origin at the focus and polar axis in the direction of decreasing ξ (see Fig. 1). Then for small ρ the power flux is

$$S \approx \frac{P_0 \cos \vartheta}{\pi \rho^2}. \quad (23)$$

IV. AXIAL TEMPERATURE DISTRIBUTION AND DISSIPATED POWER

The steady-state temperature distribution inside the lens satisfies Poisson's equation,

$$\nabla^2 T = -Q/k, \quad (24)$$

where T is the temperature above any convenient reference level, Q is the source distribution, and k is the thermal conductivity, expressed for the moment in units of watts/(degree·radius). Since the surface of the lens is assumed to be held at a constant temperature, say by air conditioning the space between the lens and the radome, the boundary condition may be taken as

$$T = 0 \quad \text{at} \quad r = 1. \quad (25)$$

The source distribution Q is a function of the coordinates r, θ only, and in all practical cases it decreases with increasing distance from the axis. It is proved in Appendix A that the maximum temperature rise then occurs on the axis; and as shown in Section I, a knowledge of the axial temperature distribution in this case enables us to put upper and lower bounds on the maximum temperature rise in a Luneberg lens illuminated from more than one direction.

The temperature distribution on the axis may easily be written down in terms of the Green's function for the interior of a sphere; thus,

$$T(\xi) = \frac{1}{k} \int_0^\pi \int_0^1 Q(r,\theta) G(r,\theta;\xi) 2\pi r^2 \sin \theta \, dr \, d\theta, \quad (26)$$

where

$$G(r,\theta;\xi) = (1/4\pi)[(r^2 + \xi^2 - 2r\xi \cos \theta)^{-\frac{1}{2}} - (1 + \xi^2 r^2 - 2r\xi \cos \theta)^{-\frac{1}{2}}]. \quad (27)$$

If desired, one may think of (26) as representing the electrostatic potential due to a distributed electric charge of density $\epsilon_0 Q(r,\theta)/k$ inside an earthed, conducting sphere of unit radius, but the analogy has nothing to do with the mathematics.

Before starting calculation, we shall assume that $\tan \delta$ is a linear function of n , say

$$\tan \delta = An + B. \quad (28)$$

Then making use of (15), we may write (26) in the form

$$T(\xi) = (P_0/k\lambda)[AT_A(\xi) + BT_B(\xi)], \quad (29)$$

where

$$T_A(\xi) = 4\pi \int_0^\pi \int_0^1 \kappa n^2 \left| \frac{\nabla F}{\partial F/\partial \kappa} \right| G(r,\theta;\xi) r \, dr \, d\theta, \quad (30)$$

$$T_B(\xi) = 4\pi \int_0^\pi \int_0^1 \kappa n \left| \frac{\nabla F}{\partial F/\partial \kappa} \right| G(r,\theta;\xi) r \, dr \, d\theta.$$

The dimensionless functions $T_A(\xi)$ and $T_B(\xi)$ are calculated numerically in the next section. Note that although the radius of the sphere has heretofore been taken as the unit of length, the factor $P_0/k\lambda$ has the dimensions of temperature, and any consistent set of units (e.g., MKS) may be used for P_0 , k , and λ in (29).

It has been tacitly assumed in the foregoing that the thermal conductivity k is constant throughout the lens. But the conductivity of polystyrene foam, out of which Luneberg lenses are usually made, is known to increase with increasing temperature, and therefore it may be greater in some parts of the lens than in others. However we know from general theory that if in a body with a fixed distribution of heat sources, the thermal conductivity is increased at any point, the steady-state temperature at each point either decreases or remains unchanged. Hence the solution of the heat flow problem with a constant value of k

less than or equal to the actual value of k at all points, provides a temperature distribution which is an upper bound to the actual temperature distribution at all points.

Finally, the fraction of the total incident power which is dissipated in the lens is given by integrating Q/P_0 over the volume. We obtain, from (15) and (28),

$$\frac{\Delta P}{P_0} = \frac{a}{\lambda} \left[A \frac{\Delta P_A}{P_0} + B \frac{\Delta P_B}{P_0} \right], \quad (31)$$

where a is the radius of the lens in the same units as λ , and

$$\begin{aligned} \frac{\Delta P_A}{P_0} &= 4\pi \int_0^\pi \int_0^1 n^2 \kappa \left| \frac{\nabla F}{\partial F/\partial \kappa} \right| r dr d\theta, \\ \frac{\Delta P_B}{P_0} &= 4\pi \int_0^\pi \int_0^1 n \kappa \left| \frac{\nabla F}{\partial F/\partial \kappa} \right| r dr d\theta. \end{aligned} \quad (32)$$

V. NUMERICAL RESULTS

The functions $T_A(\xi)$ and $T_B(\xi)$ were evaluated on an IBM 7090 by a straightforward double application of Simpson's rule to (30). The value of κ at each point was found by solving (9) by Newton's method; then $|\nabla F/(\partial F/\partial \kappa)|$ was calculated from (16)–(19) and $G(r,\theta;\xi)$ from (27). Two values of normalized focal distance, measured from the center of the lens, were considered, namely,

$$r_0 = 1.0, \quad n_0 = \sqrt{2}, \quad (33)$$

$$r_0 = 1.1, \quad n_0 = 1.36025. \quad (34)$$

The numerical results are given in Table I, and are plotted in Figs. 2 and 3. Also the total dissipated power was computed from (32). For $r_0 = 1.0$,

$$(\Delta P/P_0) = (a/\lambda)[16.91A + 13.97B]; \quad (35)$$

and for $r_0 = 1.1$,

$$(\Delta P/P_0) = (a/\lambda)[15.46A + 13.13B]. \quad (36)$$

For the numerical integration a graded net was used, as follows:

Region I	$r =$	0.00 (0.05) 0.40
	$\theta =$	$0.0^\circ (7.5^\circ) 180.0^\circ$

Region II	$r =$	0.40 (0.05) 0.80
	$\theta =$	$0.0^\circ (3.0^\circ) 12.0^\circ$

Region III	$r = 0.80$	(0.02)	1.00
	$\theta = 0.0^\circ$	(1.0°)	12.0°
Region IV	$r = 0.40$	(0.05)	1.00
	$\theta = 12.0^\circ$	(3.0°)	30.0°
Region V	$r = 0.40$	(0.05)	1.00
	$\theta = 30.0^\circ$	(7.5°)	180.0°

Experimentation with a finer net, obtained by simultaneously halving the intervals in r and θ in Regions III and V, indicates that any errors in Table I and (35)–(36) do not exceed a few units of the last figure shown. The accuracy is therefore believed to be sufficient for all practical purposes.

A few aspects of the calculation deserve comment. In the first place, the Green's function (27) is infinite when the field point coincides with the source point; but the integrand of (26) does not become infinite as the field point approaches the source point, provided that $Q(r,\theta)$ remains finite on the axis. The limiting value of the integrand may be either zero or finite, depending upon the direction from which the field point approaches the source point; but in any event the contribution of the apparent singular point during a naive application of Simpson's

TABLE I — THE FUNCTIONS $T_A(\xi)$ AND $T_B(\xi)$

ξ	$r_0 = 1.0$		$r_0 = 1.1$	
	T_A	T_B	T_A	T_B
-1.0	0.0000	0.0000	0.0000	0.0000
-0.9	0.1060	0.0861	0.0985	0.0823
-0.8	0.2155	0.1727	0.1993	0.1645
-0.7	0.3241	0.2564	0.2981	0.2431
-0.6	0.4308	0.3369	0.3940	0.3179
-0.5	0.5345	0.4140	0.4860	0.3887
-0.4	0.6345	0.4876	0.5734	0.4553
-0.3	0.7298	0.5574	0.6553	0.5174
-0.2	0.8198	0.6234	0.7310	0.5749
-0.1	0.9037	0.6856	0.7998	0.6277
0.0	0.9809	0.7440	0.8609	0.6754
0.1	1.0493	0.7974	0.9123	0.7169
0.2	1.1090	0.8464	0.9535	0.7521
0.3	1.1588	0.8907	0.9831	0.7802
0.4	1.1984	0.9306	0.9997	0.8003
0.5	1.2267	0.9659	1.0005	0.8105
0.6	1.2386	0.9937	0.9785	0.8051
0.7	1.2317	1.0132	0.9255	0.7771
0.8	1.2040	1.0251	0.8243	0.7109
0.9	1.1521	1.0324	0.6206	0.5552
1.0	1.0000	1.0000	0.0000	0.0000

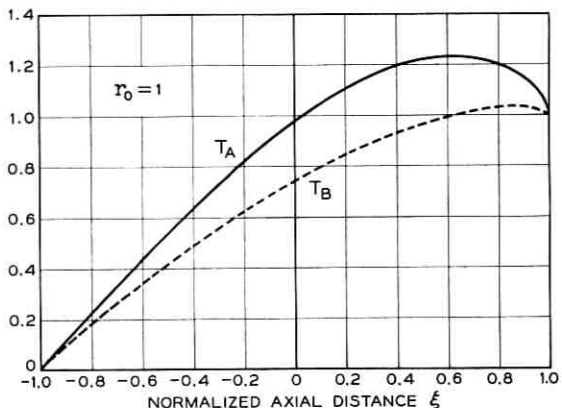


Fig. 2 — The functions T_A and T_B for a lens with focus at the surface ($r_0 = 1$).

rule is at most a finite quantity, which tends to zero as the interval of integration is reduced. In the numerical calculation the contribution from this point was omitted.

A discussion of the mathematical singularity at the focus when $r_0 = 1$ is given in Appendix B. In the mathematical model, the temperature near the focus is given by

$$T(\rho, \vartheta) \approx T_0 \cos \vartheta, \quad (37)$$

where T_0 is a finite constant and ρ, ϑ are spherical polar coordinates in the local coordinate system introduced at the end of Section III. The value of T_0 is determined by the source strength in an infinitesimal

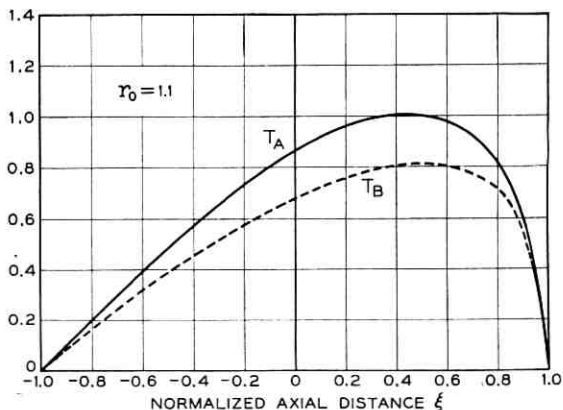


Fig. 3 — The functions T_A and T_B for a lens with focus outside the surface ($r_0 = 1.1$).

region around the focus; in the limit this region makes no contribution to the temperature at other points of the sphere. Hence $T_A(\xi)$ and $T_B(\xi)$ were calculated, for $\xi \neq 1$, by setting the integrands of (30) equal to zero at $r = 1$, $\theta = 0$; and $T_A(1)$ and $T_B(1)$ were evaluated as in Appendix B.

It goes without saying that in a physical lens the temperature at the focus will be well defined, which the limit of the expression (37) is not, and that the temperature distribution will not have an infinite gradient. The actual distribution will be determined by the amount of heat that the air conditioning can carry away from the immediate neighborhood of the focus, as well as by the physical structure of the feed, if the antenna is being used for transmission. Since, however, the numerical example at the end of this section suggests that the maximum temperature rise in a Luneberg lens with surface cooling will be well inside the lens, we shall not attempt here a more elaborate analysis of the conditions near the focus.

If $r_0 > 1$, so that the focal point is outside the lens surface, then (4) is not an exact expression for the index of refraction. However, when $r_0 = 1.1$, the maximum difference between the exact index calculated according to Ref. 2 and the approximate index is about 0.0055 at about $r = 0.87$, the approximate index being smaller. As a second test, we have calculated the distance from the center of the "approximate" lens at which various initially parallel rays intersect the axis. The distance varies from 1.0881 for paraxial rays ($\kappa = 0$) to 1.1205 for rays with $\kappa = 0.95$, compared with the design value of 1.1. It tends toward infinity for marginal rays, but such rays are insignificant so far as the heating problem is concerned anyway, since by hypothesis the surface of the lens is in contact with a constant-temperature heat reservoir. We therefore feel well justified in using (4) to compute the ray paths for $r_0 = 1.1$.

To give an idea of the size of the numbers involved, Fig. 4 shows plots of the axial temperature rise in degrees Fahrenheit per watt of incident power, as calculated from (29) and Table I for a lens with the following parameters:

$$\begin{aligned} P_0 &= 1 \text{ watt} \\ k &= 0.25 \frac{\text{BTU}}{\text{hr} \cdot \text{ft}^2 \cdot (\text{°F/in})} = 0.036 \frac{\text{watts}}{\text{m} \cdot \text{°C}} \\ \lambda &= 60 \text{ cm (500 mc)} \\ \tan \delta &= [1 + 25(n - 1)] \times 10^{-4} \\ a &= 40 \text{ ft} \end{aligned} \tag{38}$$

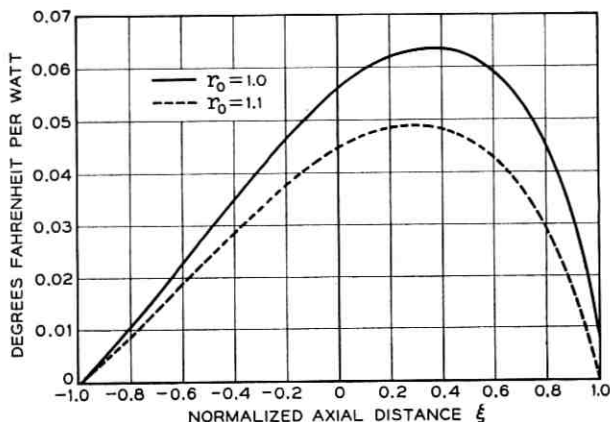


Fig. 4 — Numerical example of axial temperature distribution in two Luneberg lenses.

The assumed values of thermal conductivity and loss tangent are more or less representative of polystyrene foam loaded with metal slivers. The maximum temperature rise is roughly 0.06°F/watt, and occurs about a third of the way from the center of the lens to the surface, in the direction of the focal point. It is of interest to note that the maximum temperature differs from the temperature at the center of the lens by less than 15 per cent, even when the focus is at the surface.

The power dissipated in the lens is easily calculated from (35) or (36). For $r_0 = 1.0$,

$$(\Delta P/P_0) = 0.1777 \quad \text{or} \quad 0.85 \text{ db}; \quad (39)$$

while for $r_0 = 1.1$,

$$(\Delta P/P_0) = 0.1450 \quad \text{or} \quad 0.68 \text{ db}. \quad (40)$$

Equations (39) and (40) give the dissipated power when a uniform plane wave is incident on the lens. Observe, however, that this is not quite equal to the power loss when the lens is being used as a transmitter, since in that case there is usually a deliberate illumination taper across the lens aperture. With a conventional taper, in which the power density is higher at the center of the lens than at the edges, the loss will be higher than that obtained with uniform illumination; but one cannot deduce the total loss from the numbers given in this paper.

VI. ACKNOWLEDGMENTS

This work has had the benefit of valuable discussions with J. A. Lewis and W. A. Yager. The IBM programs were written by Mrs. Marie Dolan.

Note Added in Proof

A recent paper by Lerner⁴ is concerned with essentially the same problem as the present paper. On the basis of a considerable number of approximations, Lerner calculates the temperature distribution along the axis of a surface-focus lens when the thermal conductivity and the loss tangent are constant. The "Average" curve of his Fig. 6 is therefore comparable to the plot of $T_B(\xi)$ in our Fig. 2. The two curves do in fact lie close together except for points less than a quarter of the lens radius distant from the surface focus. Lerner's approximate analysis predicts that the maximum temperature rise will occur at the surface focus and will be equal to $1.25(P_0/k\lambda) \tan \delta$. Our calculations give a maximum rise of about $1.03(P_0/k\lambda) \tan \delta$ at a distance of about one-tenth of the lens radius from the focus, while the temperature rise at the focus is $(P_0/k\lambda) \tan \delta$.

APPENDIX A

Position of Temperature Maximum

We consider the steady-state temperature distribution which satisfies

$$\begin{aligned} \nabla^2 T &= -f \quad \text{for } r < a, \\ T &= 0 \quad \text{at } r = a. \end{aligned} \tag{41}$$

The source function f ($= Q/k$) is assumed to be axially symmetric and nonnegative, and to have continuous first derivatives in the region $r < a$.

We shall use rectangular coordinates (x,y,z) , cylindrical coordinates (r,φ,z) , or spherical coordinates (r,θ,φ) as convenient. It is assumed that f is independent of φ , and that it is a nonincreasing function of distance from the axis, i.e.,

$$(\partial f / \partial r) \leq 0. \tag{42}$$

Now consider the function

$$W \equiv -(\partial T / \partial y) \equiv -(\partial T / \partial r) \sin \varphi \tag{43}$$

in the hemispherical region S defined by

$$\mathbf{r}^2 + z^2 \leq a^2, \quad 0 \leq \varphi \leq \pi. \quad (44)$$

From (41) and (42) it follows that W is superharmonic in the interior of S , since

$$\nabla^2 W = (\partial f / \partial y) = (\partial f / \partial \mathbf{r}) \sin \varphi \leq 0. \quad (45)$$

Furthermore on the curved surface of the hemisphere we have

$$W = -(\partial T / \partial y) = -(y/r)(\partial T / \partial r) > 0 \quad \text{for } r = a, \quad y > 0, \quad (46)$$

since

$$(\partial T / \partial r) < 0 \quad \text{at } r = a \quad (47)$$

if f is nonnegative and does not vanish identically. A formal proof of this physically obvious statement can be obtained using the Green's function representation of the solution of (41). On the base of the hemisphere, (43) yields

$$W = 0 \quad \text{at } y = 0. \quad (48)$$

Let U be a harmonic function which takes the same values as W on the boundary of S . Since W is superharmonic,³ we have

$$W \geq U \quad (49)$$

in the interior of S . But U achieves its minimum value zero only on the boundary of S , so neither U nor W can vanish in the interior of S . It follows from (43) that $\partial T / \partial \mathbf{r}$ cannot vanish in the interior of S , and so T cannot have a maximum there. Hence the maximum value of T must occur on the axis.

In the present problem the source distribution is given by (15), namely

$$f(r, \theta) = \frac{Q(r, \theta)}{k} = \frac{2P_0 \tan \delta}{\lambda k} \left\{ \frac{\kappa n}{r \sin \theta} \left| \frac{\nabla F}{\partial F / \partial \kappa} \right| \right\}. \quad (50)$$

An analytic proof that the right-hand side of (50) is a decreasing function of distance from the axis would probably be very laborious. We have, however, calculated the expression in braces numerically for the two cases treated in this paper, using a square grid of about 600 points in \mathbf{r} and z , and have verified that on such a grid it is a decreasing function of \mathbf{r} , except for a very small region near the surface of the lens (where \mathbf{r} is slightly less than 1 and θ slightly greater than $\pi/2$ in Fig. 1). On the other hand, the refractive index n is a decreasing function of \mathbf{r} ,

and in practical cases $\tan \delta$ will be a sufficiently rapidly increasing function of n so that the whole source distribution will be a decreasing function of r . In particular, we have verified numerically that (42) is satisfied throughout the lens if $\tan \delta$ is given by (38).

It will be appreciated, of course, that (42) is a sufficient condition but not a necessary one to make the maximum temperature rise occur on the axis. Whether there could exist a hypothetical loss tangent, having a sharp peak at a particular value of n , which would lead to a ring-shaped temperature maximum instead of to a maximum on the axis is still an open question, though not of much practical importance.

APPENDIX B

Temperature Distribution near a Surface Focus

To determine the nature of the temperature singularity in the present mathematical model at a surface focus, we investigate the temperature distribution $T(\rho, \vartheta)$ in the half-space $\vartheta \leq \pi/2$ due to the source function

$$Q(\rho, \vartheta) = \begin{cases} \frac{C \cos \vartheta}{\rho^2}, & 0 < \rho < b, \\ 0, & \rho \geq b. \end{cases} \quad (51)$$

Here b and C are constants, and ρ, ϑ are the polar coordinates introduced at the end of Section III. All quantities are independent of the azimuth angle φ . We seek a solution which vanishes on the plane $\vartheta = \pi/2$, remains finite as $\rho \rightarrow 0$ and as $\rho \rightarrow \infty$, and is continuous, together with its normal derivative, at $\rho = b$.

Substitution of a function of the form

$$T(\rho, \vartheta) = R(\rho) \cos \vartheta \quad (52)$$

into Poisson's equation (24) yields the following equation for $R(r)$:

$$\frac{d}{dr} \left(\rho^2 \frac{dR}{d\rho} \right) - 2R = \begin{cases} -C/k, & 0 < \rho < b, \\ 0, & \rho \geq b. \end{cases} \quad (53)$$

A solution which satisfies the boundary and continuity conditions is easily found to be

$$\begin{aligned} R(\rho) &= \frac{C}{2k} \left(1 - \frac{2\rho}{3b} \right), & 0 < \rho < b, \\ R(\rho) &= \frac{C}{6k} \frac{b^2}{\rho^2}, & \rho \geq b. \end{aligned} \quad (54)$$

We observe that

$$\lim_{\rho \rightarrow 0} R(\rho) = C/2k, \quad (55)$$

and this limit is independent of b . On the other hand, if ρ has any fixed value greater than zero,

$$\lim_{b \rightarrow 0} R(\rho) = 0. \quad (56)$$

It follows that the limiting value of the axial temperature is determined by the source distribution in an arbitrarily small hemisphere around $\rho = 0$, and that in the limit this hemisphere makes no contribution to the temperature at other points of the lens.

If we make the constant C agree with the source distribution given by (15) and (23), then using (28) and the fact that $n = 1$ at the surface of the lens, we have

$$C = \frac{2\alpha P_0}{\pi} = \frac{2(A + B)P_0}{\lambda}. \quad (57)$$

Combining (57) with (55) leads to the results given in Table I, namely

$$\lim_{\xi \rightarrow 1^-} T_A(\xi) = \lim_{\xi \rightarrow 1^-} T_B(\xi) = 1. \quad (58)$$

APPENDIX C

Time Scale for Transient Heating

Suppose that in a Luneberg lens, initially at zero temperature throughout, an internal source distribution $Q(r,\theta)$ is turned on at $t = 0$ and then remains constant in time, while the surface of the lens is held at zero temperature. The temperature within the lens must satisfy

$$k\nabla^2T + Q = \rho c(\partial T / \partial t), \quad (59)$$

where k is the thermal conductivity, ρ the density, and c the specific heat of the medium. Conventional units, such as MKS, are used throughout this section.

It is well known that the solution of (59) can be written as the sum of a steady-state part and a transient part, i.e.,

$$T(r,\theta,t) = T_s(r,\theta) + T_t(r,\theta,t). \quad (60)$$

The steady-state term satisfies

$$k\nabla^2T_s = -Q, \quad (61)$$

while the transient term satisfies

$$D \nabla^2 T_t = \partial T_t / \partial t, \quad (62)$$

where

$$D = k/\rho c \quad (63)$$

is the diffusivity. The transient term vanishes as $t \rightarrow \infty$ and cancels the steady-state solution at $t = 0$; that is,

$$T_t(r, \theta, 0) = -T_s(r, \theta). \quad (64)$$

At the surface of the sphere both terms vanish; namely,

$$T_s(a, \theta) = T_t(a, \theta, t) = 0. \quad (65)$$

A transient solution sufficiently general for our needs may be written in the form

$$T_t(r, \theta, t) = \sum_{n=0}^{\infty} \sum_{m=1}^{\infty} A_{nm} j_n(\chi_{nm} r/a) P_n(\cos \theta) e^{-\alpha_{nm} t}, \quad (66)$$

where j_n is a spherical Bessel function defined in terms of the ordinary Bessel function by

$$j_n(x) = (\pi/2x)^{1/2} J_{n+1/2}(x), \quad (67)$$

P_n is a Legendre polynomial, χ_{nm} is the m th root of $j_n(x)$, and

$$\alpha_{nm} = D \chi_{nm}^2 / a^2. \quad (68)$$

The Bessel and Legendre functions form complete, orthogonal sets, so that at $t = 0$ any reasonable function of r and θ may be expanded in a double series of the form (66), where the coefficients A_{nm} are given by integrals similar to those which define the coefficients in a double Fourier series. In particular, if we had calculated the steady-state solution $T_s(r, \theta)$ at all points of the sphere, we could expand it in such a series and thus satisfy the initial condition (64). We shall not compute the coefficients A_{nm} ; we merely observe that in a transient solution of the form (66), the individual terms decay exponentially with time, the faster the larger α_{nm} . The longest-lived term is the one with smallest α , namely

$$A_{01} j_0(\chi_{01} r/a) e^{-\alpha_{01} t} = A_{01} \frac{\sin(\pi r/a)}{\pi r/a} e^{-(D\pi^2/a^2)t}. \quad (69)$$

The rate at which this term decays permits us to define an approximate "thermal time constant" for the transient solution, unless of course the steady-state solution is such that A_{01} is zero or very small compared to the other coefficients. Comparing the form of (69) with the expected form of the steady-state solution makes it appear obvious that A_{01} will not be unusually small; and therefore an estimate of the time required to establish the steady-state solution is furnished by the "half-life" of the lowest mode,

$$t_{01} = 1/\alpha_{01} = a^2/\pi^2 D. \quad (70)$$

Assuming for polystyrene foam the numerical values

$$\begin{aligned}\rho &= 1.5 \text{ lb/ft}^3, \\ c &= 0.32 \text{ cal/gm} \cdot ^\circ\text{C}, \\ k &= 0.25 \frac{\text{BTU}}{\text{hr} \cdot \text{ft}^2 \cdot (\text{ }^\circ\text{F}/\text{in})},\end{aligned} \quad (71)$$

we find after some conversions of units,

$$D = 1.12 \times 10^{-6} \text{ m}^2/\text{sec.} \quad (72)$$

For a sphere of diameter 1 ft,

$$t_{01} = 35 \text{ min}, \quad (73)$$

and for a sphere of diameter 80 ft,

$$t_{01} = 156 \text{ days.} \quad (74)$$

The heating time for a large Luneberg lens may thus be several months after the transmitter is turned on, with a similar cooling time after it is turned off.

REFERENCES

1. Warren, C. A., NIKE ZEUS, Bell Laboratories Record, **41**, March, 1963, pp. 78-86.
2. Morgan, S. P., General Solution of the Luneberg Lens Problem, J. Appl. Phys., **29**, Sept., 1958, pp. 1358-1368.
3. Kellogg, O. D., *Foundations of Potential Theory*, Ungar, New York, 1929, pp. 315-316, 223.
4. Lerner, D. S., Calculation of Radiation Heating in a Microwave Luneberg Lens, I.E.E.E. Trans. on Antennas and Propagation, **AP-12**, January, 1964, pp. 16-22.

Scattering Losses in a Large Luneberg Lens Due to Random Dielectric Inhomogeneities

By SAMUEL P. MORGAN

(Manuscript received October 7, 1963)

An approximate theoretical calculation is made of the scattering losses due to random inhomogeneities in a large Luneberg lens made of dielectric blocks. A simple model is used in which the average index of refraction of each block may differ slightly from the value called for by the lens design, and the index may vary linearly with position inside a given block. The losses are described by attributing an effective scattering loss tangent to the lens medium. Tables and curves are given to facilitate the computation of total scattering loss as a function of block size, mean-square deviation of average index, and mean-square index gradient within the blocks.

Manufacturing processes for foam dielectric blocks are monitored by testing the blocks in various orientations in an oversize resonant cavity. An approximate relationship is derived between the results of cavity resonator measurements and the parameters of the theoretical model; but it is pointed out that the assumption of linear index variation across a single block can be quite unrealistic in practice. Numerical results derived from the present theory are most likely to be meaningful if the dimensions of the individual blocks are less than one wavelength.

I. INTRODUCTION

In recent years, large Luneberg lenses have been used as antennas for long-range radars.¹ Such lenses have been built of cubical blocks of very low density polystyrene foam, loaded with varying amounts of aluminum slivers² in order to approximate the desired variation of refractive index between the surface of the lens and the center. In theory each block is perfectly homogeneous and isotropic and has a specified permittivity; in practice, however, the blocks are not perfectly homogeneous or isotropic, and the average permittivity of a block generally differs more or less from the value called for by the designer. If the tolerances on the

blocks are too loose, excessive power will be lost from the lens by scattering from the "misfits"; in extreme cases, scattering may also lead to unacceptable antenna patterns. On the other hand, if the tolerances are too tight the yield of acceptable blocks by any reasonable manufacturing process will be reduced, and the cost of the lens correspondingly increased. Considerable importance attaches, therefore, to setting the proper tolerances.

This paper treats the problem of scattering losses in a large Luneberg lens, due to random dielectric inhomogeneities, on the basis of a simple mathematical model which is described in Section II. According to the present analysis, the effect of dielectric scattering can be described by attributing to the material of the lens an effective loss tangent given by (1) of Section II. The expression for the effective loss tangent is derived in Section III. Section IV discusses the relationships between the dielectric deviations whose mean-square values appear in (1) and the results of resonant cavity measurements on individual blocks, and stresses that real blocks may not be very well represented by the idealized model. Finally, a few illustrative numerical examples are worked out in Section V.

II. DESCRIPTION OF THE MODEL

We consider a "block" lens, that is, a structure built of cubical dielectric blocks which are intended to approximate an ideal, spherically symmetric Luneberg lens with a continuously varying index of refraction. The analysis is based on the following assumptions.

(i) We suppose that a nominal design for a block lens is given. We do not attempt to decide how many different index values are necessary, or how large the individual blocks can be. We merely assume that the electrical performance of the lens would be satisfactory if all blocks were perfectly uniform and homogeneous and had exactly the specified refractive indices; and we investigate how much the performance of the lens would be degraded by deviations in the dielectric properties of the blocks.

(ii) We assume that the permittivity of each block is in fact a linear function of rectangular coordinates in the block, and that the average permittivity (which in the linear model occurs at the center of the block) may differ slightly from the value assigned to the block in the nominal design.

(iii) Since the lens is many wavelengths in diameter, we assume that the power scattered out of the lens by a particular block is equal to the power which would be scattered from a plane wave by a similar block in

an infinite, uniform medium having the dielectric properties of the nominal block at that point. We further assume that the scattering pattern of a single block is so much broader than the beamwidth of the lens that all the scattered power may be considered lost.

(iv) We assume that the deviations in permittivity are completely uncorrelated from one block to the next, and that the direction of dielectric gradient is uniformly distributed over all angles. The assumption of statistical independence permits us to add the scattered power from each block directly, instead of adding complex amplitudes and then squaring, as we would have to do if the properties of a given block were correlated with those of its neighbors.

(v) We approximate the scattering from a cubical block by the scattering from a spherical "blob" of equal volume and similar dielectric properties. This is certainly as accurate as the other approximations involved in the model, and it reduces the mathematical problem essentially to one which has already been solved in the theory of tropospheric scattering.^{3,4}

Under the foregoing assumptions and approximations, it turns out that the power lost by scattering from random dielectric inhomogeneities in a medium built of cubical blocks may be represented by an effective loss tangent:

$$\tan \delta = 3 \frac{\langle (\Delta n_0)^2 \rangle}{n_0^2} \varphi_0(x) + \frac{16}{9} \frac{\langle (\Delta n_1)^2 \rangle}{n_0^2} \varphi_1(x). \quad (1)$$

The symbols on the right side of (1) are defined as follows:

n_0 : nominal refractive index of a given block;

Δn_0 : difference between average index of a given block and nominal index;

Δn_1 : difference between average indices of the "heaviest" and "lightest" halves of a linearly-varying block (the direction of index gradient need not, of course, be parallel to any edge of the block);

$x = 2\pi a n_0 / \lambda_v$, where λ_v is the vacuum wavelength;

$a = 0.620l$: radius of a sphere whose volume is equal to that of a cube of edge l ;

$\varphi_0(x), \varphi_1(x)$: functions defined by (30) and (31), tabulated in Table I, and plotted in Figs. 1 and 2;

$\langle \rangle$: average over the neighborhood of a given block.

It must be emphasized that (1) is *not* applicable to the effects of systematic deviations from the ideal Luneberg lens structure. For example, one might be tempted to apply it to calculate how large the individual blocks could be, if each block were perfectly uniform and

had the index of refraction called for by the ideal Luneberg law at its center. In that case the index of the part of each block nearest the center of the lens would be systematically too low, while the index of the farthest part would be systematically too high. This would violate the assumption of block-to-block randomness, on the basis of which we added the scattered power to obtain (1). The equation therefore cannot be used to deduce the allowable coarseness of the nominal design. It can only tell us the effects of *random* variations in a nominal design which is believed, on other grounds, to be satisfactory.

III. SCATTERING BY A "SOFT" SPHERICAL BLOB

In this section we shall compute approximately the power scattered out of an incident plane wave by a "soft" spherical blob, that is, a spherical region whose permittivity differs but little from the permittivity of the uniform surrounding medium. This kind of scattering is often called Rayleigh-Gans scattering and has an extensive literature.⁵ We shall briefly derive the specific results that we need.

Consider a blob of radius a , centered at the origin of the spherical coordinate system (r, θ, φ) . The permittivity of the blob is taken to be

$$\epsilon(\mathbf{r}) = \epsilon_0 + \epsilon_1(\mathbf{r}), \quad (2)$$

where ϵ_0 is the permittivity of the surrounding medium, and

$$|\epsilon_1(\mathbf{r})/\epsilon_0| \ll 1. \quad (3)$$

For an anisotropic blob $\epsilon_1(\mathbf{r})$ would be a tensor function, but we shall not consider this additional complication. A linearly polarized plane wave, whose electric field is given by

$$\mathbf{E}(\mathbf{r}) = \mathbf{E}_0 \exp(-i\beta \mathbf{k}' \cdot \mathbf{r}), \quad (4)$$

is incident upon the blob. Here \mathbf{E}_0 is a constant vector, \mathbf{k}' is a unit vector in the direction of propagation, and $\beta = 2\pi/\lambda_0$, where λ_0 is the wavelength of a free wave in the surrounding medium. The time dependence $e^{i\omega t}$ is understood throughout.

According to the basic Rayleigh-Gans approximation, a typical differential volume element $d\mathbf{r}'$ at \mathbf{r}' scatters as if it were immersed in a uniform medium of permittivity ϵ_0 and had an electric dipole moment

$$d\mathbf{p} = i\omega \epsilon_1(\mathbf{r}') \mathbf{E}(\mathbf{r}') d\mathbf{r}'. \quad (5)$$

We wish to describe the scattered field at the point $\mathbf{r} = k\mathbf{r}$ in the far zone, where \mathbf{k} is a unit vector in an arbitrary direction. For this purpose

we define⁶ the magnetic radiation vector \mathbf{N} . The contribution to \mathbf{N} from a typical scattering element is

$$d\mathbf{N} = \exp(i\beta\mathbf{k}\cdot\mathbf{r}') d\mathbf{p} = i\omega\epsilon_1(\mathbf{r}')\mathbf{E}_0 \exp[i\beta(\mathbf{k} - \mathbf{k}')\cdot\mathbf{r}'] d\mathbf{r}', \quad (6)$$

so the total magnetic radiation vector in a given scattering direction is

$$\mathbf{N}(\mathbf{k} - \mathbf{k}') = i\omega\mathbf{E}_0 \int_V \epsilon_1(\mathbf{r}') \exp[i\beta(\mathbf{k} - \mathbf{k}')\cdot\mathbf{r}'] d\mathbf{r}', \quad (7)$$

where the integration is taken over the whole spherical scattering volume V .

So far the dependence of the "dielectric deviation" $\epsilon_1(\mathbf{r}')$ on position has not been specified. We now introduce the assumption that $\epsilon_1(\mathbf{r}')$ is a linear function of position with a mean value which possibly differs from zero. In symbols,

$$\epsilon_1(\mathbf{r}') = \epsilon_0 \left[a_0 + \frac{a_1}{a} \mathbf{n} \cdot \mathbf{r}' \right], \quad (8)$$

where a_0 and a_1 are real numbers whose magnitudes are small compared to unity, a is the radius of the sphere, and \mathbf{n} is a unit vector in an arbitrary direction. The expression (7) then becomes

$$\mathbf{N}(\mathbf{k} - \mathbf{k}') = i\omega\epsilon_0\mathbf{E}_0 V [a_0 I_0 + a_1 I_1], \quad (9)$$

where

$$I_0 = \frac{1}{V} \int_V \exp[i\beta(\mathbf{k} - \mathbf{k}')\cdot\mathbf{r}'] d\mathbf{r}', \quad (10)$$

$$I_1 = \frac{1}{aV} \int_V \mathbf{n} \cdot \mathbf{r}' \exp[i\beta(\mathbf{k} - \mathbf{k}')\cdot\mathbf{r}'] d\mathbf{r}', \quad (11)$$

and

$$V = 4\pi a^3/3. \quad (12)$$

We are at liberty to choose any convenient coordinate system to describe the scattering problem. We take the z -axis in the direction of propagation \mathbf{k}' of the incident wave, and the x -axis parallel to \mathbf{E}_0 . The angular coordinates of the scattering direction \mathbf{k} are denoted by (θ, φ) .

In order to evaluate the integrals I_0 and I_1 , we take advantage of the spherical symmetry of the scattering volume and introduce a new set of angular coordinates (x, α) , with the new polar axis $x = 0$ along the vector $\mathbf{k} - \mathbf{k}'$. The plane $\alpha = 0$ is defined by the two vectors $\mathbf{k} - \mathbf{k}'$ and \mathbf{n} , so that the angular coordinates of \mathbf{n} in this system are $(x_0, 0)$.

Noting that $|\mathbf{k} - \mathbf{k}'| = 2 \sin \frac{1}{2}\theta$, we have by a straightforward integration,

$$\begin{aligned} I_0 &= \frac{1}{V} \int_0^{2\pi} \int_0^\pi \int_0^a \exp(2i\beta r' \sin \frac{1}{2}\theta \cos \chi) r'^2 \sin \chi dr' d\chi d\alpha \\ &= G_0(2\beta a \sin \frac{1}{2}\theta), \end{aligned} \quad (13)$$

where

$$G_0(u) = (3/u^3)[\sin u - u \cos u]. \quad (14)$$

Similarly,

$$\begin{aligned} I_1 &= \frac{1}{aV} \int_0^{2\pi} \int_0^\pi \int_0^a [\sin \chi_0 \sin \chi \cos \alpha + \cos \chi_0 \cos \chi] \\ &\quad \times \exp(2i\beta r' \sin \frac{1}{2}\theta \cos \chi) r'^3 \sin \chi dr' d\chi d\alpha \\ &= G_1(2\beta a \sin \frac{1}{2}\theta) \cos \chi_0, \end{aligned} \quad (15)$$

where

$$G_1(u) = (3/u^4)[(3 - u^2) \sin u - 3u \cos u], \quad (16)$$

and χ_0 is the angle between \mathbf{n} and $\mathbf{k} - \mathbf{k}'$.

From (9), (13), and (15), the only component of \mathbf{N} is the one parallel to the incident electric field, and it is given by

$$N_x = i\omega\epsilon_0 E_0 V [a_0 G_0(2\beta a \sin \frac{1}{2}\theta) + a_1 G_1(2\beta a \sin \frac{1}{2}\theta) \cos \chi_0]. \quad (17)$$

The scattered power per unit solid angle is⁶

$$\Phi = \frac{\eta_0}{8\lambda_0^2} |N_x|^2 [\cos^2 \theta \cos^2 \varphi + \sin^2 \varphi], \quad (18)$$

where $\eta_0 = \sqrt{\mu_0/\epsilon_0}$ is the characteristic impedance of the medium. The total scattered energy is obtained by integrating Φ over all directions in space.

Ultimately, we are going to assume that all directions \mathbf{n} of dielectric gradient are equally probable, and it will simplify the subsequent calculations to carry out the averaging over \mathbf{n} first. We obtain

$$\begin{aligned} \frac{1}{4\pi} \int_0^{2\pi} \int_0^\pi |N_x|^2 \sin \chi_0 d\chi_0 d\alpha \\ = \omega^2 \epsilon_0^2 E_0^2 V^2 [a_0^2 G_0^2(2\beta a \sin \frac{1}{2}\theta) + \frac{1}{3} a_1^2 G_1^2(2\beta a \sin \frac{1}{2}\theta)]. \end{aligned} \quad (19)$$

If $\bar{\Phi}(\theta, \varphi)$ is the result of the preliminary averaging over \mathbf{n} , the average power scattered per unit volume of the spherical blob can be written

in the form

$$\frac{1}{V} \int_0^{2\pi} \int_0^\pi \bar{\Phi} \sin \theta \, d\theta \, d\varphi = \frac{\beta E_0^2}{8\eta_0} [3a_0^2 \varphi_0(x) + a_1^2 \varphi_1(x)], \quad (20)$$

where*

$$x = \beta a = 2\pi a/\lambda_0, \quad (21)$$

and

$$\varphi_0(x) = \frac{x^3}{9} \int_0^\pi G_0^2(2x \sin \frac{1}{2}\theta) (\cos^2 \theta + 1) \sin \theta \, d\theta, \quad (22)$$

$$\varphi_1(x) = \frac{x^2}{9} \int_0^\pi G_1^2(2x \sin \frac{1}{2}\theta) (\cos^2 \theta + 1) \sin \theta \, d\theta. \quad (23)$$

On the other hand, the average scattered power per unit volume may be written in terms of the incident power density $E_0^2/2\eta_0$ and an effective attenuation constant α , or an effective loss angle δ , as

$$\frac{2\alpha E_0^2}{2\eta_0} = \frac{2\pi}{\lambda_0} \tan \delta \frac{E_0^2}{2\eta_0}. \quad (24)$$

Comparing (20) and (24), we obtain for the effective loss tangent,

$$\tan \delta = \frac{1}{4} [3a_0^2 \varphi_0(x) + a_1^2 \varphi_1(x)]. \quad (25)$$

Since the dielectric deviations described by the constants a_0 and a_1 are assumed small, and since the index of refraction of a dielectric medium is just the square root of the relative permittivity, the refractive index of the sphere described by (2) and (8) is approximately

$$n = n_0 \left[1 + \frac{a_0}{2} + \frac{a_1 \mathbf{n} \cdot \mathbf{r}}{2a} \right]. \quad (26)$$

The relative deviation of the average index of the sphere from the surrounding value n_0 is

$$\frac{\Delta n_0}{n_0} = \frac{a_0}{2}, \quad (27)$$

and the relative difference between the average indices of the "heaviest" and "lightest" halves of the sphere is

$$\frac{\Delta n_1}{n_0} = \frac{2}{2\pi a^3/3} \int_0^{2\pi} \int_0^{\frac{1}{2}\pi} \int_0^a \frac{a_1 r \cos \theta}{2a} r^2 \sin \theta \, dr \, d\theta \, d\varphi = \frac{3a_1}{8}. \quad (28)$$

* The parameter x defined by (21) has nothing to do with the coordinate x , which will never appear in the same context.

Substituting (27) and (28) into (25) and averaging over a random collection of blobs gives

$$\tan \delta = 3 \frac{\langle (\Delta n_0)^2 \rangle}{n_0^2} \varphi_0(x) + \frac{16}{9} \frac{\langle (\Delta n_1)^2 \rangle}{n_0^2} \varphi_1(x), \quad (29)$$

which is just (1) of Section II.

The functions $\varphi_0(x)$ and $\varphi_1(x)$, which were defined by (22) and (23), may be expressed either as infinite series or in closed form; thus,

$$\begin{aligned} \varphi_0(x) &= \sum_{n=2}^{\infty} \frac{(-)^n (4x)^{2n-1} (n^2 - n + 2)}{2n(n+1)^2(2n)!} \\ &= \frac{5}{8x} + \frac{x}{2} - \frac{\sin 4x}{16x^2} - \frac{7}{64x^3} (1 - \cos 4x) \\ &\quad + \left(\frac{1}{8x^3} - \frac{1}{2x} \right) \text{Cin } 4x, \end{aligned} \quad (30)$$

$$\begin{aligned} \varphi_1(x) &= \sum_{n=3}^{\infty} \frac{(-)^{n-1} (4x)^{2n-1} (n^2 - n + 2)}{2n(n+1)^2(2n)!} \left(\frac{n-2}{n+2} \right) \\ &= -\frac{3}{32x^5} - \frac{37}{64x^3} + \frac{7}{8x} + \frac{x}{6} + \left(\frac{3}{8x^3} - \frac{1}{2x} \right) \text{Cin } 4x \\ &\quad + \left(\frac{3}{32x^5} - \frac{11}{64x^3} \right) \cos 4x + \left(\frac{3}{8x^4} - \frac{3}{16x^2} \right) \sin 4x, \end{aligned} \quad (31)$$

where

$$\text{Cin } x = \int_0^x \frac{1 - \cos t}{t} dt. \quad (32)$$

The functions $\varphi_0(x)$ and $\varphi_1(x)$ are tabulated in Table I and plotted in Figs. 1 and 2 (note the difference in scale of the two figures).

IV. RESONANT CAVITY TECHNIQUES FOR TESTING DIELECTRIC BLOCKS

In practice, the dielectric blocks are tested in an oversize resonant cavity⁷ before being assembled into the lens. A typical cavity is shown in Fig. 3; the cavity dimensions are $l \times 2l \times 3l$, and a cubical block of edge l is placed with one face against the center of one of the long sides of the cavity. If the block were perfectly uniform and isotropic, a single measurement of resonant frequency would suffice to determine its permittivity, with the aid of an experimental or theoretical calibration curve which could be derived once for all. The dissipation, which we are neglecting in the present paper, could be deduced from the change in Q

of the loaded cavity. Actually the frequency shift when a cubical block is placed in the cavity depends on the orientation of the block. Twelve orientations altogether are possible for a block in the location shown in Fig. 3, and from the measured frequency shifts one attempts to deduce something about the nonuniformity and/or anisotropy of the given block.

Ideally one would like to have a simple correlation between the results of cavity resonator measurements and the total power scattered by a given block in the lens. In a real block, however, the permittivity is a (possibly tensorial) function of position, having in principle an infinite number of degrees of freedom. A single measurement of frequency shift yields a weighted average of the dielectric deviations, according to (33) below. On the other hand, the total power scattered by the block in the lens is a different and nonlinear functional of the dielectric deviations, given by (7) and (18) of Section III. In the general case it is obviously impossible to write the scattered power as a function of the results of any finite number of resonant cavity measurements.

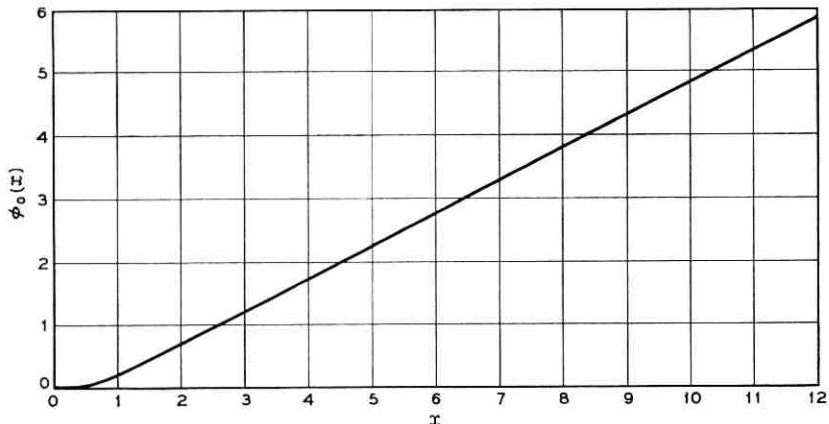
In order to make any sort of connection between cavity resonator experiments and the performance of blocks in the lens, one has to adopt some model of the dielectric deviations in the blocks, describe the model in terms of a small number of parameters, express the parameters in terms of the results of cavity measurements, and finally calculate the scattered power as a function of the parameters. The parameters which have been used in the present work are the quantities Δn_0 and Δn_1 defined in Section II. It is assumed that each block is isotropic but nonuniform, with a small constant gradient of the refractive index (or the permittivity) in an arbitrary direction. We now consider how the parameters of such a block might be deduced from cavity resonator measurements.

The average index of the block is taken as the mean of the twelve measurements corresponding to the different orientations of the block in the oversize cavity; Δn_0 is the difference between the average index and the index called for by the lens design. The theoretical dependence of resonant frequency on the permittivity of a uniform block in the cavity can be computed numerically using the Rayleigh-Ritz variational procedure.

The difference Δn_1 between the average indices of the "heaviest" and "lightest" halves of the block cannot be determined quite so directly, since the direction of dielectric gradient is not necessarily parallel to any edge of the cube. An experimentally measurable quantity, however, is the "half-block spread" H , i.e., the difference between the maximum

TABLE I—THE SCATTERING FUNCTIONS $\varphi_0(x)$ AND $\varphi_1(x)$

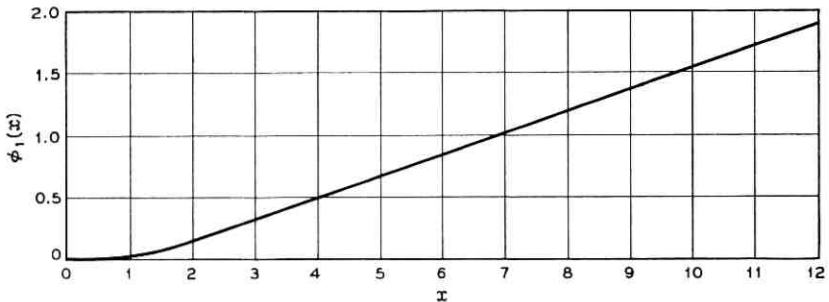
x	$\varphi_0(x)$	$\varphi_1(x)$	x	$\varphi_0(x)$	$\varphi_1(x)$
0.0	0.	0.			
0.1	0.00029512	0.00000024	6.1	2.8440	0.85496
0.2	0.0023328	0.00000746	6.2	2.8966	0.87218
0.3	0.0077182	0.00000556	6.3	2.9492	0.88947
0.4	0.017795	0.00022784	6.4	3.0016	0.90692
0.5	0.033547	0.00067025	6.5	3.0538	0.92456
0.6	0.055537	0.0015960	6.6	3.1057	0.94243
0.7	0.083883	0.0032751	6.7	3.1574	0.96048
0.8	0.11828	0.0060134	6.8	3.2088	0.97869
0.9	0.15805	0.010125	6.9	3.2601	0.99697
1.0	0.20225	0.015896	7.0	3.3113	1.0153
1.1	0.24975	0.023547	7.1	3.3624	1.0335
1.2	0.29940	0.033205	7.2	3.4136	1.0515
1.3	0.35009	0.044880	7.3	3.4649	1.0694
1.4	0.40087	0.058451	7.4	3.5164	1.0871
1.5	0.45105	0.073672	7.5	3.5680	1.1045
1.6	0.50021	0.090192	7.6	3.6197	1.1219
1.7	0.54820	0.10758	7.7	3.6715	1.1391
1.8	0.59515	0.12537	7.8	3.7234	1.1564
1.9	0.64140	0.14311	7.9	3.7752	1.1737
2.0	0.68742	0.16039	8.0	3.8269	1.1910
2.1	0.73375	0.17689	8.1	3.8784	1.2085
2.2	0.78091	0.19243	8.2	3.9298	1.2261
2.3	0.82932	0.20695	8.3	3.9811	1.2439
2.4	0.87929	0.22054	8.4	4.0322	1.2617
2.5	0.93092	0.23338	8.5	4.0831	1.2796
2.6	0.98416	0.24580	8.6	4.1341	1.2975
2.7	1.0388	0.25812	8.7	4.1850	1.3154
2.8	1.0944	0.27073	8.8	4.2359	1.3331
2.9	1.1507	0.28396	8.9	4.2870	1.3507
3.0	1.2072	0.29809	9.0	4.3381	1.3682
3.1	1.2634	0.31328	9.1	4.3893	1.3855
3.2	1.3190	0.32961	9.2	4.4406	1.4028
3.3	1.3739	0.34702	9.3	4.4920	1.4200
3.4	1.4278	0.36537	9.4	4.5434	1.4371
3.5	1.4809	0.38443	9.5	4.5947	1.4544
3.6	1.5333	0.40393	9.6	4.6460	1.4716
3.7	1.5851	0.42357	9.7	4.6972	1.4890
3.8	1.6367	0.44308	9.8	4.7482	1.5064
3.9	1.6883	0.46225	9.9	4.7992	1.5240
4.0	1.7401	0.48094	10.0	4.8500	1.5416
4.1	1.7923	0.49907	10.1	4.9008	1.5592
4.2	1.8450	0.51667	10.2	4.9515	1.5768
4.3	1.8981	0.53382	10.3	5.0023	1.5944
4.4	1.9517	0.55069	10.4	5.0530	1.6119
4.5	2.0055	0.56743	10.5	5.1039	1.6293
4.6	2.0594	0.58424	10.6	5.1548	1.6466
4.7	2.1133	0.60127	10.7	5.2058	1.6639
4.8	2.1669	0.61864	10.8	5.2568	1.6810
4.9	2.2201	0.63640	10.9	5.3079	1.6982
5.0	2.2729	0.65456	11.0	5.3590	1.7153
5.1	2.3252	0.67307	11.1	5.4100	1.7324
5.2	2.3772	0.69182	11.2	5.4610	1.7496
5.3	2.4288	0.71070	11.3	5.5119	1.7668
5.4	2.4803	0.72955	11.4	5.5627	1.7842
5.5	2.5318	0.74827	11.5	5.6135	1.8015
5.6	2.5833	0.76674	11.6	5.6641	1.8190
5.7	2.6350	0.78491	11.7	5.7148	1.8364
5.8	2.6869	0.80278	11.8	5.7654	1.8539
5.9	2.7391	0.82036	11.9	5.8160	1.8713
6.0	2.7915	0.83772	12.0	5.8666	1.8886

Fig. 1 — The scattering function $\varphi_0(x)$.

and minimum of the twelve measurements of apparent index for each block, taken in all possible orientations. Intuitively one feels that the half-block spread of a linearly-varying block must be approximately proportional to Δn_1 . To get an estimate of the proportionality factor we proceed as follows.

First let the cavity contain a uniform, isotropic block of permittivity ϵ_0 . Let the corresponding resonant frequency be f_0 and let the electric field be $\mathbf{E}_0(x,y)$, perpendicular to the broad faces of the cavity. If the relative permittivity is nearly unity, then \mathbf{E}_0 is nearly the field of the lowest mode in the empty cavity. Coefficients of the expansion of \mathbf{E}_0 in terms of the modes of the empty cavity can be obtained numerically, if desired, for any given permittivity by the Rayleigh-Ritz method.

In any case, if the permittivity of the block is now taken to be $\epsilon_0 + \epsilon_1$,

Fig. 2 — The scattering function $\varphi_1(x)$.

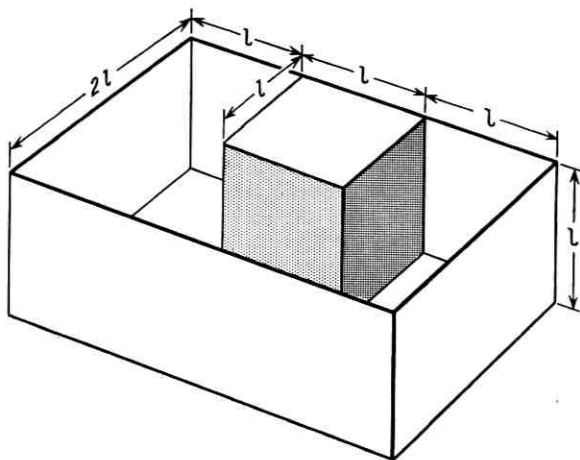


Fig. 3 — Oversize resonant cavity for testing dielectric blocks.

where ϵ_1 is an arbitrary small dielectric deviation, it is well known⁸ that the shift in resonant frequency is given approximately by

$$\frac{\Delta f}{f_0} = -\frac{\int \epsilon_1 E_0^2 dV}{2 \int \epsilon E_0^2 dV}. \quad (33)$$

The upper integral in (33) is taken over the volume of the block, since ϵ_1 vanishes elsewhere. The lower integral is taken over the volume of the whole cavity, with $\epsilon = \epsilon_0$ in the block and $\epsilon = \epsilon_v$ (free space) elsewhere. Equation (33) could be generalized to apply to anisotropic media if desired.

Let us define the effective index deviation Δn_e to be equal to the uniform deviation which would give the same shift from the frequency associated with the nominal block. From (33),

$$\Delta n_e = \frac{\int \Delta n E_0^2 dV}{\int E_0^2 dV}, \quad (34)$$

where Δn is the pointwise deviation from the nominal value and both integrals are taken over the volume of the block. We shall consider two cases: (a) a linearly varying block with the index gradient parallel to one edge, and (b) a linearly varying block with the index gradient

parallel to a body diagonal. In the present calculation we shall take \mathbf{E}_0 to be the field of the lowest mode of the empty cavity; the extra labor involved in using a more accurate field would not be justified, because of the crudeness of the approximations which have already been made in treating the scattering problem. If the origin is taken at the center of the cavity, so that the block fills the space $0 \leq x \leq l$, $|y| \leq \frac{1}{2}l$, $|z| \leq \frac{1}{2}l$, then the electric field is in the z -direction and is proportional to

$$E_0 = \cos \frac{\pi x}{2l} \cos \frac{\pi y}{3l}. \quad (35)$$

If the index gradient is in the x -direction and Δn_1 is the difference between the average indices of the heaviest and lightest halves of the block, then

$$\Delta n = \frac{\Delta n_1}{\frac{1}{2}l} (\frac{1}{2}l - x). \quad (36)$$

The maximum effective index deviation is

$$\Delta n_e = \frac{\frac{\Delta n_1}{\frac{1}{2}l} \int_0^l (\frac{1}{2}l - x) \cos^2 \frac{\pi x}{2l} dx}{\int_0^l \cos^2 \frac{\pi x}{2l} dx} = \frac{4\Delta n_1}{\pi^2}, \quad (37)$$

corresponding to a half-block spread of

$$H = \frac{8\Delta n_1}{\pi^2} = 0.811\Delta n_1. \quad (38)$$

When the index gradient is parallel to a body diagonal of the block, the calculation is a little more complicated. We shift the origin to the center of the block, so that the block occupies the space $|x'| \leq \frac{1}{2}l$, $|y'| \leq \frac{1}{2}l$, $|z'| \leq \frac{1}{2}l$, and write the electric field as

$$E_0 = \cos \frac{\pi(x' + \frac{1}{2}l)}{2l} \cos \frac{\pi y'}{3l}. \quad (39)$$

Let the index deviation be

$$\Delta n = -cs = -\frac{c(x' + y' + z')}{\sqrt{3}}, \quad (40)$$

where c is a constant and

$$\frac{x' + y' + z'}{\sqrt{3}} = s \quad (41)$$

is the equation of a plane normal to the diagonal $x' = y' = z'$ and at a distance s from the origin. The area of the part of the plane which lies inside the cubical block can be shown by a little geometry to be

$$A(s) = \begin{cases} 3\sqrt{3}(\frac{1}{4}l^2 - s^2), & 0 \leq s \leq \frac{1}{2}l/\sqrt{3}, \\ \frac{3\sqrt{3}}{2}(\frac{1}{2}\sqrt{3}l - s)^2, & \frac{1}{2}l/\sqrt{3} \leq s \leq \frac{1}{2}\sqrt{3}l. \end{cases} \quad (42)$$

The difference between the average index of the heaviest and lightest halves of the block is

$$\Delta n_1 = \frac{4}{l^3} \int_0^{\frac{1}{2}\sqrt{3}l} csA(s)ds = \frac{13\sqrt{3}cl}{48}. \quad (43)$$

From (34), the effective index deviation is

$$\begin{aligned} \Delta n_e &= - \frac{\int_{-\frac{1}{2}l}^{\frac{1}{2}l} \int_{-\frac{1}{2}l}^{\frac{1}{2}l} \int_{-\frac{1}{2}l}^{\frac{1}{2}l} \frac{c(x' + y' + z')}{\sqrt{3}} \cos^2 \frac{\pi(x' + \frac{1}{2}l)}{2l} \cos^2 \frac{\pi y'}{3l} dx' dy' dz'}{\int_{-\frac{1}{2}l}^{\frac{1}{2}l} \int_{-\frac{1}{2}l}^{\frac{1}{2}l} \int_{-\frac{1}{2}l}^{\frac{1}{2}l} \cos^2 \frac{\pi(x' + \frac{1}{2}l)}{2l} \cos^2 \frac{\pi y'}{3l} dx' dy' dz'} \quad (44) \\ &= \frac{2cl}{\pi^2 \sqrt{3}} = \frac{32\Delta n_1}{13\pi^2}, \end{aligned}$$

where we have used (43) to express cl in terms of Δn_1 . It follows that the half-block spread is

$$H = \frac{64\Delta n_1}{13\pi^2} = 0.499\Delta n_1. \quad (45)$$

It is reasonable to expect that, whatever the orientation of index gradient in a linearly varying block, the proportionality constant relating Δn_1 to H will lie between the values given by (38) and (45). When in the present approximate treatment it is necessary to express Δn_1 in terms of H , we shall take an intermediate value of the coefficient and set

$$H \approx 0.625\Delta n_1, \quad \Delta n_1 \approx 1.6H. \quad (46)$$

In view of the universal temptation to substitute numbers into any formula which appears to be written in terms of measured quantities, it must be emphasized that the linearly varying block model used in the foregoing analysis is *known to be incorrect*, at least for sufficiently large blocks produced by current manufacturing techniques. Experiments in which 2-foot cubes of loaded polystyrene foam were sawed up into smaller cubes and individually measured have shown the presence of

marked short-range fluctuations in permittivity which contribute very little to the half-block spread. If the properties of a typical block do not vary linearly but in a more complicated way with position inside the block, it is difficult to know what, if any, significance to attach to the "effective scattering loss tangent" given by (29).

V. NUMERICAL EXAMPLES

We shall use the present theory to compute some numerical examples of scattering loss in Luneberg lenses, in order to get an idea of the size of the numbers involved, even though we have just observed that the linearly varying block may in many cases be an unrealistic model.

If we assume that the probability distribution of Δn_0 is uniform between $-(\Delta n_0)_{\max}$ and $(\Delta n_0)_{\max}$, and that H is uniformly distributed between 0 and H_{\max} , then expressing Δn_1 approximately in terms of H by (46), we find that (29) becomes

$$\tan \delta = \frac{(\Delta n_0)_{\max}^2}{n_0^2} \varphi_0(x) + 1.5 \frac{H_{\max}^2}{n_0^2} \varphi_1(x), \quad (47)$$

where

$$x = 2\pi a n_0 / \lambda_v, \quad (48)$$

$$a = 0.620l, \quad (49)$$

and λ_v is the vacuum wavelength.

In a companion paper,⁹ numerical formulas have been given for the attenuation of electromagnetic energy by a uniformly illuminated Luneberg lens in which the loss tangent of the lens material is any linear function of the refractive index. In the reference cited, the loss tangent was supposed to be due to dissipation, but it can equally well be due to scattering so far as the effective power loss is concerned. It is assumed that the loss tangent can be written in the form

$$\tan \delta = An + B, \quad (50)$$

where A and B are constants determined by passing a line through the values of $\tan \delta$ corresponding to the surface and the center of the lens, or by a least-squares fit to more than two points if desired. Then, for example, the fractional power loss in a lens of radius R , whose focal point is at a distance $0.1R$ outside the surface, is given by

$$\frac{\Delta P}{P_0} = \frac{R}{\lambda_v} [15.46A + 13.13B]. \quad (51)$$

In the following examples we shall assume that $(\Delta n_0)_{\max}$ and H_{\max} are constant throughout the lens. For any given ratio of block size to wavelength, it is simple to calculate $\tan \delta$ at the surface of the lens ($n = 1$) and at the center ($n = 1.36$) from (47), and then to determine the values of A and B in (50). Finally the fractional power loss may be written in the form

$$\frac{\Delta P}{P_0} = \frac{R}{\lambda_v} [F_0(\Delta n_0)_{\max}^2 + F_1 H_{\max}^2]. \quad (52)$$

The dimensionless coefficients F_0 and F_1 are given as functions of l/λ_v in Table II, and are plotted in Fig. 4.

As a first example, consider a lens 40 wavelengths in diameter, made of one-wavelength dielectric cubes. If we take

$$R/\lambda_v = 20,$$

$$l/\lambda_v = 1,$$

$$(\Delta n_0)_{\max} = 0.005,$$

$$H_{\max} = 0.020,$$

then (52) and Table II yield

$$\Delta P/P_0 = 0.077 \quad \text{or} \quad 0.35 \text{ db loss.} \quad (54)$$

The loss would be the same if the frequency were doubled and the block size halved, while the lens diameter and the values of $(\Delta n_0)_{\max}$ and H_{\max} were held constant.

TABLE II—THE FUNCTIONS F_0 AND F_1

l/λ_v	F_0	F_1	l/λ_v	F_0	F_1
0.0	0.	0.			
0.1	0.248	0.007	1.1	22.05	9.553
0.2	1.544	0.160	1.2	24.42	10.69
0.3	3.625	0.765	1.3	26.76	11.89
0.4	5.798	1.777	1.4	29.05	13.12
0.5	7.960	2.837	1.5	31.36	14.31
0.6	10.23	3.833	1.6	33.67	15.47
0.7	12.59	4.848	1.7	35.97	16.65
0.8	15.01	5.906	1.8	38.25	17.84
0.9	17.42	7.075	1.9	40.53	19.02
1.0	19.73	8.344	2.0	42.82	20.19

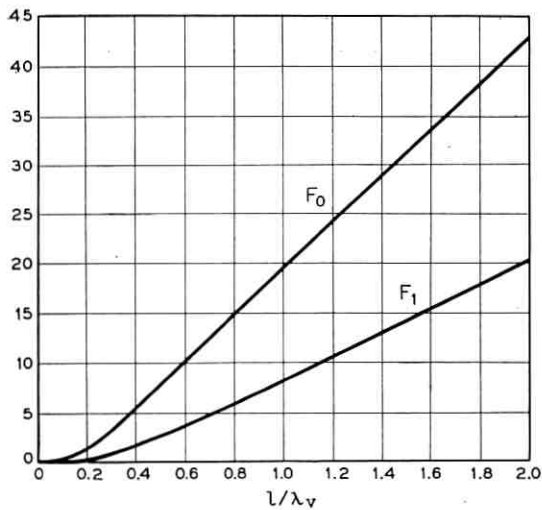


Fig. 4 — The functions F_0 and F_1 .

As a second example, consider a lens with

$$\begin{aligned} R/\lambda_v &= 40, \\ l/\lambda_v &= 2, \\ (\Delta n_0)_{\max} &= 0.005, \\ H_{\max} &= 0.020. \end{aligned} \tag{55}$$

The loss computed from (52) and Table II is

$$\Delta P/P_0 = 0.37 \quad \text{or} \quad 2.0 \text{ db loss.} \tag{56}$$

This would correspond to the lens treated in the first example if it were used at double the frequency with no alterations in physical structure. Of course it is hardly legitimate to apply (52), which was derived on the assumption that the scattering loss is a small perturbation, to predict a loss of 2 db. We can conclude from (52), however, that to reduce the scattering loss in the second lens to 0.35 db, it would be necessary to hold H_{\max} down to 0.0065 if $(\Delta n_0)_{\max}$ were still equal to 0.005.

Finally we note that the examples just given refer to blocks whose dimensions are comparable to or greater than a wavelength, and for which the assumption of linear index variation is very likely to be invalid. If the formulas were applied to blocks of fractional wavelength

size, as can easily be done using Table I or Table II, the half-block spread might be a more significant parameter, since very short-range fluctuations scatter so little energy, and the computed results might be more meaningful. The working out of additional numerical examples, however, is left to the reader.

VI. ACKNOWLEDGMENTS

I am indebted to W. A. Yager for numerous discussions of the problems of losses in foam Luneberg lenses. Miss M. C. Gray derived the expressions (30) and (31) for $\varphi_0(x)$ and $\varphi_1(x)$, and Miss P. A. Hamilton computed the tables.

REFERENCES

1. Warren, C. A., NIKE ZEUS, Bell Laboratories Record, **41**, March, 1963, pp. 78-86.
2. Yager, W. A., Edelson, D., and McMahon, W., The Theory of Loaded Foam Dielectrics, 1960 Annual Report, Conf. on Elec. Insulation, National Research Council Publ. 842, pp. 181-185.
3. Booker, H. G., and Gordon, W. E., A Theory of Radio Scattering in the Troposphere, Proc. I.R.E., **38**, April, 1950, pp. 401-412.
4. Staras, H., Scattering of Electromagnetic Energy in a Randomly Inhomogeneous Atmosphere, J. Appl. Phys., **23**, Oct., 1952, pp. 1152-1156.
5. Van de Hulst, H. C., *Light Scattering by Small Particles*, John Wiley and Sons, New York, 1957, Chap. 7.
6. Schelkunoff, S. A., *Electromagnetic Waves*, D. Van Nostrand Co., New York, 1943, pp. 331-333.
7. Edelson, D., Yager, W. A., and McMahon, W., Some Novel Resonant Cavity Techniques for the Evaluation of Artificial Dielectrics, 1960 Annual Report, National Academy of Sciences, National Research Council Publ. 842, pp. 31-34.
8. Berk, A. D., Variational Principles for Electromagnetic Resonators and Waveguides, Trans. I.R.E., AP-4, April, 1956, pp. 104-111; Eq. (24).
9. Morgan, S. P., Microwave Heating of a Luneberg Lens, B.S.T.J., this issue, pp. 659-678.

The 1962 Survey of Noise and Loss on Toll Connections

By INGEMAR NÅSELL

(Manuscript received October 14, 1963)

The 1962 sample survey of message circuit noise and loss on Bell System toll connections is described and discussed in this article. The results are presented in terms of the distribution of noise levels on toll calls as established in the present system, the distribution of end-office to end-office losses on these calls, and the distribution of airline distances between end-offices. It is shown that the noise distribution referred to the subscriber's set has a mean of 19.7 dbrnc with a standard deviation of 7.8 db, that the mean of the distribution of end-office to end-office losses is 7.7 db with a standard deviation of 3.0 db, and that 50 per cent of all toll calls are shorter than 30 miles, while only 10 per cent span a distance of more than 250 miles. The noise level versus distance and loss versus distance relationships are investigated and analyzed. The noise level is found to increase by 2.2 db for each doubling of the airline distance between end-offices, while the loss shows an increase of 0.6 db for each doubling of the distance. Finally, present performance of the Bell System toll plant is evaluated in terms of noise and volume grade-of-service estimates.

I. INTRODUCTION

Most transmission engineering studies require some knowledge about the noise and loss performance of the telephone plant. When transmission objectives are being reviewed and new ones are to be set, such knowledge is of particular importance. Because of the significance of decisions in this area, it is necessary that the data used be representative and give an accurate systemwide picture of the performance. Recognizing these needs in the current work of setting new message circuit noise objectives, a nationwide sample survey of noise and loss on toll connections in the Bell System toll network has been undertaken. It is the purpose of this article to describe the survey and discuss its results. The application of the findings of the survey to the setting of new over-

all message circuit noise objectives is treated in an accompanying article.¹

II. DEFINITION OF POPULATION

As in any sample survey, it is important that a precise definition be given of the population, in order that the extent and limitation of the survey results be known.

The population was defined to consist of all toll calls made during the busy hour of an ordinary business day and originating from Bell System central office buildings within Continental U.S.A. However, only those central office buildings were included that were in service at the beginning of 1960, while all Bell System and independent company central offices in Continental U.S.A. were included as terminating points for the toll calls. The busy hour was defined as the "official" busy hour of the toll office on which the originating central office homes. It was not considered practical to study the variation with time of the noise distribution on toll calls, and therefore the arbitrariness introduced by not specifying one or more particular "ordinary business days" was accepted.

All calls terminating within Continental U.S.A. were considered to be toll calls if they satisfied the following two criteria: (i) the customer was detail billed for the call; i.e. an operator ticket was issued or the call was recorded by automatic message accounting (AMA) equipment, and (ii) the originating and terminating central offices did not home on the same toll office. The latter criterion was introduced because, in areas with extended area service (EAS), the customers are in general not detail billed for those short-haul calls where originating and terminating central offices home on the same toll office. However, in areas where EAS has not been introduced, the opposite is in general true. This accounts for large deviations in the apparent toll calling patterns between central offices. Since these deviations are only artificial, and since they contribute toward a decrease in sampling precision, criterion (ii) above was introduced in order to make such deviations less pronounced.

III. SAMPLING PLAN AND SAMPLE SIZE

The sample was selected in two stages in the following way:^{*}

From a listing of the 7878 Bell System central office buildings in

* Detailed discussions of the sampling plan used and of methods for determining the sample size and selecting the sample are found in standard works on the subject of sample surveys. See Refs. 2 and 3.

service at the beginning of 1960, 17 were selected at random. The probability of selecting any one office was made proportional to an estimate of size, where the size of the office is defined as the number of outgoing toll calls in the busy hour of an ordinary business day. The number of lines per office served as an estimate of this size, and the assumption was made that these two numbers were approximately proportional. Randomness in the selection was assured by the use of tables of random numbers. After these offices had been chosen, information was acquired from each of them about its outgoing toll traffic. This information had the form of lists of all outgoing detail billed toll calls during the busy hour of one ordinary business day. It was, however, estimated that in some offices the total outgoing toll traffic would be less than the sample size. For these cases the lists contained the outgoing toll traffic during the busy hour of several consecutive business days. The data for the lists were obtained from operator toll tickets and AMA printouts. The main information given for each call was the terminating central office. By the use of information in the Long Lines Dept. dial routing pamphlet, it was then possible to exclude from these lists all calls that terminated in a central office that homed on the same toll office as the originating central office. Furthermore, information in the Long Lines Dept. distance dialing reference guide was used to exclude all calls that did not terminate inside Continental U.S.A.

To test the whole procedure for the survey, a pilot survey was performed at Dover, N. J., in the spring of 1962. Among other results, this survey showed the ratio of the number of long-haul calls to the number of short-haul calls to be quite low. However, in order for us to be able to perform an analysis of noise level versus distance, it was necessary that the sample contain a reasonably large number of both short-haul and long-haul calls. In view of this, the findings at Dover indicated that the sample size would have to be made very large in order for the sample to contain a reasonably large number of long-haul calls, and this would imply making an unnecessarily large number of measurements on short-haul calls. To solve this problem, it was decided to perform two separate surveys, one on toll calls terminating inside the originating numbering plan area (NPA), and the other on calls terminating outside the originating NPA. These two surveys will be referred to as subsurveys of the connection survey.

All entries on the lists of outgoing toll calls were therefore referred to one of the two categories defined above. After this had been done, the total number of calls to be included in the sample for each subsurvey and each central office was determined. Finally, this number of calls was selected from the corresponding list by the use of random number tables.

In this selection, all entries on a list had the same probability of being included in the sample.

Table I lists the 17 central offices included in the sample as well as the corresponding number of inside-NPA and outside-NPA calls. The table shows that the sample contained a total of 514 inside-NPA calls and 727 outside-NPA calls. For each of the 17 central offices, the sample size was determined in such a fashion that the resulting sample is self-weighting. This means that all measurements taken carry equal weight, and it leads to convenient and straightforward methods of data analysis.

The sample sizes were determined from estimates of variability of noise level readings within and between central offices, combined with the precision criterion that the mean of the noise distribution be stated within ± 1 db at the 90 per cent confidence level.

IV. METHOD OF MEASUREMENT

The measurement phase of the survey consisted of setting up the toll connections selected in the sample and measuring the noise and loss at the originating end; see Fig 1. The connections were set up so as to duplicate as closely as possible the conditions prevailing at the time the original call was made. All of the original calls were made during the busy hour of an ordinary business day. The probabilities of alternate

TABLE I — CONNECTION SURVEY SAMPLE SIZES

Central Office Location	Sample Size	
	Inside NPA	Outside NPA
Boston, Mass.	72	126
Brooksville, Fla.	24	88
Cheshire, Conn.	33	20
Dallas, Tex.	2	23
Detroit, Mich.	9	28
El Paso, Tex.	0	8
Fairfield, Conn.	40	50
Fort Lauderdale, Fla.	21	13
Hyattsville, Md.	3	8
Keyport, N. J.	100	22
Kingston, Pa.	17	23
Knoxville, Tenn.	11	21
Niagara Falls, N. Y.	77	30
Queens, N. Y.	0	137
Richmond, Va.	11	15
Riverside, N. J.	61	96
Selma, Cal.	33	19
Total sample size:	514	727



Fig. 1 — Connection survey measurements in a Boston central office.

routing and of high loading of the transmission facilities are then high. To keep these probabilities at the same levels, all measurements were performed during the busy period of ordinary business days.

The conditions at the time the original call was set up differed from those during our measurements in one respect: all measurements were made from the originating central office and they all terminated in the distant central office; in other words, the loops were excluded from consideration. This was done deliberately in order to isolate the transmission characteristics of the toll plant from those of the loop plant. In addition, any other procedure would have been very impractical and time-consuming, since it would involve subscribers at least at one end of the connection. In considering a toll connection from subscriber to subscriber, the influence of the loop plant must be taken into account; its performance is reported on in the accompanying article.¹

For each sample call two measurements were made. In the first one, the near-end noise level was recorded on a toll connection terminated in the distant central office. The distant termination was made either in the quiet or balanced termination of the central office, or in the "hold" circuit of a telephone set in that office, or by a telephone set itself — in the latter case with the transmitter covered so that room noise was ex-

cluded from the connection. The use of the quiet termination of the distant office was avoided in all cases where "on-hook" supervision of that termination was known or could be suspected, since this condition results in the in-band signal on some types of carrier being left on. Such a tone would tend to give an erroneously high noise reading on the connection. As can be seen by this example, care was exercised to ensure that all noise measurements gave the noise level that would occur in the silent intervals between speech on actual telephone connections.* Termination in a telephone set, with the transmitter covered, was used only in those cases where no telephone set with "off-hook" supervision in the distant central office was equipped with a "hold" feature. In these cases, monitoring at the receiving end ensured that room noise was effectively kept out of the connection.

The second measurement for each call in the sample was made to record the end-office to end-office loss. For practical reasons a standard-level tone could not be supplied from the far end on the noise measurement calls. Therefore a new connection was established, terminating in the 1000-cycle milliwatt supply of the distant office. In this way, it is entirely possible that the two calls were routed differently. No effort was made to find out what route was used in any particular case. Therefore the route length of the connections is not known. However, distance is an important parameter. The airline distance between the end-offices was therefore associated with each measured connection.

Both types of connections mentioned above were established from an ordinary telephone set connected to a "zero" loop in the originating central office. This set was located in the same building as the central office equipment.

After a particular connection had been established, the set was switched out of the circuit and replaced by a 900-ohm resistor across which a 3A noise measuring set⁴ was connected in the bridging position. The time average during 10-30 seconds of the level indicated by the 3A set was taken as the noise level reading of the circuit. The noise measuring set was always used with C-message weighting, and hence the measured levels are expressed in dbrnc. Since the C-message weighting introduces no loss at 1000 cycles, it was used also in the measurement of end-office to end-office loss.

Routing of outgoing toll calls could in general be expected to be different for operator-handled versus direct-dialed (DDD) calls. This

* When compandors are present in a connection, the noise level during speech is higher than in the silent intervals. The subjective rating of the noise is therefore poorer than that based on the measured noise level. This compandor effect will be ignored.

fact was taken into account in the natural way; connections were set up by operators or direct dialed depending on whether the original calls were operator-handled or AMA-recorded.

All of the terminating central offices were not equipped with milliwatt supplies or balanced terminations, nor were all of them attended. This meant that some measurements could not be made with distant terminations as given by the calls in the sample. The method used to treat these cases was to make measurements on a toll connection terminated in a central office geographically close to the desired one. The errors introduced by this procedure were judged to be negligibly small for long-haul calls and small enough to be disregarded even for short-haul calls. For calls terminating inside originating NPA, 1.9 per cent of the noise measurements and 8.8 per cent of the loss measurements had to be made with a substituted terminating central office. For outside-NPA calls, the corresponding figures are 1.1 per cent and 3.9 per cent.

V. CONNECTION SURVEY RESULTS

All data were punched on IBM cards, and most of the analysis reported here was made on the IBM 7090 digital computer at the Murray Hill, N. J., location of Bell Telephone Laboratories. One card was punched for each call in the sample; each card gives the originating and terminating central offices of the corresponding toll connection, the measured noise level, the measured end-office to end-office loss, and the airline distance between the central offices. The latter were computed by the use of geographical coordinates given in the Long Lines Dept. distance dialing reference guide.

In the discussion to follow, a set of measurements called the "pooled" data will be referred to several times. In particular, it will be used whenever the performance of all toll calls is discussed. This set of data consists of 998 toll calls, of which 514 are inside-NPA and 484 outside-NPA calls. In this way, all inside-NPA calls and part of the 727 outside-NPA calls are included; the percentage of outside-NPA calls included was chosen to make the pooled data representative of all toll calls. This percentage reflects the fact that 52 per cent of all toll calls terminate inside and 48 per cent outside the originating NPA.

5.1 Noise

Evaluation of grade of service¹ cannot be made directly from the survey noise distributions. The reason is that subscribers' reactions are given in terms of opinion curves for noise measured across their subset,

while all measurements in the survey were made at the end of a "zero" loop. The conversion from this point of measurement to the subscriber set is, however, quite simple. The equalizing properties of the 500 set imply that the combined response of loop and receiver is essentially constant for loop lengths up to 15,000 feet. A recent survey of loop characteristics has shown this to account for about 83 per cent of all Bell System loops.⁵ For these loops, then, an increased loop loss is compensated for by a higher sensitivity of the receiver. For the opinion curves to be applicable, the connection noise should therefore be transformed to the end of a loop equipped with a subset having the same sensitivity as the subsets used in the subjective tests that established the opinion curves. The sensitivity is determined by the dc current, which was 55 ma in the above-mentioned tests. A regression analysis of loop loss vs dc current, using data from recent loop surveys,¹ showed the average loss of a 55-ma loop terminated in a 500 set to be 5 db. Therefore the conversion to the subset is made by subtracting 5 db from the noise levels measured in the connection survey, and after this

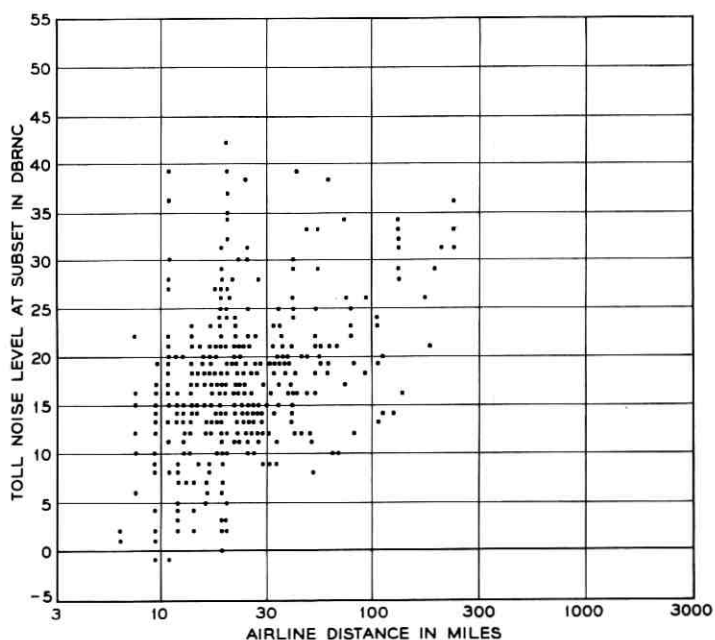


Fig. 2—Scatter diagram of noise level vs distance: toll calls terminating inside NPA.

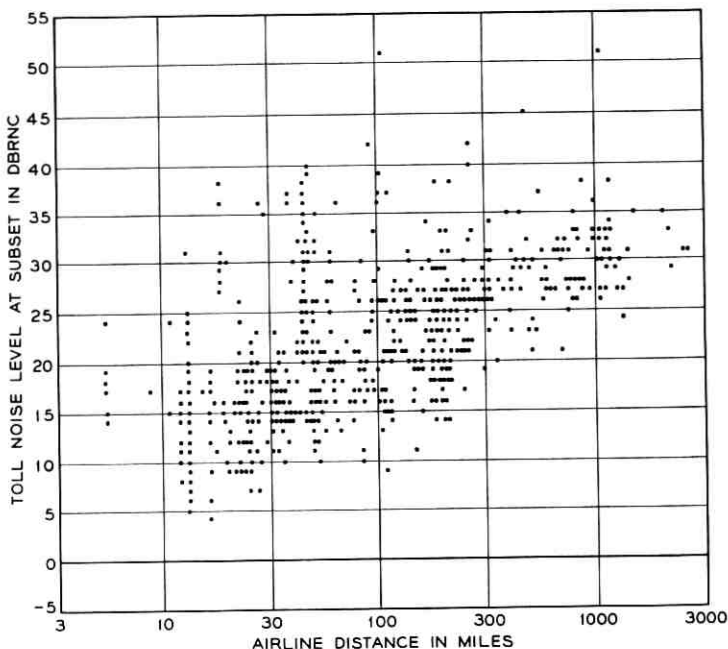


Fig. 3 — Scatter diagram of noise level vs distance: toll calls terminating outside NPA.

conversion the opinion curves can be applied directly to evaluate noise grade of service.

For loops longer than about 15,000 feet the combined loss of loop and receiver is larger than for the shorter loops. The received noise levels are therefore lower and the percentage of calls classified good or better is higher. However, the received volumes are also consistently lower, and therefore it would be incorrect to regard the service provided to these subscribers as superior to the service provided to subscribers on short loops. These arguments justify the use of one loop loss figure for all loops in the conversion of noise levels to the subscriber set. In the discussion to follow, all noise levels are referred to the subset.

The relation between noise level and distance is shown in Figs. 2 and 3, which are scatter diagrams wherein the abscissa gives the airline distance in miles and the ordinate gives the measured noise level referred to the subset. From these figures we observe that the noise levels increase with distance and that the variability of the noise levels decreases with distance. The scatter diagrams cannot be used directly

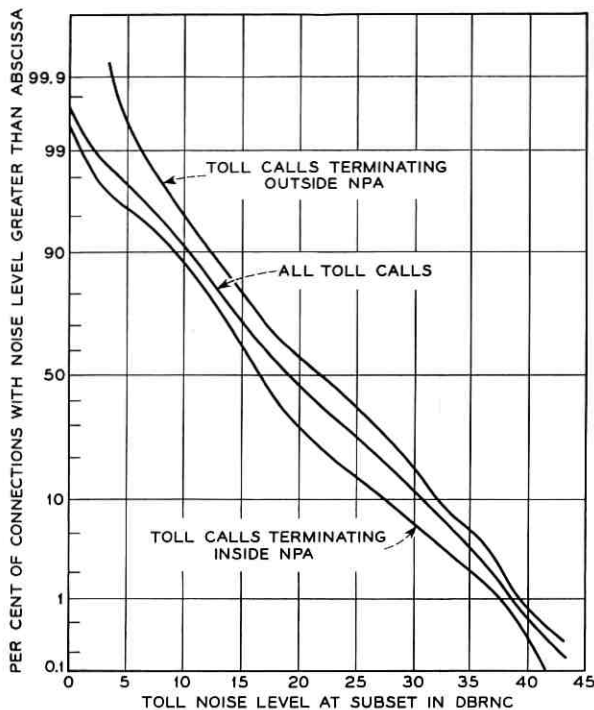


Fig. 4 — Noise level distributions.

for quantitative analysis, since two observations with coinciding distance and noise level are recorded by just one point. However, the above observations form the basis for regression analysis of noise versus distance discussed later.

Fig. 4 shows the cumulative distribution functions for noise levels on inside-NPA calls, outside-NPA calls, and all toll calls. The mean and standard deviations of these three noise distributions are given in Table II. This table also shows the precision achieved in terms of the 90 per cent confidence limits of the true mean for each of the three distributions. These confidence limits have been estimated from the sample by methods discussed in Ref. 3.

The present noise performance of the toll system in terms of the over-all objective can be estimated from Fig. 4. The "classical" over-all noise objective states that noise from all sources in a subscriber-to-subscriber connection should seldom exceed 26 dbrnc at the line terminals of the station set. Fig. 4 shows that on 23 per cent of all toll calls

TABLE II — DISTRIBUTIONS OF NOISE LEVELS ON TOLL CALLS,
REFERRED TO THE SUBSET

	Mean in dbrnc	Std. Dev. in db
Inside NPA	17.4 ± 2.7	7.2
Outside NPA	23.6 ± 3.4	7.5
All toll calls	19.7 ± 2.6	7.8

this limit is exceeded even before the influence of loop noise has been considered.

A nationwide survey of transmission conditions in the switched message network, with special regard to their influence on data transmission, was undertaken in 1959.⁶ In this survey, various transmission characteristics, among them message circuit noise, were measured on two classes of toll calls, short-haul calls of up to 400 miles airline distance, and long-haul calls 401–3000 miles long. The results of this survey have found wide application; a comparison with the results of the connection survey is therefore of interest. In this comparison, the distinction between calls terminating inside and outside originating NPA is nonessential. Therefore, the pooled data have been used to compute mean and standard deviation in the noise distribution on toll calls spanning 0–400 miles and 401–3000 miles, respectively. Table III gives these figures as well as those from the data survey, where the latter have been converted from dba to dbrnc. The deviations between the two sets of results are regarded as moderate in view of the different scopes and objectives of the two surveys.

Using regression analysis, the pooled data have been used further to analyze quantitatively the relation between toll noise level and distance between central offices. The independent variable x is defined as the logarithm to the base 2 of the airline distance in miles, and the dependent variable y as the toll noise level referred to the subset. The model used

TABLE III — COMPARISON OF NOISE DISTRIBUTIONS OF THE 1959
DATA SURVEY WITH THOSE OF THE 1962 CONNECTION SURVEY;
NOISE LEVELS REFERRED TO THE SUBSET

	Short-Haul		Long-Haul	
	Mean, dbrnc	Std. Dev., db	Mean, dbrnc	Std. Dev., db
			1959 data survey	22.0
1962 connection survey	19.1	7.4	30.3	4.5

in the analysis is that the mean noise level $E(y | x)$ for given distance is a linear function of x . The slope of the regression line will then be expressed in db per double distance (db/dd). An additional assumption must be made concerning the variance of y corresponding to a given value of x . The first assumption made here was that this variance is constant. The hypothesis of equality of the variances of y in the different length classes into which the data were grouped was then subjected to a statistical test. (In all regression analyses made of the connection survey data, these classes had length $x = 1$, or one double distance.) The outcome of this test (Bartlett's test) showed that the probability of the hypothesis being true was less than 0.1 per cent. On the basis of this the hypothesis of equality of the variances was rejected. The next step was to investigate the reason for this inequality of the variances. To this end a regression analysis was made with the same independent variable x as above, but with the variance of y for given values of x as the dependent variable. This analysis showed the variance to decrease with x according to the formula

$$E[\text{Var}(y) | x] = -6.6x + 80.7 \quad (1)$$

(valid for $3 \leq x \leq 11$); i.e., the average variance decreases at a rate of 6.6 for each doubling of the distance. The slope of the regression line (1) deviates significantly from zero; this fact is a good reason for using (1) rather than equality of the variances as an assumption in the regression analysis of y on x . Carrying through a regression analysis on this basis gave the result

$$E(y | x) = 2.2x + 7.9, \quad (2)$$

i.e. the average noise level increases by 2.2 db for each doubling of the distance. The hypothesis of linearity of the regression curve was tested and accepted. Therefore (1) and (2) give together in condensed form a description of the behavior of noise on toll connections as a function of the airline distance between originating and terminating central offices. A plot of these two regression lines is found in Fig. 5. The two dashed curves in this figure are confidence limits for the mean and will be discussed later.

The precision achieved in the survey is shown in Table II in terms of the 90 per cent confidence intervals for the true mean. These intervals are considerably wider than the required ± 1 db. It is therefore of interest to consider possible alternate ways of stating the precision. One reason for the poor precision achieved was the unexpectedly large variability of the mean noise levels between central offices. This is illustrated in

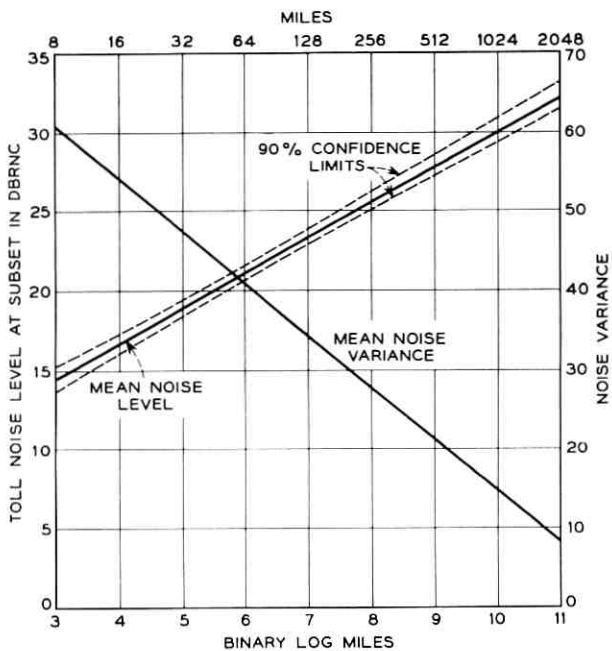


Fig. 5 — Regression lines of noise level and noise variance vs airline distance.

Table IV, which shows pooled data results for each of the 17 central offices in the sample as given by the mean of the measured noise levels, the mean of the end-office to end-office losses, and the distance in miles that corresponds to the mean of the distribution of the logarithm of the distances. One factor that contributed to this variability was the variation in calling habits and traffic patterns from one office to another. Because of the variation of noise level with distance, it seems likely that these variations should have a less pronounced effect on the precision if the latter were stated for the mean of a noise distribution on calls that are confined to a particular mileage stratum. That this is actually the case is shown in Table V, where the precision is given for the pooled data grouped into length classes, each of which is one double distance wide. Although the number of observations in each length class is considerably lower than the total, it is seen that the precision is in several cases increased, the reason being a decrease in the variability of the data.

Still another way of stating achieved precision is by way of the regression analysis. The confidence interval of the mean of y can be given

TABLE IV — CONNECTION SURVEY RESULTS: MEAN NOISE LEVEL, MEAN END-OFFICE TO END-OFFICE LOSS, AND DISTANCE CORRESPONDING TO MEAN OF DISTRIBUTION OF LOG DISTANCE

Central Office Location	Mean Noise Level at Subscriber Set, dbrnc	Mean End-Office to End-Office Loss, db	Distance Corr. to Mean of Distr. of Log Distance, Miles
Boston, Mass.	18.5	9.3	58
Brooksville, Fla.	32.5	8.3	62
Cheshire, Conn.	20.7	8.3	37
Dallas, Tex.	23.2	6.0	203
Detroit, Mich.	21.7	9.1	129
El Paso, Tex.	28.0	7.8	508
Fairfield, Conn.	18.0	7.4	28
Fort Lauderdale, Fla.	21.9	6.7	75
Hyattsville, Md.	20.9	10.3	136
Keyport, N. J.	14.1	7.3	21
Kingston, Pa.	18.2	11.5	48
Knoxville, Tenn.	25.3	6.1	121
Niagara Falls, N. Y.	24.7	6.6	33
Queens, N. Y.	16.8	8.0	36
Richmond, Va.	24.6	7.6	99
Riverside, N. J.	14.6	6.1	15
Selma, Cal.	16.8	6.2	41
Total	19.7	7.7	40

for any particular value of x . In the determination of such a confidence interval, all observations made for all x values are used. It can therefore be expected that these confidence intervals are narrower than those given in Table V. That this is true is shown by the dashed curves in Fig. 5 — the 90 per cent confidence interval has width ± 0.3 db for $x = 6.2$, and this width increases to no more than ± 0.8 db when the deviation of x from its mean value 6.2 is maximum. Looked at in this fashion, the achieved precision can certainly be regarded as satisfactory.

TABLE V — CONNECTION SURVEY PRECISION

Distance Class, Miles	Width of 90% Confidence Interval For Mean Of Noise Distribution, db
6-11	± 4.0
11-23	± 2.7
23-45	± 3.8
45-91	± 2.9
91-181	± 2.4
181-362	± 1.4
362-724	± 1.4
724-1448	± 2.1
1448-2896	± 2.2
All pooled data	± 2.6

As a conclusion of the discussion of noise results, it is of interest to examine present performance as expressed by noise grade of service. The over-all grade-of-service figures for all toll calls made are 97.0 per cent good or better and 0.3 per cent poor or worse. These figures indicate that the over-all noise performance of the present toll plant is quite good. However, a detailed study of the relation between grade of service and distance shows that the performance is less satisfactory on toll calls spanning large distances. This is discussed in some detail in the accompanying paper,¹ and the concept is actually used as a basic tool in the derivation of new over-all noise objectives.

5.2 Loss

The end-office to end-office losses are shown as a function of distance in the scatter diagrams of Figs. 6 and 7. It is apparent from these diagrams that the variation of loss with distance is only moderate. This variation is the subject of the regression analysis discussed later.

The cumulative distribution functions for end-office to end-office

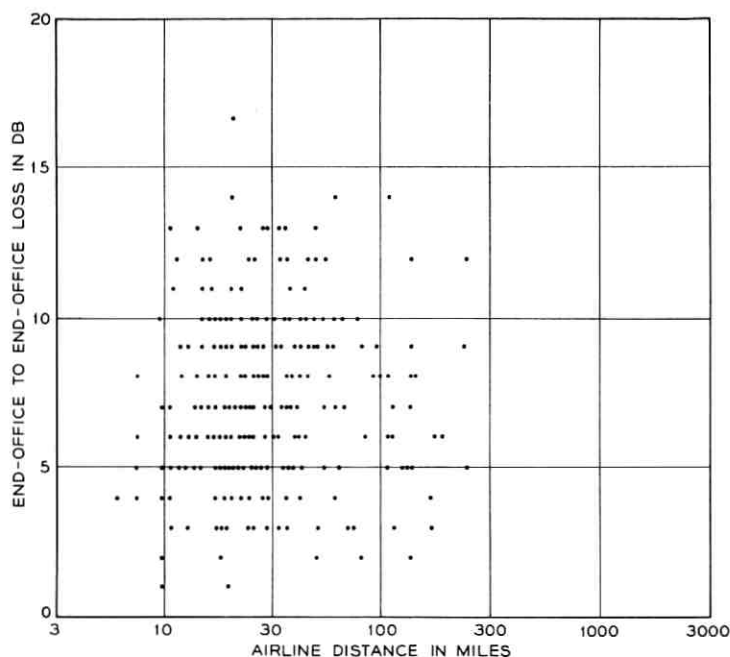


Fig. 6 — Scatter diagram of loss vs distance: toll calls terminating inside NPA.

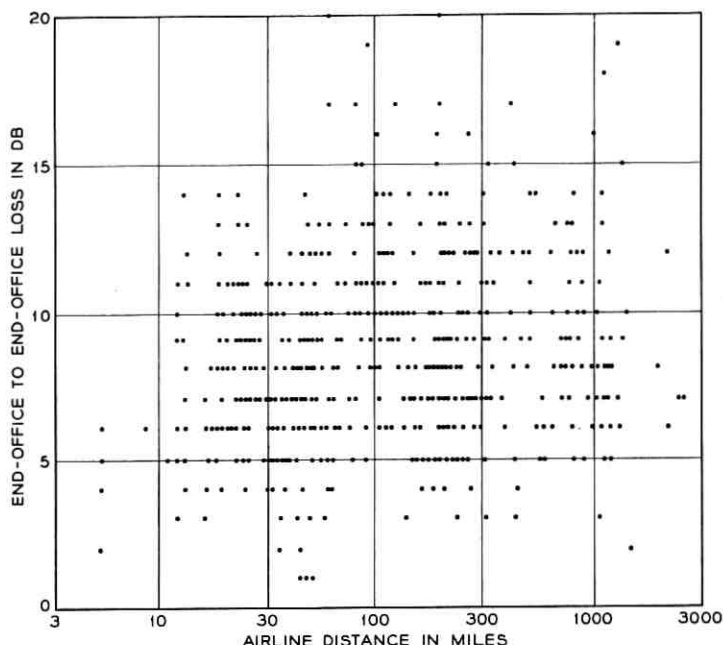


Fig. 7 — Scatter diagram of loss vs distance: toll calls terminating outside NPA.

losses on inside-NPA calls, outside-NPA calls, and all toll calls are shown in Fig. 8. The mean and standard deviations of these three loss distributions are given in Table VI.

The 90 per cent confidence intervals for the true mean loss are seen to have a width of ± 0.6 or ± 0.7 . This indicates that the precision of the loss data is considerably higher than that of the noise data. The reason is that the loss distribution variances are much lower than the variances in the distributions of noise levels.

In the 1959 data survey, loss measurements were made from which the distributions of end-office to end-office losses on short-haul and

TABLE VI — DISTRIBUTIONS OF END-OFFICE TO END-OFFICE LOSSES ON TOLL CALLS

	Mean, db	St. Dev., db
Inside NPA	6.9 ± 0.7	2.7
Outside NPA	8.3 ± 0.6	3.1
All toll calls	7.7 ± 0.7	3.0

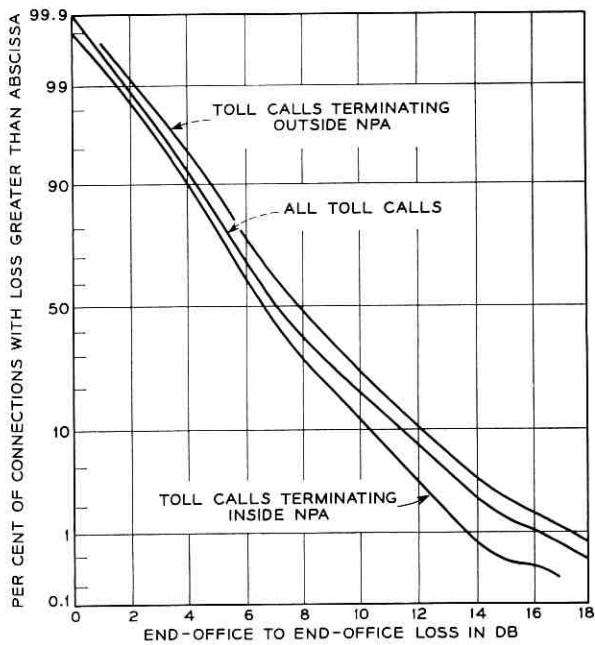


Fig. 8 — Loss distributions.

long-haul calls have been established.⁷ Again, we compare these results with the corresponding distributions of the pooled data of the connection survey. The comparison is made in Table VII, which gives means and standard deviations of the corresponding distributions.

Both parameters are seen to be lower for the connection survey distributions than for those of the data survey. The difference between the means could be taken as a measure of the decrease of the average end-office to end-office losses in the toll plant between 1959 and 1962

TABLE VII — COMPARISON OF DISTRIBUTIONS OF END-OFFICE TO
END-OFFICE LOSSES OF THE 1959 DATA SURVEY WITH
THOSE OF THE 1962 CONNECTION SURVEY

	Short-Haul		Long-Haul	
	Mean, db	Std. Dev., db	Mean, db	Std. Dev., db
1959 data survey	9.5	3.7	10.9	4.0
1962 connection survey	7.8	2.7	9.3	3.5

as a result of the continuing conversion to low-loss operation. However, this *quantitative* interpretation of the data is dangerous, since the connection survey was based on probability sampling techniques, while the data survey was not.

In the regression analysis of end-office to end-office loss versus distance, the independent distance variable x was defined in the same way as for the noise analysis, while the dependent variable y was the measured loss. The pooled data were used for this analysis. Bartlett's test showed in this case that the hypothesis of equality of the variances of y corresponding to given values of x was true with probability smaller than 0.1 per cent. Therefore this hypothesis was rejected, and a regression analysis of variance versus x was performed. This analysis showed that the variance increases with x according to the formula

$$E[\text{Var}(y) | x] = 1.5x - 0.7 \quad (3)$$

(valid for $2 \leq x \leq 10$); i.e., the average variance increases with 1.5 for each doubling of the distance. This slope deviates significantly from zero, so again we take this as a strong indication that the systematic variation of the variance with x according to (3) was the prime reason for the inequality of the variances. Proceeding with the regression analysis of y on x on this basis gave the result

$$E(y | x) = 0.6x + 4.5; \quad (4)$$

i.e., the average loss increases by 0.6 db for each doubling of the distance. The hypothesis of linearity of the regression curve was tested and accepted. It follows that (3) and (4) give, in condensed form, a description of the behavior of end-office to end-office losses on toll connections as a function of the airline distance between the offices. A plot of the two regression lines is found in Fig. 9. The two dashed curves give the 90 per cent confidence intervals for the mean of y corresponding to given values of x . The confidence interval has its minimum width of ± 0.1 db at $x = 4.7$. For low values of x the width increases to ± 0.3 db, while for high values of x the maximum width is ± 0.5 db.

It is of interest at this point to compare (1) and (3), which show that noise variance decreases and loss variance increases with distance. It can be seen from the scatter diagrams of Figs. 1 and 2 that the reason for the decrease of the noise variance with distance is the fact that a "noise floor" exists, below which no noise level occurred, and that this noise floor increases with distance, while the apparent upper limit for the noise levels is essentially constant. On the other hand, the reason for the increase of loss variance with distance is that long connections in

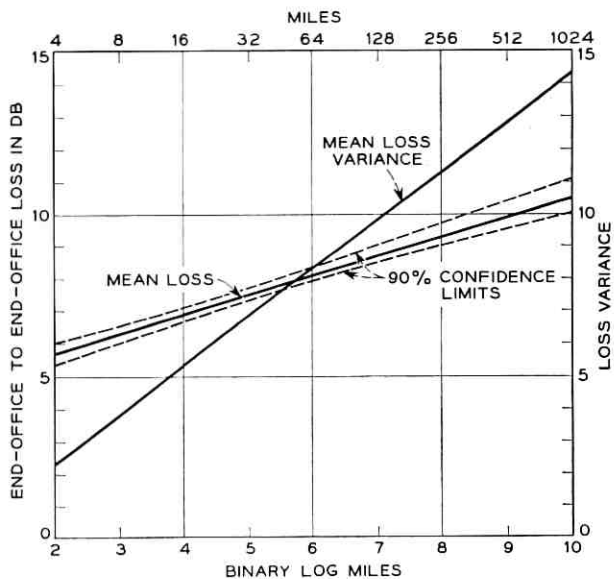


Fig. 9 — Regression lines of end-office to end-office loss and loss variance vs airline distance.

the present toll network may contain between one and seven intertoll trunks, (ITT), in tandem while for short ones the maximum possible number of ITT's is lower than seven. Over the range of distances where (1) and (3) are both valid ($3 \leq x \leq 10$), we find that the noise variance is always greater than the loss variance. It should be observed that these variances are not the squares of the standard deviations that appear in Tables II and VI. The latter are standard deviations of noise and loss distributions over all distances, while the former are the variances that appear when the distance is kept constant.

A nationwide survey of speech volumes, measured at the originating end of Bell System toll calls, was performed by Bell Telephone Laboratories in 1959-1961.⁸ The data of that survey can be used in conjunction with our loss data to evaluate volume grade of service and thus give an insight into customer satisfaction of present toll plant loss performance. The distribution of speech volumes on toll calls, referred to the originating central office, has a mean of -16.8 VU with a standard deviation of 6.4 db. By applying volume opinion curves,⁹ we find that the present distribution of losses on all toll calls gives a received volume grade of service of 87.1 per cent good or better and 1.2 per cent poor or worse.

These figures can be compared with the grade-of-service estimates of 83 per cent good and 3 per cent poor or worse that were made on the basis of a 1950 volume survey.¹⁰ The comparison indicates a substantial improvement in satisfaction of received volumes over the time period 1950-1962.

5.3 Distance

The airline distance between originating and terminating central offices is known for each call in the sample. The distributions of these distances for inside-NPA, outside-NPA and all toll calls, respectively, are shown in Fig. 10. It is seen from this figure that 50 per cent of all toll calls are shorter than 30 miles, and that only 10 per cent are longer than 250 miles. The distance scale used in Fig. 10 is logarithmic, and in this way the distributions plotted have reasonably low skewness. Had a linear scale been used instead, the distributions would have been ex-

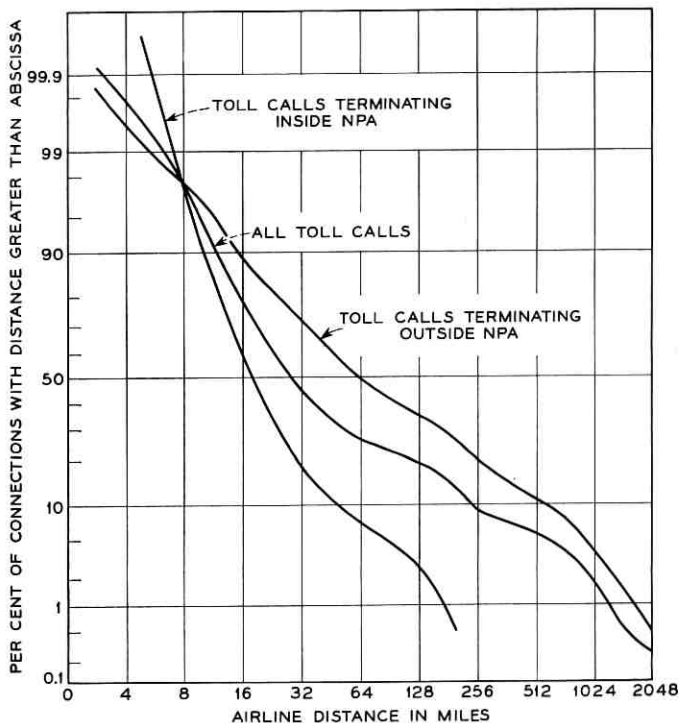


TABLE VIII—DDD CALLS EXPRESSED AS A PERCENTAGE OF ALL TOLL CALLS IN DIFFERENT DISTANT CLASSES

Distance Class, Miles	Proportion of Toll Calls Direct-Dialed by Customers
3-6	73
6-11	84
11-23	66
23-45	58
45-91	45
91-181	33
181-362	38
362-724	27
724-1448	17
1448-2896	20
All toll calls	55

tremely skew, and a plot would reveal very little about their true character.

The proportions of toll calls that are direct-dialed by customers (DDD calls) have been evaluated from the connection survey data. Table VIII shows the results of these evaluations as a function of distance. It can be seen that although an average of 55 per cent of all toll calls (as defined in Section II) are DDD calls, this percentage is not constant with distance. Thus, about 80 per cent of the short-haul toll calls are direct-dialed by customers, and this percentage decreases with distance to a value of about 20 in the longest category.

Some questions related to the routing of toll calls in the present Bell System toll network can be answered on the basis of connection survey data. Two examples are: (i) the average number of intertoll trunks and (ii) the relation between circuit length and airline distance, both given as a function of the distance spanned by the toll connection. Further studies would, however, be required to answer any of these or similar questions.

VI. CONCLUDING REMARKS

The feasibility of performing a statistically sound sample survey of the very complex Bell System toll plant has been satisfactorily shown by the survey described in this article. The prime importance of the survey lies in the information it gives about noise and loss performance of the present toll plant. However, a significant and very important part of the result is the experience that has been gained in carrying through a systemwide sample survey. Specifically, it should be pointed out that the two-stage sampling plan used is extremely well suited for surveys of

transmitted and received speech volumes, as well as noise, loss, and composition of loops, of facilities and of trunks. The acquiring of data of these types is vital in the present work of building a statistical model of the Bell System plant.

VII. ACKNOWLEDGMENTS

I wish to express my gratitude to the many people in the American Telephone and Telegraph Company and its associated companies, and in Bell Telephone Laboratories, whose contribution made the 1962 connection survey possible. Specifically, I should like to mention H. N. Lynch of A.T.&T., who was the valuable and valued coordinator during the planning and measuring phases of the survey, D. A. Lewinski of Bell Laboratories, with whom I cooperated closely throughout the whole survey, and Miss M. L. Chubb, Miss S. L. Lambert, Mr. E. S Langford, and Miss M. M. Nelan, all of Bell Laboratories, each of whom was responsible for a separate part of the data analysis with accompanying writing of programs for the IBM 7090 computer.

REFERENCES

1. Lewinski, D. A., A New Objective for Message Circuit Noise, B.S.T.J., this issue, p. 719.
2. Cochran, W. G., *Sampling Techniques*, Chap. 11, John Wiley and Sons, New York, 1963.
3. Hansen, M. M., Hurwitz, W. N., and Madow, W. G., *Sample Survey Methods and Theory*, Chap. 9, John Wiley and Sons, New York, 1953.
4. Cochran, W. T., and Lewinski, D. A., A New Measuring Set for Message Circuit Noise, B.S.T.J., **39**, July, 1960, p. 911.
5. Hardgrave, W. W., Hinderliter, R. G., and McNair, D. C., unpublished work.
6. Alexander, A. A., Gryb, R. M., and Nast, D. W., Capabilities of the Telephone Network for Data Transmission, B.S.T.J., **39**, May, 1960, p. 431.
7. Eagle, L. O., unpublished work.
8. McAdoo, K. L., Speech Volumes on Bell System Message Circuits — 1960 Survey, B.S.T.J., **42**, September, 1963, p. 1999.
9. Lewinski, D. A., unpublished work.
10. Coolidge, O. H. and Reier, G. C., An Appraisal of Received Telephone Speech Volume, B.S.T.J., **38**, May, 1959, p. 877.

A New Objective for Message Circuit Noise

By D. A. LEWINSKI

(Manuscript received October 14, 1963)

The reduction and control of noise on message circuits must be based on sound noise objectives. For many years the Bell System over-all performance objective has been "26 dbrnc (20 dba) seldom to be exceeded at the telephone station set." In this article the derivation of a more flexible and operationally feasible noise objective is presented. This objective specifies a limit of 20 dbrnc not to be exceeded on subscriber loops, and stipulates various distributions for noise originating beyond class 5 offices on built-up connections. The objective is such as to provide Bell System customers with a noise grade of service ranging from 99 per cent good or better on short connections to 90 per cent good or better on intercontinental connections spanning distances up to halfway around the world.

I. INTRODUCTION

For many years the Bell System over-all performance objective for message circuit noise has been as follows: "Noise from all sources in a subscriber-to-subscriber connection should seldom exceed 26 dbrnc* (20 dba) at the line terminals of the station set." Since its inception this objective has been a primary influence in the design of broadband transmission systems, and it has served as a guide for the engineering and maintenance of the message network. But improved and new services have gradually changed the makeup and the performance requirements of the plant. Thus, work was recently undertaken to establish a new performance objective — one better suited to the noise conditions imposed by a changing communication network.

The new objective provides a long-range Bell System goal and, as such, serves as a guide for the design of future systems and for establishing maintenance procedures. In addition, it indicates those areas where

* The new unit for noise measurement with the 3-type noise measuring set is dbrnc.¹ Reference noise, "rn," is 10^{-12} watts of 1000-eps power, whereas "c" refers to C-message weighting.

efforts to improve the noise performance of existing systems should be directed. For economic and technical reasons, however, it appears to be impractical to upgrade the performance of all existing equipment, most of which was designed to earlier standards. Therefore, it will probably be a number of years before the level of performance and customer satisfaction associated with the new objective can be fully realized in the Bell System plant.

Derivation of the new objective necessitated two major systems engineering projects: (*i*) subjective tests to establish a quantitative description of the effects of noise experienced by telephone users in terms readily translatable into an over-all transmission standard; (*ii*) noise surveys to provide data on Bell System noise performance. From this information, system noise performance estimates were made and examined from the telephone user's standpoint. In addition, a model of system noise behavior was constructed. These steps were necessary in order to (*i*) establish a framework for the statement of the objective, and (*ii*) provide insight for the derivation of the associated numerics so that a desired level of customer satisfaction could be realized. In accord with present philosophy, customer satisfaction is stated in terms of "grade of service."²

We begin by discussing the work on the subjective effects of noise and emphasize how the results lend themselves to noise grade of service estimates. We then use the latter tool to evaluate system noise performance and show in turn that this requires the new objective to be comprised of two parts, (*i*) a limit for noise attributable to the customer's loop, and (*ii*) distributions for noise on toll connections where the average values and standard deviations of these distributions are length-dependent. Last, we derive the actual numerics which constitute the new over-all objective and are the basis for new noise objectives for design and maintenance.

II. SUBJECTIVE EFFECTS OF NOISE

2.1 General

In setting performance objectives for speech transmission it is important to have a quantitative description of the subjective effects of the transmission parameter under consideration. Instead of describing these effects on a psychological scale, experience has shown that simple expressions of attitude such as absolute judgments are adequate when the experiment is properly designed. Assessments made on an absolute

basis can be readily transformed into satisfaction criteria, which in turn can be used as a foundation for over-all transmission objectives.

2.2 Description of Tests

To get a comprehensive picture of telephone user attitude toward noise, three subjective evaluations were actually undertaken. In addition to noise effects, the effects of received speech volume and signal to noise were also evaluated. Except for the relevant test instructions, each of these evaluations was conducted similarly by asking observers to appraise a series of simulated telephone calls in terms of a given set of response categories: excellent (E), good (G), fair (F), poor (P), and unsatisfactory (U).

The noise tests were conducted using 500-type station sets with received volume at a constant level of -28 VU,* and noise (a composite of power hum, switching office and thermal noise) varied between 18 and 62 dbrnc (set input) in 4-db steps. Three presentations consisting of different random permutations of the 12 test conditions were given to each participating group of observers.

The volume tests were conducted using both 302 and 500-type sets, the former being used primarily to tie in with previous work carried out by Coolidge and Reier.⁴ Noise level was held constant at 26 dbrnc (set input) with received speech volume varied between -24 and -60 VU in 4-db steps. As in the noise tests, three different random permutations of the 10 volume conditions were given to each group of observers.

The signal-to-noise tests were conducted with 500-type sets with both noise level and received volume varied over 44 randomly given conditions compatible with the range of values used in the noise and volume tests.

In each of the above tests, the simulated speech-noise conditions consisted of two short sentences of spoken material mixed with the noise. The spoken material and the noise were taped on separate recorders and played simultaneously to the observers at the required levels through a network equivalent to 6000 feet of 24-gauge cable, representing a subscriber loop. Groups of six to eight observers were accommodated in a specially constructed subjective test room, comprised of individual cubicles equipped with telephones, as shown in Fig. 1. A loudspeaker placed in the center of the oval array supplied recorded room noise at a

* VU (volume unit) is the unit for expressing the magnitude of a complex electric wave when measured with a standard volume indicator.⁵

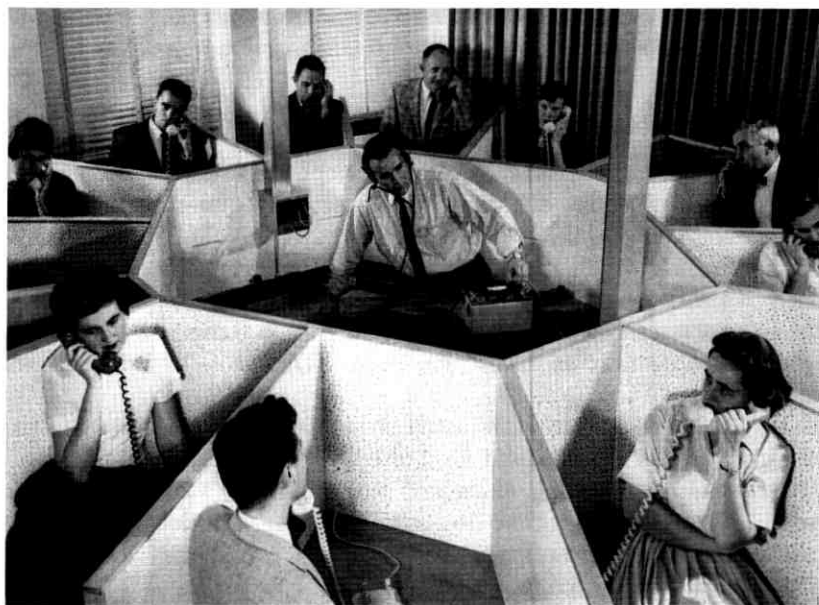


Fig. 1 — Observers at multiple listening positions during subjective test.

sound pressure level of 48 db re 0.0002 microbar. The line current in the test circuit was adjusted to 55 ma direct current to each station set.*

The test period for each group of observers fell into two parts: a preliminary period of introductory remarks which included instructions and a 15-to-25 minute period for the particular evaluation.

A total of 666 observers, both male and female, took part; all were chosen at random from among Bell Laboratories employees. None was required to participate more than once.

2.3 Test Results

While all three of the above tests are necessary to gain insight into customer attitude towards noise in the presence of speech transmission, only the noise test data are used in setting noise objectives. This reflects the present practice that transmission parameters be treated independently when deriving transmission objectives. As such, the data describing noise effects rather than the data on signal-to-noise are considered basic when deriving message circuit noise objectives. In general, however, the interdependence between noise and volume effects is recognized, and

* The significance of this choice of line current as it influences noise at the line terminals of the station set is discussed in Appendix A.

therefore the results of the noise-volume tests are potentially more useful for the evaluation and specification of over-all performance.⁵

The results of the noise tests plotted as "noise opinion curves" in cumulated categories are shown in Fig. 2. Presented in this way, the set of curves show the proportion of E (excellent), E + G (good or better), E + G + F (fair or better) and E + G + F + P (poor or better) judgments at particular noise levels over the range of values tested. In essence, these curves are estimates of $p(R | x)$, the conditional probability of placing a given noise level x in cumulated category R . A good model of opinion is obtained by fitting normal ogives, i.e., normal distribution functions, to the data points. As such, each curve can be defined by

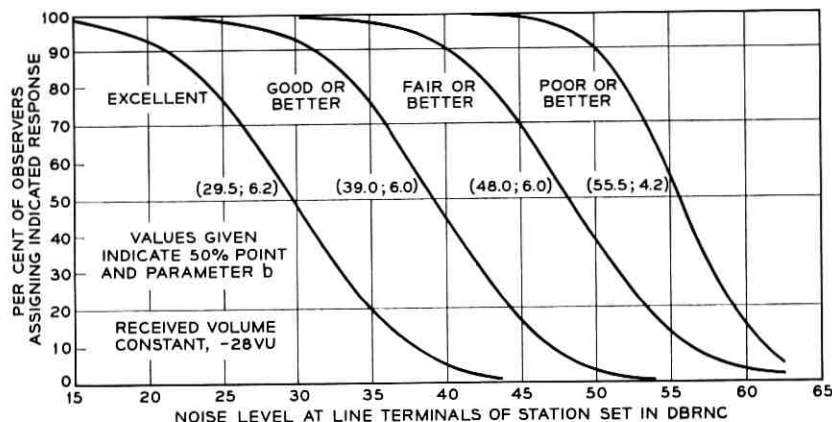


Fig. 2 — Noise opinion curves.

stating the 50 per cent point and the parameter "b," which is computed in the same way as the standard deviation of a normally distributed random variable.

The data shown are comprised only of second-presentation judgments, adjusted* for each observer where necessary to conform with

* The adjustment compensates for the uncertainty in judgment found in the neighborhood of the transition levels. As an example, consider a typical observer response

dbrne	18	22	26	30	34	38	42	46	50	54	58	62
Category	E	E	G	G	F	G	F	F	P	U	P	U

Here the first transition level is 24 dbrne, since this value of noise is equally likely to be judged excellent or good. The second is 36 dbrne since this level is equally likely to be judged good or fair and so on for 48 and 56 dbrne. Thus the corresponding adjusted judgment would become

dbrnc	18	22	26	30	34	38	42	46	50	54	58	62
Category	E	E	G	G	G	F	F	F	P	P	U	U

the four noise "transition" levels at which he essentially changed his judgment from one category to the adjacent one.

Many of the initial judgments in the first presentation appeared to be influenced by the lack of an "anchor." The observer's first judgment, for example, is either made at random or based on past experience. Thereafter his judgment is modified, so that in a short period of time his judgments tend to be made relative to the range of the stimuli presented. Thus the first set of data were the least reliable. During the third presentation it appeared that judgments were unduly biased, due to observer adaptation to the experiment. The second presentation data, between these extremes, seemed to be the best choice.

Collectively, these curves indicate that, in the presence of the desired received speech volume, noise levels up to about 30 dbrnc at the line terminals of the station set are quite acceptable. At 30 dbrnc, about 47 per cent of the subjects gave a rating of excellent, 47 per cent — good, and about 6 per cent — fair. Thereafter, degradation becomes increasingly evident: for example, notice the rapid decrease in per cent good and excellent response, as clearly indicated by the rate of change of the good-or-better noise opinion curve.

III. NOISE GRADE OF SERVICE

If it is assumed that the noise opinion curves $p(R | x)$, Fig. 2, are indicative of customer reaction to any particular telephone connection within the bounds of the noise levels tested, then for any probability density function $f(x)$ of noise levels on subscriber-to-subscriber telephone calls, the integral

$$\int_{-\infty}^{\infty} p(R | x)f(x) dx$$

evaluates the proportion of calls placed in category R , giving the expected value of customer opinion.* As such, this integral is very useful as a noise performance evaluation tool. It is also useful for specifying a desired "noise grade of service" which can be regarded as a statement of noise objective. Given a statement of objective in terms of a desired proportion of telephone connections assignable to a particular category

* Once category R is defined, $p(R | x)$ is simply treated as a function of x , say $g(x)$, called "opinion." Hence

$$\int_{-\infty}^{\infty} p(R | x)f(x) dx = \int_{-\infty}^{\infty} g(x)f(x) dx = E[g(X)]$$

that is, the expected value of $g(X)$ where the random variable X is noise level.

R , i.e., a desired level of noise grade of service, one can solve for the noise density function $f(x)$ which, in turn, can serve as the objective "numeric."

It can be shown, however, that the correspondence between noise distribution and noise grade of service is not one-to-one. Infinitely many noise distributions yield the same noise grade of service. This means that there is considerable leeway in choice of distribution to satisfy a given grade-of-service requirement. Choices of requirement, on the other hand, are fairly narrow if customer preference is to be satisfied.

IV. NOISE SURVEYS

4.1 General

Having conducted tests to describe the subjective effects of noise and having established a means for using the results in an evaluation scheme such as grade of service, the next step in the derivation of an over-all noise objective is to obtain estimates of system noise performance. The determination of which estimates are pertinent is obviously an operational one. While subscribers are aware only of the total noise from all sources, there are two distinct types of plant which contribute: loops and trunks. Hence noise performance information is needed on the two basic parts of an over-all connection: that part which is assigned to the customer at all times (the loop including subset) and that part between end-offices (i.e., connections) which he shares with other customers.

A series of noise surveys were therefore made in the loop plant in 1960 and 1961, and in the toll plant on toll connections between end-offices in 1962. Toll, rather than toll-plus-local, connections were chosen for the population of "connections," so as to associate connection noise performance with that part of the plant which is more complex in makeup and which has the most costly noise problems.

4.2 Loop Plant

The loop plant was surveyed⁶ by selecting six end-offices with at least one in each of five central office size strata characterized by offices having 1 to 999 lines, 1000 to 9999 lines, 10,000 to 19,999 lines, 20,000 to 29,999 lines and 30,000 lines or more. Using the known stratum statistics,⁷ this approach enabled an extrapolation of the individual sets of data to provide a reasonably accurate estimate of noise on loops for the entire Bell System.

TABLE I — SUMMARY DATA — EXCHANGE AREA LOOP NOISE SURVEYS

Location of Survey.....	Marshall, Va.	Enola, Pa.	Waltham, Mass.	Kenosha, Wis.	Trois- Rivières, Que.	Cambridge, Mass.
Type office	SxS	SxS	# 5 x-bar	SxS	SxS	#1 x- bar
# Lines	400	2,200	14,600	19,800	22,700	67,600
Sample size.....	148	158	149	123	178	109
Nm (all lines)	m	18.4	3.5	1.3	2.8	2.7
dbrnc	s	14.1	8.3	9.8	7.7	10.8
	max.	53	33	32	27	38
Nm (ind. lines)	m	11.0	0.1	-5.0	1.5	-2.3
dbrnc	s	11.1	5.8	4.2	7.2	6.5
Nm (party lines)	m	25.4	9.9	8.7	8.4	7.6
dbrnc	s	13.0	8.5	9.2	7.4	11.9
Ng (all lines)	m	31.4	27.2	24.4	17.6	18.5
dbrnc	s	13.3	6.3	8.2	7.3	9.8
	max.	62	47	42	37	58
Ng (all lines)	m	65.0	63.3	53.4	49.5	53.5
dbrn 3 kc	s	14.8	8.3	8.4	7.5	7.7
	max.	84	83	76	66	78
* Party line balance, db	m	-51.6	-57.8	-58.3	-52.5	-47.7
	s	6.4	6.7	6.1	6.2	6.2
Loop loss, db	m	6.4	6.1	5.2	6.6	5.3
	s	3.1	2.0	1.8	1.9	2.2
	max.	15.5	11.7	9.2	11.3	11.5
Transmitter current, ma.	m	60.4	55.6	44.9	46.3	46.5
	s	13.5	15.9	12.2	13.4	16.5
						47.8
						16.2

m = mean.

s = standard deviation.

* Balance for tip and ring party flat rate lines except Waltham, Mass., where balance is for ring party flat and tip party message rate lines.

The offices chosen were Waltham and Cambridge, Massachusetts; Kenosha, Wisconsin; Trois-Rivières, Quebec; Marshall, Virginia; and Enola, Pennsylvania. For each office a simple random sample of approximately 150 loops was selected for measurement. The loops were terminated in the central office "quiet-termination" and at the customer's location with a 500-type set. Measurements of "noise metallic" (Nm) were made with the 3A noise measuring set bridged across the line terminals of the station set and also from line terminals to ground (Ng) at the customer's location. Table I summarizes the results.

As is seen, the noise on loops in general is very low. However, it was found that there is considerable difference (7 to 14 db) between party line noise and the noise on individual lines. Except for the influence of some open wire lines in Marshall, Virginia (not uncommon for offices in stratum #1) the reason for this difference is that party lines are inherently more unbalanced than individual lines due to grounded ringers in party station sets. This is certainly evidenced by the party line balance row in Table I. Balance* is seen to be about -55 db on the average for party lines compared to -75 db for individual lines. Thus for noise induction from neighboring power lines one would expect, on the average, about 20 db more hum on party lines than on individual lines.†

Since it was found that loop noise at the higher levels is predominantly power line hum, noise-to-ground and balance data rather than actual Nm measurements were used to characterize noise in each central office area. Noise metallic (hum) distributions were derived from the expression $Nm = \text{balance} + (Ng + 40)$. To get best estimates of mean and standard deviation, regression analysis was performed over the six offices in their respective strata. Weighting these regression estimates by the corresponding stratum statistics⁷ resulted in the over-all loop noise distribution of the Bell System shown in Fig. 3.

4.3 Toll Plant

Estimates of the noise levels that subscribers are currently experiencing on end-office to end-office toll connections were supplied by the 1962 connection survey described in a companion paper.⁸ For completeness the sampling plan and the results will be summarized.

A sample of connections was selected using two-stage sampling. Sample size was determined on the basis of a desired precision of ± 1 db in the over-all mean at the 90 per cent confidence level. The population contained the toll calls originating in all end-offices in Bell System service as of January 1, 1960. Seventeen offices were selected by sampling proportional to estimated size, the size estimates being defined by the number of customer lines served. For each of these offices, a self-weighting sample of previously made toll calls was chosen. The frames for the second-stage sample consisted of listings of all toll calls made during the busy hour of one business day. The sample calls were dupli-

* Balance is defined to be $Nm - (Ng + 40)$. This is consistent with $20 \log V_m/V_g$; Ng , as measured with a 3-type noise measuring set, is 40 db below the total voltage to ground.

† This can be remedied by the use of station sets with gas-tube isolators which essentially remove the ringer from ground during the talking condition. Such sets are often employed in severe cases.

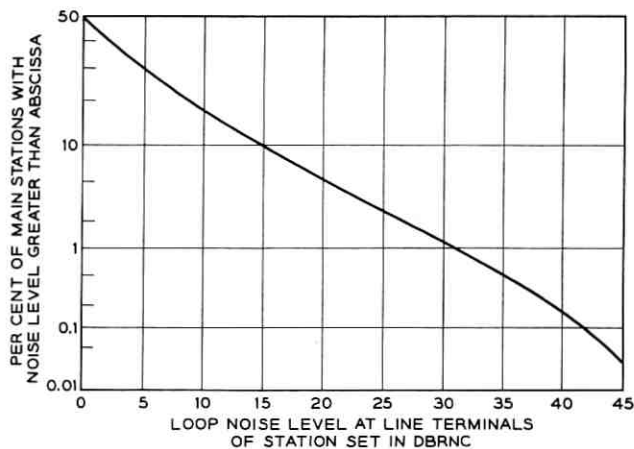


Fig. 3 — Loop survey data, 1961: estimated loop noise (power hum) distribution.

cated either via operator placement or by dialing between terminating class 5 offices. Noise and end-office to end-office loss were measured at the originating end-office with a 3A noise measuring set on a zero loop terminated in 900 ohms.

The results indicate that at the station set the toll connection noise distribution has a mean of 19.7 dbrnc and a standard deviation of 7.8 db. The data are accumulated in Fig. 4. In addition, it was found that the mean of the distribution of end-office to end-office loss is 7.7 db with a standard deviation of 3.0 db. Analysis of the relationship between noise level and airline distance indicates a linear increase in average noise level of 2.2 db per double distance, with variance decreasing with increasing distance.

V. EVALUATION OF NOISE PERFORMANCE

Once pertinent estimates of noise performance are in hand, the next step is to evaluate noise performance. Consider first an evaluation from the point of view of the present standard: 26 dbrnc (20 dba) seldom exceeded at the line terminals of the station set. From Fig. 4, it is seen that in the absence of loop noise approximately 23 per cent of the toll connections in the sample had noise in excess of 26 dbrnc at the line terminals. Whether or not this is satisfactory performance in terms of the present objective depends on the interpretation of the phrase "seldom exceeded."

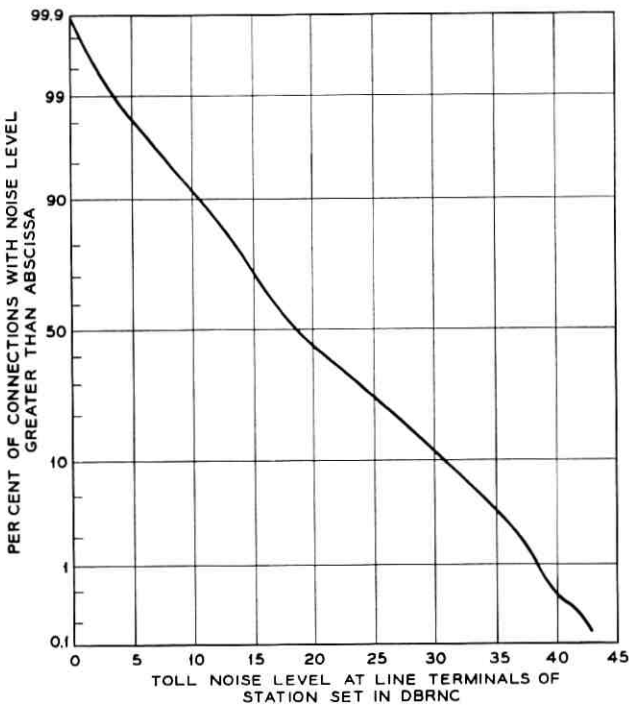


Fig. 4 — Connection survey data, 1962: distribution of noise levels on customer-placed toll connections. Mean = 19.7 dbrnc; standard deviation = 7.8 db.

A more specific statement for noise evaluation is obviously desirable. In terms of noise grade of service, discussed in Section III, 97.0 per cent of the measured values in Fig. 4 (i.e., connections) would be considered good or better and only 0.3 per cent poor or worse.* This may appear to be in contradiction to the finding that 23 per cent of the measurements do not meet the 26-dbrnc objective. The fact, however, is that when the average noise level is low, over-all grade of service is very impressive. But this does not assure satisfactory noise performance on all toll calls. For example, the noise on close to 1 per cent of the connections was found to exceed 39 dbrnc, which essentially defines a bound on the levels that telephone users consider good or better [i.e. for $x > 39$

* Grade of service for *measured* connection noise does not reflect the subjective effects associated with compandored links. In the absence of speech (i.e. when noise is measured) compandor action is such that the listener perceives a lower noise level. On the whole this effect is small. Estimates show that the above good-or-better noise grade of service figure is affected by less than 1.0 per cent and the poor-or-worse figure by less than 0.1 per cent.

dbrnc $p(E + G | x) < 0.5$. Furthermore, from Fig. 5, we see that these higher values (the tail of Fig. 4) are attributable mainly to noise on the longer and thus more costly connections. Hence it is misleading to look only at grade of service for noise on all toll calls. The customer who primarily makes calls spanning long distances is apt to get poorer performance; for example, the connection survey showed that grade of service on calls within a 100-mile radius is 97.8 per cent good or better whereas on coast-to-coast calls it is only 86.5 per cent good or better. In order to avoid this shortcoming, it appears necessary to have a particular noise requirement for various physical lengths of connections, instead of a single number seldom exceeded for all lengths.

Consider next the noise contribution from the loop plant. On the basis of data in Fig. 3, close to 2 per cent or an estimated 800,000 customers (main stations) have loop noise in excess of the present 26-dbrnc objective. While this is only a relatively small percentage, loop noise is a problem to the affected customers because the same level tends to be present at all times. As stated earlier, the principal source of audible

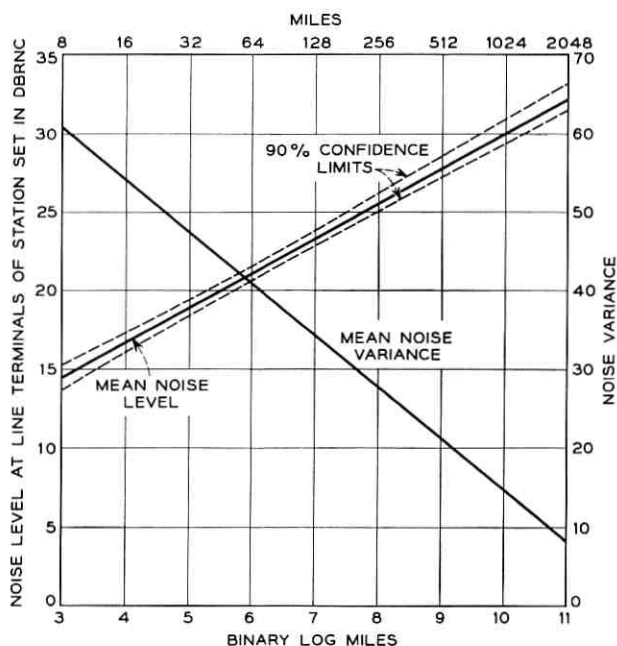


Fig. 5 — Regression of noise level vs distance and noise variance vs distance spanned by connections.

loop noise is power line induction, appearing as hum in the telephone circuit. The hum level is determined by the extent of the power system influence (which is fairly constant in any particular location) and the degree of balance of the line and terminal equipment. Party lines, because of the use of grounded ringers and other unbalanced station set circuitry, are found on the average to be much noisier than individual lines. If a telephone user has excessively high loop noise, it is almost certain that he is on a party line and that the noise is power line hum. Fig. 3 shows that an estimated 0.2 per cent of Bell System customers have 39 dbrnc of power hum loop noise. Since they can expect nearly this level on every call, their grade of service on both local and toll calls collectively will be only about 40 per cent good or better and as much as 10 per cent poor or worse.

VI. REQUIREMENTS FOR AN OVER-ALL NOISE OBJECTIVE

The present noise objective is not so formulated as to focus attention on substandard noise performance on the longer toll connections and the existence of power line hum on loops. To direct attention to areas of inadequate noise performance and emphasize the need for improvement of loops and trunks that are now substandard, we must select a noise objective that is not only satisfactory from the grade-of-service point of view, but is also in harmony with actual system noise behavior.

Fig. 5 shows that the average noise level on toll connections is positively correlated with airline distance. This implies that for noise contributed by the toll plant, the objective should be length-dependent. Short connections therefore should meet more stringent requirements than long ones, making the objective consistent with actual system performance. In addition, the objective should incorporate the inherent variability of noise level on connections spanning the same over-all distance and recognize that this variability decreases with distance, a fact also shown by Fig. 5. The most expedient way to incorporate these length dependencies is first to divide distance into a number of classes or categories (that is, short, medium, long, and intercontinental), then to establish for each class a suitable noise distribution, wherein mean noise increases and variance decreases with distance. A study of the connection survey data shows that the distributions may be assumed to be normal within each distance class.

With regard to the form and statement of the objective as it pertains to loop noise, Table I and Fig. 3 indicate that each central office area can be expected to have a small percentage of loops which will be quite

noisy. Furthermore, because the noise is predominantly power hum it may be assumed that if a customer has a noisy loop then his noise level can be expected to be about the same on every call. To alleviate this situation, it would appear desirable to adopt one universal loop limit — a limit which would insure all telephone users the same noise grade of service on a long-term average basis.* The latter requirement is satisfied by a limit having the property that the desired grade of service assigned to any class of end-office to end-office connection is not significantly altered when a noise level equal to the limit is "added" to the numeric requirement for any of the connection classes.

VII. DERIVATION OF THE NEW OBJECTIVE

From the foregoing discussions, it may be concluded that an over-all noise objective should incorporate both a connection and a loop noise objective: for connections, it should state requirements on mean and standard deviation for noise as a function of distance; for loops, a limit not to be exceeded. The actual numerics, viewed in terms of grade of service, should assure high customer satisfaction and be economically feasible for the telephone company.

From the evaluation of the connection survey data, Section V, it was evident that noise grade of service could be impressive on the whole and yet not be acceptable on the longer connections. We stated, for example, that the grade of service on coast-to-coast connections is only 86.5 per cent good or better. In general, it will be found that grade of service is less satisfying on the longer connections, because of the increase in connection noise level with increasing airline distance. However, the number of toll calls established by customers decreases rapidly with increasing airline distance, so that a subclass such as all coast-to-coast connections will have a negligible influence on over-all grade of service. It follows therefore that: (i) it is insufficient to simply satisfy one over-all grade of service requirement; (ii) the same grade of service level cannot be expected on *all* lengths of connections, since the length-dependent increase in connection noise must be recognized. Appropriate adjustment for grade of service is therefore necessary. A study of various promising adjustments showed that "balance" may be achieved if grade of service does not vary with distance more than from near 100 per cent good or better to a minimum value of 90 per

* This assumes all customers to be "average" in their calling habits. Despite variability which is known to exist, this assumption is justified from a practical standpoint. Without it each customer could have a loop limit depending on his particular calling habits. This would be impossible to administer.

cent on the longest connections and, in the same way, from near 0 per cent poor to a maximum of 0.5 per cent.

The first step then is to satisfy the extreme requirements, that is, a grade of service of at least 90 per cent good or better and at most 0.5 per cent poor on the longest connections, i.e., on the class of intercontinental calls. On the assumption that noise on such connections is normally distributed, there exist many well-defined choices of mean and standard deviation that will satisfy these conditions. However, the choice can be narrowed, since the objective for the longest connections is constrained by our noise model to large values of mean and small values of standard deviation. While it is desirable to have as large a value of mean as possible, there cannot be too small a standard deviation because of the variation in circuit losses. The practical limit for standard deviation in view of the latter appears to be a value between 3 and 4 db. With a choice of standard deviation of 3.5 db, Fig. 6* implies that a mean of 30 dbrnc is permissible for the noise at the line terminals of the station set on the class of longest possible connections spanning an airline distance halfway around the world. Using these two parameters as an anchor at the upper end, we may now assign noise requirements to the remaining shorter connections. A satisfactory breakdown is shown in Fig. 7. Using binary log-mile cells, distance is divided into the four broad categories defining short, medium, long and intercontinental connections. The corresponding allowable values of mean and standard deviation for noise in these classes and the resulting grade-of-service values are indicated. It can be seen that all of the previously mentioned requirements are fulfilled.

Fig. 8 shows the 1962 connection survey noise data for each distance category and Fig. 9 shows the desired noise distribution functions in the same coordinates. Comparison of the two demonstrates that existing and desired performance are fairly compatible and that the assumption of normality is justified. Except for whatever improvement is required to overcome the subjective impairment due to compandors, little or no noise improvement is needed on short connections other than in the tail of the distribution, while on medium and long connections noise should be decreased respectively by about 3 and 4 db on the average and somewhat more in the tails. Since these improvements seem economically feasible in future system designs, the parameters in Table II were established as the new noise performance objective for customer-to-customer connections referred to the line terminals of the station set.

* A discussion of how grade-of-service curves may be readily constructed for normal distribution is given in Appendix B.

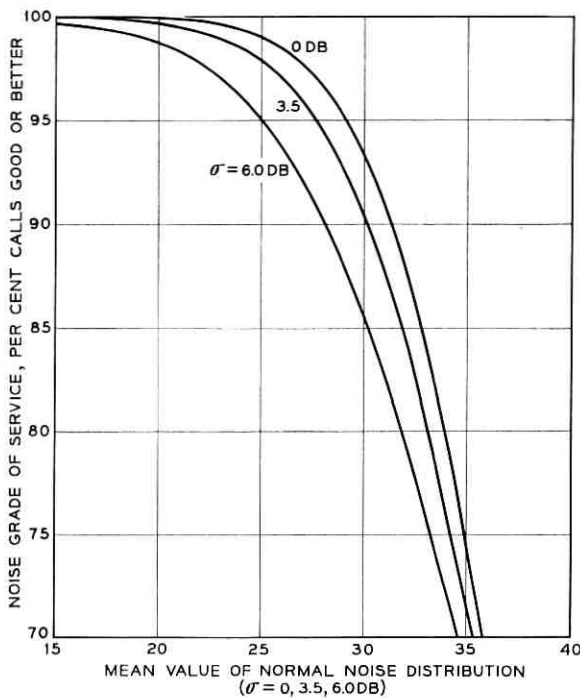


Fig. 6 — Grade of service for noise levels which are normally distributed.

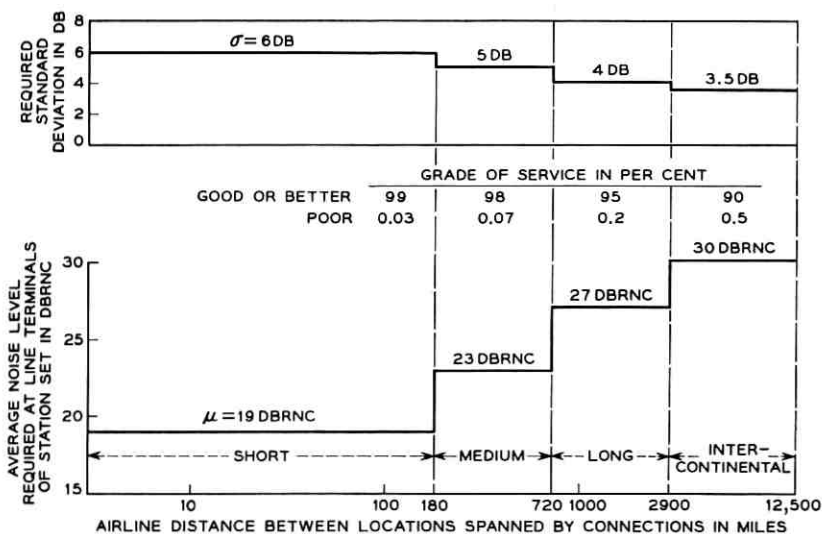


Fig. 7 — New over-all performance objective for noise on toll connections.

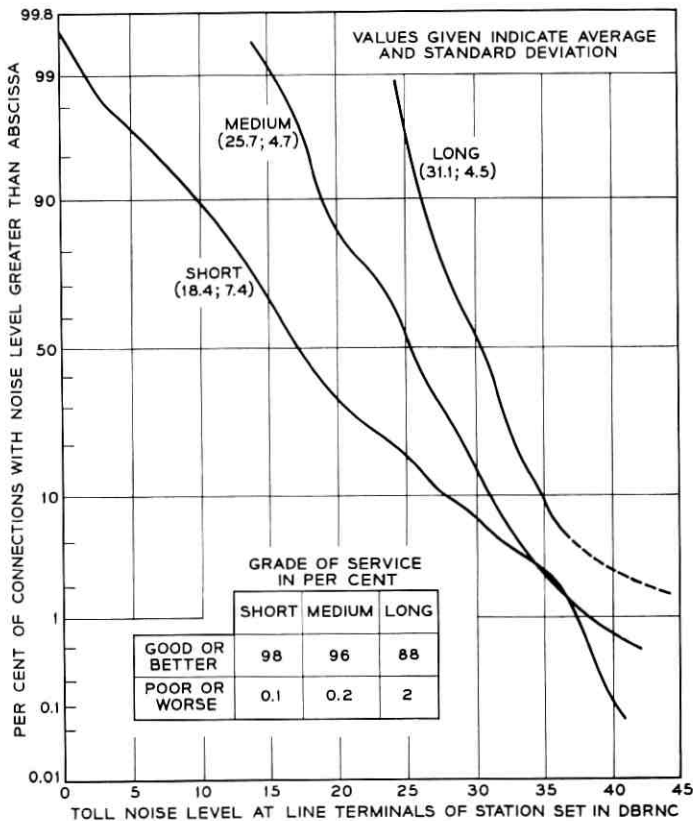


Fig. 8 — Noise performance of short, medium, and long toll connections — connection survey data, 1962.

Having this basic breakdown for the new objective for connection performance, we can now make a choice of loop limit. Fig. 10 shows grade of service for the range of loop noise levels up to 30 dbrnc in combination with the new noise requirements for each distance category. It is seen that no significant deterioration in grade of service results with loop noise less than 20 dbrnc. Above this value, however, there is a definite downward trend in per cent good or better and an upward trend in per cent poor. Hence, it is appropriate to choose a loop limit at 20 dbrnc. On the basis of Fig. 3, we see that an estimated 5 per cent, or approximately 2 million main stations, are above this value; hence corrective measures for reduction of noise on loops will be required throughout the system.

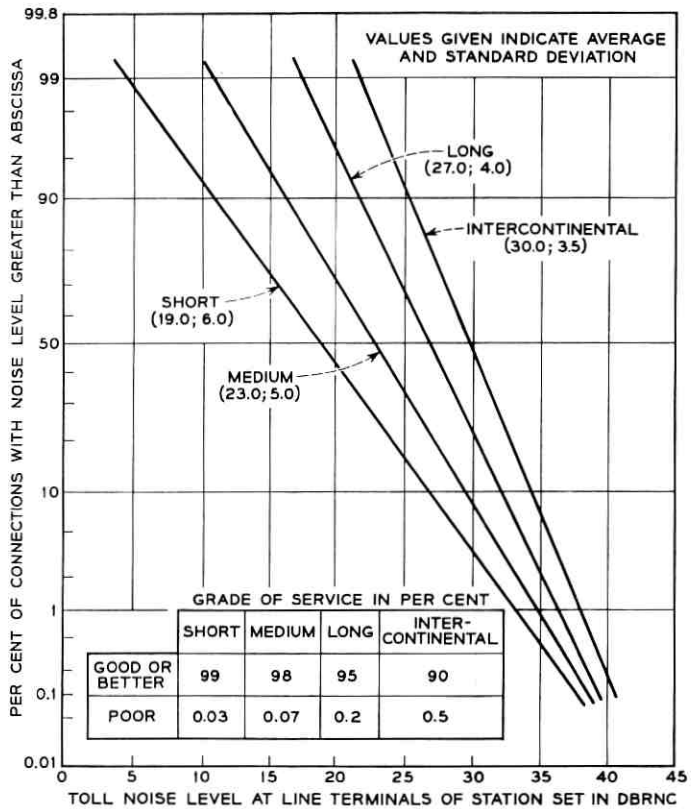


Fig. 9 — Breakdown of new over-all message circuit noise performance objective.

Finally, it is of interest to compare the new objective with the current 26 dbrnc seldom exceeded objective. We see from Fig. 9 that for connection noise 26 dbrnc may be exceeded on 12 per cent of the short connections, on 27 per cent of the medium connections, on 60 per cent of the long connections, and on 88 per cent of the intercontinental

TABLE II — NEW NOISE PERFORMANCE OBJECTIVE

Airline Distance, miles	Mean, dbrnc	Standard Deviation, db	Grade of Service	
			Good or Better	Poor
Up to 180	19.0	6.0	99%	0.03%
181-720	23.0	5.0	98	0.07
721-2900	27.0	4.0	95	0.2
2901 and above	30.0	3.5	90	0.5

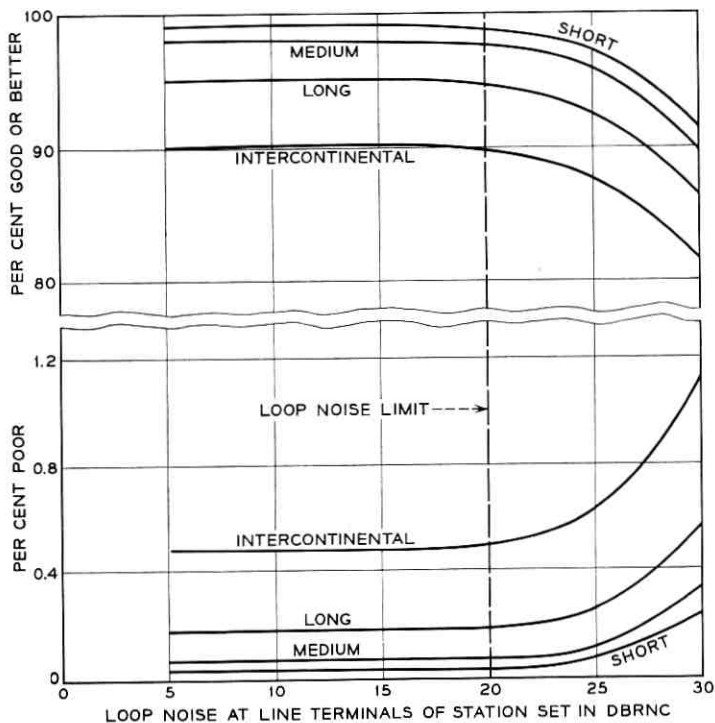


Fig. 10 — Grade of service for connection objective with loop noise.

connections. This implies that for connection noise the new performance objective is more lenient, in that it allows noise levels above 26 dbrnc for an appreciable per cent of calls. Notice, however, that the range is "restricted" to around 39 dbrnc, the 50 per cent point of "good-or-better" response, which is highly desirable. On the other hand, approximate evaluations show that the present design objective of 44 dbrnc at 0 TLP for a 4000-mile circuit would have to be made more stringent in order for the new over-all objective to be satisfied. Lastly, we note that for loop noise the limit of 20 dbrnc not to be exceeded is more stringent than the present objective would indicate.

VIII. ACKNOWLEDGMENTS

The contribution given by all those who participated in the subjective tests on noise effects and those who worked on the noise surveys is gratefully acknowledged. This includes many Bell Laboratories employees, A.T.&T.Co. personnel and operating telephone company

people. In addition, I would like to thank my co-workers, without whose help this project could not have been carried out.

APPENDIX A

Noise Opinion and Noise at the Line Terminals of the Station Set

Noise "at the line terminals of the station set" refers to noise across the line terminals of a 500CD type telephone set on a loop drawing 55 ma. While rather specific, this choice of customer reference is a natural one, since the noise opinion curves (Fig. 2) refer to noise level measured across the line terminals of a 500CD set on a 55-ma test circuit. Moreover, there is no loss in generality in having this type of customer reference as a standard.

In the evaluation of message circuit noise, we are concerned with two main noise sources: that originating on connections beyond class 5 offices and that originating on receiver loops. Consider the noise originating on connections. The first step in its evaluation is to decide on a point of measurement. Operationally, the best point is at the end-office at the input to a zero loop terminated in 900 ohms. Take any level measured there, say x dbrnc. What will be the subjective effect of this level on customers? It will be slightly different for customers on short, medium, and long loops, yet the difference is small enough to be neglected because of the "equalizing" properties of the 500 set. The combined response of a receiving loop and 500 set is reasonably constant for the majority of customers; hence it may be assumed that "received noise volume" (for noise originating beyond class 5 offices) is independent of loop length. Thus to evaluate x dbrnc, we must determine what this level will be across the line terminals of a 500 set drawing 55 ma. From loop loss data it is estimated that the average loss of a 55-ma loop terminated in a 500 set is 5 db. Hence, we may postulate that the subjective effect of x dbrnc of connection noise is the same for all customers, and that it is given by referring to $(x - 5)$ dbrnc on the noise opinion curves. As a consequence, a statement of objective for noise on connections referred to "the line terminals" (in our sense) really means that at the point of measurement, that is, the class 5 office, the requirement is 5 db less stringent.

Consider now the evaluation of noise originating on loops. If measured across the line terminals of a 500 set, we would expect a different acoustic response for the same value of noise level on short, medium, and long loops. Fortunately, the difference is hardly noticeable. Noise

originating on loops is predominantly power line hum concentrated at 180 and 300 cycles. At these frequencies the 500 set input impedance is essentially constant over the range of loop currents encountered in the field. Hence we can assume that the subjective effect of a particular loop noise level at the telephone set is the same for all values of loop current, which suggests that for loop noise the noise opinion curves are directly applicable to any line terminal measurements, whether on short, medium, or long loops. Therefore, an objective for noise on loops can be applied equally to all customers — even though specified "at the line terminals" in our sense. Finally, we note that to evaluate the combined (over-all) effect of x dbrne of noise originating on *any* connections and y dbrnc originating on *any* loop, it suffices to refer to the opinion assigned to a noise level equal to the power sum of $(x - 5)$ and y dbrne in Fig. 2.

APPENDIX B

Grade of Service for Normal Noise Distribution

In Section 2.3 we stated that normal ogives can easily be fitted to the response data which result from evaluating the subjective effects of noise by absolute judgment. As such, opinion in category R

$$p(R | x) = \int_{-\infty}^{\frac{x-a}{b}} \frac{\exp(-t^2/2)}{\sqrt{2\pi}} dt$$

where a is the value of x such that $p(R | a) = 0.5$ and b is a parameter equal to the "standard deviation" of the ogive curve. With this model for opinion, grade of service for any probability density function $f(x)$ of noise levels is given by

$$\int_{-\infty}^{\infty} \int_{-\infty}^{\frac{x-a}{b}} \frac{\exp(-t^2/2)}{\sqrt{2\pi}} f(x) dt dx.$$

If $f(x)$ is normal with mean \bar{x} and standard deviation σ , we have

$$\int_{-\infty}^{\infty} \int_{-\infty}^{\frac{x-a}{b}} \left[\frac{\exp(-t^2/2)}{\sqrt{2\pi}} \right] \left[\frac{\exp[-(x - \bar{x})^2/2\sigma^2]}{\sqrt{2\pi}\sigma} \right] dt dx.$$

On the assumption that σ is fixed, the above integral is a function of \bar{x} only, say $F(\bar{x})$. Changing variables

$$\frac{x - \bar{x}}{\sigma} = y$$

and differentiating under the integral sign we get

$$F'(\bar{x}) = \int_{-\infty}^{\bar{x}} \frac{\exp\left\{-\frac{1}{2}\left[y^2 + \frac{(\bar{x} + \sigma y - a)^2}{b^2}\right]\right\}}{2\pi b} dy.$$

Furthermore letting $b' = \sqrt{b^2 + \sigma^2}$ and $u = b'/b\{y + \sigma[(\bar{x} - a)/b'^2]\}$ we find

$$F'(\bar{x}) = \frac{\exp[-(\bar{x} - a)^2/2b'^2]}{\sqrt{2\pi b'}}$$

Finally integrating between $-\infty$ and \bar{x} , we get

$$F(\bar{x}) = \int_{-\infty}^{\bar{x}} \frac{\exp[-(t - a)^2/2b'^2]}{\sqrt{2\pi b'}} dt = \int_{-\infty}^{\frac{\bar{x}-a}{b}} \frac{\exp(-t^2/2)}{\sqrt{2\pi}} dt$$

which is the value of grade of service for a normal probability density function $f(x)$ having mean \bar{x} and constant standard deviation σ . The above integral is easily constructed with the aid of normal probability paper. Simply plot $F(\bar{x} = a) = 50$ per cent and $F(\bar{x} = a + \sqrt{b^2 + \sigma^2}) = 15.9$ per cent, for the given category R , and join the two points by a straight line.

REFERENCES

1. Cochran, W. T., and Lewinski, D. A., A New Measuring Set for Message Circuit Noise, B.S.T.J., **39**, July, 1960, p. 911.
2. MacAdam, W. K., A Basis for Transmission Performance Objectives in a Telecommunication System, Comm. and Elect., No. 36, May, 1958, p. 205.
3. Chinn, H. A., Gannett, D. K., and Morris, R. M., A New Standard Volume Indicator and Reference Level, B.S.T.J., **19**, January, 1940, p. 94.
4. Coolidge, O. H., and Reier, G. C., An Appraisal of Received Telephone Speech Volume, B.S.T.J., **38**, May, 1959, p. 877.
5. Aikens, A. J., and Lewinski, D. A., Evaluation of Message Circuit Noise, B.S.T.J., **39**, July, 1960, p. 879.
6. Lewinski, D. A. and Näsell, I., unpublished work.
7. Hardgrave, W. W., unpublished work.
8. Näsell, I., The 1962 Survey of Noise and Loss on Toll Connections, B.S.T.J., this issue, p. 697.

Propagation of Light Rays through a Lens-Waveguide with Curved Axis

By D. MARCUSE

(Manuscript received November 7, 1963)

The problem of the propagation of a light ray in a lens-waveguide with arbitrarily bent axis is solved. The solution can conveniently be expressed in form of an integral if the waveguide is bent sufficiently gradually.

In general, a ray which is incident on the axis of the straight lens-waveguide follows an undulating path after traversing the bend. The undulations can be kept arbitrarily small if the bend is tapered and if its curvature is sufficiently gentle. By properly dimensioning the bend, the undulations can be made to cancel out completely, so that a ray which follows the axis of the straight waveguide can be made to leave the bend on the axis of the outgoing straight waveguide.

The cases of circular and tapered bends as well as tilts and offsets are discussed.

I. INTRODUCTION

The invention of the laser has revived interest in light as a communications carrier. One of the many problems which have to be solved before a light communications system becomes feasible is the propagation of a light beam from transmitter to receiver. It is well known¹ that a sequence of converging lenses can guide a light beam and keep it from spreading. The losses of such a lens-waveguide can be calculated only by means of wave optics. However, even geometric optics can demonstrate the guiding properties of a lens-waveguide.² It can show that a light beam, once it is injected into a sequence of lenses, follows an undulating path without wandering away from the axis of the lens-waveguide.

The present paper is limited to describing the behavior of a light beam in a lens-waveguide whose axis is not straight everywhere, but which is allowed to follow bends of the transmission path or exhibit abrupt changes like tilts of its axis or an offset of one of its lenses from the axis on which all the other lenses are centered. The description is given in

terms of geometric optics, so that no information about the losses of light transmission through a lens-waveguide with bent axis can be obtained. It is clear, however, that the loss of power from the light beam is caused partly by diffraction losses at the edge of the lenses. These losses are certainly minimized if the center of gravity of the light distribution in the beam, which is described as the light ray, remains as far from the edges of the lenses as possible. It is desirable, therefore, that the light ray follow the axis of the structure as much as possible. The mathematical description of the light ray presented in this paper shows that a ray which follows the axis of the straight lens-waveguide will be forced into an oscillatory trajectory whenever the axis of the lens-waveguide deviates from perfect straightness.

It is necessary, at times, to lead the lens-waveguide through a bend to circumvent obstacles which might lie in its path. If it is possible to design a bend such that a beam which is incident on the axis of the straight incoming waveguide will leave the bend on the axis of the outgoing straight waveguide, we will call such a bend one of optimum design. It is, of course, equally desirable also to keep the deviations of the beam from the waveguide axis on the bend as small as possible.

We show in this paper that one can inject a light beam into a circular section of the lens-waveguide in such a way that it travels through the bend at a constant distance from the waveguide axis. It can, furthermore, be readmitted into the outgoing straight section of the lens-waveguide so as to continue along its axis. An optimization of a circular bend is thus possible.

Another way of reducing the oscillations caused by a bend is to taper its radius of curvature gradually from its infinite value on the straight section to a minimum value and back to the infinite value of the outgoing straight section.

The theory of ray optics in a lens-waveguide with curved axis is a generalization of Pierce's theory.² The solution of the difference equation can be approximated by a convenient integral expression in the limit of a lens-waveguide whose axis changes direction only gradually.

II. RAY OPTICS OF THE CURVED LENS-WAVEGUIDE

The light ray is described by its distance r from the center of the lenses at the position of each lens (see Fig. 1). The lenses are spaced a distance L apart and have a focal length $f = 1/C$. The quantity C is known as the "lens power."

If we assume that all angles are so small that $\tan \alpha$ can be taken = α , we obtain the following relations between the radii r_n and r_{n+1} of the

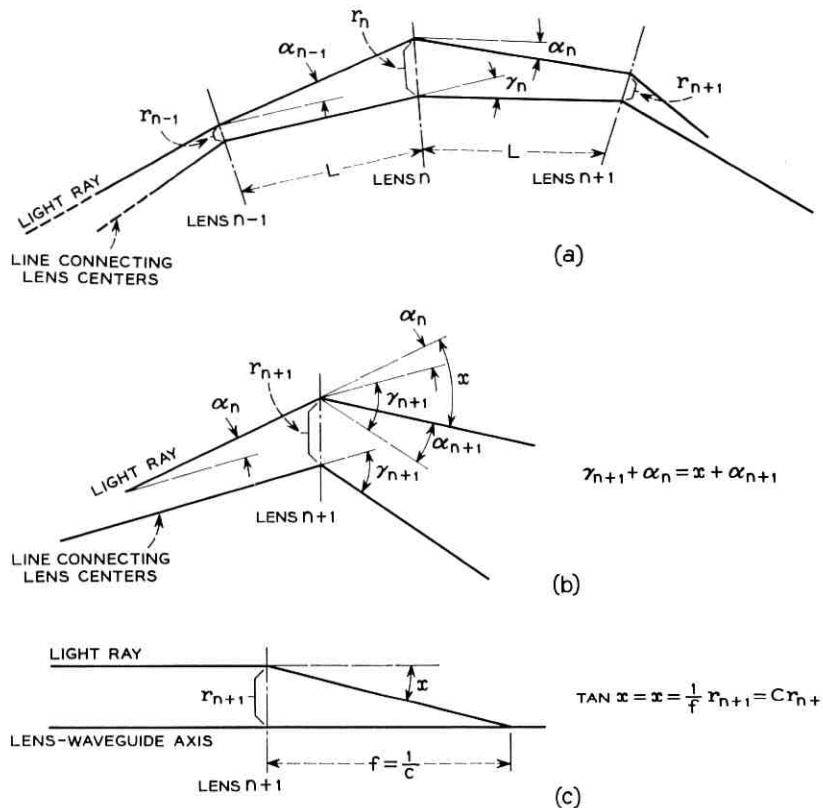


Fig. 1 — (a) Illustration of the bent lens-waveguide and the radii of the light beam at different lenses. (b) Relations among the various angles between the straight lines connecting successive lenses and the light beam and these straight lines. (c) Illustration of the relation between the angle x by which a thin lens deflects the light ray and the radius r_{n+1} of the ray.

ray at the positions of the n th and $(n+1)$ th lens

$$r_{n+1} = r_n + \alpha_n L \quad (1)$$

$$Cr_{n+1} = \gamma_{n+1} + \alpha_n - \alpha_{n+1}. \quad (2)$$

α_n is the angle between the ray and the straight line connecting successive lenses taken to the right of the n th lens. γ_n is the angle at the n th lens between the two straight lines connecting the lenses. The geometrical relations (1) and (2) can be read off Fig. 1(a) through (c).

Eliminating α_n and α_{n+1} from (1) and (2) results in

$$r_{n+2} - (2 - LC)r_{n+1} + r_n = L\gamma_{n+1} = y_{n+2}. \quad (3)$$

Equation (3) agrees with Pierce's equation for the straight lens-waveguide in the case $\gamma_{n+1} = 0$. In this case the equation has the solution

$$r_n = A \cos n\theta + B \sin n\theta \quad (4)$$

with

$$\cos \theta = 1 - (LC/2) \quad (5)$$

or equivalently

$$\sin \theta = \sqrt{LC} \sqrt{1 - \frac{LC}{4}}. \quad (6)$$

This solution shows that, in general, the ray oscillates around the axis of the lens-waveguide.

From Fig. 2 it is apparent that the quantity y_{n+2} occurring in (3) is given by

$$y_{n+2} = L^2/R_{n+1}. \quad (7)$$

Equation (3) is the mathematical description of the ray optics of the curved lens-waveguide. It allows the successive calculation of the

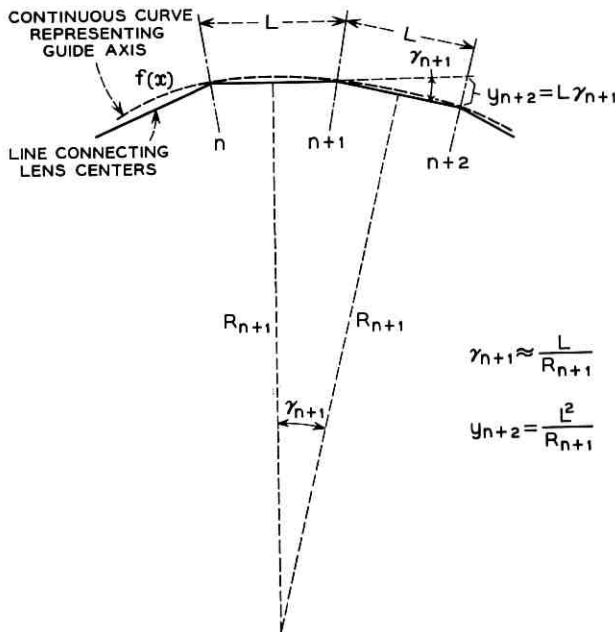


Fig. 2 — Definition of the quantities y_{n+2} and R_{n+1} .

distances r_n of the ray from the centers of the lenses for any distribution of lenses and suitable initial conditions.

III. SOLUTION OF THE RAY EQUATION

By standard methods for solving difference equations,³ a rigorous solution of (3) was obtained:

$$r_n = A \cos n\theta + B \sin n\theta + \frac{L^2}{\sin \theta} \sum_{m=0}^{n-2} \frac{\sin \theta(n-m-1)}{R_{m+1}}. \quad (8)$$

The sum in (8) is defined only for $n > 1$. The constants A and B are determined from the initial position of the ray at r_0 and r_1

$$A = r_0 \quad (9)$$

$$B = \frac{r_1 - r_0 \cos \theta}{\sin \theta}. \quad (10)$$

The validity of (8) can be checked by substitution into (3).

Equation (8) can be converted to a convenient integral expression. We use the identity

$$\sin \theta(n-m-1) = \frac{\theta}{2 \sin \theta} \int_m^{m+2} \sin \theta(n-x) dx \quad (11)$$

and obtain instead of (8)

$$r_n = A \cos n\theta + B \sin n\theta + \frac{\theta L^2}{2 \sin^2 \theta} \sum_{m=0}^{n-2} \frac{1}{R_{m+1}} \int_m^{m+2} \sin \theta(n-x) dx. \quad (12)$$

Now let us assume that R_m varies so slowly that we can write

$$R_m = R(x). \quad (13)$$

The value R_m defined in Fig. 2 has become the radius of curvature $R(x)$ of a curve $f(x)$ which smoothly connects the centers of the lenses. With the use of (13) the sum of (12) can be changed into an integral, and we obtain

$$r_n = A \cos n\theta + B \sin n\theta + \frac{L^2}{2 \sin^2 \theta} \left\{ \frac{\cos(n-1)\theta - \cos n\theta}{R_1} + \frac{1 - \cos \theta}{R_{n-1}} + 2\theta \int_1^{n-1} \frac{\sin \theta(n-x)}{R(x)} \right\} dx. \quad (14)$$

Equation (14) holds for arbitrary values of L and C as long as

$$0 < |1 - (LC/4)| < 1. \quad (15)$$

Its validity is restricted to the extent to which the approximation (13) holds. That is, (14) holds as long as the lens-waveguide is bent only gradually.

For completeness let us state the result in the limit $L \rightarrow 0$. It follows from (6) that $\theta \rightarrow \sqrt{LC}$ in that case. If we introduce the length $s = nL$ or $\sigma = xL$ as the new coordinate, we obtain from (14) in the limit of closely spaced lenses

$$r(s) = A \cos \kappa s + B \sin \kappa s + \frac{1}{\kappa} \int_0^s \frac{1}{R(\sigma)} \sin \kappa(s - \sigma) d\sigma \quad (16)$$

with

$$\kappa^2 = \lim_{L \rightarrow 0} (C/L). \quad (17)$$

The solution (16) could have been obtained by first converting the difference equation (3) into a differential equation. Equation (16) is the solution of this differential equation.

IV. BENDS, TILTS AND OFFSETS

We study first the problem of transmitting a light ray along two sections of straight lens-waveguide which are connected by a circular bend. To make the problem more general we assume that the straight sections are not tangents of the circle at the point of contact and that the axis of the straight section of the guide does not go through the center of the first lens which is located on the circle. In other words, we assume that the circle is tilted by an angle α and offset by an amount " a " with respect to the incoming and outgoing straight lens-waveguides (see Fig. 3). For the solution of this problem we go back to the exact equation (8) and limit ourselves to a beam which enters the bend on the axis of the incoming straight guide ($A = 0, B = 0$). A study of the geometry shows that

$$R_1 = R_{N-1} = \frac{L^2}{a}; \quad R_2 = R_{N-2} = \frac{2L^2R}{L^2 + 2\alpha LR - 2aR}; \quad R_m = R \quad m \neq 1, 2, N-1, N-2.$$

Using the identity

$$\sum_{m=0}^k \sin \theta(n-m) = \frac{\sin \left(n - \frac{k}{2} \right) \theta \sin \frac{1}{2}(k+1)\theta}{\sin \frac{1}{2}\theta}$$

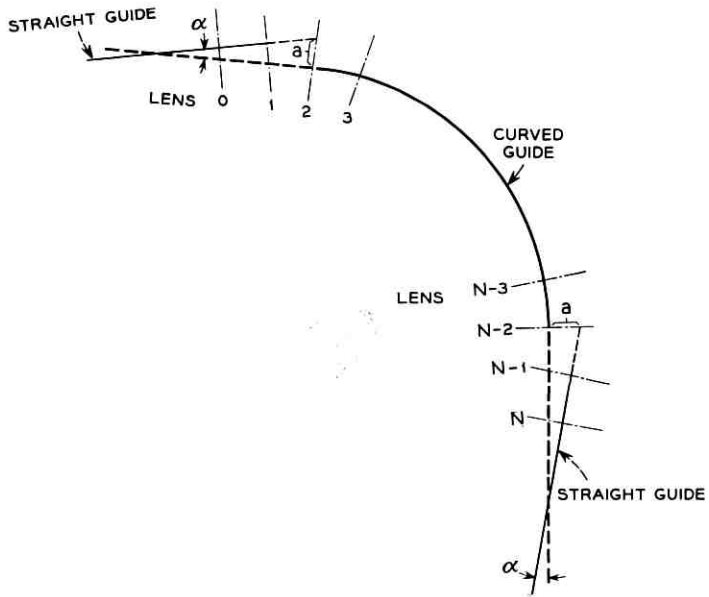


Fig. 3 — A circular bend to which the straight lens-waveguide is connected by an offset a and a tilt α .

we obtain from (8) on the circular bend

$$r_n = \frac{L^2}{\sin \theta} \left\{ \left[\frac{a}{L^2} \sin \theta - \frac{\cot \frac{1}{2}\theta}{2R} \right] \cos \theta (n - 2) + \frac{1}{L} \left[\alpha - \frac{a}{L} (1 - \cos \theta) \right] \sin \theta (n - 2) + \frac{\cot \frac{1}{2}\theta}{2R} \right\} \quad (18)$$

$2 \leq n \leq N - 2$

and on the straight outgoing section

$$r_n = 2 \frac{L^2}{\sin \theta} \sin \theta \left(n - \frac{1}{2}N \right) \left\{ - \left[\frac{a}{L^2} \sin \theta - \frac{\cot \frac{1}{2}\theta}{2R} \right] \cdot \sin \theta \left(\frac{1}{2}N - 2 \right) + \frac{1}{L} \left[\alpha - \frac{a}{L} (1 - \cos \theta) \right] \cdot \cos \theta \left(\frac{1}{2}N - 2 \right) \right\} \quad (19)$$

$N \leq n < \infty$.

By properly adjusting tilt and offset we can assure that the beam will continue to travel on the axis of the outgoing straight lens-waveguide without undulations. We adjust a and α so that both expressions in brackets in (19) vanish simultaneously. This leads to

$$a = \frac{L^2}{2R} \frac{\cot \frac{1}{2}\theta}{\sin \theta} = \frac{L}{RC} \quad (20)$$

and

$$\alpha = (a/L)(1 - \cos \theta) = L/2R. \quad (21)$$

These values for the tilt and offset, by which the circular bend is connected to the two sections of straight line, provide us with an optimum circular bend — that is, one which guides the light ray around a curve without causing it to undulate. It is apparent from (18) that these optimum values for tilt and offset assure simultaneously that the light beam traverses the circular section of the bend at a constant distance from the center of the lenses which is equal to the amount of offset (20). It is clear that the offset injects the beam into the circular bend just at the spacing at which the beam can travel around the circle without undulating.

There are other ways to design a bend to guide a light beam without introducing undulations of the outgoing beam. For example, if we connect the circular bend smoothly to the straight sections ($a = 0$ and $\alpha = 0$) we can still suppress undulations by choosing the length of the bend and the properties of the lenses such that $\sin \theta(\frac{1}{2}N - 2) = 0$. However, such a design is more complicated and depends on the length of the bend.

As a second example, we consider the case of a bend with tapered radius of curvature:

$$\frac{1}{R_t} = \begin{cases} \frac{4\delta}{D^2} Ly & 0 \leq y \leq \frac{N}{2} \\ \frac{4\delta}{D^2} (N - y)L & \frac{N}{2} \leq y \leq N. \end{cases} \quad (22)$$

Here, N is the number of periods L which fit on the bend (Fig. 4), δ is the angle through which the bend leads, and $D = NL$ is the total length of the bend.

The trajectory of the ray can be computed with the help of (14). We assume that the ray is incident on the axis of the incoming straight waveguide ($A = B = 0$).

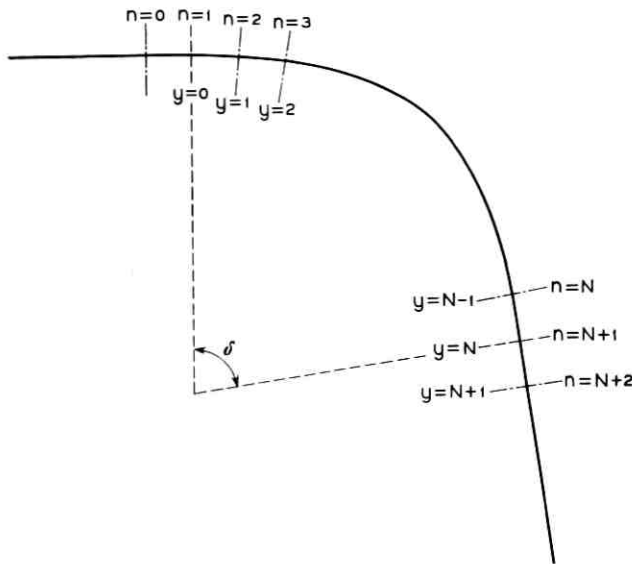


Fig. 4 — A tapered bend of the lens-waveguide.

For $2 \leq n \leq \frac{1}{2}N + 2$,

$$r_n = \frac{2\delta L^3}{D^2 \sin^2 \theta} \left\{ (n - 2)(1 + \cos \theta) + \frac{2}{\theta} [\sin \theta - \sin \theta(n - 1)] \right\}; \quad (23a)$$

for $\frac{1}{2}N + 2 \leq n \leq N + 2$,

$$r_n = \frac{2\delta L^3}{D^2 \sin^2 \theta} \left\{ (N - n + 2)(1 + \cos \theta) + \frac{2}{\theta} \left[2 \sin \theta \left(n - 1 - \frac{1}{2}N \right) - \sin \theta(n - 1) - \sin \theta \right] \right\}; \quad (23b)$$

for $N + 2 \leq n < \infty$,

$$r_n = \frac{2\delta L^3}{D^2 \sin^2 \theta} \frac{2}{\theta} \left\{ 2 \sin \theta \left(n - 1 - \frac{1}{2}N \right) - \sin \theta(n - 1 - N) - \sin \theta(n - 1) \right\}. \quad (23c)$$

Equation (23c) can be rewritten to show the amplitude of the undulation more clearly

$$r_n = \frac{16\delta L^3}{D^2 \theta \sin^2 \theta} \sin^2 \theta \frac{1}{4} N \sin \theta \left(n - 1 - \frac{1}{2} N \right). \quad (24)$$

As in the case of the circular bend, the undulations can be made to cancel out if we design the lens-waveguide and the length of the bend such that $\sin \theta \frac{1}{4} N = 0$. It is also apparent that the amplitude of oscillation decreases rapidly if the length D of the bend is increased.

Finally, we state the equations for the case of a tilt and for an offset of one lens in the waveguide (see Figs. 5 and 6). Assuming, as always, that the incident ray follows the axis of the incoming straight waveguide, we obtain from (8) in case of a tilt which is spaced a distance from the lens,

$$r_n = \frac{\delta}{\sin \theta} \sqrt{(L-a)^2 + a^2 + 2a(L-a) \cdot \cos \theta \sin [\theta(n-1) - \vartheta]} \quad (25)$$

with

$$\vartheta = \arctan \frac{a \cdot \sin \theta}{(L-a) + a \cos \theta}. \quad (26)$$

If one lens is offset by an amount Δ and if the incident ray follows the axis of the incoming straight waveguide

$$r_n = -\frac{4\Delta}{\sin \theta} \sin^2 \frac{1}{2} \theta \sin \theta (n-2) \quad (27)$$

describes the ray on the outgoing straight waveguide.

V. DISCUSSION AND NUMERICAL RESULTS

In the preceding section we have found that a light ray which is incident along the axis of the incoming straight waveguide, in general leaves a bend, an offset or a tilt undulating around the axis of the straight outgoing waveguide. We have found that these undulations can be suppressed by properly designing the bends. In this last section we will discuss the maximum undulations of the outgoing light ray if no provision for canceling the undulations has been made.

If one does not intend to use an optimum design, one would not include a tilt or an offset in the bend but would connect the circular bend smoothly to the straight sections. If we take $a = \alpha = 0$ in (19) we see that the maximum amplitude which the undulations can reach is given by

$$r_{\max} = \frac{L^2 \cot \frac{1}{2} \theta}{R \sin \theta} = 2 \frac{L}{RC}. \quad (28)$$

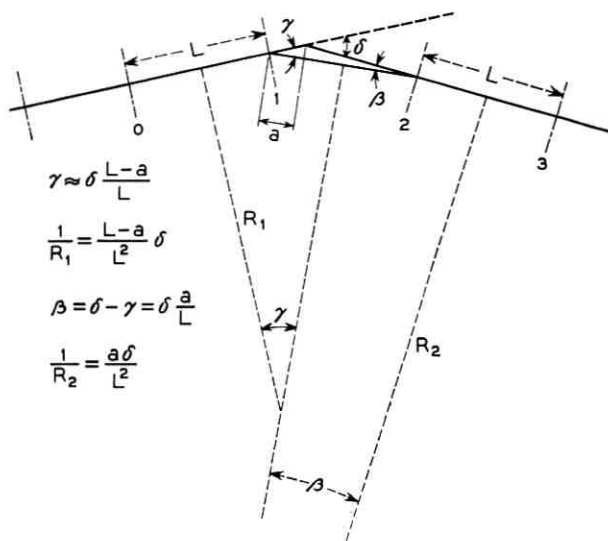


Fig. 5 — The lens-waveguide tilted by an angle δ a distance a from a lens.

The same equation describes the maximum deviation of the beam on the circular section of the bend.

The maximum deviation of the ray from the axis on the tapered bend can be obtained from (23). We assume that $N \gg 1$ and find that the maximum deviation on the tapered bend is

$$r_{\max} \approx \frac{\delta L^3 N}{D^2 \sin^2 \theta} (1 + \cos \theta) = \frac{2\delta L^2}{D(4 - LC)} \quad (29)$$

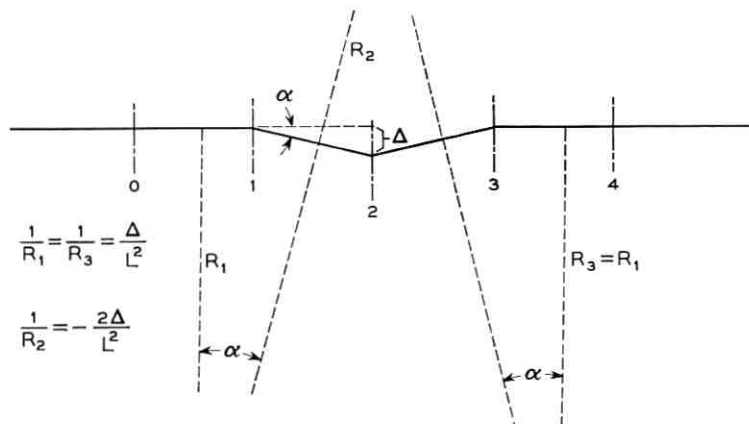


Fig. 6 — One lens of the waveguide is offset by an amount Δ .

while the maximum amplitude of the undulations on the straight outgoing section is given by (24)

$$r_{\max} = \frac{16\delta L^3}{D^2 \theta \sin^2 \theta} = \frac{64\delta L^2}{D^2 \left[\arccos \left(1 - \frac{LC}{2} \right) \right] C(4 - LC)}. \quad (30)$$

A comparison of (29) and (30) shows that the maximum deviation on the tapered bend is considerably larger than the maximum amplitudes of the undulating beam after it has left the bend. The maximum deviation on the tapered bend is larger than the maximum amplitude of the undulating beam leaving the bend by a factor of roughly $\frac{1}{32}DC$. The taper has the effect of canceling some of the oscillations which build up in the bend.

Equations (29) and (30) show that the amplitudes become infinitely large if $LC = 4$. This failure to guide the beam around a bend is not apparent from (28) for the circular bend. In fact, a beam which enters the circular bend on the axis of the incoming waveguide tangentially to the circle does not experience such a catastrophe. However, we see from (18) or (19) that this geometry is rather unique, since in general both (18) and (19) become infinite for $\sin \theta = \sqrt{LC(1 - LC/4)} = 0$. Only in the case considered ($a = \alpha = 0$) can the beam be confined even if $LC = 4$.

Table I lists the values of r_{\max} for the circular and the tapered bend for the case $LC = 2$ (confocal geometry). It is further assumed that both bends lead the waveguide through an angle of $\delta = 90^\circ$.

The maximum amplitude of undulation of a ray which has traversed a tilt is, according to (25),

$$r_{\max} = 2\delta \frac{\sqrt{L^2 - aLC(L - a)}}{\sqrt{LC} \sqrt{4 - LC}} \quad (31)$$

and the amplitude after an offset is, from (27)

$$r_{\max} = 2 \frac{\Delta \sqrt{LC}}{\sqrt{4 - LC}} \quad (32)$$

TABLE I — VALUES OF r_{\max} FOR CONFOCAL GEOMETRY

r_{\max}/L	D/L			
	10	100	1000	10,000
Circular bend	$1.57 \cdot 10^{-1}$	$1.57 \cdot 10^{-2}$	$1.57 \cdot 10^{-3}$	$1.57 \cdot 10^{-4}$
Tapered bend	on bend $1.57 \cdot 10^{-1}$	$1.57 \cdot 10^{-2}$	$1.57 \cdot 10^{-3}$	$1.57 \cdot 10^{-4}$
	after bend $1.60 \cdot 10^{-1}$	$1.60 \cdot 10^{-3}$	$1.60 \cdot 10^{-5}$	$1.60 \cdot 10^{-7}$

Both of these amplitudes become infinite for $LC = 4$. However, if the tilt is placed exactly halfway in between two lenses ($2a = L$), (31) becomes $r_{\max} = \delta L/2$ if $LC = 4$. In this way even a lens-waveguide with concentric geometry can be tilted without loss of the beam.

VII. ACKNOWLEDGMENT

E. A. J. Marcatili contributed to this article by making many helpful suggestions.

REFERENCES

1. Goubau, G., and Schwering, F., On the Guided Propagation of Electromagnetic Wave Beams, *Trans. I.R.E.*, AP-9, May, 1961, pp. 248-256.
2. Pierce, J. R., *Theory and Design of Electron Beams*, D. Von Nostrand Co., New York, 1954.
3. Gardner, M. F., and Barnes, J. L., *Transients in Linear Systems*, John Wiley and Sons, Inc., New York, 1942.

Circular Electric Wave Propagation in Periodic Structures

By G. W. LUDERER and H.-G. UNGER

(Manuscript received November 7, 1963)

TE₀₁ propagation in helix waveguide and spaced-ring guide is analyzed for frequencies where the wavelength is comparable to the period of the structures. By conformal mapping the boundary value problem is reduced to that of a waveguide with smooth walls but inhomogeneous dielectric lining. The lining modifies the magnetic field near the wall and changes the distribution of eddy currents and heat losses in the wires. As frequency increases, the field penetrates more into the space between wires, the eddy currents are more evenly distributed and the heat loss decreases from its quasistatic value of, for example, 10 per cent more than in plain waveguide to only 5 per cent more. Any substantial increase in heat loss occurs only when the wavelength is shorter than the period of the structure. Due to the periodicity, there are stop-bands when any number of half wavelengths just fit into the period. The relative width of the stop-band and its maximum attenuation per period are independent of waveguide diameter and period length and are only functions of the relative geometry of the section. Because of the stop-bands being so narrow and their attenuation being quite modest, one may well accept them within the range of operating frequencies.

I. INTRODUCTION

Low-pitch helix waveguide closely wound from insulated wire has been shown to be a good transmission medium for circular electric waves.¹ Likewise, spaced-ring or spaced-disk guides have been considered for TE₀₁ transmission.² All these structures are periodic along the axis of propagation. In analyzing them, however, the period has always been assumed short compared to the wavelength of propagation and the periodic structure then replaced by an anisotropic but homogeneous model.³⁻⁶

Recently, measurements have indicated that the TE₀₁ loss is low

enough at very high frequencies — perhaps up to 300 gc — for the helix waveguide to be operated there.⁷ At these frequencies the period could no longer be assumed to be short compared to the wavelength. Furthermore, a detailed study of the optimum jacket for most efficient unwanted mode absorption over wide frequency bands has indicated that the helix wire diameter and spacing should be nearly a third of the wavelength at the upper band limit.⁸ Both these results point out the need for a more accurate analysis of circular electric wave propagation in periodic structures, taking into account a period comparable to the wavelength of propagation. It is to be expected that the distribution of electric surface currents around the helix wires or rings and disks will depend on frequency. The losses associated with these eddy currents will therefore also depend on frequency. Furthermore, a stop-band of propagation is to be expected when the wavelength becomes half the period of the structure. Both the eddy current losses and the width and height of the stop-band will be studied here.

II. MATHEMATICAL MODELS FOR PERIODIC STRUCTURES

2.1 *Spaced-Ring Guide*

Helix waveguide for TE_{01} transmission is of very low pitch. For present purposes the pitch may be neglected entirely and the helix waveguide replaced by a spaced-ring guide. Furthermore, the dielectric material in between the wires and the lossy structure surrounding the helix are of very little influence on TE_{01} propagation. They and the helix pitch may be taken into account separately.^{4,6} The spaced-ring structure of Fig. 1 embedded in a homogeneous and isotropic medium will be used as a model for the present study. While this model with rings of round cross section refers in particular to helix wires of round cross section, it may readily be modified to refer to other wire cross sections or to other spaced-ring and spaced-disk guides. The general method of analysis will always be the same.

Dimensions and coordinates (x, φ, y) in Fig. 1 are chosen with respect to a mean radius a of the rings. The structure being periodic, it suffices to consider a section I/II/III/IV of the guide. Because of symmetry even only one-half (I/II'/III'/IV) of this section may be considered.

2.2 *Round Waveguide with Inhomogeneous Dielectric Lining*

2.2.1 *Maxwell's Equations*

Corresponding to a circular electric wave in round waveguide, the electromagnetic field in the spaced-ring guide will be assumed to have

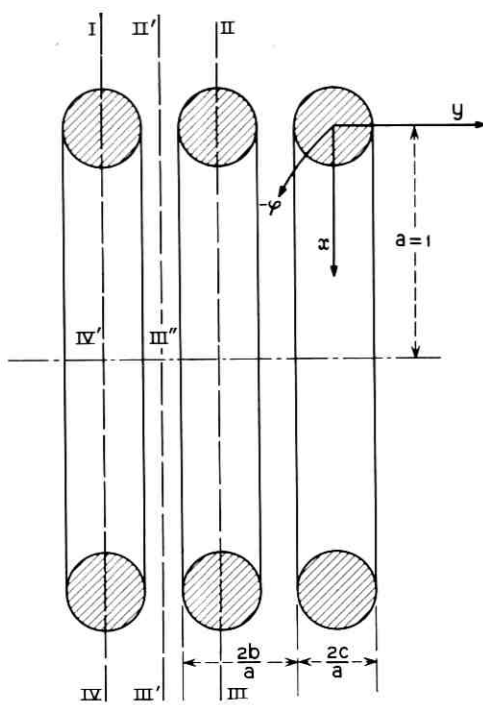


Fig. 1 — Spaced-ring guide.

only components:

$$E_\varphi, H_y, H_x.$$

For perfectly conducting rings the tangential component E_t of the electric field and normal component H_n of the magnetic field vanish on the surface of the rings

$$E_t = H_n = 0. \quad (1)$$

It is therefore expedient to use orthogonal and curvilinear coordinates which have the conducting boundaries as coordinate surfaces. Wire radius and spacing in practical structures are much smaller than the waveguide radius

$$b \ll a, \quad c \ll a. \quad (2)$$

The curvilinear coordinates should therefore approach rectilinear coordinates as the distance from the wires increases. The coordinate $a\varphi$ may be assumed rectilinear throughout.

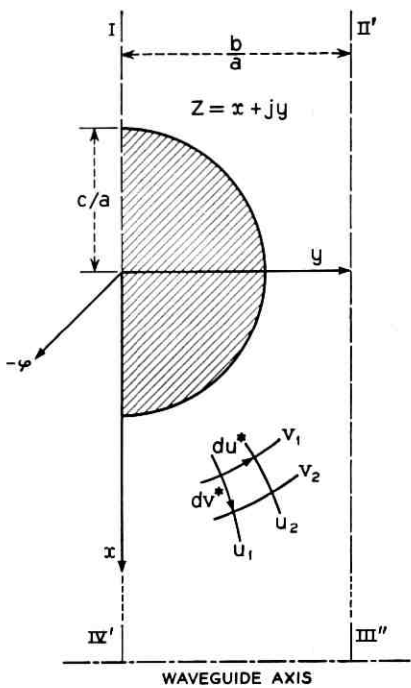


Fig. 2 — Section of spaced-ring guide in Z plane with curvilinear coordinates u and v .

Fig. 2 shows a basic section I/II'/III''/IV' of the spaced-ring line in the (x,y) plane. The curvilinear coordinates are indicated by u and v . Regarding x and y as real and imaginary coordinates in the plane of the complex variable,

$$Z = x + jy,$$

the curvilinear coordinates u and v may be regarded as real and imaginary parts of the complex variable

$$W(Z) = u(x,y) + jv(x,y). \quad (3)$$

The transition from Z to W constitutes a conformal transformation. W being an analytic function of Z , the Cauchy-Riemann equations are satisfied

$$\frac{\partial x}{\partial u} = \frac{\partial y}{\partial v}, \quad \frac{\partial x}{\partial v} = -\frac{\partial y}{\partial u} \quad (4)$$

and the derivative may be written

$$\frac{dZ}{dW} = \frac{\partial x}{\partial u} + j \frac{\partial y}{\partial u}, \quad (5)$$

$$\left| \frac{dZ}{dW} \right| = \sqrt{\left(\frac{\partial x}{\partial u} \right)^2 + \left(\frac{\partial y}{\partial u} \right)^2} = M. \quad (6)$$

The elements of length in the Z plane of Fig. 2 are

$$du^* = \left(\frac{\partial x}{\partial u} + j \frac{\partial y}{\partial u} \right) du \quad (7)$$

$$\begin{aligned} |du^*| &= M du \\ |dv^*| &= M dv. \end{aligned} \quad (8)$$

The metrical coefficients of the curvilinear coordinates u^* , φ , v^* follow from

$$h_{v^*} = M, \quad h_\varphi = 1, \quad h_{u^*} = M. \quad (9)$$

Maxwell's equations written in the curvilinear system are

$$\begin{aligned} \frac{\partial}{\partial u} (E_\varphi) &= j\omega\mu_0 M H_{v^*} \\ \frac{\partial}{\partial v} (E_\varphi) &= -j\omega\mu_0 M H_{u^*} \\ \frac{\partial}{\partial u} (M H_{v^*}) - \frac{\partial}{\partial v} (M H_{u^*}) &= j\omega\epsilon_0 M^2 E_\varphi \\ \frac{\partial}{\partial v} (M H_{v^*}) + \frac{\partial}{\partial u} (M H_{u^*}) &= 0. \end{aligned} \quad (10)$$

Substituting

$$H_u = M H_{u^*}, \quad H_v = M H_{v^*}, \quad \epsilon = M^2(u, v) \quad (11)$$

Maxwell's equations for a fictitious W plane of rectilinear coordinates u and v obtain

$$\begin{aligned} \frac{\partial}{\partial u} (E_\varphi) &= j\omega\mu_0 H_v \\ \frac{\partial}{\partial v} (E_\varphi) &= -j\omega\mu_0 H_u \\ \frac{\partial}{\partial u} (H_v) - \frac{\partial}{\partial v} (H_u) &= j\omega\epsilon_0 \epsilon E_\varphi \\ \frac{\partial}{\partial v} (H_v) + \frac{\partial}{\partial u} (H_u) &= 0. \end{aligned} \quad (12)$$

Comparing (10) and (12), the problem of finding the electromagnetic field between curved boundaries has been transformed into the problem of finding the field between straight and parallel boundaries in a medium of varying permittivity $\epsilon(u,v)$. The transition from one plane to the other ensues by conformal mapping. The analytic function of this conformal transformation by (6) and (9) determines the permittivity $\epsilon(u,v)$. This method was first developed by Routh,⁹ who studied the vibration of a membrane of irregular shape by transforming it into a rectangle. The method was first applied to electromagnetic boundary value problems by Meinke¹⁰ and Rice.¹¹ While in the more general field problem a fictitious inhomogeneous medium of anisotropic character has to be dealt with, at present, due to the axial symmetry ($\partial/\partial\varphi = 0$) of the fields, the fictitious inhomogeneous medium is isotropic.

2.2.2 Conformal Transformation

A suitable analytic function to effect the desired transformation approximately was found by Richmond¹² and used by Morrison¹³ to calculate the heat loss of circular electric waves in helix waveguide. The function is in parameter form

$$Z = \frac{2(b/a)}{\pi(1 + \Psi)} \left[\tanh^{-1} \frac{\sqrt{\xi - 1}}{\sqrt{\xi + \nu}} + \Psi \tanh^{-1} \frac{\sqrt{\xi + 1}}{\sqrt{\xi + \nu}} \right] \quad (13)$$

$$W = \frac{b/a}{2\pi} \left[\sin^{-1}(\xi) + \sin^{-1} \left(\frac{2\xi + \nu - 1}{\nu + 1} \right) \right]. \quad (14)$$

The plane of the complex variable $Z = x + jy$ is by means of an auxiliary variable $\xi = \xi + j\eta$ mapped onto the plane of the variable $W = u + jv$. The parameter Ψ is the smallest positive root of

$$\sin \left[\frac{\pi c}{2b} (1 + \Psi) \right] = \tanh \left[\frac{\pi c}{2b} \left(1 + \frac{1}{\Psi} \right) \right] \quad (15)$$

and ν is given by

$$\nu = \coth^2 \left[\frac{\pi c}{2b} \left(1 + \frac{1}{\Psi} \right) \right] + \cot^2 \left[\frac{\pi c}{2b} (1 + \Psi) \right]. \quad (16)$$

The derivative of the above analytic function is

$$\frac{dZ}{dW} = -j \frac{2}{(1 + \Psi)} \frac{\sqrt{\xi + 1} + \Psi \sqrt{\xi - 1}}{\sqrt{\xi + 1} + \sqrt{\xi + \nu}}. \quad (17)$$

The transformation of the Z plane boundaries via the ξ plane into

straight lines of the W plane is shown in Fig. 3. The waveguide radius a has been set equal to one and is the unit of length in the Z and W planes.

The transformation by (13) and (14) is only approximate and will give circular contours (D, C, B) in the Z plane only if c is somewhat smaller than b . For $c/b \rightarrow 1$ the transformation will be into a square

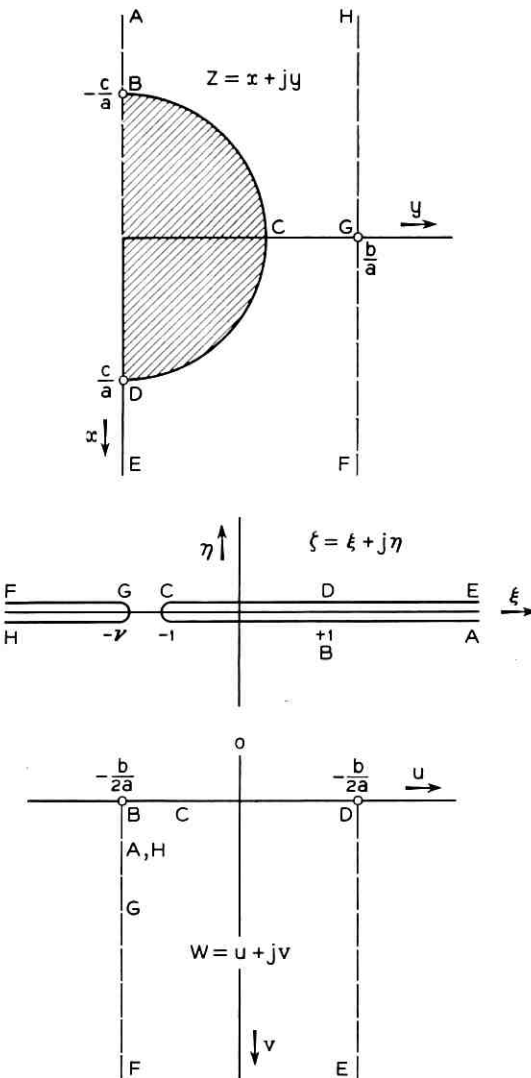


Fig. 3 — Conformal transformations by (13) and (14).

contour. For $c/b < 0.5$ the largest deviation from a circle is 2 per cent of c . In a closely wound helix the wire spacing will be determined by its insulation. Presently used helix wires have $c/b = 0.70 \dots 0.85$. The maximum deviation from a circular radius is here between 8 and 20 per cent.

Fig. 4 shows three contours for different ratios c/b . They are obtained from (13) by letting

$$-1 \leq \xi \leq +1, \quad \eta = \pm 0.$$

The resulting equations are

$$\begin{aligned} x &= \operatorname{sgn}(\eta) \frac{2 \frac{b}{a} \Psi}{\pi(1 + \Psi)} \tanh^{-1} \sqrt{\frac{\xi + 1}{\xi + \nu}} \\ y &= \frac{2 \frac{b}{a}}{\pi(1 + \Psi)} \tan^{-1} \sqrt{\frac{1 - \xi}{\nu + \xi}}. \end{aligned} \quad (18)$$

The deviations from a circular contour will be neglected subsequently.

The inverse trigonometric and hyperbolic functions in (13) and (14) are multiple valued. To obtain the rectilinear boundaries in the W plane a suitable combination of principal and other values of these functions has to be chosen (see Appendix, Section A.1).

In Fig. 5 a number of elementary cells $BDEF$ of Fig. 3 have been arranged back-to-back to form a round waveguide filled with periodically varying permittivity. The waveguide is bound by the conducting surface BCD of the rings transformed into a straight contour.

Asymptotic values of the permittivity are obtained from (17).

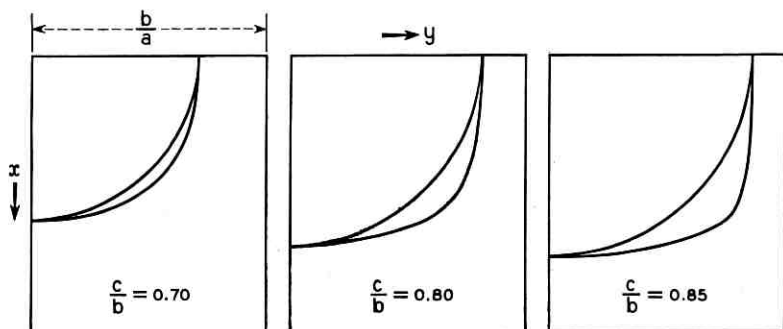


Fig. 4 — Wire contours according to (13) and (14).

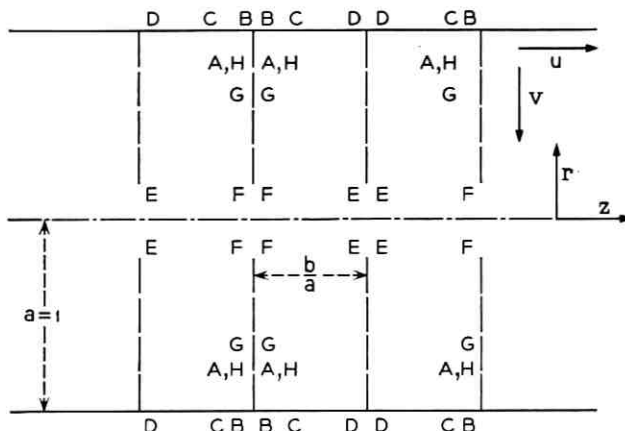


Fig. 5 — The smooth-wall waveguide formed by arranging transformed sections of Fig. 3 back-to-back.

Moving from the spaced rings towards the center of the guide:

$$\lim_{z \rightarrow +\infty} \left| \frac{dZ}{dW} \right|^2 = 1. \quad (19)$$

Moving outwardly in the opposite direction

$$\lim_{z \rightarrow -\infty} \left| \frac{dZ}{dW} \right|^2 = \infty. \quad (20)$$

According to (19), inside the guide sufficiently far from the rings, the permittivity is uniform and as in free space.

Because of (2) it differs from free space only close to the walls and may therefore be regarded as a thin dielectric lining.

According to (20), at A, H in Figs. 3 and 5 the permittivity is infinitely large. Because of (11) the region outside the rings is therefore practically free of magnetic fields.

The mathematical model thus obtained for the spaced-ring guide is a closed round waveguide with inhomogeneous dielectric lining. The permittivity of the lining may be found from (14) and (17) anywhere in the W plane.

2.3 Approximate Model for Closed Structures

As it is, the present model is not suitable for perturbational analysis of loss and wave interaction. Such perturbational analysis requires the relative permittivity to be distributed in the guide such that

$$\frac{1}{S} \iint_s (M^2 - 1) ds \ll 1$$

for any cross section. In cross sections containing the pole A,H of permittivity this condition will not be satisfied. The pole at A,H is of such a nature that not even the integral $\iint M^2 du dv$ over an area in the W plane including A,H is finite.

Actually, one should expect such poles in the transformed structure. The original structure extends to infinity in cross-sectional direction. Circular electric waves in the original structure cannot be lossless normal modes but must be leaky waves, since there is some leakage of power, however small, through the gaps between the helix wires. The transformed structure, on the other hand, is bound by conducting surfaces and cannot support leaky waves.

In order to get around this difficulty and still meet the objectives of this analysis, the original structure is according to Fig. 6(a) surrounded by a magnetically conducting shield ($\epsilon = 0, \mu = \infty$) close to the wires. In the transformed structure of Fig. 6(b) the shield will appear as a thin wire of magnetic conductor located at A,H . This magnetic wire, being so very thin and so close to the wall, will not change the field distribution very much. It will only displace the electric field somewhat and modify the magnetic field so that it has no tangential components on its surface. For all wire spacings of practical interest this magnetic wire will be of so little influence that it may be neglected entirely and the small cross-sectional area of the wire be assumed to have $\epsilon = \mu = 1$.

The mathematical model thus obtained no longer represents the open structure of spaced wires but is an approximate representation of the magnetically closed structure. It will serve well to calculate eddy current losses and stop-bands but will not show the leakage of power through the gaps. The latter has been calculated approximately elsewhere.³

In all subsequent calculation the magnetic shield will be assumed at $e = b$. The corresponding small area near A,H in the transformed structure will be assumed to have $\epsilon = \mu = 1$ and will be excluded from integrations over the W plane.

III. HEAT LOSS IN HELIX WIRES

3.1 *The Magnetic Field near the Conducting Surfaces*

In round waveguide with smooth walls a dielectric lining will modify the tangential magnetic field of circular electric waves near the wall. In general, the field will be increased and will therefore add to the heat

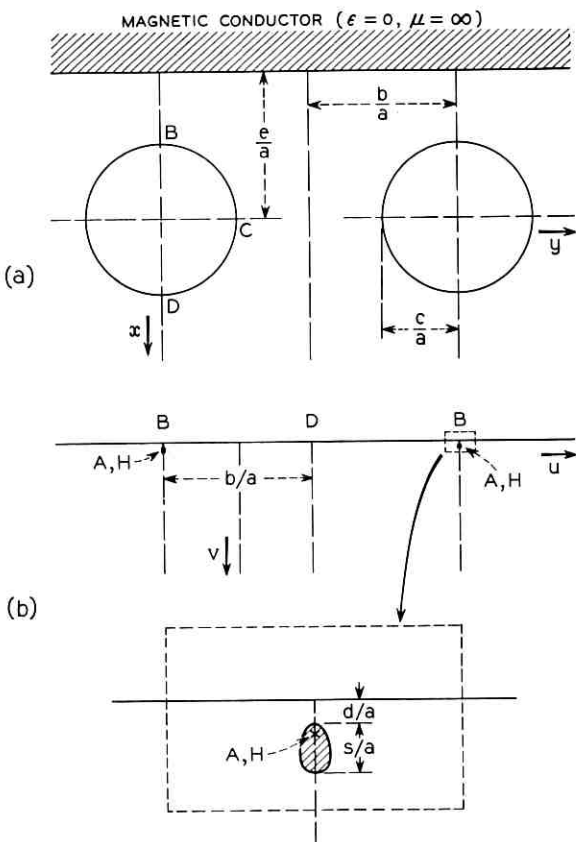


Fig. 6 — A magnetic shield (a) transformed into thin magnetic wires (b). For $c/b = 0.5$ and $e/b = 1$ the wire size is $s/b \approx 0.015$ and its distance from the wall is $d/b \approx 0.009$. For larger values of c/b , wire size and spacing decrease rapidly.

loss of circular electric waves. In helix waveguide this effect has to be taken into account in addition to the eddy current loss of the current distribution around the wire.

The change in magnetic field at the wall due to a lining, the permittivity of which is only a function of guide radius, has been calculated before¹⁴

$$\frac{\Delta H_u}{H_{u0}} = \omega^2 \mu_0 \epsilon_0 \int_0^a [\epsilon(r) - 1][a - r] dr. \quad (21)$$

H_{u0} is the longitudinal magnetic field at the smooth wall of a waveguide filled with a medium of uniform wave number $\omega\sqrt{\mu_0\epsilon_0}$. The relation may readily be generalized to take into account also a z -dependence

of permittivity (Appendix, Section A.2). Introducing the free-space wavelength

$$\lambda = \frac{2\pi}{\omega\sqrt{\mu_0\epsilon_0}}$$

and coordinates u and $v = (1/a)(a - r)$, the u -dependent change in magnetic field may be calculated from

$$\frac{\Delta H_u}{H_{u0}} = 4\pi^2 \left(\frac{a}{\lambda}\right)^2 \int_0^1 [M^2(u,v) - 1]v dv. \quad (22)$$

According to (11), the actual magnetic field H_u tangent to the conducting surfaces of the spaced-ring guide can now be written as

$$\begin{aligned} & \left[\frac{H_{u*}}{H_{u0}} \right]_{BCD} \\ &= \frac{1}{M(u,0)} \left\{ 1 + 4\pi^2 \left(\frac{a}{\lambda}\right)^2 \int_0^1 [M^2(u,v) - 1]v dv \right\} = f(u). \end{aligned} \quad (23)$$

No closed-form solution of the integral in (23) is available. Evaluation of (23) requires (14) to be solved numerically for ξ and η . M may then be computed from (17). Representative distributions of magnetic field around the wire surface are plotted in Fig. 7. φ_w is the azimuthal angle of a slightly deformed wire cross section.

At low frequencies the space between the rings forms a waveguide below cutoff for circular electric wave fields. The magnetic field decreases rapidly with increasing φ_w . For $a/\lambda \rightarrow 0$ the quasistatic approximation obtains from (17) with

$$\frac{H_{u*}}{H_{u0}} = \left| \frac{dW}{dZ} \right| = \left| \frac{\partial u}{\partial x} - j \frac{\partial u}{\partial y} \right| = |\text{grad } (u)|. \quad (24)$$

As the frequency increases the magnetic field penetrates more and more into the space between the rings. Eventually, at very high frequencies substantial circular electric wave loss will result from radiation through the rings.

3.2 Heat Loss at High Frequencies

Assuming the skin depth δ to be small compared to the curvature radius of a conductor surface, the power P_v lost as heat through a surface F with conductivity σ may be found from the tangential magnetic

field according to

$$P_v = \frac{1}{2\sigma\delta} \int_F |H_t|^2 dF. \quad (25)$$

In a waveguide section of length $2b$ and radius a with uniform magnetic field H_{u0} at the walls, the power lost as heat is

$$P_{v0} = \frac{2\pi(b/a)}{\sigma\delta} H_{u0}^2 a^2. \quad (26)$$

The power lost in one section of the spaced ring guide is

$$P_v = \frac{2\pi}{\sigma\delta} H_{u0}^2 a^2 \int_{-(b/2a)}^{+(b/2a)} \left[\frac{H_u}{H_{u0}} \right]^2 du.$$

The attenuation constant is proportional to these power losses. The ratio of attenuation due to heat loss in the spaced-ring guide to attenua-

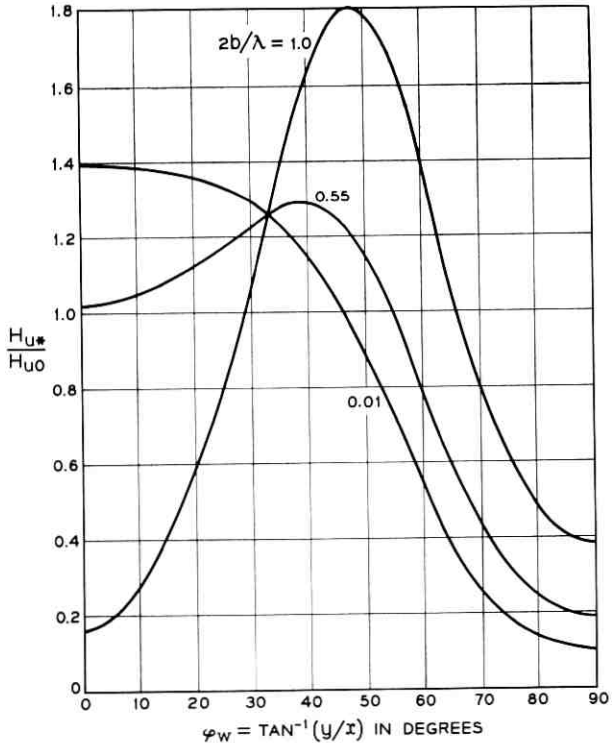


Fig. 7 — Magnetic field at the wire surface: $c/b = 0.70$.

tion in plain waveguide is therefore

$$\frac{P_v}{P_{v0}} = \frac{a}{b} \int_{-(b/2a)}^{+(b/2a)} \frac{1}{M^2} \left[1 + 4\pi^2 \left(\frac{a}{\lambda} \right)^2 \int_0^1 (M^2 - 1)v dv \right]^2 du$$

which by substitution of $u = (b/a) \bar{u}$ is independent of b/a

$$\frac{P_v}{P_{v0}} = \int_{-\frac{1}{4}}^{+\frac{1}{4}} \frac{1}{M^2} \left[1 + 4\pi^2 \left(\frac{a}{\lambda} \right)^2 \int_0^1 (M^2 - 1)v dv \right]^2 d\bar{u}. \quad (27)$$

As in (23), no closed-form solution of the integrals is available. From a numerical evaluation of (27) representative curves of loss ratio versus frequency are plotted in Fig. 8. From its quasistatic value at low frequencies the loss ratio decreases a few per cent with increasing frequency.

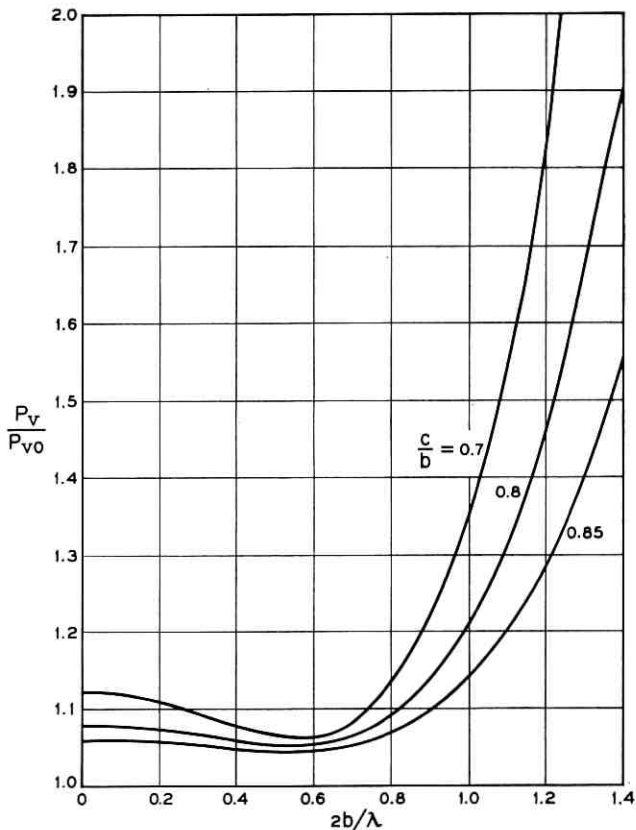


Fig. 8 — Heat loss of TE_{01} wave in helix waveguide compared to heat losses in smooth-wall waveguide.

There is a minimum of loss ratio when the free-space wavelength is nearly twice the period ($\lambda \approx 4b$). This minimum in loss ratio is due to more evenly distributed currents around the wire surface, when the magnetic field penetrates more into the space between the wires.

Any substantial increase in loss ratio will only occur when the free-space wavelength is less than the period of the structure ($\lambda < 2b$). But here the present approximations are beginning to fail.

At low frequencies for $a/\lambda \rightarrow 0$, heat loss in the quasistatic case obtains from

$$\frac{P_v}{P_{v0}} = \frac{a}{b} \int_{-(b/2a)}^{+(b/2a)} \frac{1}{M^2} du. \quad (28)$$

The integral in (28) has been evaluated by Morrison:¹³

$$\begin{aligned} \frac{P_v}{P_{v0}} = (1 + \Psi) \left\{ \frac{1 - \Lambda_0(\sin^{-1} \Psi, \kappa)}{\sqrt{1 - \Psi^2}} \right. \\ \left. + \cos \left[\frac{\pi c}{2b} (1 + \Psi) \right] \cot \left[\frac{\pi c}{2b} (1 + \Psi) \right] \frac{K(\kappa)}{\pi \Psi} \right\} \end{aligned} \quad (29)$$

where

$$\kappa^2 = 1 - \frac{1}{\Psi} \cos \left[\frac{\pi c}{2b} (1 + \Psi) \right].$$

Here $K(\kappa)$ is the complete elliptic integral of the first kind and modulus κ , $\Lambda_0(\beta, \kappa)$ is Heumann's lambda function.

IV. PROPAGATION CHARACTERISTICS OF SPACED-RING SECTION

4.1 *Transmission Line Equations*

Wave propagation in the mathematical model of round waveguide with periodically inhomogeneous lining may be represented in terms of normal modes of the round waveguide without lining. The effect of the lining is to introduce coupling between these normal modes.¹⁵

Interaction will be strongest between those modes the beat wavelength of which is near the period of lining variations. As the frequency increases, such interaction will first occur between forward- and backward-traveling components of the circular electric wave when the guide wavelength is near twice the period length of the structure. When it is exactly twice this period length, reflections from each section will add in phase and propagation will suffer from destructive interference. Interaction with all other modes may be neglected in this range.

Coupled line equations for forward-traveling components A and backward-traveling components B of one and the same wave are written as¹⁶

$$\begin{aligned}\frac{dA}{dz} &= -\gamma(z)A - k(z)B \\ \frac{dB}{dz} &= k(z)A + \gamma(z)B.\end{aligned}\tag{30}$$

A and B are the amplitudes of traveling waves normalized with respect to power. $\gamma(z)$ is the propagation factor γ_0 of the wave in empty waveguide modified by the presence of the lining⁵

$$\gamma(z) = \gamma_0 - \frac{\omega^2 \mu_0 \epsilon_0 \Delta(z)}{2\gamma_c}. \tag{31}$$

$k(z)$ is the coupling or reflection coefficient between forward- and backward-traveling components of the wave¹⁵

$$k(z) = \frac{\omega^2 \mu_0 \epsilon_0 \Delta(z)}{2\gamma_c} \tag{32}$$

$\Delta(z)$ depends on the permittivity of the lining and its distribution over the cross section as well as on the particular wave under consideration. For TE₀₁ with cylinder coordinates (r, φ, z)

$$\Delta(z) = - \int_0^a \frac{2[\epsilon_r(r, z) - 1] J_1^2\left(\frac{\rho_{01}}{a} r\right) r dr}{a^2 J_0^2(\rho_{01})}. \tag{33}$$

The relative permittivity differs from unity only close to the wall. The Bessel function in (33) may therefore be replaced by its linear approximation at its first zero ρ_{01} .

In normalized coordinates u and v , one obtains instead of (33)

$$\Delta(u) = -2\rho_{01}^2 \int_0^1 [M^2(u, v) - 1] v^2(1 - v) dv. \tag{34}$$

The coupling coefficient may now be written as

$$ak(z) = -j \frac{4\pi^2 \rho_{01}}{\frac{\lambda}{a} \sqrt{\left(\frac{2\pi}{\rho_{01}}\right)^2 - \left(\frac{\lambda}{a}\right)^2}} \int_0^1 [M^2 - 1] v^2(1 - v) dv \tag{35}$$

where

$$\gamma_0^2 = \frac{\rho_{01}^2}{a^2} - \omega^2 \mu_0 \epsilon_0 \quad (36)$$

and u has been replaced by z .

Since $|k| \ll |\gamma|$ the modification of γ from (31) may be neglected in (30). Thus simplified, the transmission line equations written in matrix notation are

$$\frac{d}{dz} \begin{bmatrix} A \\ B \end{bmatrix} = \begin{bmatrix} -\gamma & -k(z) \\ k(z) & \gamma \end{bmatrix} \begin{bmatrix} A \\ B \end{bmatrix} \quad (37)$$

or

$$[A]' = [\gamma(z)] \cdot [A]. \quad (38)$$

In Fig. 9 the coupling coefficient $k(z)$ is plotted for representative values of c/b . As $c/b \rightarrow 1$ the coupling disappears because of deformation of the round wire into a square cross section by the conformal transformation.

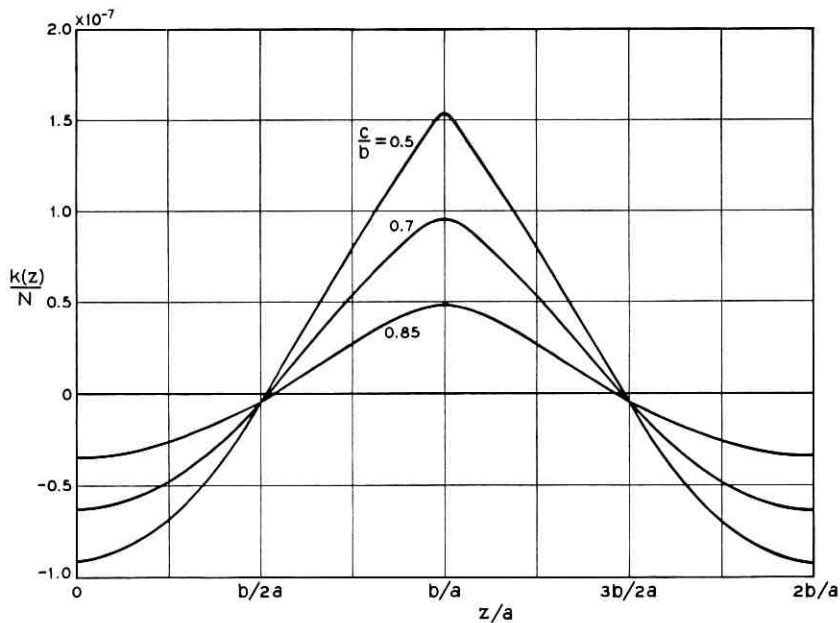


Fig. 9 — Coefficient of coupling between forward- and backward-traveling TE_{01} waves in spaced-ring waveguide.

4.2 The Transmission Matrix

The matrix $[\gamma(z)]$ in (38) is almost diagonal for all values of z . An approximate solution to (38) is therefore easily found by iterative integration. Thus without specifying any initial values the general transmission matrix of (38) will be calculated.

Formally integrating (38), one obtains

$$[A(l)] = [A(0)] + \int_0^l [\gamma(z)] [A(z)] dz \quad (39)$$

in form of an iterative procedure

$$[A_{\nu+1}(l)] = [A(0)] + \int_0^l [\gamma(z)] [A_\nu(z)] dz. \quad (40)$$

After two iterations, as shown in Section A.3 of the Appendix, a suitable approximation is found for the transmission matrix $[T]$ in

$$[A(l)] = [T] \cdot [A(0)]. \quad (41)$$

The elements of

$$[T] = \begin{bmatrix} T_{11} & T_{12} \\ T_{21} & T_{22} \end{bmatrix} \quad (42)$$

are

$$\begin{aligned} T_{11} &= e^{-\gamma l} \left[1 - \int_0^l k(z) e^{2\gamma z} \int_0^z k(z') e^{-2\gamma z'} dz' dz \right] \\ T_{12} &= -e^{-\gamma l} \int_0^l k(z) e^{2\gamma z} dz \\ T_{21} &= e^{\gamma l} \int_0^l k(z) e^{-2\gamma z} dz \\ T_{22} &= e^{\gamma l} \left[1 - \int_0^l k(z) e^{-2\gamma z} \int_0^z k(z') e^{2\gamma z'} dz' dz \right]. \end{aligned} \quad (43)$$

Substantial interaction between forward- and backward-traveling components A and B will be found only in a narrow band of frequencies centered about $\lambda = 4b$. Of all the Fourier components contained in $k(z)$, only the component k_1 of first order will contribute to the elements of the transmission matrix at frequencies near $\lambda = 4b$. Replacing $k(z)$ in (43) by this Fourier component according to

$$k(z) \approx N k_1 \cos \left(\frac{\pi z}{b} \right) \quad (44)$$

where

$$N = - \frac{j \frac{4\pi^2}{b} \rho_{01}}{\lambda \sqrt{\left(\frac{2\pi}{\rho_{01}}\right)^2 - \left(\frac{\lambda}{a}\right)^2}} \quad (45)$$

is therefore indicated.

The integrals in (43) have been evaluated with this substitution and $\gamma = \alpha + j\beta$. In case of perfectly conducting walls for a period $2b$ corresponding to one section of the spaced-ring line the transmission matrix is

$$[T] \equiv \begin{bmatrix} e^{-j2\beta b} (1 - C_{11}) & -e^{-j2\beta b} C_{12} \\ e^{+j2\beta b} C_{21} & e^{+j2\beta b} (1 - C_{22}) \end{bmatrix} \quad (46)$$

where

$$\begin{aligned} C_{11} &= (e^{+j4\beta b} - 1) \left[p \frac{4\beta^2 b^2 + q^2}{4\beta^2 b^2 - \pi^2} \right]^2 - j \frac{p^2}{2\beta b} \frac{(4\beta^2 b^2 + q^2)^2}{(4\beta^2 b^2 - \pi^2)} \\ C_{22} &= (e^{-j4\beta b} - 1) \left[p \frac{4\beta^2 b^2 + q^2}{4\beta^2 b^2 - \pi^2} \right]^2 + j \frac{p^2}{2\beta b} \frac{(4\beta^2 b^2 + q^2)^2}{(4\beta^2 b^2 - \pi^2)} \\ C_{12} &= (e^{+j4\beta b} - 1) \left[p \frac{4\beta^2 b^2 + q^2}{4\beta^2 b^2 - \pi^2} \right] \end{aligned} \quad (47)$$

$$\begin{aligned} C_{21} &= -(e^{-j4\beta b} - 1) \left[p \frac{4\beta^2 b^2 + q^2}{4\beta^2 b^2 - \pi^2} \right] \\ p &= -\frac{\rho_{01}^2 k_1}{2} \end{aligned} \quad (48)$$

$$q = 2 \frac{b}{a} \rho_{01}. \quad (49)$$

In case of $2\beta = \pi/b$ when the section is just half the guide wavelength

$$\begin{aligned} C_{11} &= -\frac{p^2}{2} \left[\frac{\pi^2 + q^2}{\pi} \right]^2 \pm j \frac{p^2}{4\pi} \left[\frac{\pi^2 + q^2}{\pi} \right]^2 \\ C_{21} &= jp \left[\frac{\pi^2 + q^2}{\pi} \right]. \end{aligned} \quad (50)$$

4.3 Transmission Factor

To evaluate wave propagation in the periodic structure, its normal modes should be considered as they are composed of forward- and backward-traveling components of modes in plain guide. The normal modes propagate along the structure, changing their fields only by a constant factor from section to section. This transmission factor G of normal modes is found by looking for solutions

$$\begin{aligned} A(l) &= GA(0) \\ B(l) &= GB(0) \end{aligned} \quad (51)$$

of (41). Substituting (51) for $A(l)$ and $B(l)$ into (41), a homogeneous system of linear equations obtains which can have nontrivial solutions only for

$$\det ([T] - G [U]) = 0 \quad (52)$$

where $[U]$ is the unit matrix. Values of G solving the characteristic equation (52) are

$$G_1 = \frac{1}{2} [T_{11} + T_{22} \pm \sqrt{(T_{11} - T_{22})^2 + 4T_{12}T_{21}}]. \quad (53)$$

They are eigenvalues of the transmission matrix $[T]$ and transmission factors of normal modes of the periodic structure. Substituting from (47), (48) and (49) for the elements of $[T]$:

$$\begin{aligned} G_1 = & \cos(2\beta b) + 4p^2 \left[\frac{4\beta^2 b^2 + q^2}{4\beta^2 b^2 - \pi^2} \right]^2 \sin^2(2\beta b) \cos(4\beta b) \\ & - \frac{p^2(4\beta^2 b^2 + q^2)^2}{(4\beta^2 b^2 - \pi^2)} \sin(2\beta b) \pm \left\{ 4 \left[p \frac{4\beta^2 b^2 + q^2}{4\beta^2 b^2 - \pi^2} \right]^2 \sin^2(2\beta b) \right. \\ & - \sin^2(2\beta b) - 4 \left[p \frac{4\beta^2 b^2 + q^2}{4\beta^2 b^2 - \pi^2} \right]^4 \sin^2(2\beta b) \cos^2(4\beta b) \\ & - \frac{p^4(4\beta^2 b^2 + q^2)^4}{4\beta^2 b^2(4\beta^2 b^2 - \pi^2)^2} \cos^2(2\beta b) \\ & + 4 \left[p \frac{4\beta^2 b^2 + q^2}{4\beta^2 b^2 - \pi^2} \right]^2 \sin^2(2\beta b) \cos(4\beta b) \\ & - \frac{p^2(4\beta^2 b^2 + q^2)^2}{2\beta b(4\beta^2 b^2 - \pi^2)} \sin(4\beta b) \\ & \left. + 2 \frac{p^4(4\beta^2 b^2 + q^2)^4}{2\beta b(4\beta^2 b^2 - \pi^2)^3} \sin(4\beta b) \cos(4\beta b) \right\}^{\frac{1}{2}}. \end{aligned} \quad (54)$$

Since for $b \ll a$, $|p| \ll 1$, also, the terms of second order in p may be neglected. The transmission factors reduce to

$$\begin{aligned} G_1 = \cos(2\beta b) &\pm \left\{ 4 \left[p \frac{4\beta^2 b^2 + q^2}{4\beta^2 b^2 - \pi^2} \right]^2 \sin^2(2\beta b) \right. \\ &+ 4 \left[p \frac{4\beta^2 b^2 + q^2}{4\beta^2 b^2 - \pi^2} \right]^2 \sin^2(2\beta b) \cos(4\beta b) \quad (55) \\ &\left. - \frac{p^2 (4\beta^2 b^2 + q^2)^2}{2\beta b (4\beta^2 b^2 - \pi^2)} \sin(4\beta b) \right\}^{\frac{1}{2}}. \end{aligned}$$

In case of $2\beta b = \pi$:

$$\begin{aligned} G_1 = -1 &\mp p \left(\pi + \frac{q^2}{\pi} \right) \\ = -1 &\pm \frac{k_1 \pi \rho_{01}^2}{2} \pm \frac{2k_1 \left(\frac{b}{a} \right)^2 \rho_{01}^4}{\pi}. \quad (56) \end{aligned}$$

4.4 Evaluation of the Transmission Factor

Writing $G = e^{-\gamma' l}$, attenuation factor

$$2\alpha' b = \ln |G| \quad (57)$$

and phase factor

$$2\beta' b = \angle G \quad (58)$$

of one section of a spaced-ring guide obtain.

Frequency ranges for which G is real constitute stop-bands of the periodic structure. There is no phase change from section to section in stop-bands, but only a decrease in amplitude by G . Stop-bands are characterized by a positive quantity under the square root of (55). Outside of stop-bands this quantity is negative. The stop-bands extend to the zeros of the square root.

Since $|p| \ll 1$, the square root will be zero only when $|\sin 2\beta b| \ll 1$ also; letting $2\beta b = \pi - \theta$ with $|\theta| \ll 1$, (55) may be approximated near the stop-band by

$$G_1 \approx -1 \pm \sqrt{p^2 \pi^2 - \theta^2}. \quad (59)$$

Within the stop-band for

$$|\theta| < |p\pi| = \left| \frac{\rho_{01}^2 k_1 \pi}{2} \right|$$

the attenuation constant is:

$$\alpha' a = \frac{a}{2b} \sqrt{\left(\frac{\rho_{01}^2 k_1}{2}\right)^2 - \theta^2}.$$

With

$$2\beta b \approx 4\pi \frac{b/a}{\lambda/a}$$

for waves sufficiently far from cutoff, the deviation θ from the half-wavelength condition may be expressed by

$$\theta = \pi \left(1 - \frac{4b}{\lambda}\right)$$

and the attenuation constant be written

$$\alpha' a = \frac{a}{2b} \sqrt{\left(\frac{\rho_{01}^2 k_1 \pi}{2}\right)^2 - \pi^2 \left(1 - \frac{4b}{\lambda}\right)^2}. \quad (60)$$

For $\theta = 0$ the center frequency of the stop-band obtains, corresponding to

$$\begin{aligned} \frac{a}{\lambda} &= \sqrt{\left(\frac{a}{4b}\right)^2 + \left(\frac{\rho_{01}}{2\pi}\right)^2} \\ &\approx \frac{a}{4b} \quad \text{when} \quad \frac{b}{a} \ll 1. \end{aligned} \quad (61)$$

Here the attenuation constant is

$$\alpha' a = \frac{\rho_{01}^2 k_1 \pi a}{4b/a}. \quad (62)$$

With $\theta = \pm(\rho_{01}^2 k_1 \pi)/2$, for the stop-band limits the relative width of the stop-band is

$$\frac{\Delta\omega}{\omega} = \rho_{01}^2 k_1. \quad (63)$$

In the present approximation, neglecting heat losses in the conductors, there is no attenuation outside of stop-bands.

Taking these heat losses into account, $2\beta b$ in (55) has to be replaced by $2\beta b - j2\alpha b$, where

$$\alpha = \alpha_{01} \frac{P_v}{P_{v0}}$$

according to Section II. Since $2\alpha b \ll 1$, the attenuation constant at

the center of the stop-band is in this case

$$\alpha' a = \frac{\rho_{01}^2 k_1 (\pi - 4\alpha b) a}{4b/a}. \quad (64)$$

The numerical evaluations in Section II and plots of Fig. 8 show $\alpha \approx \alpha_{01}$ well beyond the first stop-band. Since $4\alpha b \ll \pi$ also the stop-band attenuation and width will not be affected noticeably by the finite conductivity of the wires.

For numerical evaluation of stop-band attenuation and width the Fourier coefficient k_1 according to (44) has been computed and plotted in Fig. 10 versus c/b . k_1 is larger the smaller the ratio c/b . For $c \rightarrow b$ the present conformal transformation is into square wires without spaces. In this case $k_1 \rightarrow 0$. But for $c/b < 0.80$ the approximation of round wires is satisfactory.

Stop-band attenuation $2\alpha'b$ per section and relative stop-band width $\Delta\omega/\omega$ according to (62) and (63) are both proportional to k_1 . Fig. 10 has therefore been provided with additional scales to also represent these two quantities as a function of c/b .

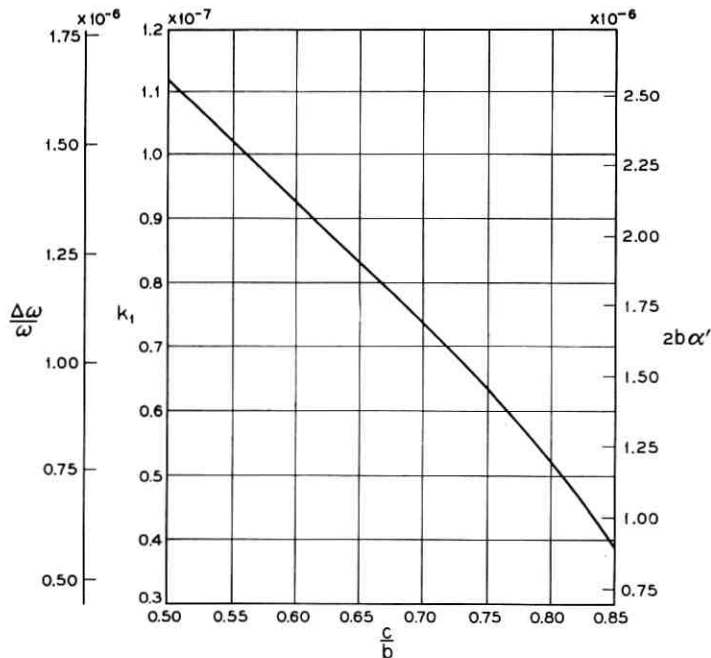


Fig. 10 — First-order Fourier coefficient of TE_{01} coupling in spaced-ring guide; additional scales indicate stop-band width and attenuation.

It is most important for practical purposes that the stop-band attenuation reach only quite modest values and that the stop-band be very narrow. $2\alpha'b$ and $\Delta\omega/\omega$ being only functions of c/b , the absolute quantities α' and $\Delta\omega$ of the stop-band will both be smaller the larger the length $2b$ of the section, provided of course one stays within the range where present approximations hold.

Take for example a helix wire spaced by $2b = 0.15$ mm with $c/b = 0.75$, corresponding to present design practices.¹⁷ The stop-band would occur at $\lambda = 0.3$ mm, corresponding to $f = 1000$ gc. The width $\Delta f = 925$ kc and attenuation $\alpha' = 35$ db/mile of the stop-band would not be objectionable because it is well beyond the frequency range where the helix waveguide will be operated.

Helix wires spaced by $2b = 0.3$ mm with $c/b = 0.75$ corresponding to an optimum design for wideband unwanted mode absorption⁸ would have a stop-band at 500 gc of width $\Delta f = 462.5$ kc and attenuation $\alpha' = 67$ db/mile. Both quantities are smaller but also not objectionable since still outside the operating range.

If, however, no other limitation is imposed on the wire geometry but the space between to be cutoff for circular electric wave fields at the highest operating frequency, then with $c/b = 0.75$ and $\epsilon_r = 3$ for the space between wires:

$$2(b - c) < \frac{1}{2\sqrt{\epsilon_r}} \lambda_{\min}$$
$$2b < \frac{2}{\sqrt{\epsilon_r}} \lambda_{\min}$$

To utilize the full range of mm-waves $\lambda_{\min} = 1$ mm. Then $2b = 1$ mm will keep the space between wires sufficiently below cutoff.

The stop-band will now occur within the operating range at $f = 150$ gc but it will only be $\Delta f = 139$ kc wide and have the attenuation $\alpha' = 20$ db/mile. Both values are small enough not to be objectionable.

V. CONCLUSIONS

Helix waveguide, spaced-ring or spaced-disk guides or other periodic structures for circular electric wave transmission may well be operated close to or beyond the frequency where the wavelength of propagation is twice the period of the structure. The nonuniform but periodic structure of the conducting boundaries in such waveguides will cause an increase in wall current losses due to nonuniform distribution of the eddy currents. From its quasistatic value at low frequencies this distri-

bution will become more even as the frequency increases and the magnetic field penetrates more into the grooves or spaces between wires, rings or disks. The relative loss with respect to smooth wall guide will thus decrease by up to 5 per cent before it shows any substantial increase when the wavelength of propagation becomes smaller than the period of the structure.

The periodic structure causes a stop-band in circular electric wave transmission, when the wavelength of propagation is twice the period length. The stop-band attenuation is, however, quite modest and, what is even more important, the stop-band is very narrow. The relative width of the stop-band and the stop-band attenuation per section are independent of waveguide size and frequency and are functions only of the ratio of wire size to wire spacing or of corresponding dimensionless factors describing the geometry. Deviating from present design practices, one may therefore make the structure of relatively large period, accepting a very narrow stop-band within the operating range. In 2-inch I.D. helix waveguide of optimum design for unwanted mode absorption the wire size is $2c = 0.225$ mm and wire spacing $2b = 0.300$ mm. The stop-band occurs near 500 ge; its width is $\Delta f = 462.5$ kc and maximum attenuation $\alpha' = 67$ db/mile. Keeping the ratio $c/b = 0.75$ the same, but increasing the spacing to $2b = 1$ mm, the stop-band will occur at 150 ge but will be only 139 kc wide and have a maximum attenuation of 20 db/mile.

APPENDIX

A.1 Conformal Transformation

Parameter Ψ of the transformation was found for several values of c/b by solving (15) numerically using Newton's formula. Subsequently ν was calculated from (16). Both quantities are listed in Table I. Also listed in this table for all values of c/b is the largest deviation of the

TABLE I

c/b	Ψ	ν	r_{\max}/c	P_v/P_{v0}
0,5	0.653 257 600 1	1.155 982 500	1.018	1.225
0,6	0.528 077 816 1	1.034 531 436	1.039	1.170
0,7	0.391 940 793 8	1.003 248 064	1.078	1.126
0,8	0.247 192 783 0	1.000 024 889	1.149	1.082
0,85	0.176 268 291 6	1.000 000 146	1.199	1.060

contour DCB in Fig. 3 from a circle as it is found from (18) and

$$\frac{r_{\max}}{c} = \left[\sqrt{\left[\frac{x}{(c/b)(b/a)} \right]^2 + \left[\frac{y}{(c/b)(b/a)} \right]^2} \right]_{\max}. \quad (65)$$

For further reference the loss ratio P_v/P_0 in the quasistatic case according to (29) is likewise listed in Table I.

The area in the Z plane to be mapped on to the W plane is multiple-connected. Hence care has to be taken to select suitable values of the multiple-valued functions in (13) and (14). From (14)

$$\frac{2\pi a}{b} (u + jv) = \sin^{-1}(\xi) + \sin^{-1}(\chi) \quad (66)$$

$$\chi = \frac{2\xi + \nu - 1}{\nu + 1}. \quad (67)$$

To obtain rectilinear boundaries in the W plane, principal and other values of $\sin^{-1}\xi$ and $\sin^{-1}\chi$ must be combined. Suitable combinations are listed in Table II.

TABLE II

Phase range of	$X = \operatorname{Re}[\sin^{-1}(\xi)]$	$Y = \operatorname{Im}[\sin^{-1}(\xi)]$
$0 < \arg \xi < \pi/2$	$\pi/2 > X > 0$	$Y > 0$
$\pi/2 < \arg \xi < \pi$	$0 > X > -\pi/2$	$Y > 0$
$-\pi/2 < \arg \xi < 0$	$\pi > X > \pi/2$	$Y > 0$
$-\pi < \arg \xi < -\pi/2$	$3\pi/2 > X > \pi$	$Y > 0$
$X = \operatorname{Re}[\sin^{-1}(\chi)]$	$Y = \operatorname{Im}[\sin^{-1}(\chi)]$	
$0 < \arg \chi < \pi/2$	$\pi/2 > X > 0$	$Y > 0$
$\pi/2 < \arg \chi < \pi$	$0 > X > -\pi/2$	$Y > 0$
$-\pi/2 < \arg \chi < 0$	$-2\pi < X < -3\pi/2$	$Y < 0$
$-\pi < \arg \chi < -\pi/2$	$-5\pi/2 < X < -2\pi$	$Y < 0$

Of the inverse hyperbolic functions in (13) the principal value is used throughout, but both values of the square roots of the arguments are taken alternatively.

Likewise, suitable values of the square roots in the derivative (17) must be selected as well as in

$$\frac{dZ}{d\xi} = \frac{b/a}{\pi(1+\Psi)} \left[\frac{1}{\sqrt{\xi-1} \cdot \sqrt{\xi+\nu}} + \frac{\Psi}{\sqrt{\xi+1} \cdot \sqrt{\xi+\nu}} \right] \quad (68)$$

and

$$\frac{dW}{d\xi} = j \frac{b/a}{2\pi} \left[\frac{1}{\sqrt{\xi-1} \cdot \sqrt{\xi+\nu}} + \frac{1}{\sqrt{\xi+1} \cdot \sqrt{\xi-1}} \right] \quad (69)$$

where $\xi = \xi + j\eta$, which are subsequently used in numerically solving (13) and (14).

Since only areas of the Z plane with $y \geq 0$ are being mapped, the square roots $\sqrt{\xi - 1}$ and $\sqrt{\xi + \nu}$ in $Z(\xi)$ according to (13) must be chosen of equal sign in case of $\eta \geq 0$ and opposite sign in case of $\eta < 0$. This choice will insure the proper asymptotic values of $|dZ/dW|^2$ in (19) and (20).

A.2 Magnetic Field and Wall Current of Circular Electric Waves in Lined Waveguide

From Maxwell's equations in cylindrical coordinates

$$\frac{\partial H_r}{\partial z} - \frac{\partial H_z}{\partial r} = j\omega\epsilon\epsilon_0 E_\varphi.$$

For the difference of magnetic field $\Delta H = H - H_0$ in lined waveguide and empty waveguide

$$\frac{\partial \Delta H_z}{\partial r} = -j\omega\epsilon_0(\epsilon E_\varphi - E_{\varphi 0}) + \frac{\partial \Delta H_r}{\partial z} \quad (70)$$

may be written.

The radial component H_r of magnetic field vanishes at the wall; close to the wall it is small. In order to find the change in magnetic field at the wall due to a thin lining (70) may be approximated by

$$\frac{\partial \Delta H_z}{\partial r} = -j\omega(\epsilon - 1)\epsilon_0 E_{\varphi 0} \quad (71)$$

and the change in magnetic field at the wall calculated from the relative permittivity $\epsilon(r, z)$ and the electric field

$$E_{\varphi 0} = jA\mu_0\omega\rho_{01}J_0'(\rho_{01}r)e^{-\gamma z} \quad (72)$$

of a circular electric wave in empty guide.

Substituting for $E_{\varphi 0}$ from (72) into (71) and integrating

$$\Delta H_z = A\omega^2\mu_0\epsilon_0 \int_0^a (\epsilon - 1)\rho_{01}J_0'(\rho_{01}r) dr e^{-\gamma z}. \quad (73)$$

For a thin lining

$$\Delta H_z = A\omega^2\mu_0\epsilon_0\rho_{01}^2 J_0(\rho_{01}a) \int_0^a (\epsilon - 1)(a - r) dr e^{-\gamma z} \quad (74)$$

which, when compared to the magnetic field

$$H_{z0} = A \rho_{01}^2 J_0(\rho_{01}r) e^{-\gamma z}$$

at the wall of the empty guide, gives

$$\frac{\Delta H_z}{H_{z0}} = \omega^2 \mu_0 \epsilon_0 \int_0^a (\epsilon - 1)(a - r) dr.$$

The relative change in wall current is given by the same expression.

A.3 Integration of Coupled Line Equations

By substituting

$$\begin{aligned} A &= ve^{-\gamma z}, & A(0) &= v(0), & A(l) &= v(l)e^{-\gamma l} \\ B &= we^{\gamma z}, & B(0) &= w(0), & B(l) &= u(l)e^{\gamma l} \end{aligned} \quad (75)$$

for A and B in (37) the following system of equations for v and w obtains:

$$\frac{d}{dz} \begin{bmatrix} v(z) \\ w(z) \end{bmatrix} = \begin{bmatrix} 0 & -ke^{2\gamma z} \\ ke^{-2\gamma z} & 0 \end{bmatrix} \cdot \begin{bmatrix} v(0) \\ w(0) \end{bmatrix}. \quad (76)$$

Integrating according to the procedure (40), the first-order approximation to a solution is

$$\begin{bmatrix} v(z) \\ w(z) \end{bmatrix} = \begin{bmatrix} 1 & - \int_0^z ke^{2\gamma z} dz \\ \int_0^z ke^{-2\gamma z} dz & 1 \end{bmatrix} \cdot \begin{bmatrix} v(0) \\ w(0) \end{bmatrix}. \quad (77)$$

Another iteration results in the second-order solution

$$\begin{bmatrix} v(z) \\ w(z) \end{bmatrix} = \begin{bmatrix} 1 - \int_0^z ke^{2\gamma z} \int_0^{z'} ke^{-2\gamma z'} dz' dz & - \int_0^z ke^{2\gamma z} dz \\ \int_0^z ke^{-2\gamma z} dz & 1 - \int_0^z ke^{-2\gamma z} \int_0^{z'} ke^{2\gamma z'} dz' dz \end{bmatrix} \cdot \begin{bmatrix} v(0) \\ w(0) \end{bmatrix} \quad (78)$$

which is adequate for present purposes. Replacing v and w by A and B , the transmission matrix is contained in

$$\begin{bmatrix} A(l) \\ B(l) \end{bmatrix} = \begin{bmatrix} \left[1 - \int_0^l ke^{2\gamma z} \int_0^z ke^{-2\gamma z'} dz' dz \right] e^{-\gamma l} & - \int_0^l ke^{2\gamma z} dz e^{-\gamma l} \\ \int_0^l ke^{-2\gamma z} dz e^{\gamma l} & \left[1 - \int_0^l ke^{-2\gamma z} \int_0^z ke^{2\gamma z'} dz' dz \right] e^{\gamma l} \end{bmatrix} \cdot \begin{bmatrix} A(0) \\ B(0) \end{bmatrix}.$$

REFERENCES

1. Morgan, S. P., and Young, J. A., Helix Waveguide, B.S.T.J., **35**, Nov. 1956, pp. 1347-1348.
2. Piefke, G., Wellenausbreitung in der Scheibenleitung, Arch. Elektr. Übertrag., **11**, 1957, pp. 49-59.
3. Katzenelenbaum, B. Z., Attenuation of H_{0n} -modes in a Helical Waveguide, Radioteknika i Elektronika, **4**, 1959, pp. 428-432.
4. Malin, W. W., and Siwow, A. N., The Theory of H_{01} -Wave Propagation in Helical Waveguide, Radioteknika i Elektronika, **4**, 1959, pp. 433-439.
5. Unger, H. G., Waveguides with Anisotropic Impedance Walls, Proc. Symposium on Electromagnetic Theory and Antennas, Copenhagen, 1962.
6. Unger, H. G., Winding Tolerances in Helix Waveguide, B.S.T.J., **40**, Mar. 1961, pp. 627-643.
7. King, A. P., and Mandeville, G. D., The Observed 33 to 90 kmc Attenuation of Two-Inch Improved Waveguide, B.S.T.J., **40**, Sept. 1961, pp. 1323-1330.
8. Unger, H. G., Wendelhohleiter für sehr weite Frequenzbänder, Archiv Elektr. Übertr., **17**, 1963, pp. 359-369.
9. Routh, E. J., *Advanced Rigid Dynamics*, 6th Edition, London, 1905, pp. 461-467.
10. Meinke, H. H., Die Anwendung der konformen Abbildung auf Wellenfelder, Zeitschrift angew. Phys., **1** 1949, pp. 245-252.
11. Rice, S. O., Reflection from Corners in Rectangular Waveguides, Conformal Transformation, B.S.T.J., **28**, Jan., 1949, pp. 104-134.
12. Richmond, H. W., On the Electrostatic Field of a Plane or Circular Grating Formed of Thick Rounded Bars, Proc. London Math. Soc., Ser. 2, **22**, 1923, pp. 389-403.
13. Morrison, J. A., Heat Loss of Circular Electric Waves in Helix Waveguides, I.R.E. Trans. MTT-**6**, 1958, pp. 173-176.
14. Unger, H. G., Round Waveguide with Double Lining, B.S.T.J., **39**, Jan., 1960, pp. 161-167.
15. Morgan, S. P., Theory of Curved Circular Waveguide Containing an Inhomogeneous Dielectric, B.S.T.J., **36**, Sept., 1957, pp. 1209-1252.
16. Miller, S. E., Coupled Wave Theory and Waveguide Applications, B.S.T.J., **33**, May 1954, pp. 661-719.
17. Beck, A. C., and Rose, C. F. P., Waveguide for Circular Electric Mode Transmission, Proc. I.E.E., **106**, 1959, Pt.B., Supp. 13, p. 159.

The ALPAK System for Nonnumerical Algebra on a Digital Computer—II: Rational Functions of Several Variables and Truncated Power Series with Rational-Function Coefficients

By W. S. BROWN, J. P. HYDE and B. A. TAGUE

(Manuscript received November 13, 1963)

This is the second in a series of papers describing the ALPAK system for nonnumerical algebra on a digital computer. The first paper, Ref. 1, is concerned with polynomials in several variables and truncated power series with polynomial coefficients. This paper is concerned with rational functions of several variables and truncated power series with rational-function coefficients. A third paper, Ref. 3, will discuss systems of linear equations with rational-function coefficients.

The ALPAK system has been programmed within the BE-SYS-4 monitor system on the IBM 7090 computer, but the language and concepts are machine-independent. Several practical applications are described in Ref. 1.

This paper is divided into five sections. The first deals with basic concepts, the second defines canonical forms, and the third describes ALPAK's greatest common divisor algorithm. These three sections do not presuppose any knowledge of computers or computer programming. Section IV describes the use and the implementation of the algebraic operations relating to rational functions of several variables and truncated power series with rational-function coefficients. The reader of this section is assumed to be familiar with the basic concepts of computer programming and with Ref. 1. Finally, Section V discusses very briefly some of our plans and hopes for the future.

TABLE OF CONTENTS

	Page
I. SUMMARY OF THE AVAILABLE RATIONAL FUNCTION OPERATIONS.....	786
1.1 <i>Introduction</i>	786

1.2 <i>Input-Output</i>	786
1.3 <i>An Example of the ALPAK Language</i>	787
II. CANONICAL FORMS	788
2.1 <i>Introduction</i>	788
2.2 <i>Polynomial Canonical Form</i>	788
2.3 <i>Rational-Function Canonical Form</i>	788
III. THE GREATEST COMMON DIVISOR ALGORITHM	788
3.1 <i>Introduction</i>	788
3.2 <i>The Euclidean Algorithm</i>	789
3.3 <i>The ALPAK G.C.D. Algorithm</i>	789
3.4 <i>Special Strategies</i>	791
3.5 <i>Concluding Remarks</i>	793
IV. INFORMATION FOR THE ALPAK PROGRAMMER	794
4.1 <i>Introduction</i>	794
4.2 <i>Input-Output Operations</i>	794
4.3 <i>Arithmetic Operations</i>	797
4.4 <i>Truncated Power Series Operations</i>	800
4.5 <i>Miscellaneous Operations</i>	801
V. OUTLOOK	803

I. SUMMARY OF THE AVAILABLE RATIONAL-FUNCTION OPERATIONS

1.1 *Introduction*

The ALPAK system is a programming system for performing routine manipulations of algebraic expressions on a digital computer. The system operates on rational functions of several variables and on truncated power series in several variables with rational functions of several other variables as coefficients. It is capable of performing the operations of addition, subtraction, multiplication, division, substitution and differentiation. In the present version of the program the coefficients of the rational functions are integers, but the change to coefficients from any other integral domain can be made without major program reorganization. ALPAK is also capable of solving systems of equations linear in certain variables with coefficients which are rational functions of other variables (see Ref. 3). The ALPAK system as described in this paper has been programmed for the IBM 7090 computer.

1.2 *Input-Output*

Rational functions can be entered into the machine from punched cards, and the output can be printed and/or punched. The polynomial

$$P(x,y,z) = 8xy^2z + 2xy^2z^2 - 10x^3yz^3$$

can be entered into the machine by punching the following array of coefficients and exponents one term per card:

8	1,2,1
2	1,2,2
-10	3,1,3
0	

The zero coefficient is an end-of-polynomial signal. The subroutine which reads these cards must have access to a *polynomial format statement* (previously read from cards) containing the names of the variables and the number of bits to be allocated for the exponents of each. One full word (35 bits plus sign) is allocated for the coefficient of each term, thus permitting coefficients up to $2^{35} - 1$ in magnitude. Rational functions which are not polynomials are entered by punching the numerator and denominator polynomials successively and calling the rational-function reading subroutine.

The punched and printed output consists of arrays of coefficients and exponents similar to those that are accepted as input. Input and output are accomplished by simple commands such as

RFNRDF	FMT	read format statement <i>FMT</i>
RFNRDD	R,FMT	read rational function <i>R</i>
RFNPRT	R	print rational function <i>R</i> .

1.3 An Example of the ALPAK Language

The simplicity of ALPAK programming is illustrated by the following example. Suppose rational functions *A*, *B*, *C*, and *D* and a format statement *FMT* have been punched on cards, and we wish to compute and print the rational function

$$F = (A * B / C) + D,$$

where the asterisk denotes multiplication.

The required program is

RFNBEG	10000	begin (reserve 10000 words of storage for data and working space)
RFNRDF	FMT	read polynomial format statement <i>FMT</i> from cards
RFNRDD	A,FMT	read polynomial <i>A</i> from cards
RFNRDD	B,FMT	read polynomial <i>B</i> from cards
RFNRDD	C,FMT	read polynomial <i>C</i> from cards
RFNRDD	D,FMT	read polynomial <i>D</i> from cards
RFNMPY	F,A,B	replace <i>F</i> by <i>A*B</i>
RFNDIV	F,F,C	replace <i>F</i> by <i>F/C</i> (<i>C</i> must not be zero)
RFNADD	F,F,D	replace <i>F</i> by <i>F + D</i>
RFNPRT	F	print <i>F</i>
TRA	ENDJOB	go to ENDJOB.

II. CANONICAL FORMS

2.1 *Introduction*

All rational functions stored by the program are kept in a unique canonical form which is the subject of this section. The read routines place the input functions in canonical form and all operations leave their results in canonical form. The uniqueness of the canonical form ensures that two equal rational functions with the same format are precisely identical in storage and that, in particular, zero is uniquely represented.

2.2 *Polynomial Canonical Form*

A polynomial is always represented as an ordered list of its nonzero terms. It is convenient to order the terms according to the magnitude of the first exponent, and to order those terms having the same first exponent according to the magnitude of the second, etc. The order of the variables is the order in which they appear in the format statement.

2.3 *Rational-Function Canonical Form*

A rational function is represented as an ordered pair of polynomials, namely its numerator and denominator respectively. These must be in polynomial canonical form, and they must be relatively prime. In addition, the sign of the numerator must be chosen so that the first term of the denominator is positive.

III. THE GREATEST COMMON DIVISOR ALGORITHM

3.1 *Introduction*

Since rational functions in canonical form must have numerator and denominator relatively prime, the ALPAK program must be capable of finding the *greatest common divisor* (G.C.D.) of polynomials in several variables. This is the essential ingredient in the extension of ALPAK from polynomials to rational functions. Since each rational-function operation must leave its result in canonical form, the G.C.D. operation will be performed very frequently in most programs involving rational functions.

Let a_1, a_2, \dots, a_n be a set of nonzero polynomials. A G.C.D. of a_1, a_2, \dots, a_n is defined to be a polynomial g such that

(i) g divides each of a_1, a_2, \dots, a_n ; and

(ii) any polynomial g' that divides each of a_1, a_2, \dots, a_n also divides g . We denote a G.C.D. of a_1, a_2, \dots, a_n by (a_1, a_2, \dots, a_n) . Since every polynomial has a decomposition into primes that is unique up to sign, this definition implies that a G.C.D. is unique up to sign. In the special case of integers, the positive value is often referred to as the G.C.D.

The next three subsections discuss the Euclidean algorithm for integers, ALPAK's generalization of it for polynomials, and some special strategies which make the latter more effective. The final subsection attempts to present a balanced picture of the present capabilities of the ALPAK algorithm.

Algebraic background relevant to the following discussion can be found in Chapter 1 of Ref. 2, or almost any other algebra text that treats polynomial rings.

3.2 The Euclidean Algorithm

The G.C.D. of a set of n nonzero integers can be obtained by a series of pairwise computations, because

$$(a_1, \dots, a_n) = (((\dots((a_1, a_2), a_3), \dots), a_{n-1}), a_n). \quad (1)$$

The *Euclidean algorithm* obtains the G.C.D. of two nonzero integers a and b . Without loss of generality we can assume that both are positive and that $a \geq b$. By the division algorithm we can write

$$a = qb + c \quad (2)$$

with

$$0 \leq c < b. \quad (3)$$

If $c = 0$, then b divides a , so $(a, b) = b$. Otherwise the common divisors of a and b are the same as those of b and c , so $(a, b) = (b, c)$. Since $b + c < a + b$, the process terminates in a finite number of steps.

3.3 The ALPAK G.C.D. Algorithm

We shall consider a polynomial in v variables as a polynomial in one variable, to be called x , with coefficients from the integral domain of polynomials in the remaining $v - 1$ variables. We shall represent these $v - 1$ variables by the vector y . If $p(x, y)$ is such a polynomial, then $\partial_x(p)$ denotes the degree in x of p .

Now let a and b be a pair of nonzero polynomials. We shall present an inductive definition of the ALPAK algorithm, to be called POLGCD, for obtaining their G.C.D. Let v' be the number of variables in the pair.

If $v' = 0$, then a and b are both integers and the Euclidean algorithm is used. Assume POLGCD works for $v' < v$. We shall define it for $v' = v$. To begin, we write

$$\begin{aligned} a(x,y) &= a_r(y)x^r + a_{r-1}(y)x^{r-1} + \cdots + a_0(y) \\ b(x,y) &= b_s(y)x^s + b_{s-1}(y)x^{s-1} + \cdots + b_0(y). \end{aligned} \quad (4)$$

Our first task is to rewrite this as

$$\begin{aligned} a(x,y) &= x^\alpha f(y)a'(x,y) \\ b(x,y) &= x^\beta g(y)b'(x,y) \end{aligned} \quad (5)$$

where a' and b' are primitive in x ; that is, neither is divisible by x or by any polynomial independent of x except ± 1 . Clearly, α and β are the largest integers such that x^α divides $a(x,y)$, and x^β divides $b(x,y)$; while $f(y)$ is the G.C.D. of the nonzero $a_i(y)$, and $g(y)$ is the G.C.D. of the nonzero $b_j(y)$. Since the a_i and the b_j depend on fewer than v variables, our induction hypothesis implies that POLGCD will obtain f and g . Next we observe that

$$(a,b) = (x^\alpha, x^\beta)(f,g)(a',b'). \quad (6)$$

(The proof of this depends on the fact that a' and b' are primitive.) It is obvious that

$$(x^\alpha, x^\beta) = x^\gamma \quad (7)$$

where γ is the smaller of α and β . Since f and g depend on fewer than v variables, our induction hypothesis implies that we can use POLGCD to obtain (f,g) .

We shall now define a subalgorithm, to be called PRMGCD, for obtaining the G.C.D. of the primitive polynomials $a'(x,y)$ and $b'(x,y)$. To begin, we write

$$\begin{aligned} a'(x,y) &= a_m'(y)x^m + a_{m-1}'(y)x^{m-1} + \cdots + a_0'(y) \\ b'(x,y) &= b_n'(y)x^n + b_{n-1}'(y)x^{n-1} + \cdots + b_0'(y), \end{aligned} \quad (8)$$

where a_m', a_0', b_n', b_0' are all nonzero. Without loss of generality we can assume that $\partial_x(a') \geq \partial_x(b')$. If $\partial_x(b') = 0$, then $b' = b_0' = \pm 1$,* so $(a', b') = 1$. Otherwise, we use POLGCD to compute

$$h = (a_m', b_n'). \quad (9)$$

Then we form

$$c(x,y) = \left[\frac{b_n'(y)}{h(y)} \right] a'(x,y) - \left[\frac{a_m'(y)}{h(y)} \right] b'(x,y)x^{m-n}, \quad (10)$$

* Here we have used the definition of primitivity which is given following (5).

in which the bracketed fractions are polynomials. If $c = 0$, then $a' = \pm b'$;* so $(a', b') = b'$. Otherwise, let $c'(x, y)$ be the primitive part of $c(x, y)$, defined as in (6). Then the common divisors of a' and b' are the same as those of b' and c' ,* so $(a', b') = (b', c')$. (Note the similarity of this algorithm to the Euclidean algorithm, which was defined in the preceding subsection.) By construction

$$\partial_x(c') \leq \partial_x(c) < \partial_x(a'). \quad (11)$$

Hence

$$\partial_x(b') + \partial_x(c') < \partial_x(a') + \partial_x(b'), \quad (12)$$

and so the process terminates in a finite number of steps.

3.4 Special Strategies

From a practical point of view the POLGCD algorithm leaves much to be desired. As the degree in x is reduced, the coefficients grow. This phenomenon is vividly illustrated by the following example. It is desired to find the G.C.D. of the primitive polynomials

$$\begin{cases} -39x^4 + 125x^3 - 15x^2 - 135x - 44 \\ -12x^4 - 89x^3 + 192x^2 - 6x - 85. \end{cases} \quad (13)$$

The successive pairs of primitive polynomials produced by the PRMGCD algorithm are:

$$\begin{aligned} & \begin{cases} -12x^4 - 89x^3 + 192x^2 - 6x - 85 \\ -1657x^3 + 2556x^2 + 462x - 929 \end{cases} \\ & \begin{cases} 178145x^3 - 312600x^2 - 1206x + 140845 \\ -1657x^3 + 2556x^2 + 462x - 929 \end{cases} \\ & \begin{cases} -1657x^3 + 2556x^2 + 462x - 929 \\ 5219965x^2 - 6692054x - 5656955 \end{cases} \\ & \begin{cases} 2253497062x^3 - 6961950605x - 4849347485 \\ 5219965x^2 - 6692054x - 5656955 \end{cases} \end{aligned} \quad (14)$$

To proceed farther would require double-precision coefficients, which are not now available in ALPAK. For polynomials in many variables this problem is even more acute. If POLGCD were programmed to handle coefficients and exponents of arbitrary size, the time it would

* Here we have used the definition of primitivity which is given following (5).

require to find the G.C.D. of two *general* polynomials in n variables, each having degrees d_1, \dots, d_n respectively and each having coefficients of modest size, can be shown to be proportional to

$$\frac{(c^{d_1})}{(c^{d_{n-1}})} \cdot \frac{(c^{d_n})}{\dots} \quad (15)$$

where $c \approx 2.6$ is the square of the Fibonacci ratio, $\frac{1}{2}(1 + \sqrt{5})$.

It is apparent that any real solution to the problem of coefficient growth would require a fundamentally different algorithm. However, many of the G.C.D. problems which arise in practice exhibit special properties which can be exploited.

The most important of these special properties is variable independence. If one of the inputs to POLGCD is independent of one or more of the variables, then the other can immediately be broken into subpolynomials, and we obtain a set of subproblems each involving only those variables which both of the original inputs depend on. For example, it is clear by inspection that the G.C.D. of the pair

$$\begin{aligned} & 2z(2x^4 - 17x^3 + 65x^2 - 144x + 72) \\ & \quad - 3y^2(2x^3 - 17x^2 + 66x - 72) \\ & 6x^4 - 41x^3 + 104x^2 - 116x + 48 \end{aligned}$$

is equal to the G.C.D. of the triple

$$\begin{aligned} & 2x^4 - 17x^3 + 65x^2 - 144x + 72 \\ & 2x^3 - 17x^2 + 66x - 72 \\ & 6x^4 - 41x^3 + 104x^2 - 116x + 48, \end{aligned}$$

and the POLGCD algorithm will discover this provided that x is the last variable in the format statement. Unfortunately POLGCD does not now optimize the order of the variables. If the preceding example is attempted using the variable ordering (x,y,z) , disaster ensues. The inputs are viewed as

$$\begin{aligned} & 4zx^4 - (6y^2 + 34z)x^3 + (51y^2 + 130z)x^2 \\ & \quad - (198y^2 + 288z)x + (216y^2 + 144z) \\ & 6x^4 - 41x^3 + 104x^2 - 116x + 48, \end{aligned}$$

and it is easily seen that both are primitive in x . The next two pairs of primitive polynomials produced by PRMGCD are

$$\left\{ \begin{array}{l} 6x^4 - 41x^3 + 104x^2 - 116x + 48 \\ (18y^2 + 20z)x^3 - (153y^2 + 182z)x^2 \\ \quad + (59y^2 + 452z)x - (648y^2 + 336z) \\ (45y^2 + 68z)x^3 - (423y^2 + 158z)x^2 \\ \quad + (450y^2 - 76z)x + (216y^2 + 240z) \\ (18y^2 + 20z)x^3 - (153y^2 + 182z)x^2 \\ \quad + (59y^2 + 452z)x - (648y^2 + 336z). \end{array} \right.$$

•
•
•

The variable independence has now been lost, and the subsequent pairs will have progressively higher degrees in y and z , and progressively larger coefficients.

Both POLGCD and PRMGCD test their inputs to see whether either divides the other. Since a given G.C.D. problem may involve many recursive calls to POLGCD and PRMGCD, this strategy pays frequent dividends. POLGCD and PRMGCD also make full use of the fact that the G.C.D. of the set of terms of a polynomial, and similarly the G.C.D. of a monomial and a polynomial, can be computed simply and directly.

Finally, we remark that the PRMGCD process is terminated as soon as the degree in x of either input is zero or one. A primitive polynomial of degree zero is obviously equal to ± 1 , while a primitive polynomial of degree one is irreducible. At the last variable level the PRMGCD process is terminated as soon as the degree in x of either input is three or less. A quadratic polynomial can be factored, if it is reducible, with the aid of the quadratic formula. A reducible cubic must have at least one rational root. A simple change of variable produces a related cubic which must have at least one integral root, and it is easy to test for this numerically.

3.5 Concluding Remarks

As we have already stated, the G.C.D. operation is the essential ingredient in the extension of ALPAK from polynomials to rational functions. The weakness of the ALPAK G.C.D. algorithm is apparent from (15). Its strength lies in the fact that most G.C.D. computations which arise in problems of practical interest have a degree of immunity from that formula because of their special structure.

As an example we wish to mention the problem of a single-server

queue with feedback. The computation of the first two moments of the total time is outlined in Section II of Ref. 1 and in the Appendix of Ref. 5. We recently obtained the third moment in a six-minute run on the 7090. This involved solving a triangular linear system of nine equations in nine unknowns. The equations, expressed as polynomials in the nine unknowns and five additional parameters, have over 900 terms. The result is a rational function of the five parameters with a numerator of 200 terms and a denominator of 39 terms. The coefficients of largest magnitude are 1896 in the numerator and 1460 in the denominator. The degrees are 1, 1, 3, 7, and 9 for the numerator and 0, 0, 0, 7, and 9 for the denominator.

IV. INFORMATION FOR THE ALPAK PROGRAMMER

4.1 *Introduction*

This section is an extension of Section III of Ref. 1. The use and implementation of the ALPAK polynomial operations are described there, while the use and implementation of the rational-function operations are described here. The loading instructions are unchanged except that an additional binary deck, called ALPAK3, must be included for a run.

A nonpolynomial rational function is stored as an ordered pair of polynomials, namely its numerator and denominator, as illustrated in Fig. 1. It consists of a pointer, a rational-function heading, and two polynomials stored in the usual way (see Fig. 2 of Ref. 1). The rational-function heading contains pointers to the polynomials, which must have a common format.

Integers and polynomials are always recognized as special cases of rational functions. If a rational-function operation is used where a polynomial operation might have been used, the only penalty will be a fraction of a millisecond of additional overhead.

A rational function can be constructed from its numerator and denominator polynomials by using RFNDIV (divide) or RFNFRM (form). RFNDIV duplicates the two polynomials and constructs the rational function from the copies. RFNFRM constructs the rational function from the given polynomials and clears their pointers. RFNFRM has an optional argument which can be used to indicate that the numerator and denominator are known to be relatively prime.

4.2 *Input-Output Operations*

RFNRDF	F	read format	(a)
F RFNCVF	(X,15,Y,21,Z,36)	convert format	(b)

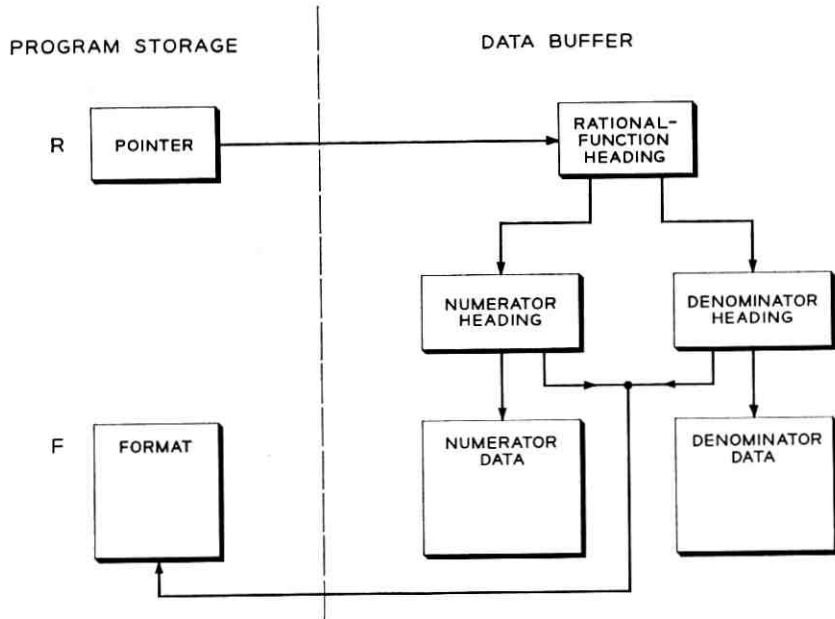


Fig. 1 — A rational function R with format F .

RFNRDD	R,F	read data	(c)*
RFNCVD	R,F,HN,HD	convert data	(d)
RFNCLR	R	clear	(e)
RFNSTZ	R	store zero	(f)
RFNSTI	R	store identity	(g)
RFNSTC	R,A,B	store constant	(h)
RFNSTV	R,X,F	store variable	(i)
RFNPRT	R,CC,(NAME)	print	(j)
RFNPCH	R,(NAME)	punch	(k)*
RFNPRP	R,CC,(NAME)	print and punch	(l)*
RFNRDP	R,F,CC,(NAME)	read and print	(m)
RFNCVP	R,F,HN,HD,CC,(NAME)	convert and print	(n)

A = numerator of constant

B = denominator of constant; if omitted, the denominator is understood to be one

* RFNRDD reads two polynomials from cards, interpreting the first as the numerator and the second as the denominator of a rational function. If a polynomial is to be read by RFNRDD, a unit denominator with a complete set of zero exponents must be provided. A rational function with a constant numerator (denominator) punched by RFNPCH or RFNPRP cannot be read by RFNRDD unless a complete set of zero exponents is added to the numerator (denominator).

CC = control character for printer

F = format (symbolic address of/for format statement)

HN = Hollerith data for numerator (symbolic address of data)

HD = Hollerith data for denominator (symbolic address of data);
if omitted, the denominator is understood to be one

NAME = alternative name for rational function (not exceeding 21
characters)

R = rational function (symbolic address of pointer)

X = variable (specified in the manner indicated by the last previous
VARTYP declaration. See Ref. 1, Section 3.5).

(a) RFNRDF F

Same as POLRDF. See Ref. 1, Section 3.2.

(b) F RFNCVF (X,15,Y,21,Z,36)

Same as POLCVF. See Ref. 1, Section 3.2.

(c) RFNRDD R,F

Read the rational function *R* from cards according to format F. *R* is the
address of a pointer for the rational function and F is the address of a
format statement. *R* must consist of a polynomial numerator and poly-
nomial denominator punched in cards in that order as specified by Ref. 1,
Section 3.2.

(d) RFNCVD R,F,HN,HD

Same as RFNRDD except that the numerator and denominator poly-
nomials are to be found in core in blocks of no more than 12 BCI words
each starting at HN and HD, respectively.

(e) RFNCLR R

Clear the rational function *R*. This clears both numerator and denomi-
nator polynomials as well as the *R* heading if *R* is not itself a polynomial.
If the *R* pointer contains zero or points to an idle heading, then RFNCLR
is a no-op.

(f) RFNSTZ R

Same as POLSTZ. See Ref. 1, Section 3.2.

(g) RFNSTI R

Same as POLSTI. See Ref. 1, Section 3.2.

(h) RFNSTC R,CN,CD

Same as POLSTC if CD is omitted. See Ref. 1, Section 3.2. If CD is present, then CN and CD are the addresses of constants which become the numerator and denominator, respectively, of the rational constant $R = CN/CD$.

(i) RFNSTV R,X,F

Same as POLSTV. See Ref. 1, Section 3.2.

(j) RFNPRT R,CC,(NAME)

Print the rational function R using CC for the control character of the first line of print and NAME (not more than 21 characters) for the name. If NAME is not provided, "R" will be used for the name; and, if CC is not provided, a minus (for triple spacing) is used for the control character. A rational function not a polynomial is printed by printing the name on the first line, followed by two polynomial prints with the names "NUMERATOR" and "DENOMINATOR" respectively

(k) RFNPCH R,(NAME)

Punch the rational function R on cards using NAME (no more than 21 characters) for the name. If NAME is not provided "R" will be used for the name. A rational function not a polynomial will be punched as two polynomials, numerator and denominator in that order.

(l) RFNPRP R,CC,(NAME)

Same as RFNPRT followed by RFNPCH.

(m) RFNRDP R,F,CC,(NAME)

Same as RFNRDD followed by RFNPRT.

(n) RFNCVP R,F,HN,HD,CC,(NAME)

Same as RFNCVD followed by RFNPRT.

4.3 Arithmetic Operations

RFNADD	R,P,Q	$R = P + Q$	add	(a)
RFNSUB	R,P,Q	$R = P - Q$	subtract	(b)
RFNMPY	R,P,Q	$R = P * Q$	multiply	(c)
RFNDIV	R,P,Q	$R = P/Q$	divide	(d)*
RFNSST	G,F(LISTR) (LISTV)	$G = F(LISTV)$ $= LISTR$	substitute	(e)

* RFNDIV can form the quotient of any two rational functions provided the divisor is not zero. In contrast, POLDIV has a "no divide" return which is used whenever the quotient is not a polynomial.

RFNDIF	Q,P,X	$Q = \partial P / \partial X$	differentiate	(f)
RFNZET	R	Skip iff $R = 0$	zero test	(g)
RFNNZT	R	Skip iff $R \neq 0$	nonzero test	(h)
RFNEQT	P,Q	Skip iff $P = Q$	equality test	(i)
RFNDUP	Q,P	$Q = P$	duplicate	(j)
RFNCHS	R	$R = -R$	change sign	(k)

F,G,P,Q,R = rational functions (symbolic addresses of pointers)

X = variable (specified in the manner indicated by the last previous VARTYP declaration) †

LISTR = list of rational functions.

LISTV = list of variables (specified in the manner indicated by the last previous VARTYP declaration) †

4.3.1 Notation

In the following descriptions, if R denotes a rational function, we denote its numerator by RN and its denominator by RD . In particular, if R is a polynomial, RD is the constant polynomial 1.

4.3.2 Descriptions

(a) RFNADD R,P,Q

The inputs P and Q are rational functions in canonical form. First POLGCD is used to obtain

$$G = (PD, QD).$$

Then the polynomials

$$AN = PN * (QD/G) + QN * (PD/G)$$

and

$$AD = (PD/G) * (QD/G) * G$$

are computed. Note that the parenthesized fractions are polynomials. Next,

$$H = (AN, G)$$

is obtained and

$$R = \frac{(AN/H)}{(AD/H)}$$

† See Ref. 1, Section 3.5.

is formed. RN and RD are now relatively prime (the proof of this is an exercise for the reader), so POLGCD need not be used when placing R in canonical form.

(b) RFNSUB R,P,Q

RFNCHS [see (k) below] and RFNADD are applied to compute

$$R = P + (-Q).$$

(c) RFNMPY R,P,Q

First the functions

$$A = PN/QD$$

and

$$B = QN/PD$$

are formed and placed in canonical form. Then

$$R = AN*BN/AD*BD$$

is formed. RN and RD are already relatively prime, so POLGCD need not be used when placing R in canonical form.

(d) RFNDIV R,P,Q

RFNDIV is identical to RFNMPY except that Q must be not zero and the roles of QN and QD are interchanged. If Q is zero, the diagnostic remark "ZERO DENOMINATOR" is printed and the job is terminated.

(e) RFNSST G,F(LISTR) (LISTV)

RFNSST is exactly the rational function equivalent of POLSST; in particular, the format constraints on F and G are identical. If F is a polynomial, the rational functions of LISTR are substituted for the variables in LISTV term-by-term to accumulate the final result. If F is a rational function, this procedure is applied to the numerator and denominator polynomials of F in succession and the resulting rational functions are divided (using RFNDIV) to obtain G .

(f) RFNDIF Q,P,X

First POLDIF is used to compute

$$PN' = \partial(PN)/\partial X$$

$$PD' = \partial(PD)/\partial X,$$

and POLGCD is used to obtain

$$G = (PD, PD').$$

Next the polynomials

$$AN = (PD/G)*PN' - PN*(PD'/G)$$

and

$$AD = PD*(PD/G) = (PD/G)^2 * G$$

are computed. Note that the parenthesized fractions are polynomials. Finally

$$H = (AN, G)$$

is obtained, and

$$Q = \frac{(AN/H)}{(AD/H)}$$

is formed. Since QN and QD are relatively prime, POLGCD need not be used when placing Q in canonical form.

(g) RFNZET R

Same as POLZET. See Ref. 1, Section 3.3

(h) RFNNZT R

Same as POLNZT. See Ref. 1, Section 3.3.

(i) RFNEQT P,Q

If P and Q are both polynomials, POLEQT is applied. If only one of them is a polynomial, they are not equal. If neither is a polynomial, POLEQT is applied to both numerators and both denominators. If the rational functions are unequal, the next instruction is executed, if they are equal, then the next instruction is skipped.

(j) RFNDUP Q,P

Q is replaced by a copy of P .

(k) RFNCHS R

If R is a polynomial, POLCHS is applied to R . If R is not a polynomial, POLCHS is applied to its numerator polynomial.

4.4 Truncated Power Series Operations

ALPAK contains two macros for dealing with truncated power series with rational function coefficients. These are RFNTRC (truncate) and

RFNMPT (multiply and truncate). Addition can be handled with RFNTRC and RFNADD. Each truncated power series must be stored as a rational function in a format whose first k variables are the power series variables. The denominator, if any, must be independent of these variables. The command

RFNTRC P,ORD,K

where K contains the number of power series variables k and ORD contains an integer n , causes P to be truncated to order n . That is, all terms of order greater than n in the first k variables are deleted. The command

RFNMPT R,ORDR,P,ORDP,Q,ORDQ,K

is represented by the equation

$$R = P * Q$$

where P and Q are truncated power series. K is the address of the number of power series variables, ORDP and ORDQ are the addresses of the orders of P and Q respectively, and ORDR is an address for the order of R , which is to be computed. If $P(Q)$ contains any terms of order greater than ORDP(ORDQ), they will be deleted.

4.5 Miscellaneous Operations

(Caution: read descriptions carefully.)

POLGCD	G,A,B	greatest common divisor of polynomials	(a)
INTGCD		greatest common divisor of integers in AC and MQ	(b)
PWVSTO	XK,K,W,FA	store a power of the Wth variable	(c)
VARNUM	W,X,FA	variable number	(d)
RFNFRM	R,N,D	form	(e)
EXPAND	N,D,R,IORP	expand	(f)
SUBLCK	PJ,P,J,W	sub-block	(g)
PWVFAC	K,P,W	factor off a power of the Wth variable	(h)
DEGREE	K,P,W	degree.	(i)
(a)	POLGCD	G,A,B	

Replace G by a greatest common divisor of the polynomials A and B .

(b) INTGCD

Replace the integer in the AC by the greatest common divisor of it and the integer in the MQ.

(c) PWVSTO XK,K,W,FA

Replace XK by the Kth power of the Wth variable in the format whose address is at FA. K is the address of the power, and W is the address of the variable number.

(d) VARNUM W,X,FA

Replace the contents of W by the variable number of the variable X in the format whose address is at FA. X is the address of the variable name in BCI.

(e) RFNFRM R,N,D

Same as RFNDIV except: (i) N and D must be polynomials; (ii) N and D become the property of R, and their pointers in the calling program are replaced by zeros; (iii) R must be distinct from N and D; and (iv), if N and D are known to be relatively prime, a fourth argument NOGCD can be added to the calling sequence in order to save the time which would otherwise be spent in finding their greatest common divisor.

(f) EXPAND N,D,R,IORP

This is the inverse of RFNFRM. N and D must initially contain zeros. They are filled in with pointers to the numerator and denominator of R respectively. The R heading is marked as idle. If R is an integer or a polynomial, N is filled in with a pointer to R, the R pointer is replaced by zero, and control is transferred to IORP. If IORP is omitted, control is transferred to the next instruction.

(g) SUBLCK PJ,P,J,W

P must be a polynomial independent of the first $W - 1$ variables, if any. Then, by the definition of the polynomial canonical form, the terms of P are ordered according to the powers of the Wth variable. SUBLCK replaces PJ by the polynomial consisting of that sub-block of P, if any, whose terms all involve the Jth power ($0 < J <$ degree of P) of the Wth variable. If P contains no terms involving the Jth power of the Wth variable, SUBLCK replaces PJ by the zero polynomial.

(h) PWVFAC K,P,W

P must be a polynomial independent of the first $W - 1$ variables, if

any. PWVFAC replaces the contents of K by the smallest exponent of the W th variable in P , and divides P by that power of the W th variable.

(i) DEGREE K,P,W

P must be a polynomial independent of the first $W - 1$ variables, if any. DEGREE replaces the contents of K by the degree of P in the W th variable.

V. OUTLOOK

A new version of ALPAK (to be called ALPAKB) is now being developed. Its foundation is a programming system (see Ref. 4) called STGPAK (*storage package*), which provides (i) dynamic storage allocation, (ii) automatic recursion, and (iii) "delayed-decision diagnostics."

The storage allocation orders make it possible to obtain contiguous blocks of storage of arbitrary length as needed (provided that sufficient space is available) and to return idle space to the system. A block may contain sub-blocks and/or pointers to other blocks. This will permit the introduction of higher level data structures including formal products of polynomials, thereby helping to alleviate the greatest-common-divisor problem.

The use of a public push-down list for subroutine storage makes recursive programming fully automatic. That is, a subroutine can call itself without taking special measures to preserve its arguments and intermediate results. The diagnostic facilities permit the decision regarding what to do about an overflow (shortage of space or time) or error detected in a given subroutine, to be delayed until control has been returned to some higher level subroutine or to the main program.

The authors hope that STGPAK together with a macro compiler now being developed by Miss D. C. Leagus and W. S. Brown will simplify and expedite the programming of ALPAKB subroutines. The compiler should also be useful in the writing of main programs.

Apart from these matters, which are not directly related to algebra, our plans for ALPAKB include multiple precision integer arithmetic, an improved strategy for finding greatest common divisors, and a complete set of operations for truncated power series.

REFERENCES

1. Brown, W. S., The ALPAK System for Nonnumerical Algebra on a Digital Computer — I: Polynomials in Several Variables and Truncated Power Series with Polynomial Coefficients, B.S.T.J., 42, September, 1963, p. 2081.

2. Zariski, O., and Samuel, P., *Commutative Algebra*, Vol. I, D. Van Nostrand, Princeton, 1958. (See especially Chapter 1.)
3. Hyde, J. P., The ALPAK System for Nonnumerical Algebra on a Digital Computer — III: Systems of Linear Equations and a Class of Side Relations, to be published.
4. Brown, W. S., and Leagus, D. C., STGPAK: A Programming System for Dynamic Storage Allocation, Automatic Recursion, and "Delayed-Decision Diagnostics," to be published.
5. Takaes, L., A Single-Server Queue with Feedback, B.S.T.J., **42**, March, 1963, p. 505. (See especially the Appendix by W. S. Brown.)

The Theory of Direct Transitions in Semiconductors

By R. H. PANTELL, M. DIDOMENICO, JR., and O. SVELTO

(Manuscript received November 26, 1963)

The problem of direct interband transitions in semiconducting crystals is considered in detail. The solution of the problem is shown to lead to a system of simultaneous coupled nonlinear differential equations. These equations do not distinguish between static and dynamic fields, and are obtained without recourse to any approximation procedures. They therefore apply for electromagnetic fields of arbitrary amplitude. It is shown, finally, that the linearization of these equations correctly predicts the fundamental optical absorption edge and the photoconductive rate equations which result in photomixing phenomena.

I. INTRODUCTION

Within the past year there has been an increasing interest in semiconductor behavior, resulting from the development of the optical maser. In addition to the fact that the semiconductor can be used as an optically active medium, this interest results, in part, from a variety of nonlinear effects which can occur in semiconductors at infrared and optical frequencies.

Optical masers are capable of providing very high-intensity fields at photon energies corresponding to the energy gap between valence and conduction bands. Since nonlinear effects generally vary as some power of field strength, the laser has stimulated keen interest in semiconductor nonlinear phenomena. Examples of such phenomena are the Franz-Keldysh^{1,2} effect and the multiple-photon process.³ Closely allied with these nonlinear interband effects is the process of photomixing^{4,5} (photoconductivity), where two coherent optical signals are beat together to produce a photosignal which is proportional to the instantaneous density of photoexcited electrons and hence contains sum and difference frequency terms.

The aforementioned phenomena have been analyzed previously by

calculating the interband transition probabilities from time-dependent perturbation theory¹⁻³ for the case where an electrostatic and electromagnetic field act on an electron in a crystal. This approach involves discarding quadratic terms in the vector potential in the Hamiltonian (the static and dynamic fields are treated differently), and neglecting higher-order nonlinearities in the population distribution.

In this article, a more general theory of direct transitions in semiconductors is presented. A semiclassical approach is used, wherein the semiconductor properties are quantized and the electromagnetic field is treated classically. A set of rather simple coupled nonlinear differential equations is obtained for the equations of motion governing the fundamental absorption process, without resorting to any perturbation or approximation procedures. In contrast to the usual method of analysis, these equations do not distinguish between static and dynamic fields. The linearization of the nonlinear equations correctly predicts the fundamental optical absorption, and is shown to lead to the photoconductive rate equation for the generation of conduction band electrons.

II. SOLUTION TO THE WAVE EQUATION

The equation of motion for an electron in a crystal is the wave equation

$$\mathfrak{H}\psi = i\hbar(\partial\psi/\partial t), \quad (1)$$

where \mathfrak{H} is the Hamiltonian operator and ψ is the one-electron wave function. Without the presence of the radiation or static fields the Hamiltonian, \mathfrak{H}_0 , is

$$\mathfrak{H}_0 = (\mathbf{p}^2/2m) + V(\mathbf{r}).$$

Here m is the electron mass, $V(\mathbf{r})$ is the lattice potential, and \mathbf{p} is the momentum operator. With \mathfrak{H}_0 as the operator in (1), the eigenfunctions of \mathfrak{H}_0 are the Bloch functions:

$$\mathfrak{H}_0\{u_N(\mathbf{r}; \mathbf{k}) \exp(i\mathbf{k} \cdot \mathbf{r})\} = \varepsilon_N(\mathbf{k})u_N(\mathbf{r}; \mathbf{k}) \exp(i\mathbf{k} \cdot \mathbf{r}), \quad (2)$$

where

$$\varphi_N(\mathbf{r}; \mathbf{k}) = u_N(\mathbf{r}; \mathbf{k}) \exp(i\mathbf{k} \cdot \mathbf{r}),$$

are the Bloch functions, and $\varepsilon_N(\mathbf{k})$ are the energy eigenvalues. The subscript N refers to the different energy bands, and the function $u_N(\mathbf{r}; \mathbf{k})$, which is normalized over the volume of the unit cell, has the periodicity of the lattice. In the presence of a static and dynamic field, the Hamiltonian becomes

$$\mathfrak{H} = \frac{1}{2m} \left(\mathbf{p} - \frac{e}{c} \mathbf{A} \right)^2 + V(\mathbf{r}) - \mathbf{F} \cdot \mathbf{r}, \quad (3)$$

where e is the electronic charge, c is the vacuum light velocity, \mathbf{A} is the vector potential for the dynamic field (the gauge $\Phi = 0$ and $\nabla \cdot \mathbf{A} = 0$ is chosen), and $\mathbf{F} = e\mathbf{E}_0$ is the force due to the static field \mathbf{E}_0 . The static and dynamic fields enter differently in (3), because of the fact that the vector potential for the static field increases linearly with time. It will be shown, however, that in the solution there is no distinction between the two fields.

With the Hamiltonian given by (3), the wave function ψ is chosen so that the equation of motion (1) does not contain secular terms, and so that the solution to the wave equation [(7) and (8) below] takes a relatively simple form in which the time-dependent and time-independent fields both appear. A normalized wave function that satisfies these two criteria is given by

$$\begin{aligned} \psi(\mathbf{r}, t) &= \frac{\Delta^{\frac{1}{2}}}{(2\pi)^{\frac{3}{2}}} \sum_N \int d^3 k a_N(t; \mathbf{k}) u_N(\mathbf{r}; \mathbf{K}(t)) \\ &\times \exp i \left\{ \mathbf{k} \cdot \mathbf{r} + \frac{1}{\hbar} \mathbf{F} \cdot \mathbf{r} t - \frac{1}{\hbar} \int_0^t \mathcal{E}_N[\mathbf{K}(\tau)] d\tau + S_N(t; \mathbf{k}) \right\}, \end{aligned} \quad (4)$$

where Δ is the volume of a unit cell, and where, for the sake of simplicity, the function $S_N(t; \mathbf{k})$ has been defined as

$$S_N(t; \mathbf{k}) = i \frac{e}{\hbar} \int_0^t d\tau \mathbf{E} \cdot \int d\mathbf{v}_0 u_N^*(\mathbf{r}; \mathbf{K}) \nabla_{\mathbf{K}} u_N(\mathbf{r}; \mathbf{K}). \quad (5)$$

Here $\nabla_{\mathbf{K}}$ is the gradient operator in \mathbf{K} -space and the asterisk denotes the complex conjugate. One result of the added force on the electron, determined by the total electric field vector

$$\mathbf{E} = \mathbf{E}_0 - \frac{1}{c} \frac{\partial \mathbf{A}}{\partial t},$$

is to change the electron wave vector from the constant value \mathbf{k} to the time-varying value

$$\mathbf{K}(t) = \mathbf{k} + \frac{1}{\hbar} \mathbf{F} t - \frac{e}{\hbar c} \mathbf{A}(t), \quad (6)$$

which describes the intraband electronic motion. The integral over \mathbf{k} -space entering in (4) extends over all values of the wave number within an energy band, and the volume integral over coordinate space appearing in (5) extends over the volume of a unit cell. It should be noted that

the dc field does not appear symmetrically with the time-varying field in (4); this is due to the fact that the Hamiltonian has a different form for static and time-dependent fields. The form of the wave function given by (4) was suggested by Houston's choice of wave function for an applied dc field.⁶

It is assumed now that the wavelength of the applied radiation is much greater than the dimensions of the unit cell, and that the electron wave vector \mathbf{k} has the same value for the lowest state in the conduction band as for the highest state in the valence band. Thus the electron momentum vector for the final state is the same as the momentum vector for the initial state (direct transitions). In Appendix A, it is shown that the substitution of the wave function ψ from (4) into the wave equation (1) yields a differential equation for the undetermined probability coefficients $a_N(t; \mathbf{k})$. Considering only direct transitions between valence and conduction bands, there results [see (29)]

$$\begin{aligned}\partial a_c / \partial t &= -Q a_v \\ \partial a_v / \partial t &= Q^* a_c,\end{aligned}\tag{7}$$

where

$$Q = i \frac{e}{m} \frac{\mathbf{E} \cdot \mathbf{M}}{\omega_{cv}} \exp i \left[\int_0^t \omega_{cv} d\tau - (S_c - S_v) \right].\tag{8}$$

The subscripts c and v refer, respectively, to the conduction and valence bands; \mathbf{M} is the matrix element for transitions between the two bands,

$$\mathbf{M} = \int dv_0 u_c^* \nabla u_v;$$

and ω_{cv} is an angular frequency given by

$$\omega_{cv} = \frac{\epsilon_c - \epsilon_v}{\hbar}.$$

In taking the complex conjugate of Q it should be noted that the function S_N defined by (5) is real. This follows from the fact that the electric field \mathbf{E} is chosen to be real, and that the integral

$$\int dv_0 u_N^* \nabla_K u_N$$

is imaginary, since

$$\nabla_K \int u_N^* u_N dv_0 = \nabla_K \delta_{NN} = 0.$$

The interaction between the semiconductor and the electromagnetic field results in the generation of a probability current density in the crystal. The expectation value of this current, in turn, acts as a source of radiation in the Maxwell equation for the curl of \mathbf{H} . Therefore a complete solution of the problem of the interaction between the semiconductor and radiation field requires an evaluation of this current source. The expectation value of the probability current density, \mathbf{J} , can be expressed as follows, by noting that the canonical momentum operator \mathbf{p} is Hermitian,

$$\mathbf{J} = \frac{e}{mV} \left\langle \mathbf{p} - \frac{e}{c} \mathbf{A} \right\rangle, \quad (9)$$

where V is the crystal volume and the angular brackets denote averaging over the volume V .

It is now convenient to define a vector \mathbf{j} by

$$\mathbf{j} = \int d^3k \mathbf{j}$$

such that \mathbf{j} is the averaged current density per unit volume in \mathbf{k} -space. In Appendix B it is shown that \mathbf{j} satisfies the simple relationship [see (36)]

$$\mathbf{j} \cdot \mathbf{E} = \partial W / \partial t, \quad (10)$$

where W is the energy of the system per unit volume, i.e.,

$$W = (1/V) (|a_e|^2 \mathcal{E}_e + |a_v|^2 \mathcal{E}_v). \quad (11)$$

Equation (10) is just the statement of conservation of power flow, for the left-hand side of this equation is the power transferred into the semiconductor, as given by the scalar product of current density and *total* electric field. The right-hand side of (10) is, of course, the resultant rate of increase of energy density in the quantized semiconductor system.

Equations (7), (10), and (11) contain the necessary information to solve various types of semiconductor problems involving direct transitions. The derivation of these equations did not require discarding \mathbf{A}^2 terms in the Hamiltonian, and the solution for the unknown amplitudes a_N did not necessitate using perturbation or approximation methods. It should be emphasized at this point that the results do not distinguish between static and dynamic fields. The set of equations (7), (10), and (11) is nonlinear and may be solved to any order in the electric field \mathbf{E} to determine the various nonlinear interband phenomena. The remainder

of this paper will be devoted to a detailed treatment of the linear solutions, which will be shown to lead to the rate equation for the generation of electron-hole pairs (photoconductivity).

III. SMALL-SIGNAL SOLUTIONS AND DERIVATION OF THE PHOTOCONDUCTIVE RATE EQUATION

The equations of motion for optical interband transitions [(7), (10), and (11)] can be greatly simplified by seeking solutions for a_c and a_v correct to first order in the electric field \mathbf{E} . Under this condition, which applies when the external electromagnetic force influencing the electronic motion in the crystal is small, the wave vector $\mathbf{K}(t)$ can be replaced by \mathbf{k} , so that ω_{cv} becomes time-independent. It is then easy to show from (7) and (8) that the solutions for a_c and a_v correct to first order are:

$$\begin{aligned} a_c &= a_c^{(0)} - a_v^{(0)} \frac{ie}{m\omega_{cv}} \mathbf{M} \cdot \int \mathbf{E} e^{i\omega_{cv} t} dt \\ a_v &= a_v^{(0)} - a_c^{(0)} \frac{ie}{m\omega_{cv}} \mathbf{M}^* \cdot \int \mathbf{E} e^{-i\omega_{cv} t} dt. \end{aligned} \quad (12)$$

The superscript (0) indicates the zero-order solutions which, for this example, are independent of time. For the case where the crystal is in thermal equilibrium at 0°K, the constant amplitudes $a_c^{(0)}$ and $a_v^{(0)}$ can be determined by noting that the electrons are confined to states in the valence band only, i.e.,

$$|a_c^{(0)}|^2 = 0, \quad (13a)$$

and

$$|a_v^{(0)}|^2 d^3 k = \rho(\mathbf{k}) d^3 k, \quad (13b)$$

where $\rho(\mathbf{k})$ is the density of states. Integrating (13b) over a spherical shell gives for the number of states in a range dk

$$|a_v^{(0)}|^2 dk = (V/\pi^2) k^2 dk, \quad (13c)$$

in which V is the crystal volume.

A second-order linear differential equation can now be derived for the crystal current density \mathbf{j} . Since the external forces are assumed to be small, $\mathbf{K}(t) \approx \mathbf{k}$, whereupon one obtains from (10) and (11)

$$\mathbf{j} \cdot \mathbf{E} = \frac{\hbar\omega_{cv}}{V} \frac{\partial |a_c|^2}{\partial t}, \quad (14)$$

where use has been made of the relation $|a_c|^2 + |a_v|^2 = \text{constant}$. By substituting the first-order solution for a_c from (12) into (14), it is found after some manipulation that \mathbf{j} satisfies the equation of motion for a forced harmonic oscillator, i.e.,

$$\frac{\partial^2 \mathbf{j}}{\partial t^2} + \omega_{cv}^2 \mathbf{j} = G \frac{\partial \mathbf{E}}{\partial t}, \quad (15)$$

where

$$G = \frac{2\hbar}{\omega_{cv} V} \left(\frac{e}{m}\right)^2 |M_E|^2 |a_v^{(0)}|^2, \quad (16)$$

and M_E is the component of \mathbf{M} in the direction of the electric field \mathbf{E} .

The validity of (15) may be checked by calculating the absorption coefficient $\alpha(\omega)$ for the fundamental absorption edge. It is assumed that the semiconductor has spherical energy surfaces with the same reduced effective mass, $1/m^* = 1/m_c^* - 1/m_v^*$, along all crystal axes, and that in consequence

$$\omega_{cv} \approx \omega_0 + (\hbar/2m^*)k^2, \quad (17)$$

where $\hbar\omega_0$ is the minimum energy gap between the two bands. By making use of (13c) for $|a_v^{(0)}|^2$ and (17) for ω_{cv} , the observable crystal current density \mathbf{J} can be found by integrating \mathbf{j} , as determined from (15), over \mathbf{k} -space. The resultant expression is given by the following constitutive relation between \mathbf{J} and \mathbf{E}

$$\mathbf{J} = \frac{1}{\pi} \sqrt{\frac{2}{\hbar}} \left(\frac{e}{m}\right)^2 |M_E|^2 (m^*)^{\frac{1}{2}} \frac{\sqrt{\omega - \omega_0}}{\omega} \mathbf{E}, \quad (18)$$

where ω is angular oscillation frequency of the radiation field. The absorption coefficient can now be found directly by observing that in the frequency domain the coefficient of \mathbf{E} in (18) is the macroscopic conductivity, σ , of the solid and is related to the absorption coefficient by

$$\alpha = 4\pi\sigma/n_0c,$$

in which n_0 is the index of refraction of the crystal. The value for α obtained in this manner from (18) is the same as that given elsewhere.⁷

The photoconductive rate equation for generation of conduction electron-hole pairs also follows from the small-signal solution. If n is the number of conduction electrons per unit volume (equal to the number of holes), then one may express n as the \mathbf{k} -space integral of $|a_c|^2$:

$$n = \int d^3k \frac{|a_c|^2}{V}. \quad (19)$$

The rate of increase of conduction electrons is obtained from (14), whereby

$$\frac{\partial n}{\partial t} = \mathbf{E} \cdot \int d^3k \frac{\mathbf{j}}{\hbar\omega_{cv}}. \quad (20)$$

In order to account for lattice collisions which produce intraband transitions and eventual interband recombinations, it is necessary to add a phenomenological loss term to (20). This is accomplished by adding a term n/τ_n to the left-hand side of (20), where τ_n is the lifetime of an electron in the excited states of the conduction band. Equation (20) then leads to the photoconductive rate equation

$$\frac{\partial n}{\partial t} + \frac{n}{\tau_n} = \mathbf{E} \cdot \int d^3k \frac{\mathbf{j}}{\hbar\omega_{cv}}. \quad (21)$$

A situation of particular interest is where \mathbf{E} is an optical field made up of several coherent frequencies. Combining (15) and (21) then results in the rate equation for photomixing

$$\frac{\partial n}{\partial t} + \frac{n}{\tau_n} = \frac{n_0 c}{4\pi} \sum_{p,q} \frac{\alpha_p}{\hbar\omega_p} \mathbf{E}_p \cdot \mathbf{E}_q. \quad (22)$$

In this equation the subscripts p and q enumerate the different frequency components in the incident radiation. It is seen from (22) that n contains the sum and difference beat frequencies of the incoming radiation. This equation may be used to calculate the optical mixing properties of semiconductor crystals, where the mixing process results from photoconductivity.⁸

IV. CONCLUSIONS

The analysis of the problem of direct transitions in semiconductors has led to several simultaneous nonlinear differential equations. Linearization of these equations correctly predicts the fundamental optical absorption and photoconductive mixing effects. Nonlinear effects such as might result from the time dependence of ω_{cv} (Franz-Keldysh effect), or from the time dependence of $|a_c|^2$ and $|a_v|^2$ (multiple-photon effects) can be predicted by appropriate higher-order approximation procedures.

V. ACKNOWLEDGMENT

The authors are grateful to Dr. Lazlo Solymar of Standard Telecommunication Laboratories for useful discussions pertaining to this work.

APPENDIX A

Derivation of the Equations of Motion Governing Direct Transitions

Equation (2) can be rewritten as

$$\left[\frac{\mathbf{p}^2}{2m} + V(\mathbf{r}) \right] u_N(\mathbf{r}; \mathbf{k}) \exp(i\mathbf{k} \cdot \mathbf{r}) = \varepsilon_N(\mathbf{k}) u_N(\mathbf{r}; \mathbf{k}) \exp(i\mathbf{k} \cdot \mathbf{r}), \quad (23)$$

where $u_N(\mathbf{r}; \mathbf{k}) \exp i\mathbf{k} \cdot \mathbf{r}$ are the stationary Bloch functions, and \mathbf{p} is the operator $-i\hbar\nabla$. It follows directly from (23) that in the presence of an electromagnetic field

$$\begin{aligned} \left[\frac{1}{2m} \left(\mathbf{p} - \frac{e}{c} \mathbf{A} \right)^2 + V(\mathbf{r}) \right] u_N(\mathbf{r}; \mathbf{K}) \exp i\left(\mathbf{k} + \frac{1}{\hbar} \mathbf{F}t\right) \cdot \mathbf{r} \\ = \varepsilon_N(\mathbf{K}) u_N(\mathbf{r}; \mathbf{K}) \exp i\left(\mathbf{k} + \frac{1}{\hbar} \mathbf{F}t\right) \cdot \mathbf{r}. \end{aligned} \quad (24)$$

Equation (24) can be verified by performing the indicated operations and invoking (23).

The substitution of the wave function $\psi(\mathbf{r}, t)$ from (4) into the wave equation with the Hamiltonian of (3) yields, with the help of (24),

$$0 = \sum_N \int d^3k \left\{ \frac{\partial a_N}{\partial t} u_N(\mathbf{r}; \mathbf{K}) + a_N \left[\frac{\partial \mathbf{K}}{\partial t} \cdot \nabla_{\mathbf{K}} u_N(\mathbf{r}; \mathbf{K}) \right. \right. \\ \left. \left. + i \frac{\partial S_N}{\partial t} u_N(\mathbf{r}; \mathbf{K}) \right] \right\} \exp i(\mathbf{r}, t, \mathbf{k}, N), \quad (25)$$

where $\exp i(\mathbf{r}, t, \mathbf{k}, N)$ is an abbreviation for the exponential function

$$\exp i\left\{ \mathbf{k} \cdot \mathbf{r} + \frac{1}{\hbar} \mathbf{F} \cdot \mathbf{r}t - \frac{1}{\hbar} \int_0^t \varepsilon_N(\mathbf{K}) d\tau + S_N(t; \mathbf{k}) \right\}.$$

Equation (25) is now multiplied by

$$u_{N'}^*(\mathbf{r}; \mathbf{K}') \exp -i(\mathbf{r}, t, \mathbf{k}', N'),$$

and integrated over all coordinate space. The resulting equation is then simplified by making use of the lemma⁹

$$\int_{\text{all space}} dv \int d^3k \Phi(\mathbf{r}; \mathbf{k}, \mathbf{k}') \exp i(\mathbf{k} - \mathbf{k}') \cdot \mathbf{r} = \frac{(2\pi)^3}{\Delta} \int dv_0 \Phi(\mathbf{r}; \mathbf{k}, \mathbf{k}),$$

where $\Phi(\mathbf{r}; \mathbf{k}, \mathbf{k}')$ is a lattice periodic function. Recall that the volume integral on the right-hand side of this expression extends over the volume of a unit cell.

The result of performing the above operations on (25) is

$$\begin{aligned} \frac{\partial a_L}{\partial t} + ia_L \frac{\partial S_L}{\partial t} = & - \sum_N a_N \frac{\partial \mathbf{K}}{\partial t} \cdot \left\{ \int dv_0 u_L^* \nabla_K u_N \right\} \\ & \times \exp i \left[\int_0^t \omega_{LN} d\tau + (S_N - S_L) \right], \end{aligned} \quad (26)$$

where $\hbar\omega_{LN} = \varepsilon_L - \varepsilon_N$. It can be shown from the definition of S_L [see (5)] that the time derivative, $\partial S_L / \partial t$, is

$$\frac{\partial S_L}{\partial t} = i \frac{\partial \mathbf{K}}{\partial t} \cdot \int dv_0 u_L^* \nabla_K u_L,$$

so that (26) may be rewritten as

$$\begin{aligned} \frac{\partial a_L}{\partial t} = & - \sum'_N a_N \frac{\partial \mathbf{K}}{\partial t} \cdot \left\{ \int dv_0 u_L^* \nabla_K u_N \right\} \\ & \times \exp i \left[\int_0^t \omega_{LN} d\tau + (S_N - S_L) \right], \end{aligned} \quad (27)$$

where \sum'_N indicates that $N = L$ is excluded from the sum.

There is a rather simple relationship between the matrix element of the gradient operator in \mathbf{K} -space and in coordinate space, which for $N \neq L$, can be expressed as⁹

$$\int dv_0 u_L^* \nabla_K u_N = \frac{i\hbar}{m\omega_{LN}} \int dv_0 u_L^* \nabla u_N. \quad (28)$$

By combining (27) and (28) and noting from (6) that $\partial \mathbf{K} / \partial t = e\mathbf{E}/\hbar$, the results

$$\begin{aligned} \frac{\partial a_L}{\partial t} = & - i \frac{e}{m} \mathbf{E} \cdot \sum'_N a_N \frac{1}{\omega_{LN}} \left\{ \int dv_0 u_L^* \nabla u_N \right\} \\ & \times \exp i \left[\int_0^t \omega_{LN} d\tau + (S_N - S_L) \right]. \end{aligned} \quad (29)$$

For transitions between valence and conduction bands only, (29) reduces to (7).

APPENDIX B

The Relationship between Current Density and Energy

The expectation value, or volume average, of the probability current density in the presence of an electromagnetic field is given by

$$\mathbf{J} = \frac{e}{mV} \langle \mathbf{p} - \frac{e}{c} \mathbf{A} \rangle. \quad (30)$$

Considering only transitions between the valence and conduction bands for the wave function of (4), the current density determined from (30) becomes

$$\begin{aligned} \mathbf{J} = & -i \frac{e\hbar}{mV} \int d^3k \left\{ i\mathbf{K}(|a_c|^2 + |a_v|^2) + |a_c|^2 \int dv_0 u_c^* \nabla u_c \right. \\ & + |a_v|^2 \int dv_0 u_v^* \nabla u_v + a_c^* a_v \mathbf{M} \exp i \left[\int_0^t \omega_{cv} d\tau + (S_v - S_c) \right] \\ & \left. - a_c a_v^* \mathbf{M}^* \exp -i \left[\int_0^t \omega_{cv} d\tau + (S_v - S_c) \right] \right\}. \end{aligned} \quad (31)$$

Equation (31) can be simplified considerably by making use of the relationship⁹

$$i \frac{m}{\hbar^2} \nabla_K \mathcal{E}_N(\mathbf{K}) = i\mathbf{K} + \int dv_0 u_N^*(\mathbf{r}; \mathbf{K}) \nabla u_N(\mathbf{r}; \mathbf{K}). \quad (32)$$

Combining (31) and (32) results in the expression

$$\begin{aligned} \mathbf{J} = & -i \frac{e\hbar}{mV} \int d^3k \left\{ i \frac{m}{\hbar^2} (|a_c|^2 \nabla_K \mathcal{E}_c + |a_v|^2 \nabla_K \mathcal{E}_v) \right. \\ & + a_c^* a_v \mathbf{M} \exp i \left[\int_0^t \omega_{cv} d\tau + (S_v - S_c) \right] \\ & \left. - a_c a_v^* \mathbf{M}^* \exp -i \left[\int_0^t \omega_{cv} d\tau + (S_v - S_c) \right] \right\}. \end{aligned} \quad (33)$$

The energy density, W , for the quantized semiconductor system is given by (11). By differentiating W with respect to time, one has

$$\begin{aligned} \frac{\partial W}{\partial t} = & \frac{1}{V} \left[|a_c|^2 \frac{\partial \mathbf{K}}{\partial t} \cdot \nabla_K \mathcal{E}_c + |a_v|^2 \frac{\partial \mathbf{K}}{\partial t} \cdot \nabla_K \mathcal{E}_v \right. \\ & + \left(a_c^* \frac{\partial a_c}{\partial t} + a_c \frac{\partial a_c^*}{\partial t} \right) \mathcal{E}_c + \left(a_v^* \frac{\partial a_v}{\partial t} + a_v \frac{\partial a_v^*}{\partial t} \right) \mathcal{E}_v \left. \right]. \end{aligned} \quad (34)$$

Now, from the preceding work in Appendix A the time dependences of a_c and a_v are known and, for the present situation, are given by (7). Thus by combining (7) with (34) and noting that $\partial \mathbf{K} / \partial t = e\mathbf{E}/\hbar$, one obtains the following formula for $\partial W / \partial t$:

$$\begin{aligned} \frac{\partial W}{\partial t} = & \frac{1}{V} \frac{e}{\hbar} \mathbf{E} \cdot \left\{ |a_c|^2 \nabla_K \mathcal{E}_c + |a_v|^2 \nabla_K \mathcal{E}_v \right. \\ & - i \frac{\hbar^2}{m} a_c^* a_v \mathbf{M} \exp i \left[\int_0^t \omega_{cv} d\tau + (S_v - S_c) \right] \\ & \left. + i \frac{\hbar^2}{m} a_c a_v^* \mathbf{M}^* \exp -i \left[\int_0^t \omega_{cv} d\tau + (S_v - S_c) \right] \right\}. \end{aligned} \quad (35)$$

A comparison of (33) and (36) illustrates the desired relationship between current density and energy density, viz.,

$$\mathbf{j} \cdot \mathbf{E} = \partial W / \partial t, \quad (36)$$

where $\mathbf{J} \equiv \int d^3 k \mathbf{j}$.

REFERENCES

1. Franz, W., Z. Naturforsch, **13a**, 1958, p. 484.
2. Keldysh, L. V., Soviet Phys. JETP, **7**, 1958, p. 788; Keldysh, L. V., Vavilov, V. S., and Britsyn, K. I., in *Proceedings of the International Conference on Semiconductor Physics, Prague, 1960*, publ. Czechoslovakian Academy of Sciences, Prague, 1961, p. 824.
3. Braunstein, R., Phys. Rev., **125**, Jan. 15, 1962, p. 475.
4. Riesz, R. P., Rev. Sci. Instr., **33**, Sept., 1962, p. 994.
5. DiDomenico, M., Jr., Pantell, R. H., Svelto, O., and Weaver, J. N., Appl. Phys. Letters, **1**, Dec., 1962, p. 77.
6. Houston, W. V., Phys. Rev., **57**, Feb. 1, 1940, p. 184.
7. Bardeen, J., Blatt, J., and Hall, L., in *Photoconductivity Conference*, John Wiley and Sons, New York, 1956, p. 146.
8. Pantell, R. H., DiDomenico, M., Jr., Svelto, O., and Weaver, J. N., paper presented at the Third International Quantum Electronics Conference, Paris, France, February, 1963.
9. Wilson, A. H., *The Theory of Metals*, 2nd. ed., Cambridge University Press, Cambridge, England, 1953.

Contributors to This Issue

W. S. BROWN, B.S., 1956, Yale University; Ph.D., 1961, Princeton University; Bell Telephone Laboratories, 1961—. Since joining Bell Laboratories, Mr. Brown has been working on the theoretical and practical problems of symbolic computing. Member, American Physical Society, Association for Computing Machinery, Phi Beta Kappa, Sigma Xi, and AAAS.

M. DiDOMENICO, Jr., B.S., 1958, M.S., 1959, Ph.D., 1963, Stanford University; Bell Telephone Laboratories, 1962—. He has been engaged in investigations on electro-optics and electro-optic light modulators. He has also worked on photoconductive detectors of microwave modulated light, and has been concerned with the physical processes involved in solid-state photodetectors. Member, American Physical Society, IEEE, Sigma Xi and Tau Beta Pi.

G. P. ESPINOSA, B.A., 1961, University of Connecticut; Bell Telephone Laboratories, 1961—. He has been chiefly concerned with crystal-chemical studies of garnets.

SEYMOUR GELLER, A.B., 1941, and Ph.D., 1949, Cornell University; DuPont Postdoctoral Fellow at Cornell, 1949–50; DuPont Company, 1950–52; Bell Telephone Laboratories, 1952—. At Bell Laboratories he has specialized in studies of crystal structure, with emphasis on crystal chemistry studies and the relation of the properties of crystals to their structures. Fellow, American Physical Society; Member, American Crystallographic Association, Mineralogical Society of America, Summit Association of Scientists (of the Research Society of America), Sigma Xi and Phi Kappa Phi.

JOHN P. HYDE, A.B., Princeton University, 1959; M.S., Northwestern University, 1960; Bell Telephone Laboratories, 1960—. He has worked on machine aids to design, and especially computer aids to sequential

circuit synthesis. He is presently engaged in further development of the ALPAK system and other aspects of computer algebra.

DAVID A. LEWINSKI, B.Sc. Hons., 1952 and M.Sc., 1956, University of Manitoba; Bell Telephone Company of Canada, 1954-1956; Bell Telephone Laboratories, 1956—. At Bell Laboratories he has been concerned mainly with the systems engineering aspects of message circuit noise evaluation, in particular with studies to describe the subjective effects of noise on speech transmission and surveys to assess Bell System message circuit noise performance. He has taught in the out-of-hours study program. At present he supervises a group working on transmission objectives for voice-band data communications. Member, The Mathematical Association of America.

GOTTFRIED W. LUDERER, Dipl. Ing. E.E., 1959, Technische Hochschule, Braunschweig, Germany; 1959-62, Scientific Assistant at the Computation Center, Technische Hochschule Braunschweig; since 1962 at the Institut fuer Hoechstfrequenztechnik, Technische Hochschule, Braunschweig. Mr. Luderer is presently engaged in research in microwaves. Member, IEEE, German Association for Applied Mathematics and Mechanics, German Communication Engineering Society.

DIETRICH MARCUSE, Diplom Vorprüfung, 1952, and Dipl. Phys., 1954, Berlin Free University; D.E.E., 1962, Technische Hochschule, Karlsruhe, Germany; Siemens and Halske (Germany), 1954-1957; Bell Telephone Laboratories, 1957—. At Siemens and Halske Mr. Marcuse was engaged in transmission research, studying coaxial cable and circular waveguide transmission. At Bell Laboratories he has been engaged in studies of circular electric waveguides and work on gaseous masers. Member, IEEE.

SAMUEL P. MORGAN, B.S., 1943, M.S., 1944, and Ph.D., 1947, California Institute of Technology; Bell Telephone Laboratories, 1947—. A research mathematician, Mr. Morgan has been particularly concerned with the applications of electromagnetic theory to microwave and other problems. As Head, Mathematical Physics Department, he now supervises a research group in various fields of mathematical physics. Fellow, IEEE; member, American Physical Society, Sigma Xi, Tau Beta Pi and AAAS.

INGEMAR NÅSELL, Civilingenjör, 1955, Royal Institute of Technology, Stockholm, Sweden; M.E.E., 1962, New York University; Research

Institute of National Defense, Stockholm, Sweden, 1955-1960; Bell Telephone Laboratories, 1960-. At Bell Laboratories he has been engaged in various aspects of the work on new noise objectives. In this connection, he has introduced probability sampling techniques as a tool for surveying the transmission performance of different parts of the toll network. He is presently engaged in further work on such surveys in order to acquire the information necessary for building a mathematical model of the Bell System toll network. Member, Svenska Teknologföreningen, Acoustical Society of America, and Eta Kappa Nu.

RICHARD H. PANTELL, B.S. and M.S., 1950, Massachusetts Institute of Technology; Ph.D., 1954, Stanford University; Instructor in Electrical Engineering, Brooklyn Polytechnic Institute, 1950-51; Research Assistant, Stanford Electronics Research Laboratory, 1951-54; Assistant Professor of Electrical Engineering, Stanford University, 1954-56; Visiting Assistant Professor, University of Illinois, 1956-57; Professor of Electrical Engineering, Stanford University, 1957-. At Stanford University he is continuing his research into the generation of microwave energy.

E. O. SCHULZ-DUBOIS, Dipl. phys., 1950, and Dr. phil. nat., 1954, Johann Wolfgang Goethe University (Germany); Purdue University, 1954-1955; Raytheon Manufacturing Co., 1956-1957; Bell Telephone Laboratories, 1957-. At Purdue Mr. Schulz-DuBois was engaged in paramagnetic resonance studies of irradiated semiconductors. At Raytheon he was concerned with the development of ferrite materials and devices. After joining Bell Laboratories his work was with paramagnetic materials, slow-wave structures, and ferrimagnetic isolators for application to solid state maser devices. More recently he was responsible for a group engaged in advanced development of traveling-wave masers and in related exploratory studies. Since September 1963 he has been on sabbatical leave as visiting professor at Technische Hochschule, Karlsruhe (Germany).

RICHARD C. SHERWOOD, Cert. Ind. Chem., 1952, Franklin Technical Institute; Bell Telephone Laboratories, 1952-. He has worked on research in magnetism, including studies of ferromagnetic domains. At present he is working on susceptibility measurements at low temperatures. Member, American Physical Society.

ORAZIO SVELTO, degree in nuclear engineering, Politecnico di Milano, Milan, Italy, 1960; Instituto di Fisica del Politecnico di Milano, 1960-61;

Microwave Laboratory, Stanford University, 1961-62; Instituto di Fisica del Politecnico di Milano, 1963—. He has worked on nuclear paramagnetic resonance studies, optical masers, and is presently working on optical masers and nonlinear optical effects.

BERKLEY A. TAGUE, B.A., 1958 Wesleyan University, S.M., 1960, Massachusetts Institute of Technology; Bell Telephone Laboratories, 1960—. He has worked in the general field of digital computers, with particular emphasis on stochastic simulation, instruction in computers and computer programming, and new computer applications. Member, Association for Computing Machinery, Mathematical Association of America, Sigma Xi and Phi Beta Kappa.

HANS-GEORG UNGER, Dipl. Ing., 1951 and Dr. Ing., 1954, Technische Hochschule, Braunschweig (Germany); Siemens and Halske (Germany), 1951-55; Bell Telephone Laboratories, 1956-1961. His work at Bell Laboratories was in research in waveguides, especially circular electric wave transmission. He is now Professor of Electrical Engineering at the Technische Hochschule in Braunschweig. Senior member, IEEE; member, German Communication Engineering Society.

H. J. WILLIAMS, A.B. 1925, University of Wisconsin; Western Electric Co., 1926-27; graduate studies at University of Wisconsin 1927-29; Bell Telephone Laboratories, 1929—. He has been engaged in the study of magnetic materials and magnetic domain structures. He is presently investigating the magnetic properties of alloys and compounds at low temperatures. Fellow, American Physical Society.

47n
7086-7-3